DEVELOPMENT OF SCAFFOLDS FOR OESOPHAGEAL TISSUE ENGINEERING

LEONG MENG FATT

School of Mechanical and Aerospace Engineering

A thesis submitted to the Nanyang Technological University
in fulfillment of the requirement for the degree of
Doctor of Philosophy

2009

To my wife, Ching Yee and our son, Amos

ACKNOWLEDGEMENTS

Many people have contributed either directly or indirectly to this project; I would like to mention them in acknowledgement of their contributions.

(1) Associate Professor Sandy Chian deserved many thanks for his invaluable advice and tireless tutelage throughout the course of this project. He has provided me with many opportunities, which have developed my skills and enriched my experiences in the field of research tremendously.

(2) Associate Professor Walter Hunziker, who is the project co-supervisor from the Institute of Molecular and Cell Biology (IMCB), has shared his knowledge in isolating primary porcine oesophageal epithelial cells at the onset of the project.

(3) Professor Buddy Ratner and his associates from University of Washington Engineered Biomaterials (UWEB) have provided the training and resources during my two month stint in his laboratory to learn histochemical techniques.

(4) Ms. Lim Tze Chiun has altruistically shared her knowledge in frost formation and cryogenic system, which has led to the development of the cryogenic electrospinning technique.

(5) Dr. Mohamed Zulfikar Rasheed has performed the animal surgeries and assisted in the analysis of the explants in the *in vivo* studies.

(6) Mr. Chan Wing Yue has conducted the primary harvesting of porcine oesophageal cells and co-developed the co-culture protocols for the cells.

(7) Ms. Pamela Gopal has supplied the acellular porcine oesophageal tissue for the work involving the hybrid scaffold.

(8) Ms. Heng Chee Hoon and Mr. Simon Teo have provided the logisitics support throughout the project.

Lastly, I would like to thank the Agency of Science, Technology and Research (A*STAR) for providing the graduate scholarship for the past 4 years.

PUBLICATIONS

The list of publications reported over the course of this candidature is as follows:

Patent applications

(1) M.F. Leong, T.C. Lim, K.S. Chian, *Manufacturing three-dimensional scaffolds using electrospinning at low temperatures*, PCT application no: PCT/SG2007/000413. 5th December 2006.

(2) K.S. Chian, M.F. Leong, E.W. Gopal, B.D. Ratner, *Three-dimensional porous hybrid scaffold and manufacture thereof*, PCT application no: PCT/SG2007/000414. 5th December 2006.

Journal papers

(1) M.F. Leong, M.Z. Rasheed, T.C. Lim, K.S. Chian, *In vitro cell infiltration and in vivo cell infiltration and vascularization in a fibrous, highly porous poly(D,L-lactide) scaffold fabricated by cryogenic electrospinning technique*, Journal of Biomedical Materials Research Part A. Accepted June 2008. DOI 10.1002/jbm.a.32208.
Impact factor = 2.612, Citation = Not applicable.

(2) M.F. Leong, K.S. Chian, P.S. Mhaisalkar, W.F. Ong, B.D. Ratner, *Effect of electrospun poly(D,L-lactide) (PLA) fibrous scaffold with nano-porous surface on attachment of porcine oesophageal epithelial cells (PEECs) and protein adsorption*, Journal of Biomedical Materials Research Part A. 2009, 89A, 1040-1048.
Impact factor = 2.612, Citation = 0.

(3) Y.B. Zhu, M.F. Leong, W.F. Ong, M.C. Park, K.S. Chian, *Oesophageal epithelium regeneration of fibronectin grafted poly(L-lactide-co-caprolactone) (PLLC) nanofiber scaffold*, Biomaterials. 2007, 28, 861-868.
Impact factor = 6.262, Citation = 12 (as of 15th May 2009).

Conference papers (speaker underlined)

(1) M.Z. Rasheed, M.F. Leong, K.S. Chian, C. Song, A novel cryogenic electrospun scaffold with large three dimensional pores enhances cellular infiltration and vascular ingrowth, Singapore General Hospital (SGH) 17th Annual Scientific Meeting, SGH, Singapore, April 2008.

(2) M.F. Leong, T.C. Lim, K.S. Chian, B.D. Ratner, *Novel cryogenic electrospinning technique to enlarge the pore size of electrospun scaffolds*, TERMIS North America 2007 Conference and Exposition, Toronto, Canada, June 2007.

(3) K.H. Lim, S. Salgues, E.T. Ooi, N. Grousson, M.F. Leong, J.H. Yeo, W.A. Goetz, *Is the single point attached commissures implantation technique reliable? A computational study*, 14th Annual Meeting of the Asian Society for Cardiovascular Surgery, Osaka, Japan, June 2006.

(4) K.S. Chian, M.F. Leong, P.Gopal, B.D. Ratner, *Development of electrospun tissue engineered scaffold with porous nanofibres and their effect on cell adhesion,* 8th Tissue Engineering Society International (TESI) Meeting, Shanghai, China, October 2005.

(5) A.W.C. Chua, M.F. Leong, I.C. Song, R. Ng, C. Song, K.S. Chian, *A bilayered scaffold for the development of composite skin construct*, 7th Annual NTU-SGH Symposium 2005, Singapore, August 2005.

Journal paper in preparation

(1) Bilayered electrospun scaffold and its effects on *in vitro* and *in vivo* cell infiltration and *in vivo* vascularization.

TABLE OF CONTENTS

Chapter 6 Results and Discussion

LIST OF FIGURES

LIST OF TABLES

ABSTRACT

Tissue engineering has emerged as a potential solution to replace diseased or defective organs. This project describes the development and characterization of a tissue engineered scaffold that is suitable for the replacement of the oesophagus. Electrospinning is chosen as the fabrication method for the scaffold. Despite the versatility of the electrospinning process in fabricating fibrous scaffold, it suffers from the severe limitation of producing scaffold with microscale pores (< 5μm) that inhibit cell infiltration. In this project, a technique that uses ice crystals as templates to fabricate cryogenic electrospun scaffolds (CES) with large three-dimensional and interconnected pores using poly(D,L-lactide) (PLA) was developed. The pore sizes were controlled by manipulating the environment's humidity, mandrel temperature and solution flow rate. Our results show that cells infiltrated the CES up to 50μm in thickness i*n vitro* under static culture conditions whereas cells infiltration was limited in the ES. A bilayered electrospun scaffold (BLES) consisting of an ES layer and a CES layer was fabricated for the co-culture of porcine oesophageal epithelial (PEECs) and smooth muscle cells (PESMCs) *in vitro*. The BLES was successful in separating both cells types, with the ES layer acting as the basement membrane for the PEECs while the CES layer supporting the growth and infiltration of the PESMCs. *In vivo* studies demonstrated improved cell infiltration and vascularization in the CES compared to ES. These results demonstrate the feasibility of using the cryogenic electrospinning technique to fabricate scaffolds for oesophageal regeneration. In overcoming the limitation of conventional ES, it is believed that the contributions made in this project will advance the adoption of cryogenic electrospinning as a method of scaffold fabrication in tissue engineering.

Chapter 1 Introduction

1.1 Tissue Engineering – a solution to organ shortages

Organ failure is one of the most severe and expensive conditions in medicine. In the United States alone, the total expenditure on healthcare services related to organ failure amounts to US$400 billion annually.[1] Organ transplantation is the typical therapy to treat patients with loss or failure of organs. Over the past 50 years, advances in surgical techniques, anaesthesia practices and immunosuppressive drugs had facilitated the development of organ transplantation to include ectodermal, endodermal and mesodermal tissues.[1-3] Other therapies such as synthetic prostheses (e.g. artificial hip joint), pharmaceutical delivery systems (e.g. insulin for diabetic patients), and medical devices (e.g. kidney dialyzers) are also available to treat patients with organ failure.[4]

However, these treatment methods have their shortcomings in solving the issues related to organ failure. Organs for transplantation can be of xenogeneic, autologous or allogeneic origins.[5] Xenogeneic transplantation has risks of immunogenic rejection and transmission of animal diseases.[6] Autologous transplantation depends largely on the availability of donor sites and the health of the patient. Allogeneic organ transplantation has problems of immunogenic rejection and donor shortage.[7] There is a lack of good strategies for immunosuppression. This is worsened by the lack of suitable organ donors. In the United States, patients on the waiting list were approximately 6.7 times the number of transplants performed in 2006.[8] As shown in Figure 1.1, the difference between the number of patients on the waiting list and the number of transplants performed has been increasing for the past decade. In addition to this large discrepancy, since 2001, approximately 7,000 patients die each year

while waiting for a transplant.[8] Hence, although allogeneic transplantation is beneficial, the lack of a constant supply of suitable organs often causes practitioners to look for alternative methods of treatment. Alternative treatment such as the use of synthetic prostheses has issues of biocompatibility, thrombogenicity and durability. Other therapies using drugs and medical devices are short-term solutions that require multiple dosages and frequent treatments respectively, which often cause discomfort and inconvenience to the patients.

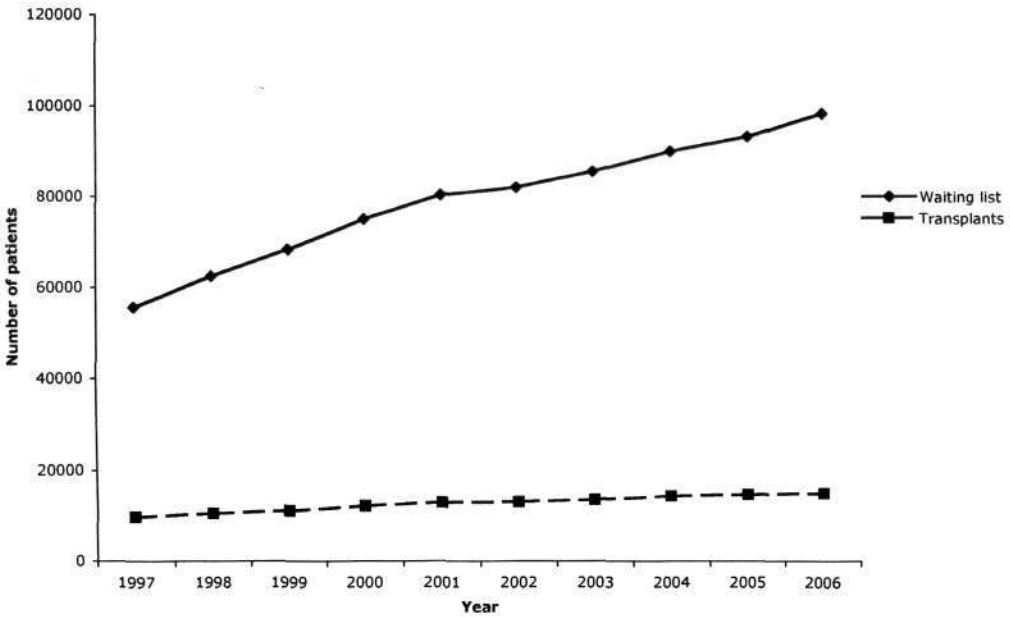

Figure 1.1 Graph showing the increasing number of patients on the waiting list, compared to the small number of transplants performed between 1997 – 2006. Data as of May 1st 2007. Adapted from UNOS, 2007.[8]

Tissue engineering has become a potential solution to organ shortages while attempting to exclude the shortcomings of current therapies. It is an emerging field that involves the principles of engineering and the knowledge of biological sciences to design functional substitutes for tissue replacement.[1,2] It combines techniques in cell harvesting, scaffold fabrication and bioreactor design, and aims to create three-

dimensional functional constructs by integrating cells with an engineered scaffold *in vitro* or using these scaffolds to recruit the appropriate cells *in vivo*.[9-11] Tissue engineered products such as Apligraf® (Organogenesis), Carticel® (Genzyme Biosurgery) and Dermagraft® (Advanced Tissue Science) have been approved by the United States Food and Drug Administration (FDA) and used for clinical applications.[12,13] To date, Apligraf® has been successfully applied to 150,00 patients in the United States.[14] The success of these products shows that tissue engineered products have the potential to solve the problem of organ shortages on the clinical platform.

1.2 Oesophagus and oesophageal cancer

Tissue engineering offers an opportunity to create a functional replacement for the diseased tissue. The tissue of interests in this project is the oesophagus. Cancer can develop in the oesophagus, affecting the normal function of the tissue. Oesophageal cancer is the sixth most common cancerous malignancy among male and ninth most common among female worldwide in 2002.[15] It affects approximately twice as many male than female. In Singapore, there were 166 cases with 144 reported deaths associated with oesophageal cancer in 2002.[15] In the United States, there were 14,351 patients diagnosed with oesophageal cancer in 2002, and there were an estimated 12,689 deaths associated with the disease in the same year.[15] Although its incidence rate remains low in the American and European continents, a disturbingly high occurrence has been reported in regions spanning from Iran to China. In Year 2002, of the 462,117 cases reported worldwide, 331,130 cases (approximately 72%) were from

these regions known as the 'Oesophageal Cancer Belt of South-Central Asia'.[15] Figure 1.2 shows the distribution of the disease around the world.

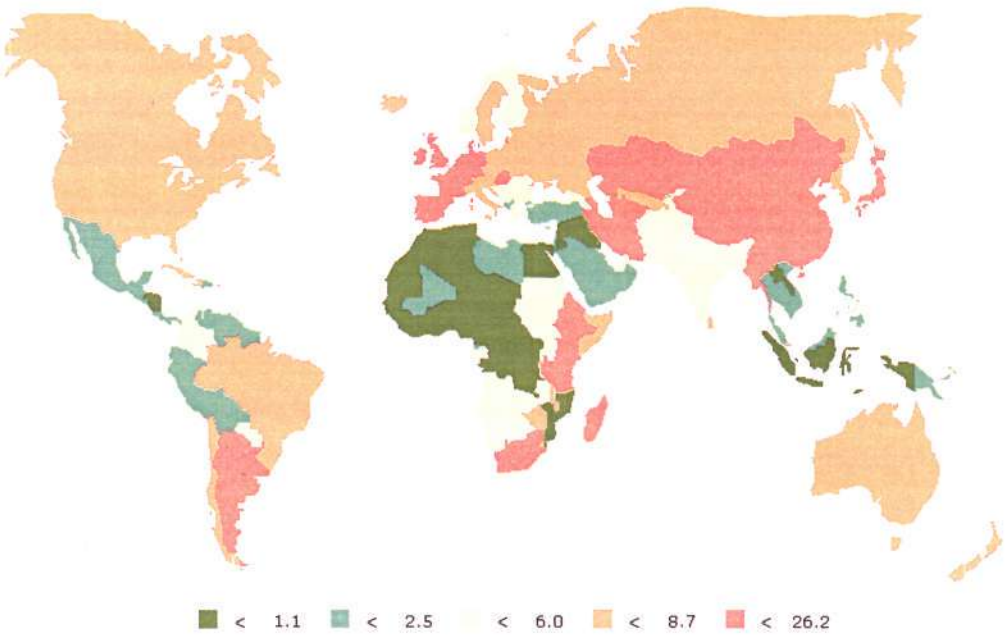

(a)

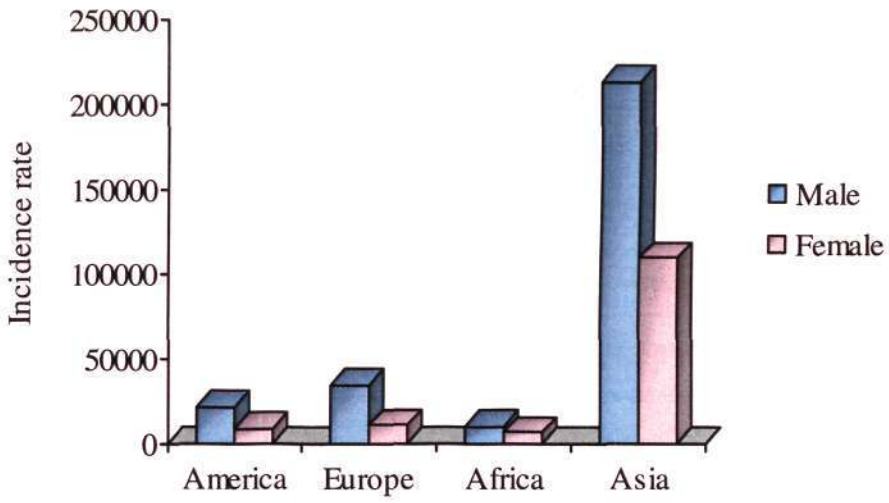

(b)

Figure 1.2 (a) Geographical distribution of oesophageal cancer incidence per 100,000 in Year 2002, (b) Incidence rate by continents and gender in Year 2002. Data used to plot figures are adapted from Ferlay, 2004.[15]

Oesophageal cancer is one of the most challenging gastrointestinal diseases to treat. There are two main types of oesophageal cancer: squamous cell carcinoma and adenocarcinoma. Depending on the cancer type, the carcinoma can occur anywhere along the oesophagus. Currently, two common types of surgical treatments for oesophageal cancer are: oesophagectomy and oesophagogastrectomy.[16] Oesophagectomy involves the removal of affected areas of the oesophagus and nearby lymph nodes. Oesophagogastrectomy involves the removal of affected areas of the oesophagus, nearby lymph nodes and the upper part of the stomach. In both types of operation, the oesophagus is re-connected to the stomach, either directly or by extending with an autologous small intestine. The efficiency for nutrients intake of the gastrointestinal tract, especially for patients who have undergone oesophagogastrectomy, is lowered as the reduction in length causes the function of the tract to be compromised.[16] Hence, these surgical treatments are traumatic for patients. On the contrary, if oesophageal cancer is left untreated, 92% of the cancer patients will not survive after 5 years of diagnosis.[15] This is partly due to the fact that the disease is normally diagnosed at the later stage of the cancer.

In order to reduce patients' post-operative stress, improve the success rate of surgical treatments and preserve the healthy segment of the gastrointestinal tract, there is a need to develop a functional replacement for the diseased oesophagus.

1.3 Objectives of project

The objective of this project is to develop a scaffold that is suitable in creating a functional replacement for the diseased oesophagus. Electrospinning is developed as a scaffold fabrication technique for the regeneration of the oesophageal tissue.

Electrospinning of polymeric fibers has recently gained interest as one of the methods for fabricating tissue engineered scaffolds.[17] One notable advantage of electrospinning is that it can closely mimic the nano-scale fibrous and porous nature of the extracellular matrices in different organs.[18] This similarity is important in promoting cell attachment and providing three-dimensional guidance for cell proliferation. However, the major obstacle to the use of electrospun scaffolds in tissue engineering is the lack of control of the inherently small pore size.[19] This limits cell infiltration and vascular ingrowth, which are important factors when creating large tissue constructs.

Our key goals are to (1) develop a technique to enlarge and control the pore size of electrospun scaffold to allow *in vitro* cell infiltration and *in vivo* cell infiltration and vascularization, (2) design and fabricate scaffolds with suitable pore size to serve as surrogate structures for the anchorage, proliferation, infiltration and organization of various oesophageal cells and (3) test the performance of these scaffolds *in vitro and in vivo* to show the feasibility of using these constructs as functional replacements for oesophageal regeneration.

Chapter 2 Literature Review

This chapter provides a comprehensive review on the topics related to this project. The function and anatomy of the oesophagus are presented to highlight the intricacy in the tissue engineering of a complex organ. Next, the requirements for tissue engineered scaffolds are listed to serve as guidelines for our scaffold designs. A review on current techniques for scaffold fabrication is provided. This is followed by a review on two separate topics that are used extensively in this project, namely electrospinning and frost formation, in subsequent chapters.

2.1 The oesophagus

2.1.1 Function of the oesophagus

The oesophagus is a muscular tissue that is connected to the pharynx by the upper oesophageal sphincter and to the stomach by the lower oesophageal sphincter.[20,21] On the average, an adult oesophagus is 25cm in length and 2cm in diameter. In children, the length of the oesophagus varies with height.[22] The primary function of the oesophagus is to transport food from the oral cavity to the stomach.[23] After ingestion, the synchronized voluntary peristaltic motions of skeletal muscle cells, located in the cervical segment of the oesophagus, transport food bolus towards the stomach. The convoluted folds of the lumen facilitate these coordinated contractions and expansions of the oesophagus. Figure 2.1 shows the complex structure of the oesophagus.

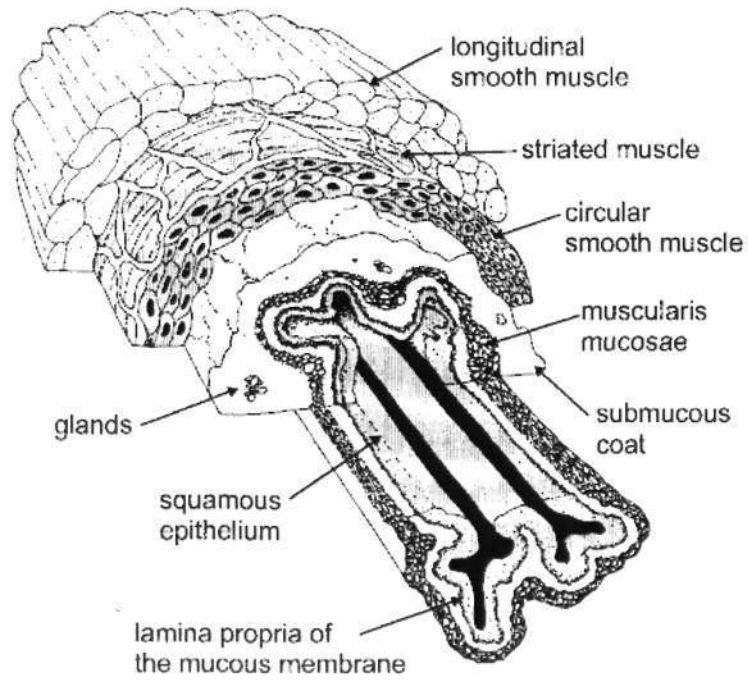

Figure 2.1 Different layers of the eesophagus. Adapted from Squier, 2001.[23]

2.1.2 Anatomy of the oesophagus

The oesophagus comprises of four distinct layers: the mucosa, submucosa, muscularis externa and adventitia.[22,24] The mucosa consists of a stratified squamous epithelium, lamina propria and muscularis mucosa. The stratified squamous epithelium spans the entire luminal side of the oesophagus and provides a non-keratinized primary protective layer for the remaining tissue. Basal epithelial cells are columnar and subsequent layers of epithelial cells gradually become flattened as differentiation occurs. Typical human epithelium has 20-24 layers of stratification to protect the underlying tissues.[24,25] The basal epithelial cells are attached to a dense basement membrane made up of collagen fibers. The collagen fibers are randomly oriented and are generally less than 1μm in diameter.[18,26] This basement membrane, typically 5μm thick, physically separates the epithelial cells from the underlying fibroblasts and muscle cells in the lamina propria and mucosa[27]. It is important that the basement

membrane remains intact and continuous to serve as a physical barrier. Structural fragmentation of the basement membrane has been correlated to the development of inflammatory lesions progressing from hyperplastic to dysplastic epithelium and to squamous cell carcinoma.[27] Lamina propria is a continuous layer of loose connective tissue between the epithelium and the muscularis mucosa.[22] It provides a secondary defensive front as it contains lymphocytes. The muscularis mucosa is scattered between the mucosa and submucosa. It comprises of smooth muscle cells oriented longitudinally to provide localized contractility to the mucosa.[22,24] The submucosa is made up of loose connective tissues that facilitate the movement of the mucosa during peristalsis. The collagen fibers located in the submucosa are less dense as compared to the basal membrane. The muscularis externa is made up of skeletal muscle cells in the cervical and upper thoracic segments (top one-third) and smooth muscle cells in the middle thoracic and lower thoracic segments (lower two-thirds).[22] The smooth muscle cells are organized into two distinct layers, the circular smooth muscle layer and the longitudinal smooth muscle layer (Figure 2.1).[22-24] These muscles are oriented to provide the coordinated contractility during peristalsis. The adventitia is a loose connective tissue that forms a sheath around the abluminal side of the oesophagus. It connects the oesophagus to adjacent organs, hence providing structural support for the oesophagus.[22,24]

In order to study the histological and morphological structure of the oesophageal extracellular matrix, an analysis of the histoarchitecture of the porcine oesophagus is conducted in this project. The methodology can be found in Section 5.1 and the results are presented in Section 6.1.

2.1.3 Oesophageal tissue engineering

Early attempts with oesophageal reconstruction using non-biodegradable prostheses such as silicone and polyethylene tubes were not satisfactory and had severe complications.[28-32] These complications included excessive scarring, failure for complete healing, anastomotic leakages and stenosis of the prostheses. Other attempts using collagen with biodegradable polyesters[25,33,34] or silicones[35-40] showed more promising results. The biodegradable collagen promoted tissue remodeling and regeneration, hence it was an improvement from using synthetic prosthesis alone. However, these trials also presented issues such as anastomotic stenosis[33,35,36,38-41], leakage[34], shrinkage of the construct[37,39] and incomplete stratification of the epithelium.[25] Lately, more emphasis has been placed on acellular biologically derived scaffolds such as small intestinal submucosa (SIS), urinary bladder matrix (UBM), AlloDerm (Decellularized human dermal tissue) and porcine acellular aorta for oesophageal repair and reconstruction.[41-43] Isch *et al.* and Badylak *et al.* have shown that these acellular extracellular matrices offered promise as a patch replacement for oesophageal regeneration with complete re-epithelialization and vascularized loose connective tissues. However, stricture was still observed when these matrices were used for complete circumferential replacement. In 2006, Marzaro *et al.* reported using a homologous decellularized porcine oesophageal tissue repopulated with autologous oesophageal smooth muscle cells for oesophageal patch replacement *in vivo*.[44] The presence of the autologous cells improved the integration of the implant to the host tissues with lower inflammatory response. These preliminary results have demonstrated the feasibility of using a tissue engineered construct for oesophageal tissue repair.

2.2 Scaffolds for tissue engineering

2.2.1 Definition of scaffolds[1,45-47]

Scaffolds are temporary constructs that support cell attachment, proliferation, migration and differentiation. They are templates that orchestrate the three-dimensional organization of cells and tissue regeneration. They have interconnected porous micro-structures to allow cell infiltration and vascularization such that a thick three-dimensional construct can be supported *in vitro* or *in vivo*. In addition, they provide sufficient mechanical support during tissue regeneration and remodeling. Ideally, scaffolds should degrade during the formation of neo-tissue within the host.

2.2.2 Requirements of scaffolds

In order to engineer successful scaffolds for tissue regeneration, the design criteria need to be defined. These design requirements are: (1) interconnected pores with suitable pore sizes, (2) biocompatibility, (3) matching mechanical properties with host tissues, (4) controllable biodegradation behaviour and (5) appropriate surface chemistry and topography.[48] It is also desirable that the manufacturing process of the scaffold can be scaled-up consistently.[1]

2.2.2.1 Interconnected pores with suitable pore sizes

Tissue engineered scaffolds should have interconnected porous structures with suitable pore sizes for specific tissue applications. In general, it is known that large interconnected pores allow nutrients diffusion, cell infiltration and vascularization within the scaffolds.[49] For cell infiltration, it has been suggested that pore sizes greater than the diameter of a cell in suspension (5 – 15μm) allow limited cell infiltration when cells are seeded *in vitro*.[49,50] It has also been reported that optimum

ranges of pore size affect cell infiltration and tissue ingrowth differently.[51] These pore size ranges are summarized in Table 2.1. These values serve as good references when engineering specific tissues replacements.

Table. 2.1 Optimum pore size ranges for different tissue types. Adapted from Oh, 2007.[51]

Tissue types	Optimum pore size range (μm)
Fibroblast ingrowth	5 – 15
Hepatocyte ingrowth	~ 20
Chondrocyte ingrowth	70 – 120
Liver regeneration	45 – 150
Bone regeneration	100 - 400

In native extracellular matrices, it is also evident that size exclusion is used to prevent cell infiltration and separate different cell types. For example, basement membranes have pore sizes that are approximately 100nm and these are usually thin collagenous membranes that separate epithelial or endothelial cell types from the underlying connective tissues.[18,26] This is an important biomimetic cue to incorporate into the scaffold design for oesophageal tissue engineering since the oesophagus contains a basement membrane that separates the epithelium from the underlying connective tissue.

Another aspect of pore size is its effect on vascularization in implanted cell-scaffold constructs. Vascularization is essential to supply cells with oxygen and nutrients and to remove waste metabolites.[52,53] Hence, in order to engineer a thick tissue construct (100-200μm), the scaffold porous architecture has to promote rapid vascularization to ensure long term viability of the construct.[54,55] It has been reported that the optimum pore size for angiogenesis in an interconnected porous scaffold is 5μm in one report[56] and 35μm in another.[57] Although the values are different, it can be concluded that

pore sizes larger than 5μm are necessary for vascularization. Hence, tissue engineered scaffolds should have pores larger than 5μm in order to construct vascularized thick tissues.

Having reviewed the pore size requirements of a scaffold, it can be concluded that different ranges of pore size are needed for different tissue engineering applications. The pore sizes can vary from hundreds of nanometers to hundreds of micrometers. It is thus important that the scaffold fabrication technique is able to create different pore sizes for different applications.

2.2.2.2 Biocompatibility

Tissue engineering constructs can consist of biomaterials, cellular materials or combinations of both. When implanted in the body, these constructs are intended to serve as functional replacements for diseased tissues. Biocompatibility is the ability of the biomaterials, cellular materials or combination of both to elicit suitable host responses in specific tissue application.[58] It is important to understand the interactions between the constructs and the host in order to engineer successful tissue replacements with acceptable biocompatibility.

When an implant is introduced into the host, an injury is created at the implantation site. This brings about a cascade of mechanisms from the host to maintain homeostasis,[59,60] with the magnitude and duration of the variations in these mechanisms indicating the level of biocompatibility of the implant.[59] The subsequent host responses include acute and chronic inflammation, tissue granulation, foreign body reaction and the development of fibrous encapsulation.[59,61,62] The initial blood-

implant interactions are characterized by the injury to surrounding vascularized tissues, leading to formation of blood clots. Cytokines are released to recruit inflammatory cells to the injury site. During acute inflammation, leukocytes such as neutrophils and monocytes are recruited to the site. The monocytes then differentiate to macrophages, and these macrophages are responsible for recruiting fibroblasts and endothelial cells by releasing cytokines and growth factors in the chronic inflammation stage. The existence of fibroblasts, endothelial cells and vascularized capillaries are characteristics of granulation tissues. Due to the relatively large size of the implant, the macrophages usually do not phagocytose the entire implant, but undergo frustrated phagocytosis that results in the multi-nucleated foreign body giant cells engulfing the implants in the foreign body reaction.[63] The last stage of foreign body reaction involves deposition of a collagenous fibrous capsule around the implants, typically 50-200μm in thickness.[61] The description provided thus far is a general host response for implanted tissue constructs and the actual responses might defer due to the size and shape of the implant, the surface chemistry of the implant and the type of cells present in the tissue constructs. The characteristics of a normal foreign body reaction include the presence of macrophages and foreign body giant cells at the biomaterial-host tissue interface, fibroblasts depositing collagen and capillaries within the tissue construct.[60]

Other issues of biocompatibility such as immunological reactions, blood compatibility, carcinogenicity, mutagenicity and tetratogenicity are equally important but are beyond the scope of the studies presented in this project. The issues of immunology become particularly important when dealing with allogeneic or xenogeneic biomaterials or cell sources.

While the concepts of biocompatibility and host response to implanted tissue constructs have been discussed, questions regarding the assessment of biocompatibility remain unanswered thus far in this report. *In vitro* biocompatibility such as cytotoxicity can be tested using methods described by Northup.[64] These methods are documented in the International Standard Organization (ISO) 10,993 standard (Part 5) and they include direct contact test, agar diffusion test and elution test. *In vivo* host response of implants is studied by implantation of biomaterial at subcutaneous sites.[65] The response at the subcutaneous tissue is modulated by macrophages. These macrophages release cytokines and can affect the behaviour of fibroblasts at the implant site. Consequently, the thickness of the fibrous capsule deposited by the fibroblasts differs accordingly and it has been used as a measure of biocompatibility for the implant.

2.2.2.3 Mechanical properties

Macroscopically, for scaffolds to be used for tissue engineering implants, they have to be strong enough to withstand handling and to be sutured in place during surgical procedures.[48] In addition, the mechanical strength of the scaffolds has to be similar to that of the host tissue to avoid compliance mismatch. This implies that requirements in mechanical properties of scaffolds are different in engineered soft tissue from engineered hard tissue. Microscopically, Choquet *et al.* has shown that localized rigidity of scaffolds resulted in an increase in the strength of the cytoskeletal linkages.[66] This increase in strength affects the migration of cells on the scaffolds.

2.2.2.4 Controlled degradation behaviour

There are two aspects of degradation that have to be accounted for. They are namely (1) the degradation products and (2) the rate of degradation. Tissue engineered scaffolds are surrogate structural supports that are designed to degrade during the remodeling process to minimize foreign body response.[53,67] The degraded products of biomaterials should not cause any toxic or immunological response from the host body. This concept of degradation also relies heavily on the fact that the rate of degradation can be synchronized with the rate of tissue remodeling by the transplanted cells.[9,50,53] Any imbalance in the equilibrium will cause excessive fibrosis if tissue remodeling predominates or structural failure if degradation predominates. Using a dog model, Badylak *et al.* reported using a biodegradable acellular porcine extracellular matrix that had a ultimate tensile strength 10 times higher than that of the native oesophageal tissue for oesophageal reconstruction.[68] The implant was able to degrade and remodel progressively to match the ultimate tensile strength of the host tissue by 91 days after implantation, and a functionally acceptable oesophageal tissue was obtained.

2.2.2.5 Surface chemistry and topography

The surface chemistry and topography of a biomaterial is important as it is the surface that interacts with cells, adsorbs proteins and when implanted, affects the host response.[61] It has been shown that surface chemistry and topography affect cell attachment, proliferation and protein adsorption *in vitro*.[69,70] In an *in vivo* environment, the strategy is to modify surfaces with the right chemistry and topography to minimize foreign body reaction and non-specific protein

adsorptions.[61,63] Ideally, the surfaces of the implant should have the same signaling components as a wound surface such that normal healing response is promoted.[63]

2.2.2.6 Batch consistency

For tissue engineered scaffolds to be used as "off-the-shelf" products, batch consistency is essential as the outcome for each application has to be predictable. Hence, techniques used to fabricate tissue engineered scaffolds have to be suited for mass production to ensure the consistent quality of the products.

2.3 Current techniques for scaffold fabrication

There are many techniques developed to fabricate scaffolds that attempt to fulfill the requirements of tissue engineered scaffolds described in Section 2.2. These techniques include decellularization of tissues, rapid prototyping, self assembly, electrospinning and other multi-step techniques such as particulate leaching, phase separation and fiber bonding. In this section, these techniques will be reviewed for a better understanding of their potential in fabricating tissue engineered scaffolds.

2.3.1 Decellularization of tissues

Decellularization of tissues involves the removal of native cellular components with minimal impact on the structural and functional proteins in the extracellular matrices (ECM).[71,72] Two most widely used acellular matrices produced by decellularization of porcine and bovine tissues are the small intestinal submucosa (SIS)[73] and urinary bladder submucosa matrix (UBM).[74] These two acellular matrices, along with many other derived from porcine heart valves[71], porcine oesophagus[44] and bovine pericardia[75], have been used as allografts and xenografts in the repair and regeneration

of the oesophageal[41,44], dermal[76], vascular[77] and urethral[78-80] tissues in animal models. On the clinical platform, human pulmonary heart valves were decellularized and implanted successfully as allografts in patients that needed cardiac valve replacements.[81]. To produce these acellular matrices, tissues are typically treated with enzymes, chelating agents, detergents and sterilizing media and/or with mechanical abrasion to remove cellular components.[71-75] Figure 2.2 shows the surface morphology of the SIS after decellularization.[76] The SIS has a dense morphology on the luminal surface and a highly fibrous and porous structure on the ablumnial surface.

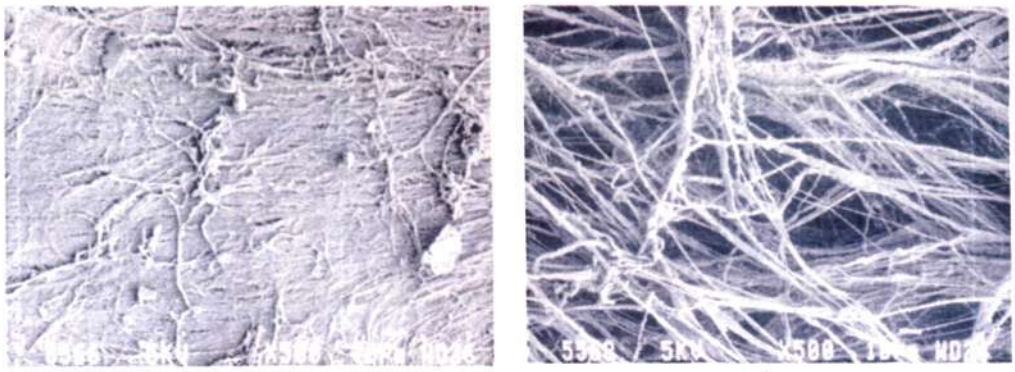

(a) (b)

Figure 2.2 SEM micrographs showing (a) luminal surface of SIS and (b) abluminal surface of SIS. Adapted from Lindberg, 2001.[76]

The advantages of fabricating scaffolds by decellularization of tissues are the preservation of native topography of extracellular matrices, inherent histo-architectures of structural collagen and the functional proteins. These are components necessary in promoting and simulating cell-matrix interactions in the native environment. Badylak *et al.* and Sandusky *et al.* have reported an improved wound healing response with acellular matrices compared to synthetic materials.[82,83] Acellular matrices, which consist predominantly of collagen fibers, are biodegradable and they are generally resorbed during tissue remodeling processes. In a particular

case, it has been reported that the degraded products of acellular matrices promoted migration of endothelial cells, hence inducing angiogenesis within the matrices.[84] And lastly, since structural proteins such as collagen and elastin are preserved in their native histo-architecture, both macroscopic and microscopic mechanical properties will be suitable for use in tissue engineering applications.

However, there are some disadvantages with using acellular matrices as tissue engineered scaffolds. When used as xenografts and allografts, these acellular matrices might induce immunogenic response from the host. There are risks of xenogeneic diseases transmission from donor to host.[6] It is difficult to maintain batch consistency as the naturally occurring matrices can differ from donors.[85] Supplies of the tissue are limited as they have to be harvested from suitable donors. In the case of xenogeneic transplantation, there are also ethical issues regarding humans receiving animal body parts as tissue replacements. Thus, despite acellular matrices satisfying most of the requirements of tissue engineered scaffolds, several issues have to be resolved before using them for tissue engineering applications.

2.3.2 Rapid prototyping

Rapid prototyping is a technique that involves the fabrication of precise microstructures using complex computing algorithm and advanced manufacturing technologies[86]. There are many different sub-fields in rapid prototyping, namely (1) selective laser sintering (SLS)[87,88], (2) fused deposition modeling (FDM)[89,90], (3) three-dimensional ink jet printing, and (4) photolithography.[91,92] SLS uses infrared laser beam to fuse powdered materials at elevated temperatures. The fusing of the powder produces porous structures that contain micro-scale features. The minimum

size of these features is typically 400μm and is limited by the dimension of the laser beam.[86] It has been used to fabricate porous structures with hydroxyapatite composites[87] and Nylon-6.[88] FDM involves heating a reservoir of material to molten state and dispensing this material as droplets to form a pre-programmed pattern.[86] Figure 2.3 shows the setup of FDM technique. The deposited droplets solidify as temperature decreases and subsequent molten droplets can be deposited on the solidified layers to create a three-dimensional microstructure. Fusion between layers is induced by the elevated temperature of the newly deposited molten droplets. The minimum diameter of the droplet is limited by the size of the nozzle. It has been used to fabricate porous scaffolds from polycaprolactone and thermoplastic elastomers for tissue engineering of cartilage.[89,90] Three-dimensional ink jet printing is similar to FDM, except that a binder layer is separately deposited to fuse two layers together. Photolithography uses templates created from silicon wafers and photoresists to mould microstructures with biomaterials.[86] The minimum size of the features is limited by the resolution of the stereolithography systems and is approximately 70μm.

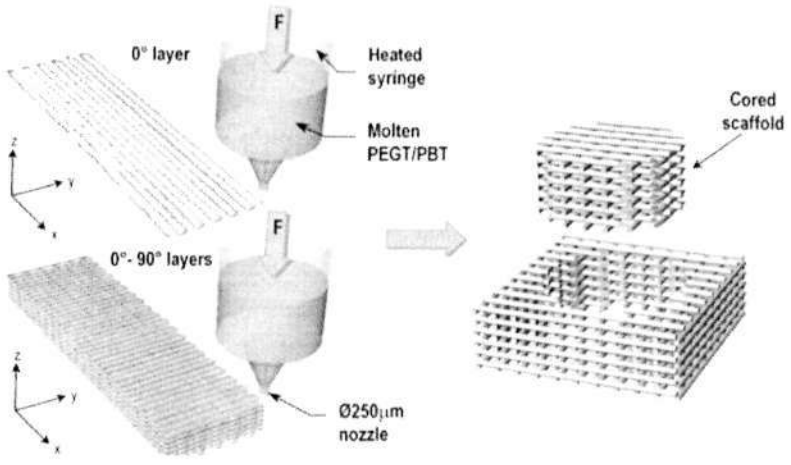

Figure 2.3 Fused deposition modeling technique. Adapted from Woodfield, 2004.[90]

The advantages of rapid prototyping techniques are the precise control of pore sizes and complex scaffold architectures.[47,86] Computing algorithm allows the use of stereolithographic data, obtained from scanning tissue using micro-computer tomography, to fabricate scaffolds that have similar architectural features.[88] In this way, it is possible to match the shape and size of the scaffolds with patients' tissues.

In tissue engineering applications, there are many limitations to the use of rapid prototyping. As most rapid prototyping techniques require elevated temperatures, biomaterials that undergo thermal degradation cannot be processed. As such, many materials used for rapid prototyping are neither biocompatible nor biodegradable.[86] Although complex scaffold designs can be fabricated, most rapid prototyping techniques are limited to micro-scale features. Therefore, the nano-scale pore size and features of the ECM described in Section 2.2.2.1 cannot be replicated using rapid prototyping techniques.

2.3.3 Multi-steps techniques

There are several scaffold fabrication techniques that require multiple steps in their processes. These techniques are grouped in this section as they can be used alone or in combination to produce porous scaffolds for tissue engineering. They are namely (1) particulate leaching[93-97], (2) phase separation[46,98-100] and (3) fiber bonding.[101]

2.3.3.1 Particulate leaching

Particulate leaching is a technique whereby the biomaterial is dissolved in a solvent and the particulates are suspended within the solution.[47] The mixture is cast in a mould and the solvent is allowed to evaporate. The particulates are leached out to

form the voids and a porous scaffold is formed with the remaining biomaterial.[95] This technique is often used to fabricate scaffolds from polyester based biomaterials with water-soluble particulates such as sodium chloride or sugar.[93,94] The scaffolds produced by this technique are highly porous (> 95%) and the pore sizes range from 30μm to 500μm (Figure 2.4).[93-97] Interconnectivity between the pores is ensured by fusing the particulates such that the pores were interconnected through the scaffold.[57,93,102]

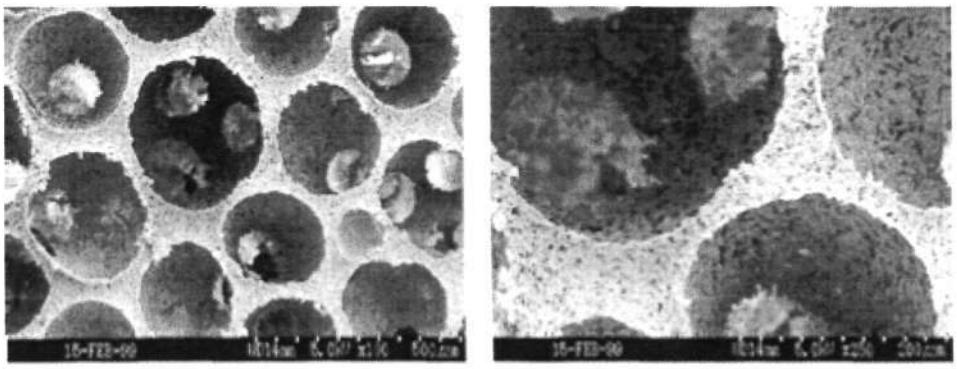

Figure 2.4 SEM micrographs of particulate leached scaffolds. Adapted from Ma, 2001.[95]

2.3.3.2 Phase separation

Phase separation is a technique which involves dissolving a biomaterial in a solvent and freezing the resulting solution at low temperatures.[47] The removal of the solvent by freeze drying leaves the biomaterial behind to form a porous and fibrous scaffold. As before, polyester based materials are often used[46,98,99]. It has been reported that the porosity of the scaffold is greater than 93% and fiber diameters range from 50 to 500nm.[99] Figure 2.5 shows the typical surface morphology of scaffolds fabricated by phase separation. When phase separation technique was combined with particulate leaching, the pore sizes ranged from 250 to 420μm.[46,100]

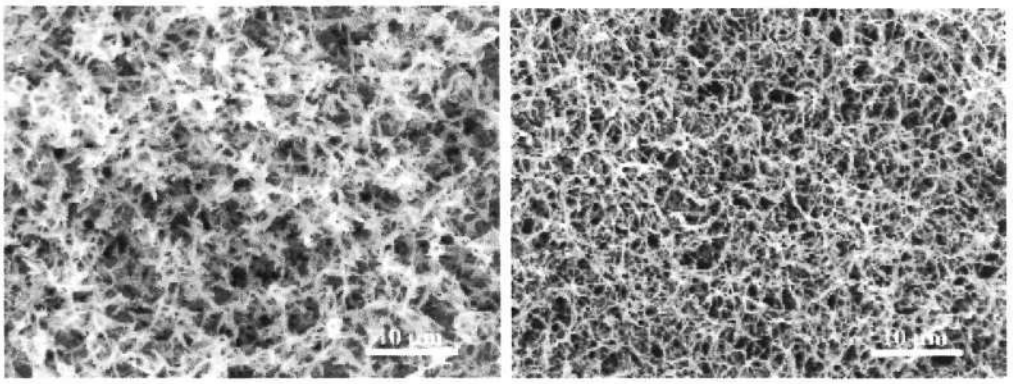

Figure 2.5 SEM micrographs of scaffolds fabricated using phase separation techniques. Adapted from Ma, 1999.[99]

2.3.3.3 Fiber bonding

Mikos *et al.* have developed a fiber bonding technique to produce a highly porous scaffold.[101] In this technique, poly(glycolide) (PGA) fibers were embedded in a solution containing methylene chloride and poly(lactide) (PLA). Methylene chloride was removed after evaporation and the two remaining polyesters were fused above their melting temperatures. PLA was removed by selective dissolution and the PGA fibers fused together to form a fibrous and porous matrix.

In summary, these multi-step techniques offer the advantage of having a highly porous scaffold design. The biomaterials that are processed by these techniques are biocompatible and biodegradable. In addition, the rate of biodegradation can be controlled by changing the pore sizes. However, the high porosity affects the macroscopic mechanical strength of the scaffolds. Thickness of the scaffold is limited as the leaching process will be inhibited. The techniques also involve multiple steps, which can be time consuming in mass production.

2.3.4 Self assembly

Self assembly is the non-intervened, reversible organization of components into regular patterns.[103] Zhang has provided a comprehensive review on the fabrication of nano-fibers using self assembly of protein and peptide molecules.[104] These molecules self assemble into nano-fibers with diameters less than 10nm by formation of intermolecular attractions such as hydrogen bonds, van der Waals forces and electrostatic attractions. A particular class of biomaterials, the peptide-amphiphiles, can be fabricated into nano-fibrous scaffolds by self-assembly.[105] Peptides-amphiphiles are unique as biological signals can be grafted within the backbone as peptide sequences that promote bioactivity. Malkar *et al.* have reported the selective bioactivity that can be incorporated within peptide-amphiphiles to promote cell recognition and signaling.[106] This technique is unique as nano-fibrous protein molecules can be assembled to form a scaffold that can be useful in tissue engineering applications. However, limited sample thickness, low productivity and availability of large pore sizes are issues that have to be addressed.[18,107]

Having reviewed the techniques available for scaffold fabrication, it is evident that each technique has its own advantages and disadvantages. The characteristics of these techniques are assessed using the criteria for tissue engineered scaffolds in Table 2.2. The technique of decellularization of tissue has the greatest potential due to the biomimetic nature of the acellular matrices. However, issues with batch consistency and biocompatibility have to be addressed. Other techniques are neither adequate in mimicking the features found in extracellular matrices nor mechanically strong for surgical implants. In an attempt to closely mimic the extracellular matrix while fulfilling the requirements for tissue engineered scaffolds, an alternative scaffold

fabrication technique is necessary. In this project, we propose electrospinning as an option to fabricate tissue engineered scaffolds.

Table 2.2 Criteria and techniques for fabricating tissue engineered scaffolds.

Techniques	Criteria for tissue engineered scaffolds						
	Biomimetics			Engineering principles			
	ECM components	Micro-scale pore size and features	Nano-scale pore size and features	Biocompatibility	Biodegradability	Mechanical properties	Batch consistency
Decellularization	✓	✓	✓		✓	✓	
Rapid prototyping (SLS, FDM, 3D printing, photolithography)		✓			✓	✓	✓
Multi-step techniques (Particulate leaching, phase separation, fiber bonding)		✓	✓		✓		✓
Self assembly			✓		✓		

Chapter 3 Electrospinning

3.1 Introduction to electrospinning

Electrospinning is a process in which non-woven fibers of diameter ranging from 100nm to 5μm are produced by drawing a droplet of polymer solution across a high potential difference. From 1934 to 1944, Formals published a series of patents on using an electrostatic force to produce polymeric thread.[108-111] Since then, this technique has been used in the manufacturing of textiles[108,112], composites[113] and filtration membranes.[114] In the past 3 decades, there has been a growing interest in using electrospinning in the field of tissue engineering.[115-118] Historical development, particularly in the textile and filtration industries, show that electrospinning is a process suited for mass production. This is an indication that this technique has the potential of maintaining batch consistency during mass production.

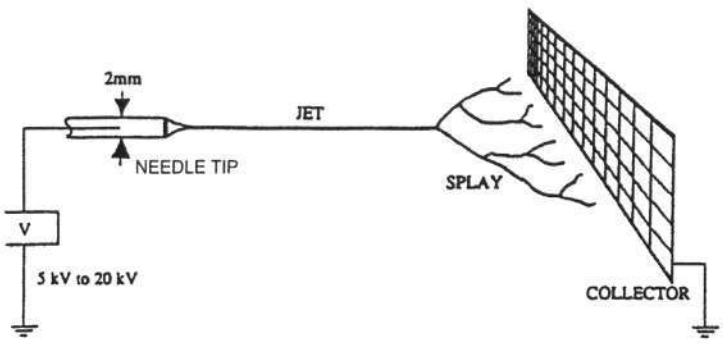

Figure 3.1 Schematic diagram showing the electrospinning process. Picture adapted from Reneker, 1996.[119]

Figure 3.1 shows the schematic diagram of an electrospinning process. The polymer solution is drawn from the tip of a needle. A droplet is formed due to a combination of the gravitational force, pneumatic pressure and electrostatic charge depending on the relative position of the nozzle and the collector. As the potential difference across the tip of the needle and the collector increases, the droplet exists in a conical shape

known as the Taylor cone.[120-122] A polymer jet is formed when the electrostatic force of attraction becomes greater than the surface tension of the droplet. The polymer jet thins as it is drawn over a distance with the simultaneous evaporation of the volatile solvent. This decrease in surface area causes an increase in surface charge density, which results in random whipping of the jet due to charge instabilities.[107,119] In an attempt to lower the surface charge density, the polymer jet further splits into nano-fibers[119], as can be observed in the splaying segment of Figure 3.1. The resulting nano-fibers are deposited onto a rotating mandrel to form a tubular interconnected porous mesh.[123] Researchers have also collected the nano-fibers in flat sheets by using grounded plates.[119,124]

3.2 Parameters of electrospinning

Electrospinning is a multi-parameter process. These parameters are divided into two main categories: polymer solution properties and process parameters.[124,125] The polymer solution properties include the surface tension, net charge density, viscosity, concentration and rate of evaporation of the solution. The process parameters include the potential difference across the charged needle and collector ('+' and '-' electrodes), the speed of rotation of the collector, the distance between the two electrodes, the flow rate of the polymer solution, the needle size and the environmental conditions. Some of these parameters are inter-related. For example, (1) as the temperature of the environment increases, viscosity of the solution decreases which in turn causes an increase in the flow rates of the solutions, and (2) as the potential difference increases between the electrodes, the flow rate of the solution increases as the charged solution accelerates towards the oppositely charged electrode. These inter-relationships often complicate the analysis of the effects that

the different parameters have on the fiber morphology and make it almost impossible to conduct an analysis involving single parameter. These properties will be discussed in details in the following sections.

3.2.1 Solution properties

3.2.1.1 Surface tension of polymer solution

In electrospinning, three forces are involved in the free body analysis of the electrically drawn jet and they are namely (1) electrical force, (2) viscoelastic force and (3) surface tension.[119,125-127] With reference to Figure 3.2, the electrical force stretches the polymer jet and accelerates it towards the oppositely charged electrode. The viscoelastic force resists any sudden change in shape while the surface tension attempts to reduce the surface area of the jet. Initially, a sufficient amount of surface tension is needed to maintain a droplet of solution at the tip of the needle.[126] This is the lower critical limit of surface tension for electrospinning. As the electrical force overcomes the surface tension and viscoelastic force of the solution at the tip of the needle, a jet is drawn out at the tip of the Taylor cone. If the surface tension is low, uniform fibers are formed as the electrical force stretches the polymer jet and accelerates it towards the collector. However, if the surface tension of the solution is high, the polymer jet will attempt to restore the elongated fiber back to a spherical configuration to minimize surface area. Fong *et al.* reported that as surface tension of PEO in water/ethanol solution increased, more beaded fibers were observed.[127] The fibers varied from bead free to spindle-like to beaded fibers as surface tension of the solution was increased from low to high values. Other researchers used surfactants such as Triton X-100™ and concentrated acetic acid to lower the surface tension of

aqueous chitosan/acetic acid solutions in order to produce electrospun bead-free chitosan fibers.[128,129]

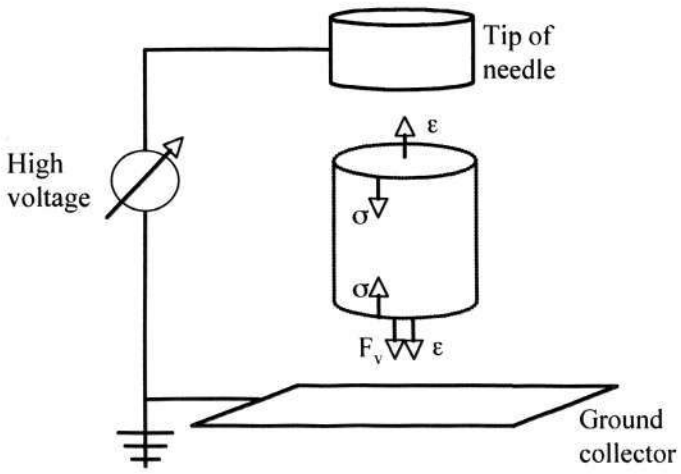

Figure 3.2 Illustration showing the forces involved in electrospinning of a polymer jet. F_v represents the force due to the electric field, ε represents the viscoelastic force and σ represents the surface tension of the solution. Note that ε can act in both directions since it is a restoring force to change in shape.

3.2.1.2 Net charge density of solution

Net charge density (NCD) is defined as the total amount of charges (Q, both positive and negative) that is present in a unit volume of solution (NCD = Q_{tot} / Vol.). Dielectric constant of a solvent measures the polarity of the solvent.[130] Son *et al.* suggested that solvents with higher dielectric constants often constitute solutions with higher net charge density.[130] This is because the polarity of the solvent results from a separation of charges within the solvent. Hence, a more polar solvent will have separation of a large amount of charges. When a more polar solvent is used to dissolve a polymer, it results in a solution with higher net charge density. Polymer solutions with higher net charge densities have better electrical conductivities and hence, they can form fibers at lower electric field strength during electrospinning.[129,130] This is because the solutions contain more charges which allows the electric field to impose a stronger force, F_v, to stretch the jet.[130] In another

perspective, if the electric field strength is kept constant, the diameter of the electrospun fibers will decrease as net charge density increases. Researchers have used various ionic or organo-soluble salts to increase the net charge density of polymer solutions. Fong *et al.* reported that the addition of sodium chloride into an aqueous solution of PEO increased the net charge density of the solution. As a result, the fibers were stretched more effectively by electric field and the number of beaded fibers in the collected specimen were reduced.[127] It is also interesting to note that when Fong *et al.* used an external ionizer to fill the surroundings with oppositely charged ions (relative to the jet), the ions neutralized the net charge density of the jet and beaded fibers were observed. Son *et al.* used polyelectrolytes such as poly(allylamine hydrochloride) (PAH) and poly(acrylic acid sodium salt) (PAA) to increase the net charge density of PEO solutions.[130] The diameter of the electrospun fibers decreased with increasing concentrations of PAH and PAA. Tetraethyl benzylammonium chloride (TEBAC) was added to a solution of poly(lactide) and dichloromethane to increase the electrical conductivity of the solution.[131] Similarly, the diameter of the electrospun fibers decreased after the addition of TEBAC.

3.2.1.3 Viscosity of polymer solution

In electrospinning, the viscosity of polymer solution affects the stability of the electrically drawn jet by affecting the flow rate of the solution. The mass balance of the jet is such that the flow rate of the ejected polymer solution is equal to the flow rate of the solution entering the needle. At fixed pneumatic pressures, a more viscous solution will have a lower flow rate through the needle. With less polymer solution at the inlet, the flow rates are not balanced and the ejected jet cannot be sustained [128]. As such, there is an upper viscosity limit beyond which the polymer solution is rendered

unspinnable.[129] On the other hand, there is a lower viscosity limit for uniform fiber formation. Geng *et al.* reported that chitosan solution between 484 to 590 centipoise produced uniform fibers when the solution was electrospun.[129] Fong *et al.* have reported that when a solution of polyethylene oxide (PEO) in water was electrospun, beaded fibers were observed for solution viscosity below 1250 centipoise.[127] This was due to the fact that as viscosity of the solution decreased at a fixed pneumatic pressure and electric field, the flow rate of the solution at the inlet increased. This increase in flow rate resulted in inadequate charging of the ejected jet since the electric field was maintained at the same value. This drop in charge density caused insufficient stretching of the fibers and as a result, the surface tension of the solution would dominate.

3.2.1.4 Concentration of polymer in solution

At low concentrations, the solution does not contain enough polymer material to produce a stable jet for electrospinning.[128] Matthews *et al.* observed that collagen solution at concentrations at 0.008g/ml of acetic acid formed droplets that cannot be electrospun.[123] Similarly, Deitzel *et al.* obtained a mixture of polymer beads and fibers when the PEO/ water solution concentration was below 4wt.%.[124] As concentration increases, the morphology of the beads become spindle-like and the fibrous mesh become more uniform. This phenomenon was observed by different researchers.[124,128,129] At higher concentrations, the polymer solution become too viscous and the solution is rendered unspinnable for the same reason given in the previous section. Besides affecting the morphology of the fibers, the concentration of polymer solution also affects the diameter of the electrospun fibers.[123,124,133] Mo *et al.* reported that as the concentration of poly(L-lactide-co-caprolactone) in acetone was

increased, the diameter of the electrospun fibers increased.[133] The diameter of electrospun PEO fibers was observed to increase with PEO/water solution concentration in a power-law relationship.[124] This relationship was also highlighted by Huang *et al.* in a review article.[125] Dietzel *et al.* also pointed out that at a PEO/water solution concentration of 7wt.% or higher, splaying resulted in a bimodal distribution of fiber diameters.[124] Finer secondary fibers were formed from the mainstream electrospun fibers due to static charge repulsion.

3.2.1.5 Rates of evaporation of solvents in polymer solution

When the electrically drawn jet is stretched during electrospinning, the solvents evaporate simultaneously so that the fibers can be collected with an appropriate amount of residual solvent.[119] If the fibers are collected wet, they will be re-dissolved by the solvents into a film. If the fibers are collected dry, subsequent layers of fibers will not fuse with the underlying layers and the structure of the electrospun mesh will be weak. As such, the rates of evaporation of these solvents are important as they can be used to regulate the amount of moisture in the collected fibers during electrospinning. Vapour pressures of solvents provide an indication of the rate of evaporation. The higher the vapour pressure is at a given temperature, the faster the evaporation. This parameter is not well studied for electrospinning as researchers always use similar conventional volatile solvents and hence, there were not many reports documenting the effects of evaporation of different solvents on fiber morphology. In our work, we have observed that by selecting solvents with different vapour pressures (different evaporation rates) for the same polymer, we were able to form fibers with nanoporous surface characteristics.[70]

3.2.2 Process parameters

3.2.2.1 Potential difference between the electrodes (V)

The potential difference applied between the electrodes is the most important process parameter in electrospinning. The effects of the electric field strength (E) on the behaviour of the ejected jet will be discussed first. As the potential difference exceeds a critical voltage, a jet is drawn from the tip of the Taylor cone.[120-122,124,125] The critical voltage is defined as the voltage that is just enough to overcome the surface tension of the droplet at the tip of the needle. As the voltage increases, the jet is elongated, surface charge density of the jet is increased and electrospinning results.[119,134] Once critical voltage has been exceeded, increasing the electrodes' potential difference has similar effects on fiber diameter as the effects caused by increasing net charge density. Mo *et al.* reported that increasing the electrospinning voltage caused a decrease in electrospun fiber diameter.[133] Researchers have reported that as the electrodes' potential difference increased further, beaded fibers were observed due to increased flow rate of the solution and jet instability caused by the increasing electric field strength.[124,129] Shin *et al.* reported that the jet instability was caused by the Taylor cone shifting into the needle as the electric field strength increased.[126] The pointed Taylor cone is formed due to the acceleration of charges at the tip of the cone in an electric field. As the strength of the electric field (potential difference) increases, the Taylor cone becomes concave and shifts into the needle, hence resulting in instability of the jet. This suggests that in order to form uniform fibers, the voltage has to be kept above the critical voltage but below a certain threshold voltage to maintain stability. Next, the direction of the electric field can cause a change in behaviour of the electrospun jet. Huang *et al.* reviewed that different configurations of electrodes resulted in different electric fields that could

affect the morphology of the fibers. Figure 3.3 shows the different auxiliary electric fields and electrode configurations that were used to change the morphology of electrospun fibers, in particular, the alignment of fibers.

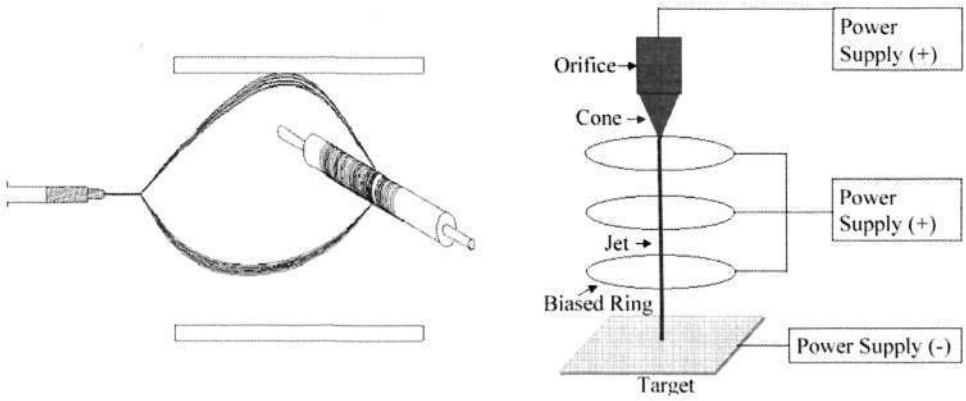

Figure 3.3 Different auxiliary electric field produced by different electrode configurations. Pictures adapted from Huang, 2003.[125]

3.2.2.2 Speed of rotation of collector

In electrospinning, the speed of rotation and shape of collector can influence the alignment of the electrospun fibers.[125,126] In the study where a circular disc collector were rotated at high angular velocity (1000rpm), fibers were collected at the surface of the rotating collector (Diameter = 200mm) at a linear speed of 22m/s.[135] The fibers were wound with a high tangential speed to the rotating surface and were stretched and aligned on the disc's edge. In other cases where speed of rotation is slow, randomly aligned fibers were collected.

3.2.2.3 Distance between the electrodes (D)

The distance between the electrodes affects the electric field strength (since E=V/D) and evaporation behaviour of the polymer jet. As the working distance is increased at a fixed potential difference, the electric field weakens and the influence on fiber formation is similar to that of decreasing voltage mentioned in Section 3.2.2.1. The

evaporation behaviour of the electrically drawn jet is affected by changing the working distance in the following way. As the fibers are being accelerated towards the collector, the time taken for the fibers to land on the collector increases with increasing distance. More solvents can be evaporated and hence, the fibers are dryer at the collection point.

3.2.2.4 Flow rate of solution

The flow rate of the polymer solution determines the throughput of the electrospinning process. The flow rate of the polymer solution can be controlled by constant weight plunger[124], syringe pump[126,130,136] and gravity[128,134,137] in most electrospinning setups. Typical values of flow rates are low and they vary from 0.5 – 5ml/hr.[130] Increasing solution flow rate has the same effects on morphology of electrospun fibers as decreasing the viscosity of solution, which has been described in Section 3.2.1.3.

3.2.2.5 Needle size

Typically, electrospinning needle sizes varied from 18G to 27G.[133] Mo *et al.* demonstrated that large needle sizes produced beaded fibers while small needle sizes produced bead-free fibers.[133] It was also reported that the diameter of fibers decreased with smaller needle size. The selection of needle size has to be appropriate for different solution viscosity, surface tension and electrospinning voltage since these parameters can affect the flow rate of the solution.

3.2.2.6 Environmental conditions

There have not been many publications that discuss the effects of temperature and relative humidity on the formation of electrospun fibers. Most authors have not reported these conditions for their electrospinning experiments. Theron *et al.* reported carrying out their electrospinning experiments at 25°C.[135] The technique that we have developed in this project depends largely on the environment's humidity and the temperature difference between the mandrel and the environment. These two parameters affect the formation of ice crystals on the mandrel surface and leads to different pore size of the eventual electrospun scaffold. These parameters and their effects on the formation of frost crystals are discussed in Chapter 4.

3.3 Biomaterials suitable for electrospinning

The suitability of the biomaterial for electrospinning will depend on its solubility, especially in solvents frequently used for electrospinning such as acetone, chloroform, dichloromethane (DCM) and 1,1,1,3,3,3-hexafluoroisopropanol (HFIP). The following section describe both natural and synthetic biomaterials that have been electrospun.

3.3.1 Natural biomaterials

Natural polymers that have been electrospun include collagen, chitin and chitosan. Collagen has been thought by many researchers in tissue engineering to be the "ideal" scaffold material as it is the major structural protein present in the extracellular matrix. The major difficulty involved in the electrospinning of collagen nano-fibers is the identification of a suitable volatile solvent that could adequately dissolve collagen in sufficient concentration for electrospinning. The solvents that meet this

requirement are fluorinated alcohols such as HFIP. With this solvent, type I collagen (calf skin) has been electrospun successfully by Matthews *et al.*[123] Shields *et al.* electrospun collagen Type II (chicken sternae) nano-fibers in their research on the development of articular cartilage tissue repair.[138] However, it was reported recently that the use of fluorinated alcohols to electrospin collagen denatures the protein, thus resulting in gelatin (denatured collagen) fibers.[139] This work refutes previous reports that used electrospun collagen fibers to mimic the natural ECM.

Chitin, a linear polysaccharide consisting of β-linked N-acetyl-D-glucosamine, is a renewable resource and is easily obtainable from crab and shrimp waste. It is biodegradable and also the second most abundant polysaccharide in nature after cellulose. Upon hydrolysis, chitin yields chitosan, a β-linked D-glucosamine polysaccharide that is also biodegradable and biocompatible.[140] Chitosan has been a much studied biomaterial for scaffold fabrication in cartilage tissue engineering [141]. Min *et al.* have demonstrated that electrospun chitosan nano-fibers was obtained by first electrospinning chitin dissolved in HFIP, followed by hydrolyzing the chitin nano-fibers in NaOH.[142] Geng *et al.* reported the use of acetic acid in the electrospinning of chitosan.[129] With the use of both alkaline and acidic solvents, it is important to neutralize the electrospun fibers before using them for tissue engineering applications.

3.3.2 Synthetic biomaterials

Among the synthetic biomaterials, the biodegradable polyesters, such as polycaprolactone (PCL)[137,143-145], polylactic acid (PLA)[146], and polyglycolic acid (PGA)[146,147] have been popular candidates for electrospinning. These polymers have a

long history of use in medical devices and drug delivery and are being produced commercially[148]. They exhibit tolerable biocompatibility with controllable biodegradability and possess acceptable mechanical properties.[148,149] Co-polymers of lactides, glycolides and caprolactones have also been successfully electrospun.[69,150-152]

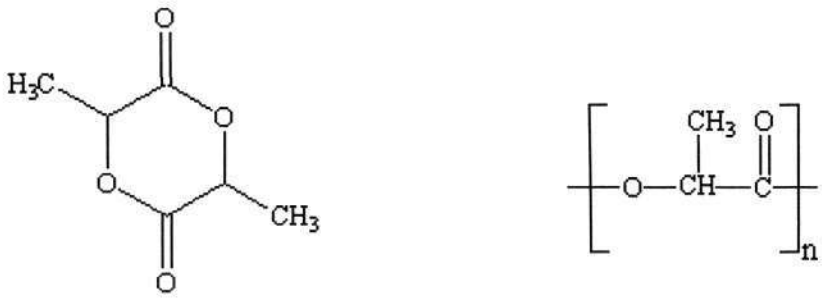

(a) (b)

Figure 3.4 Chemical structures of (a) lactide and (b) polylactide.

The polymer that is used extensively in this project is poly(D,L-lactide) (PLA). The chemical structures of the polymer are shown in Figure 3.4. PLA has been used in applications such as sutures, drug delivery devices and bone tissue engineering.[148,153-155] The advantages of PLA as a biomaterial are its biodegradability, biocompatibility, good mechanical strength, thermal stability and processability.[153,155] However, its major drawback is its degradation product that results from the hydrolysis of the ester bonds.[148,153,154] This degradation product, lactic acid, is acidic and may cause biocompatibility issues when implanted.[154] While it might not be the ideal material choice for tissue engineering applications, it is used as a test material in the development of a novel electrospinning technique in this project.

3.4 Electrospinning and its applications in tissue engineering

Having discussed the various parameters of electrospinning, the applications of electrospinning to tissue engineering are briefly reviewed in this section.

3.4.1 Bone tissue engineering

Bone defects are usually large and require extensive therapeutic replacements.[156] Electrospinning can be used to fabricate scaffolds of comparable size for tissue engineering of bone replacements. Yoshimoto *et al.* proposed an electrospun PCL scaffold for bone tissue engineering.[144] Mesenchymal stem cells (MSCs) were harvested from bone marrow of neonatal rats. The MSCs were seeded onto the nano-fibrous scaffold and cultured in a bioreactor. The MSCs differentiated into osteoblasts after 1 week. The resulting construct was observed to be stiffer than the electrospun scaffold, indicating an increase in density of the bone tissue. The attachment and proliferation of MSC-derived osteoblasts on the scaffold was an encouraging phenomenon of cell-matrix interactions. Furthermore, the osteoblasts deposited their own collagen, indicating ECM synthesis had taken place, which demonstrates the feasibility of using electrospinning to produce scaffolds for tissue engineering of bone.

3.4.2 Blood vessel

In vascular graft design, porosity is necessary to induce attachment and proliferation of endothelial cells.[157] Electrospinning can be used to create fibrous, porous scaffolds for the tissue engineering of blood vessels. Researchers have reported integration of human coronary artery endothelial and smooth muscle cells on electrospun scaffolds.[133,151] The specific phenotypes of the endothelial cells were confirmed. Aligned electrospun fibers were used to guide the proliferation of human coronary artery smooth muscle cells[158] The organization of these cells is important in the design of vascular grafts to provide maximum resistance to the dynamic tensile and compressive forces of the circulatory system.

3.4.3 Contractile cardiac grafts

Researchers have cultured cardiomyocytes from neonatal Lewis rat on electrospun PCL scaffolds *in vitro*.[159] The tissue engineered myocardium was observed to be beating after 3 days. The cardiomyocytes expressed their specific phenotypes after 14 days of culture. This *in vitro* cell-scaffold interaction, though restricted to the surface of the scaffold, demonstrates the feasibility of the electrospun scaffold to support a contracting and expanding tissue.

3.4.4 Ligaments

To fabricate a successful replacement for ligament, the tissue engineered ligament has to possess similar mechanical properties to the original ligament.[160] Lee *et al.* have reported using electrospun nano-fibrous scaffold to mimic the ECM of ligament.[161] Human ligament fibroblasts were seeded onto the scaffolds *in vitro*. The aligned electrospun fibers guided the proliferation of the fibroblasts. The aligned cell-matrix construct also showed improved mechanical strength and increased ECM production compared to the randomly oriented construct.

3.4.5 Wound dressing

Electrospinning can be used as a fabrication technique for wound dressing. Wound dressing has to be highly porous to promote oxygen diffusion and relatively stretchable to provide a physical barrier to protect the wound. In addition, wound dressing is usually large in size. Min *et al.* has seeded human dermal keratinocytes and fibroblasts on electrospun silk scaffolds *in vitro* to evaluate the feasibility of using electrospun scaffold for wound dressing.[162] The fibrous scaffolds promoted adhesion and proliferation of the keratinocytes. Khil *et al.* carried out *in vivo* testing of

electrospun polyurethane scaffold with guinea pigs.[163] Epithelialization was observed after 15 days. Both studies indicate that electrospun scaffold is a potential candidate for wound dressing applications.

3.5 Advantages and limitations of electrospinning in fabricating scaffolds for tissue engineering applications

3.5.1 Advantages of electrospinning

The technique of electrospinning is capable of producing a fibrous, highly porous and interconnected mesh that resembles the connective tissue in the extracellular matrix.[139,164] This biomimicry has been shown to positively influence cell–scaffold interaction such as cell attachment, migration, proliferation and function.[76,107,165] When biomaterials are electrospun, the typical range of fiber diameters is 100nm to few microns.[123,139,144,152] The nano-scale range fibers are similar in size to the collagen fibrils. The high surface area to volume ratio of electrospun fibers have been reported to promote cell attachment and proliferation.[162] Inter-connected pores of the electrospun scaffolds also serve as channels for transportation of nutrients and waste materials. Pore sizes are typically less than 5μm. This results in a dense electrospun fibrous mesh that offer promise as basal membranes to support growth of endothelial cells in vascular tissue engineering[18,133,151,158] and keratinocytes in dermal tissue engineering.[162] It follows that the dense ES is capable of supporting epithelium regeneration when applied to oesophageal tissue engineering.[69]

3.5.2 Limitations of electrospinning

The major disadvantage of using electrospun scaffolds for tissue engineering applications is the lack of control of their inherently small pore size (typically under 5μm).[19] This is due to the nature of the electrospinning process, which randomly

deposits layers of non-woven fibers on each other. Few researchers have addressed this issue, but there are several implications. Firstly, cell infiltration is poor as cells are unable to migrate through the small pores and populate the thickness of the scaffold.[166] Cell-scaffold interaction is thus limited to the surface, whereas most tissue engineered constructs are three-dimensional. Secondly, the small pores prevent vascular ingrowth.[56] This limits the thickness of the scaffold, as cells within the construct rely on diffusion from the vasculature for nutrient and waste transfer.[52,167,168] Thirdly, the lack of control of the pore sizes of electrospun scaffolds prevents its customization for its intended tissue application as specific cell types are known to interact optimally with scaffolds of specific pore sizes.[51,57,107] These factors limit the application of electrospun scaffolds in tissue engineering.

The mechanical strength of electrospun scaffolds is often compromised due to the highly porous nature of the construct. It has been reported that the mechanical properties of electrospun scaffolds were reduced up to 40% in tensile strength and 60% in elongation at break when compared to their cast films counterparts.[169] Such weakening in the mechanical properties limits the applications of electrospun scaffolds.

Electrospinning is also a slow process that involves the progressive building of submicron fibers layer by layer. It has been suggested that the thickness of electrospun scaffolds were built at an average speed of 20μm/hr when a single nozzle was used.[18] Though the area of the scaffold fabricated was not immediately clear at this rate, the average speed serves as an indication of the rate of construction. The fabrication can be sped up with the use of multiple nozzles.[170,171] However, the use of

multi-jets is limited by the number of nozzles that can be arranged within a specified area. For example, in order to build a 0.5mm thick scaffold within an hour, 25 nozzles will be needed and it will be technically challenging to pack all these nozzles in close proximity without affecting the electrospun jets. Hence, the slow fabrication, coupled with the high cost for solvents such as HFIP, means that electrospinning is not as efficient and cost effective as desired.

3.6 Current techniques to address small pore limitation in electrospun scaffolds

The main limitation of using electrospun scaffold in tissue engineering applications is due to its small pore size, which prevents cell infiltration and vascularization. This problem has to be solved as it prevents the fabrication of large and thick tissue constructs. In this section, we review several current techniques that attempt to either increase the cell density or pore size within electrospun scaffolds.

3.6.1 Increasing cell density by the use of bioreactors and microintegration

There have been various strategies used to improve cell infiltration into electrospun scaffolds. One approach permeates the scaffolds with cells and nutrients under dynamic culture conditions through the use of bioreactors.[144,172] However, it is not known if the cell-infiltrated constructs allowed *in vivo* vascularization as the constructs were not subsequently implanted. Another approach microintegrated cells at the time of scaffold fabrication by simultaneously electrospraying cells while electrospinning the polymeric mesh.[166] With these techniques, high cell densities within thick scaffolds could be achieved *in vitro* with the use of bioreactors. However, they do not address the lack of vascular ingrowth when these constructs are subsequently implanted, as the pore size of the electrospun scaffold remains small. To

overcome these limitations, it would be necessary to enlarge the pore size of electrospun scaffolds.

3.6.2 Techniques that increase the pore size of electrospun scaffolds

One reported technique combines gas forming and salt-leaching processes with electrospinning to expand the pores of electrospun scaffolds.[173] Ammonium bicarbonate and sodium chloride were added between layers of fibers during electrospinning. The resulting mesh was compressed between a mold. The ammonium bicarbonate salt was subsequently removed in a heated water bath (90°C) where ammonia and carbon dioxide were released as gases. Removal of sodium chloride was carried out in a water bath at 60°C. The eventual electrospun mesh has enlarged pore size ranging from 100 – 300μm due to the presence of the salts. However, under SEM examination, the fibers appear compressed and the pores within the pore walls remain small. Figure 3.5 shows the morphology of the scaffolds under SEM.

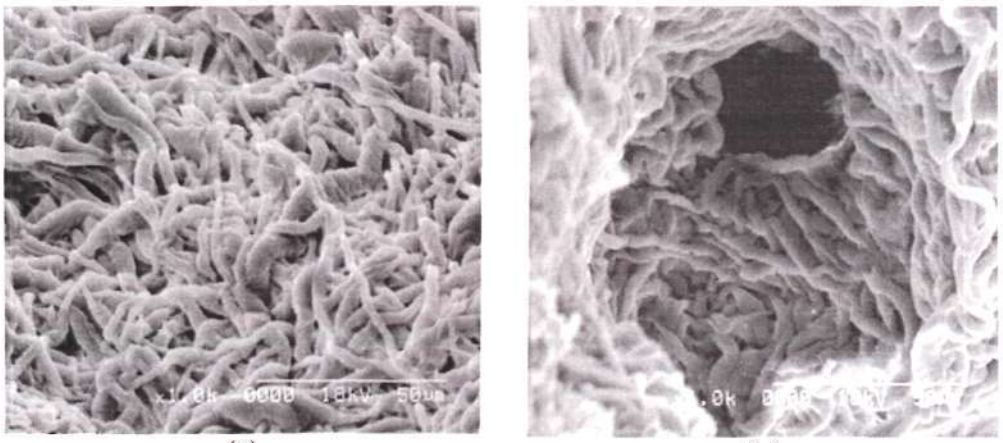

(a) (b)

Figure 3.5 SEM micrographs of scaffolds combining gas forming/salt leaching with electrospinning. Pictures adapted from Lee, 2005.[173]

One of the more recent attempts to enlarge the pore size of electrospun scaffold was reported by Simonet *et al.*[174] This was achieved by low temperature electrospinning

technique that used ice crystals as removable void templates. They reported an increase in porosity, primarily arising from an increase in the distance between layers of fibers (interlayer distance, z-axis) (Figure 3.6(a)). This was due to the presence of ice crystals between the fiber layers during electrospinning. However inter-fiber spaces within the same plane (x-y plane) remained the same as those observed in conventional electrospun scaffolds (Figure 3.6(b)). While *in vivo* studies were not presented in the report, it can be deduced that these small inter-fiber spaces within the laminar structure may impede cell infiltration and vascularization since they are of the same size as conventional electrospun scaffolds. Hence, the small pore size limitation of conventional electrospinning technique is not addressed.

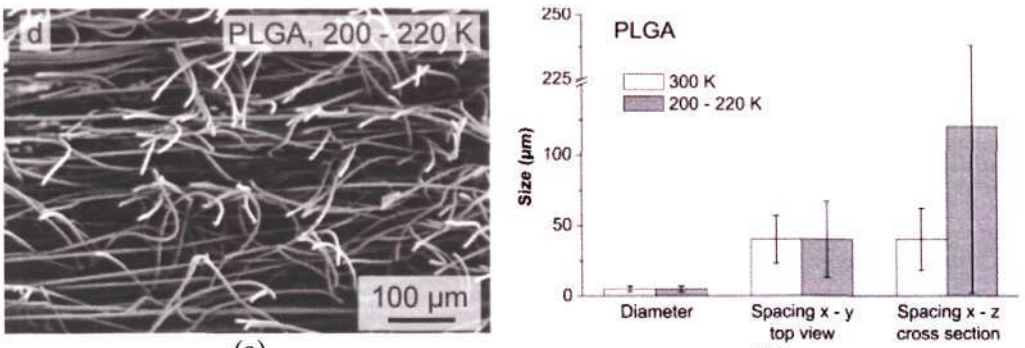

(a) (b)

Figure 3.6 (a) SEM micrograph showing cross-section of electrospun scaffold with increased distance between layers of fibers and (b) Graph showing the pore size variation for scaffolds fabricated at a temperature of 300 K (without ice crystals) and 200 – 220 K (with ice crystals). Both figures adapted from Simonet, 2007.[174]

3.7 Cryogenic electrospinning

Having reviewed the requirements of tissue engineered scaffold and the limitations of current electrospinning techniques, it is obvious that a new technique is needed to expand the pores while retaining the fibrous nature of electrospun scaffold. In this project, we develop a cryogenic electrospinning technique that uses ice crystals as templates to create electrospun scaffolds with large, three-dimensional interconnected pores.[175,176] With reference to the project goals listed in Section 1.3, we hypothesized

that these large pores of the cryogenic electrospun scaffolds (CES) would improve cell infiltration and vascular ingrowth compared to conventional electrospun scaffolds. Hence, the fabrication of a large tissue construct such as an oesophageal tissue replacement is possible.

While the technique is similar to the one reported by Simonet *et al.*, it should be pointed out that our patent application for this technique was filed in December 2006[175], which precedes Simonet's publication. In addition, the morphologies of the scaffolds obtained by the two techniques are very different.

This thesis describes the mechanism of cryogenic electrospinning, the process study, the preparation and characterization of the cryogenic electrospun scaffold (CES) and the effects of its large pores on cell infiltration *in vitro* and *in vivo*, and vascularization *in vivo*.

Chapter 4 Frost Formation

As the cryogenic electrospinning technique presented in this thesis involves the use of ice crystals as templates for the formation of the eventual scaffold, a chapter on the mechanism of frost formation is included.

4.1 Mechanism of frost formation

As a surface is chilled below the frost point of water vapour at a given pressure, ice crystals are deposited on the surface. The frost forming process on a cold surface can be divided into 3 stages, namely the (1) crystal growth period, (2) frost layer growth period and (3) frost layer fully growth period. [177-182]

4.1.1 Crystal growth period

This is the initial period of frost formation on a cold surface and is typically very short in duration.[178,182] Cheng *et al.* suggested a duration of 30 seconds for a surface temperature of -7.2°C and this duration was shortened with decreasing temperature of the cold surface.[178] During the crystal growth period, small isolated needle-shaped crystals grow perpendicularly on the surface.[181] These crystals are spaced out and the frost layer is irregular.[179]

4.1.2 Frost layer growth period

The frost layer growth period is characterized by the formation of branched dendritic ice crystals.[178,179,181] The deposited ice crystals serve as ice nuclei for subsequent deposition, resulting in columns of ice crystals spaced apart from each other.[178] A mathematical model presented by Tao *et al.* predicts that the spatial distribution of ice crystals in this period affects the distribution of subsequent ice crystals.[183] As more

dendritic crystals are deposited, they begin to form a mesh with the branches of the ice crystals such that a porous homogeneous frost layer results.[182] The thickness and density of the frost layer increase due to two aspects of mass transfer of water vapour.[178,181,182,184] One aspect involves the deposition of ice crystals on the frost layer, thereby increasing its thickness. The other aspect involves the diffusion of water vapour into the frost layer, thereby causing densification within the frost layer. The end of this growth period is indicated by the formation of a flat top surface of the frost layer due to the crystal growth and densification processes.[181] Cheng *et al.* reported a duration of 30 minutes for this frost layer growth stage at a surface temperature of -7.2°C, with the duration shortened with decreasing surface temperature.[178]

4.1.3 Frost layer full growth period

As the thickness of the frost layer increases, its top surface temperature approaches 0°C due to its thermal resistance.[178,179,181,182] Ice crystals begin to melt at the top surface. The melted water seeps into the underlying porous frost layer, increasing the frost density as it re-freezes when it reaches colder region within the frost layer. This further increases the thermal resistance, resulting in more melting and re-freezing until equilibrium is established.

4.2 Parameters that affect frost formation on a cold surface

4.2.1 Humidity of surrounding air

Relative humidity is defined as the ratio of the partial pressure to the saturated vapour pressure of water at that temperature. Typically, increasing the moisture content in the atmosphere increases the mass, thickness and the density of the frost layer that forms

on a cold surface.[178,180,185-187] At low to intermediate humidities (< 70%), the main driving force for frost formation is the concentration gradient of the moisture content from the surrounding air to the cold surface.[186] As humidity of the surrounding air increases, this concentration driving force is higher, thus more water vapour is transported towards the cold surface and deposited as ice crystals.[185] Thickness of the frost layer is increased by deposition of the ice crystals on the existing frost layer, while density is increased due to an increase in mass transfer of the water vapour into a fixed volume of frost, which is a consequent of the increased concentration driving force (Figure 4.1). For higher humidities (> 70%), increasing the moisture content leads to an increase in frost thickness rather than density. This is because as a denser frost layer is formed, the diffusion of water vapour into the frost layer, and consequently the heat transfer from the water vapour to the frost layer is significantly reduced.[186] Lee *et al.* suggested that at high humidities, the moisture content at the interface between the surrounding air and the frost layer is increased.[185] As a result, super saturation of water vapour leads to deposition of ice "particles" at the interface, which increases the density of the frost surface, thus limiting the mass and heat transfer of the water vapour into the frost layer.

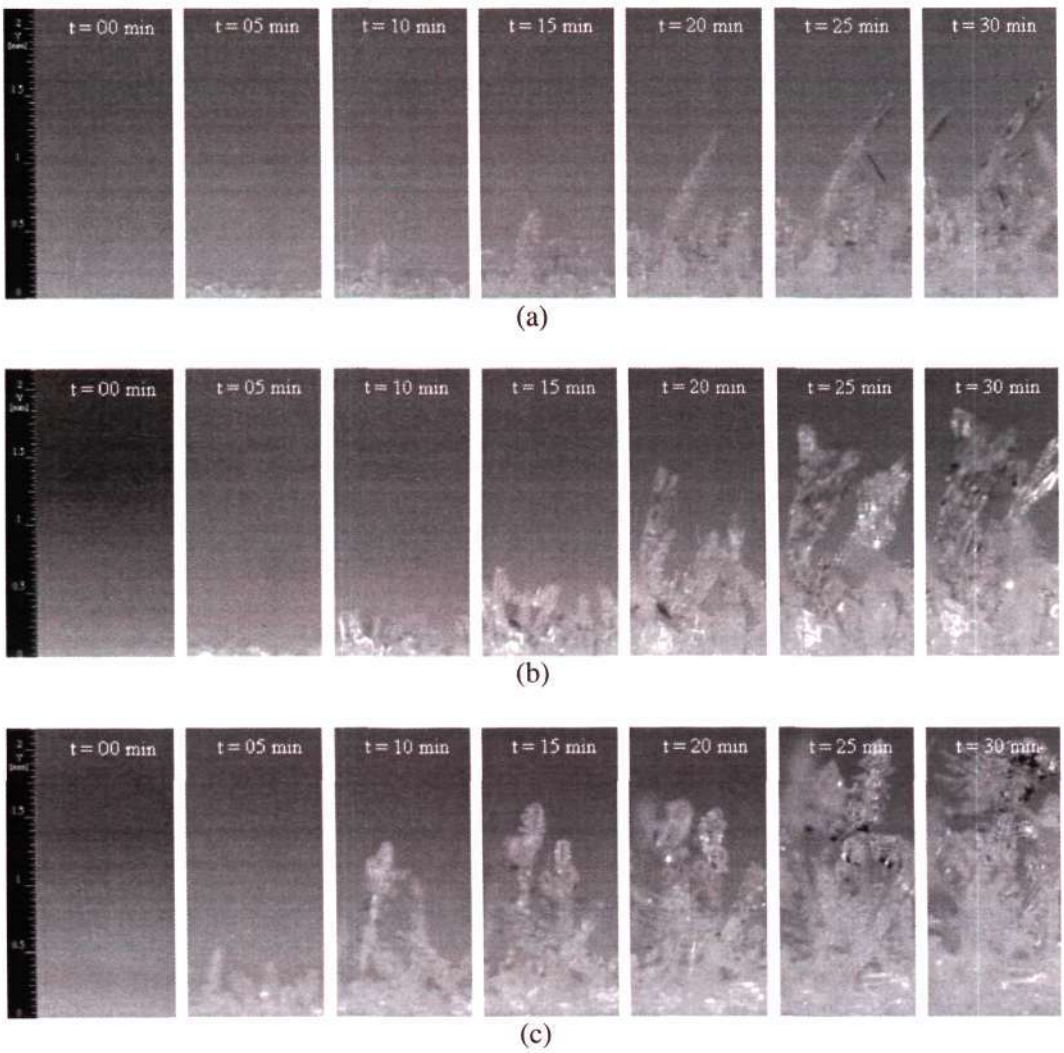

Figure 4.1 Pictures showing side view of frost layer at different relative humidities. The growth of ice crystals was carried out at a cold plate temperature of -10.2°C and atmospheric temperature of 27.0°C. Relative humidities vary from (a) 42%, (b) 48% and (c) 59%. Pictures adapted from Cheng, 2002.[180]

4.2.2 Temperature of cold surface

At a given surrounding air temperature, decreasing the temperature of the cold surface increases the thickness of the frost layer.[178,180,185,186] A colder surface results in super saturation at the interface between the surrounding air and the surface, hence more water vapour will be deposited as ice crystals.[185] This further reduces the humidity of the air at the interface, which results in a large concentration driving force for the diffusion of water vapour from the surrounding air to the interface. This phenomenon is more obvious at lower humidities as the cold surface temperature is less perturbed by the deposited ice crystals.[185,186] At higher humidities, the thickness of the frost layer increases at a rapid rate such that the top surface of the frost layer reaches the freezing point of water vapour. Melting results and the frost layer full growth period is established faster.

4.2.3 Velocity of air flow above the cold surface

The thickness and density of the frost layer increase with increasing air velocity at a given relative humidity and temperature of the surrounding air.[180,185,188] By increasing the velocity of air flowing over the cold surface, the mass transfer of water vapour to the cold surface increases, thereby increasing the thickness and density of the frost layer. Figure 4.2 shows that both thickness and density of the frost layer was increased when air velocity increased to 3m/s. The densification effect is more pronounced as the diffusion of water vapour into the frost layer is enhanced by the air flow.[185]

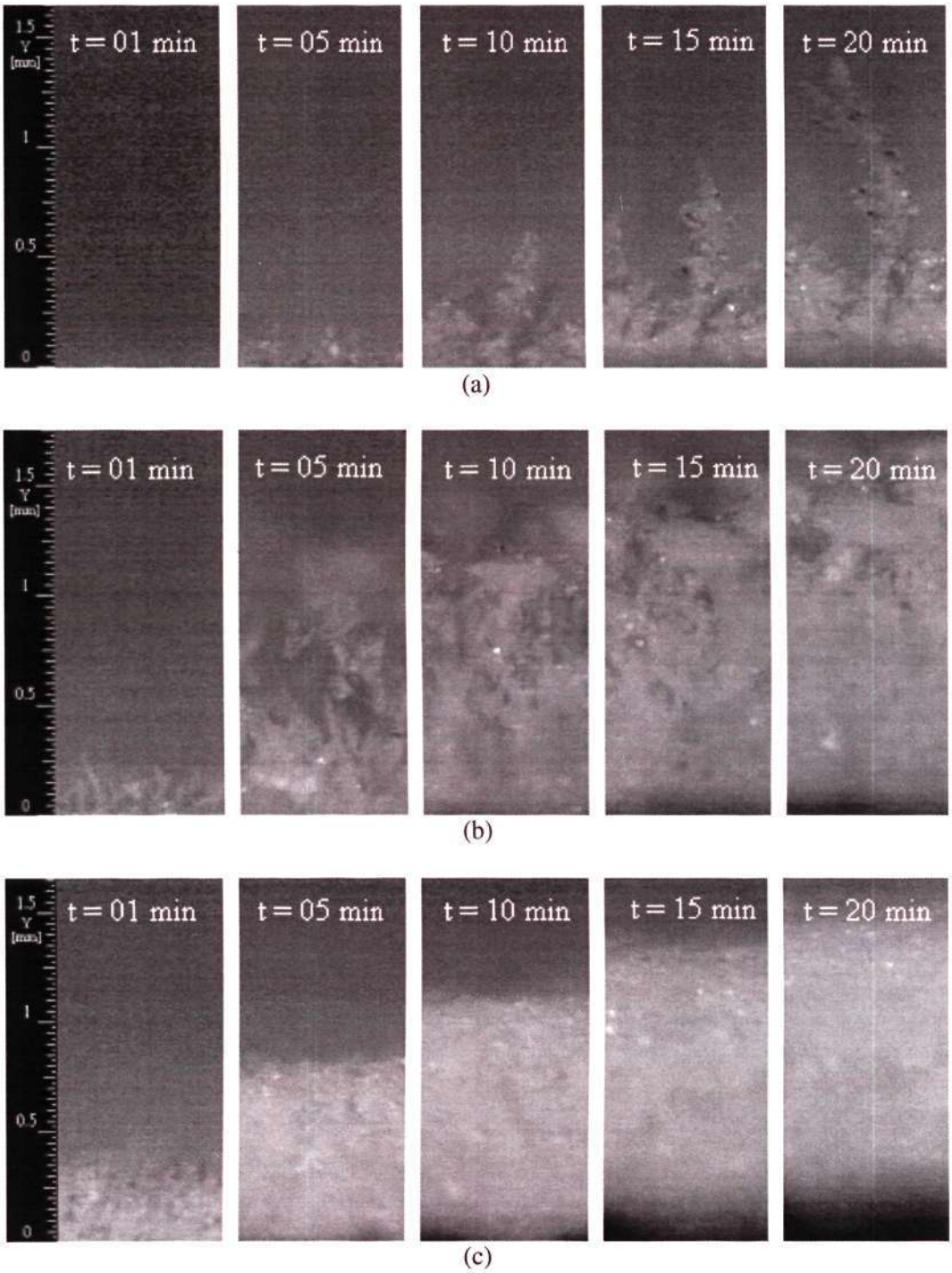

Figure 4.2 Pictures showing side view of frost layer at different air velocities. The growth of ice crystals was carried out at a cold plate temperature of -14.7°C, atmospheric temperature of 25.0°C and relative humidity of 73%. Air velocities vary from (a) 0 m/s, (b) 1 m/s and (c) 3 m/s. Pictures adapted from Cheng, 2002.[180]

4.2.4 Presence of electric field

As the cryogenic electrospinning technique is performed in the presence of an electric field, it is important to understand how electric field influences the formation of ice crystals. Ice crystals are known to align their major axes with the electric field.[189] Due to this alignment, the density of the frost layer in the electric field is considerably lower than without electric field.[190] This is because the aligned ice crystals, which are electrically charged, serve as nucleation sites for subsequent deposition of ice crystals that will further be aligned in the electric field. This results in columns of ice crystals spaced apart from each other, thereby reducing the density of the frost layer, as shown in Figure 4.3. The voids between the columns also serve to facilitate mass and heat transfer between water vapour and the ice crystals. This observation was reported using an electric field of potential difference ranging from 5 to 15kV, which is in the typical range for electrospinning. It was also reported that the branches of dendritic ice crystals grow at a significantly faster rate in the presence of electric field.[191-193] With their long axes aligned with the electric field, the branches of these dendrites extend outwards into the voids between the columns of ice crystals. This may in turn increase the density of the frost layer.

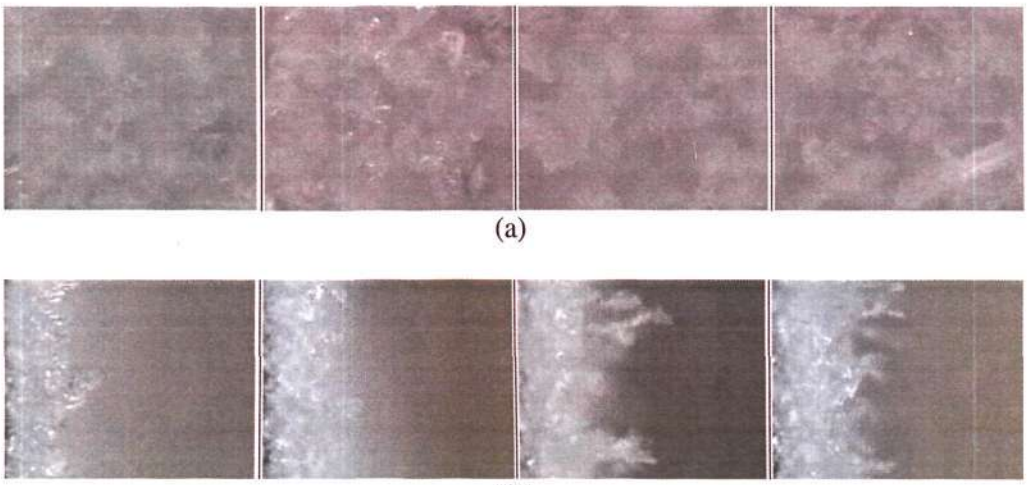

Figure 4.3 Pictures showing frost formation at different electric potential. The frost was collected at a cold plate temperature of -20°C and an environmental temperature of -1°C at a relative humidity of 80%. (a) Top view and (b) side view. The potential differences applied are as indicated. Pictures adapted from Wang, 2004.[190]

Another interesting observation is the break-off effect of ice crystals in the presence of an electric field (Figure 4.4).[190] As these ice crystals are loosely packed, they can break-off from the underlying crystals and accelerate towards the oppositely charged electrode. This phenomenon reduces the thickness of the frost layer.

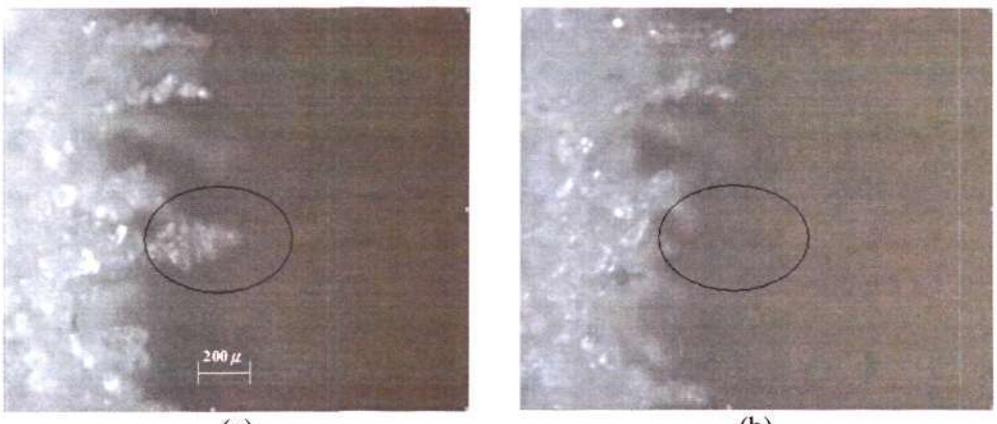

Figure 4.4 Pictures of frost layer side view showing the break-off of the ice structure under electric field. (a) Before break-off and (b) after break-off. Pictures adapted from Wang, 2004.[190]

4.3 Development of an empirical model for frost formation

Dimensional analysis is an algebraic manipulation of units that is used as an alternative solution when the process contains many inter-related variables and it is difficult to solve the engineering problem completely by theoretical or mathematical methods.[194] In this section, an empirical model is developed using dimensional analysis to derive the relationship between frost density and other process variables. Previous studies have shown that the spacing between the ice crystals affects pore size of cryogenic electrospun scaffold (CES). Hence, the frost density, which is related to the spacing between the ice crystals, predicts the porosity of the CES since frost is used as a template in the cryogenic electrospinning technique.

4.3.1 Buckingham Pi Method

According to the Buckingham Pi theorem, the number of independent dimensionless groups (π) that can be formed from the variables in the system is equal to the number of variables (m) minus the number of primary dimensions of the variables (d).[195]

$$\pi = m - d \qquad \textbf{Eq 4.1}$$

Using this method, the variables of the system can be organized into dimensionless groups, which streamline data collection and analysis. The dimensionless groups are related by some functions as shown in Equation 4.2.

$$\pi_1 = f(\pi_2, \pi_3, \ldots \pi_{m-d}) \qquad \textbf{Eq 4.2}$$

The Buckingham Pi method is used to develop an empirical correlation to relate the frost properties to the relevant dimensionless groups.

4.3.2 Empirical correlation

An empirical correlation was reported by Yang *et al.* to relate frost density on a flat plate to dimensionless frosting parameters as shown in Equation 4.3.[196] This model was developed for a system with air flowing over a chilled flat plate in the absence of an electric field. Although the conditions are different from the experimental conditions used in this project, Equation 4.3 provides insights to the dimensionless groups involved in frost formation and serves as a reference for the derivation of the empirical correlation in this study.

$$\rho_f^* = \rho_f / \rho_{ice} = 1.54 \times 10^{-4} (Re)^{0.351} (Fo)^{0.311} (\omega)^{-0.368} (\exp(T^*))^{2.4} \qquad \textbf{Eq 4.3}$$

where ρ_f^* is the dimensionless frost density, Re is the Reynolds number, Fo is the Fourier number, ω is the absolute humidity and T^* is the dimensionless temperature.

The empirical correlation proposed in this section aims to predict frost density from process parameters and properties of the surrounding air. The derivation of the correlation by dimensional analysis is shown and a dimensionless electric field strength is included in the correlation. The parameters and the dimensionless groups that are used in the correlation are listed in Table 4.1 with their respective symbols and units. The assumptions are as follows:

(1) Properties of air are measured at an average temperature of the surrounding.

(2) Velocity of air, V_a, is taken at the surface of the mandrel assuming non-slip conditions and is equal to the tangential velocity of the mandrel. That is, $V_a = L_c / t_R$.

(3) Density of ice is measured at 0^oC and assumed to be constant at all T_p.

(4) The frost layer is modeled as a uniform porous mesh with ice crystals equally spaced out on the mandrel surface. The mandrel surface is homogeneous and the ice crystals are equally likely to be deposited on any location on the surface.

(5) For the case of cryogenic electrospinning, the deposited fibers do not cause the ice crystals to melt by heat transfer or collapse by weighing down on the ice crystals.

Table 4.1 List of parameters used in the empirical correlation

Symbol	Parameter, units
Process parameters	
A	Area that ice crystals were deposited, m^2
E	Electric field strength, V/ m
L_c	Circumference of mandrel, m
N	Number of revolutions of the mandrel
T_p	Temperature of plate, K
T_{tp}	Triple point of water, K
t	Frosting time, s
t_R	Time taken for 1 revolution of the mandrel, s
Properties of air	
α_a	Thermal diffusivity, m^2/ s
$C_{p,a}$	Specific heat capacity, J/ kg K
ε_a	Dielectric permittivity, F/ m
K_a	Thermal conductivity, W/ m K
μ_a	Viscosity, kg/ m s
ρ_a	Density, kg/ m^3
T_a	Temperature of air, K
V_a	Velocity of air, m/ s
ω	Absolute humidity, kg of water/ kg of air
Properties of frost	
m_f	Mass of ice crystals, kg
ρ_f	Density of frost layer, kg/ m^3
ρ_{ice}	Density of ice, kg/ m^3
y_f	Thickness of frost layer, m

The properties chosen for the dimensional analysis are the frost density (ρ_f), electric field strength (E), circumference of mandrel (L_c), frosting time (t), temperature difference between the surrounding air and the mandrel (T_a - T_p), properties of air

such as specific heat capacity ($C_{p,a}$), thermal conductivity (K_a), viscosity (μ_a), density (ρ_a), dielectric permittivity (ε) and absolute humidity (ω). The primary dimensions of these properties are listed in Table 4.2.

Table 4.2 Primary dimensions of properties and the respective powers that the dimensions are raised. For example, ρ_f [=] $[M]^1[L]^{-3}$.

	Mass [M]	**Length [L]**	**Time [T]**	**Temperature [K]**	**Ampere [A]**
ρ_f	1	-3	0	0	0
E	1	1	-3	0	-1
L_c	0	1	0	0	0
t	0	0	1	0	0
$T_a - T_p$	0	0	0	1	0
$C_{p,a}$	0	2	-2	1	0
K_a	1	1	-3	1	0
μ_a	1	-1	-1	0	0
ρ_a	1	-3	0	0	0
ε	-1	-3	4	0	2
ω	0	0	0	0	0

Based on Buckingham pi theorem, the dimensional analysis should result in 6 dimensionless groups according to Equation 4.1 since there are 11 variables and 5 primary dimensions. Five variables were chosen to represent the 5 primary dimensions and they are namely ρ_a, K_a, L_c, t and E. A sample calculation of a dimensionless group is shown here and the derivations of remaining dimensionless groups are included in the Appendix A.

$$\pi_1 = \rho_a^A K_a^B L_c^C t^D E^E \mu_a$$

$$[=] [ML^{-3}]^A [MLT^{-3}K]^B [L]^C [T]^D [MLT^{-3}A^{-1}]^E [ML^{-1}T^{-1}]$$

By equating the sum of exponents for each primary dimension,

$$[M]: \quad A + B + E + 1 = 0$$

$$[L]: \quad -3A + B + C + E - 1 = 0$$

[T]: $-3B + D - 3E - 1 = 0$

[K]: $B = 0$

[A]: $E = 0$

Solving for A, C and D yields,

$A = -1$

$C = -2$

$D = 1$

This implies that

$$\pi_1 = \frac{t\mu_a}{L_c^{\,2}\rho_a}$$

$$= \frac{Nt_R\mu_a}{L_c^{\,2}\rho_a}$$

$$= \frac{N\mu_a}{L_c\rho_a V_a} \quad , V_a = \frac{L_c}{t_R}$$

$$= \frac{N}{\mathrm{Re}} \quad , \text{Reynolds number, } \mathrm{Re} = \frac{L_c\rho_a V_a}{\mu_a}$$

$$\pi_1 = \frac{N}{\mathrm{Re}}$$

$$\pi_2 = \frac{1}{Fo} \quad , \text{Fourier number, } Fo = \frac{\alpha_a t}{L_c^{\,2}}$$

$\pi_3 = \mathrm{N}^2\,\psi$, Dimensionless E, $\psi = \frac{\varepsilon_a E^2}{\rho_a V_a^{\,2}}$, taken from this report.[197]

$\pi_4 = \mathrm{T}^*$, Dimensionless T, $T^* = \frac{(T_a - T_{ip})}{(T_a - T_p)}$

$\pi_5 = \omega$

$\pi_6 = \rho_f^*$, Dimensionless ρ_f, $\rho_f^* = \frac{\rho_f}{\rho_{ice}}$

From Equation 4.2, the dimensionless groups can be correlated as follows:

$$\rho_f^* = f(Re, Fo, \psi, T^*, \omega) \qquad \textbf{Eq 4.4}$$

Frost density, ρ_f, can be defined by the following equation:

$$\rho_f = \frac{m_f}{Ay_f}$$

$$= \frac{V_{ice}\rho_{ice}}{V_f}$$

$$\frac{\rho_f}{\rho_{ice}} = \frac{V_{ice}}{V_f}$$

ρ_f^* = Volume fraction of ice in frost layer

The porosity of the frost layer is defined as:

Porosity = (1 – Volume fraction of ice in frost layer) × 100%

$$= (1 - \frac{V_{ice}}{V_f}) \times 100\%$$

$$= (1 - \frac{\rho_f}{\rho_{ice}})) \times 100\%$$

Hence, this allows the correlation of the porosity of the frost layer to the empirical formula as follows:

$$\text{Porosity} = [1 - f(Re, Fo, \psi, T^*, \omega)] \times 100\% \qquad \textbf{Eq 4.5}$$

With Equation 4.5, the relationship of porosity of the frost layer with each dimensionless group can be determined experimentally. To simplify the equation

further, let's assume that Re, Fo, ψ and T^* are weak functions of ω such that they are kept constant when ω is varied. Hence, Equation 4.5 is reduced to Equation 4.6.

$$\text{Porosity} = [1 - C_1 \omega^{C_2}] \times 100\% \qquad \textbf{Eq 4.6}$$

where C_1 and C_2 are constants.

It follows that

$$(1 - \frac{\rho_f}{\rho_{ice}}) \times 100\% = [1 - C_1 \omega^{C_2}] \times 100\%$$

$$\frac{m_f}{A y_f \rho_{ice}} = C_1 \omega^{C_2}$$

$$\log (\frac{m_f}{y_f}) = C_2 \log \omega + \log (C_1 A \rho_{ice}) \qquad \textbf{E.q 4.7}$$

C_1 and C_2 can be determined from the plot of $\log (m_f / y_f)$ vs. $\log(\omega)$ where C_2 is the gradient and $\log (C_1 A \rho_{ice})$ is the y-intercept of the linear fitted line.

Chapter 5 Methodology

In this chapter, the methodologies of the experiments are presented. Figure 5.1 shows the organization of the various methodology sections, which are listed as follows:

- Section 5.1 – Analysis of surface morphology and histoarchitecture of porcine oesophagus. In this section, the structure of the porcine oesophagus was studied. The results provide clues for designs of scaffolds pertaining to oesophageal tissue engineering.

- Section 5.2 – Electrospinning setup. In this section, the setup is described and several experiments are conducted to determine the process capabilities.

- Section 5.3 – Frost formation experiments. In this section, a study of the frost deposition process on the mandrel is conducted in the presence of an electric field. An empirical correlation is proposed to predict the frost porosity at different humidities according to Equation 4.6.

- Section 5.4 – Development of cryogenic electrospinning. In this section, a study is carried out to understand the mechanism of the cryogenic electrospinning process. The effects of process parameters, such as temperature, environmental humidity and rate of fiber deposition on the pore size of cryogenic electrospun scaffolds (CES) are evaluated.

- Section 5.5 – Scaffold fabrication. In this section, the procedures in fabricating three different types of scaffold, namely conventional electrospun scaffold (ES), cryogenic electrospun scaffold (CES) and bilayered electrospun scaffold (BLES), are described.

- Section 5.6 – *In vitro* cell-scaffold interactions. In this section, the three different types of scaffold are tested for their cytotoxicity. In addition, they are used for *in vitro* cell culture work to study the effect of pore sizes on cell

infiltration and their different functions to support co-culture of porcine oesophageal epithelial and smooth muscle cells.

- Section 5.7 – *In vivo* subcutaneous implantation. In this section, the three different types of scaffolds are implanted to assess *in vivo* cell infiltration and vascularization.

- Section 5.8 – Methods of characterization. In this section, the methods used to characterize the scaffolds, *in vitro* cell-scaffold constructs and explants from animal studies are described.

- Section 5.9 – Statistical analysis. In this section, the statistical methods used to compare different sets of experimental data are described.

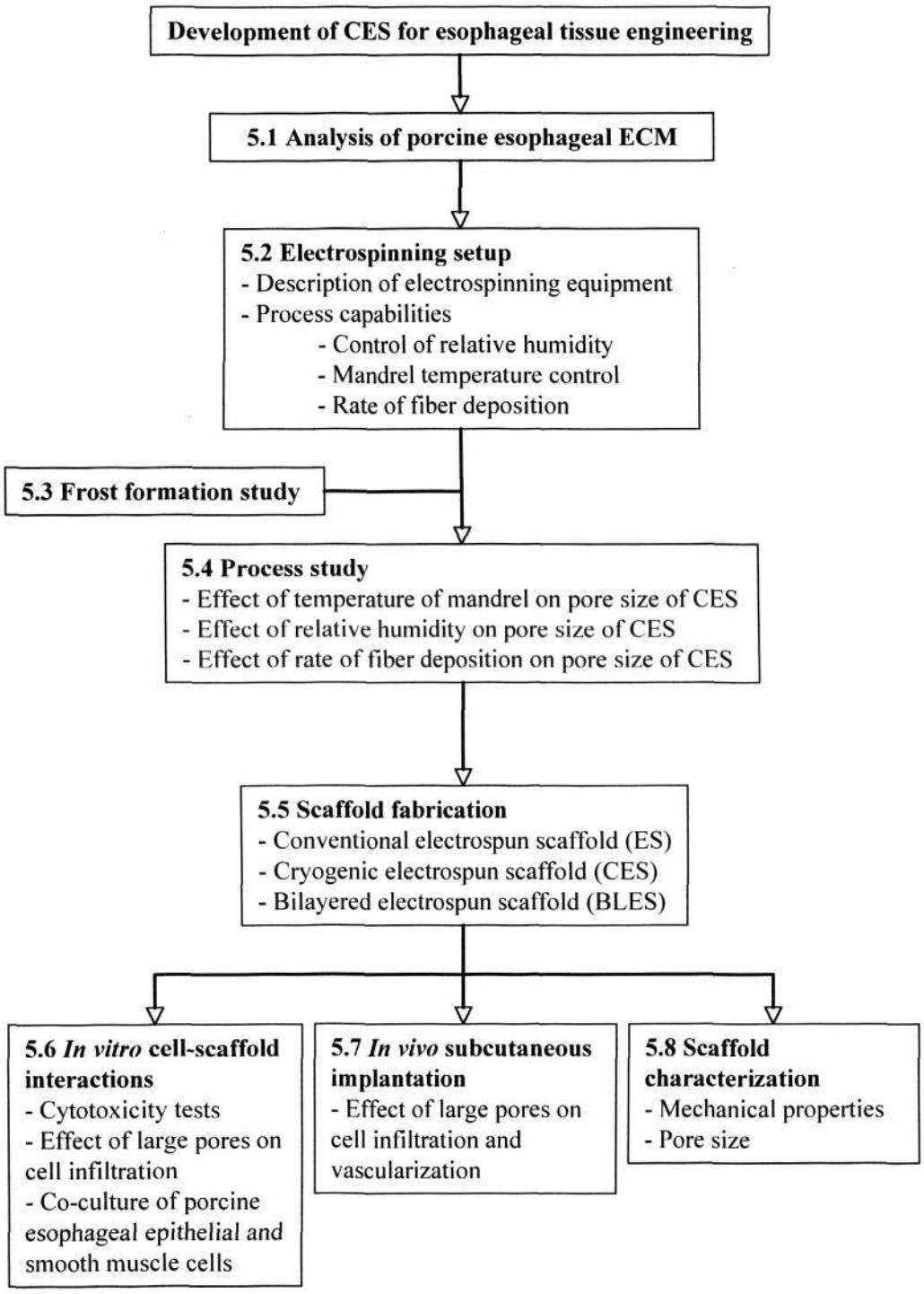

Figure 5.1 Organization of the sections in Chapter 5.

5.1 Analysis of histoarchitecture of porcine oesophagus

Chapter 2 showed that different pore size ranges in scaffolds are needed for different tissue applications. In order to engineer the oesophageal tissue, a better understanding of the ECM of porcine oesophageal tissue, such as the features and pore sizes that are present in the native ECM, is necessary. Porcine oesophagus is chosen for this study as it is anatomically similar to a human oesophagus. The histoarchitecture of the tissue was studied using scanning electron microscope (SEM) and histochemical staining techniques respectively.

The tissue harvesting procedures are as follows. The entire length of the porcine oesophageal tissue was freshly harvested from the abattoir (Agri-Food & Veterinary Authority (AVA) Singapore) and stored in sterile phosphate buffered saline (PBS) supplemented with antimycotics antibiotics solution (AAS) (1µl in 1ml PBS) for transportation. For SEM, the muscularis externa was excised and the remaining mucosal-submucosal tissue was incubated in dispase overnight at 4°C to remove the epithelium. The adluminal and abluminal surfaces of the remaining mucosal-submucosal tissue were observed under SEM as described in Section 5.8.1. For histochemical characterization, a 1cm long segment of the oesophagus mid-section was processed and stained as described in Section 5.8.5.

5.2 Electrospinning setup

5.2.1 Description of the electrospinning equipment

The basic design of the electrospinning equipment is based on descriptions published by other researchers.[119,123,124,131] The equipment setup is shown in Figure 5.2 and the main components are labeled as follows:

(1) Control terminal
- High voltage generator (Glassman EH series)
- Speed control unit for rotating mandrel (Oriental Motor Co. Ltd, USP 20 2E)
- Pneumatic pressure controller (Keyence AP-33)

(2) Two-axes robot with dispensing syringe
- Linear actuator robot (Intelligent Actuator, Inc, IS-M-X-S-10-100-300SU)
- Syringe and needle (Dou Yee Enterprise Pte Ltd, PS-Y30E and SN-26G)

(3) Rotating mandrel and environmental chamber
- Motor for rotating mandrel (Oriental Motor Co. Ltd, USM 206-402W)
- Humidifier (Novita Ultrasonic Humidifier NH 259)
- N_2 flow regulator (Controls Corporation of America, 2023332-67-000)
- Compressed nitrogen gas (Soxal, Singapore)

Pictures of the equipment setup are included in Appendix B for reference.

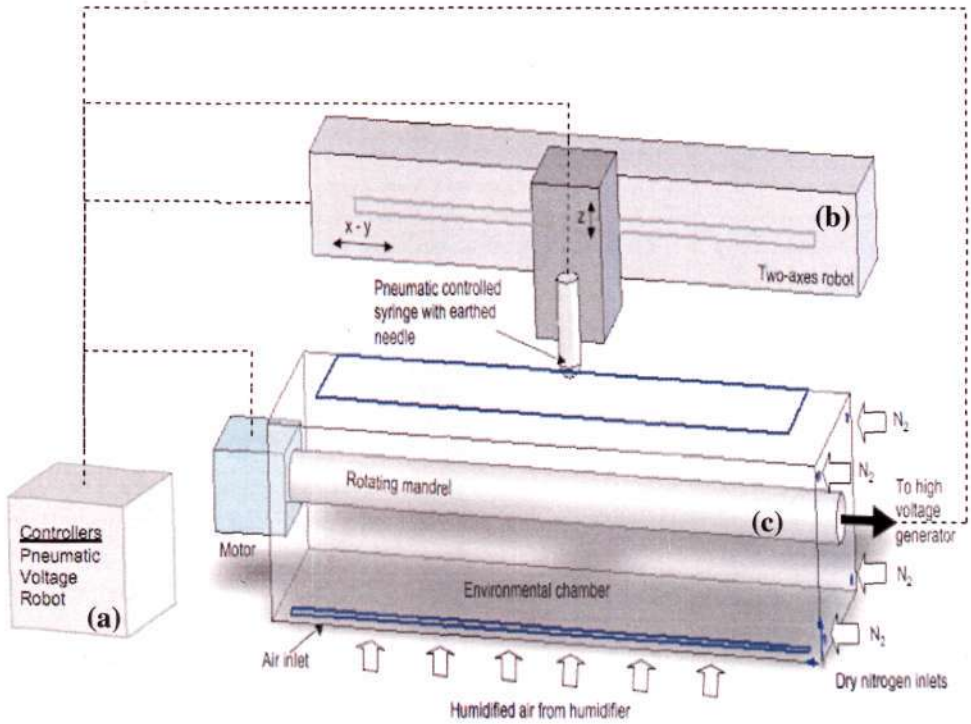

Figure 5.2 Picture illustrating the electrospinning setup. The main modules are (a) control terminal, (b) two-axes robot with pneumatically controlled dispensing syringe and (c) rotating mandrel in an environmental chamber.

The polymeric solution is placed in the plastic syringes fitted with a 26 Gauge metal needle that is connected to the earthed potential. The housing for the syringes is mounted onto 2-axes robot that can traverse in the X-Y and Z directions. The total lateral displacement of the X-Y axis is 300mm while the total vertical displacement of the Z-axis is 200mm. Traverse speed of the X-Y axis can be varied from 0 to 100mm/s. The flow rate of the polymer solution is controlled by pneumatic pressure that is applied to the syringes. Pneumatic pressure can be varied from 0 – 5psi with graduations of 0.2psi. A maximum potential difference of +35kV can be applied to the mandrel, which is rotated to a maximum of 700rpm. An environmental chamber is fitted to the electrospinning machine to provide humidity control. The entire setup is

placed in a fume hood to allow removal of volatile organic solvents during electrospinning.

5.2.2 Process capabilities

5.2.2.1 Humidity control in electrospinning chamber

In order to regulate the humidity of the spinning condition, an environmental chamber was used. The relative humidity was monitored with digital hygrometers placed within the chamber. Relative humidity was increased with the use of a humidifier that directed a stream of water vapour into the environmental chamber. When lower humidity was required, dry nitrogen cylinder gas was introduced into the environmental chamber and the gas flow rate was controlled by a regulator. By adjusting the flow rates of water vapour and nitrogen gas, the relative humidities of the chambers was controlled at 25%, 40%, 50% and 70%. The experiment was not started until the variations in humidity were controlled within ±3% of the stated values. It is important that the streams of water vapour and nitrogen gas flowing into the chamber was not directed towards the mandrel so as to minimize the draft effect on frost formation.

5.2.2.2 Controlling the mandrel temperature

The mandrel temperature was controlled by packing different amount of dry ice within the hollow stainless-steel cylindrical mandrel shown in Figure 5.2(c). To obtain the temperature profile with different amount of dry ice added, a thermocouple (RS components 363-0339) was attached to the mandrel surface and the temperature was recorded every second with a data logger (Pico thermocouple data logger TC-08). The thermocouple was in contact with the mandrel and insulated from the surrounding

air such that it is predominantly measuring the chilled mandrel surface. As shown in Figure 5.3, a steady temperature was achieved after 200s and maintained till 1,800s when 60g and 160g of dry ice were used. The average temperatures maintained were -29 ± 2°C and -36 ± 1°C respectively (for discussion purpose, these temperatures are referred as -30°C and -35°C respectively). When 30g of dry ice were used, a steady temperature was not maintained till 1,800s. Hence, temperature variations were confined to 2 distinct values of approximately -30°C (60g dry ice) and -35°C (160g dry ice). Lower temperatures were not investigated as the maximum amount of dry ice that could be packed into the mandrel was 160g.

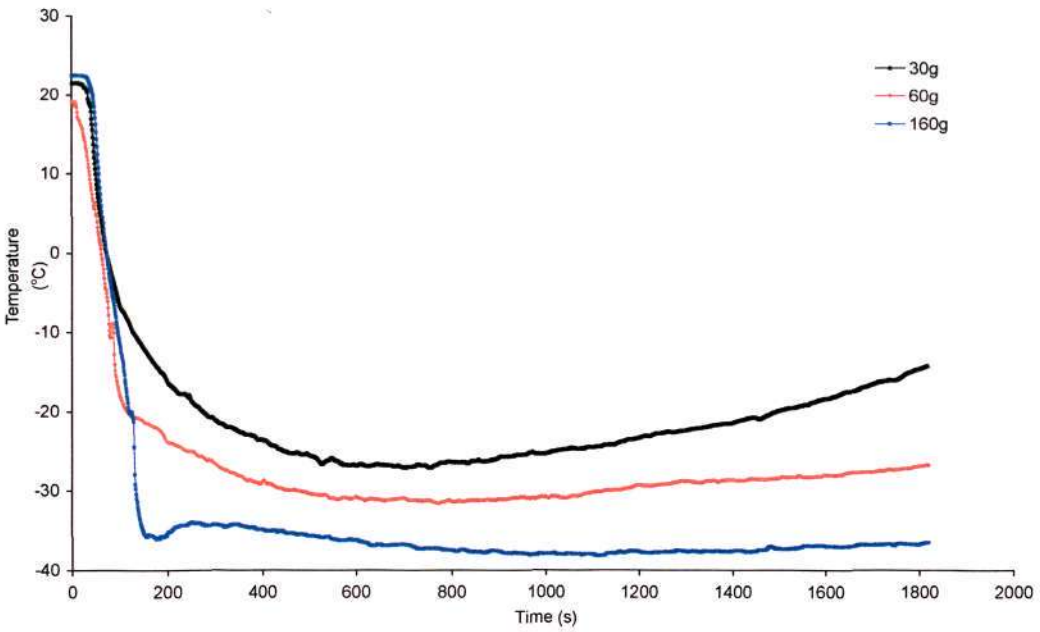

Figure 5.3 Temperature profile of mandrel with different amount of dry ice as indicated.

5.2.2.3 Controlling the rate of fiber deposition

The flow rate of the polymer solution is controlled by pneumatic pressure, which in turn controls the rate of electrospun fiber deposition since the throughput of fibers at the nozzle is determined by the solution flow rate. To determine the relationship between syringe pneumatic pressure and solution flow rate, a 0.15g/ml solution of

PLA in HFIP was electrospun at pneumatic pressures of 1psi, 2psi and 3psi, with all other parameters kept constant (potential difference = 25 kV, transverse displacement = 50mm, vertical displacement = 100mm, needle size = 26G, mandrel rotation = 350rpm). The duration of electrospinning was fixed at 60 minutes for all experiments. After 60 minutes, the electrospun mesh was removed from the mandrel and dried in a vacuum oven at 58°C for 48 hours to remove residual solvent (complete solvent removal is verified with Thermogravimetric analysis as shown in Appendix C). Finally, the mesh was weighed to determine the dry weight of the electrospun fibers collected, which was further converted to the flow rate of the solution. The experiment was carried out in triplicates for all pneumatic pressures. Figure 5.4 shows the relationship between pneumatic pressure and weight of fibers collected. The relationship is linear within the pressure range of 1 – 3psi and thus, syringe pneumatic pressure was used to vary solution flow rate in the experiments.

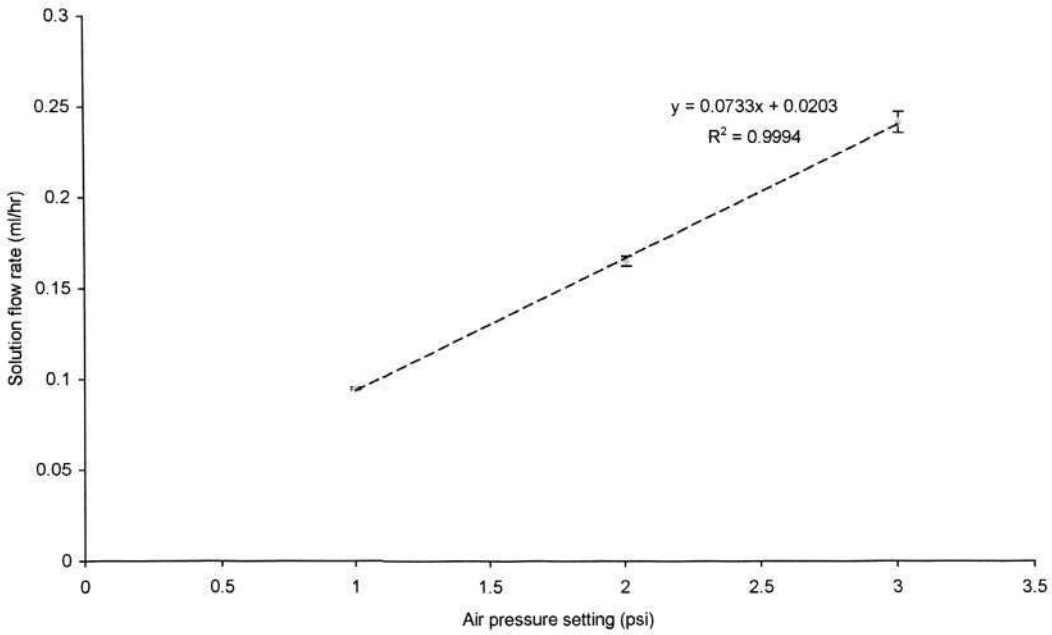

Figure 5.4 Relationship between syringe pneumatic pressure and solution flow rate. The relationship is linear for pressures between 1 – 3psi. Mean ± SD. n=3.

5.2.3 Materials

5.2.3.1 Materials for electrospinning

The polymer used was poly(D,L-lactide) (PLA)(Lasia H100J). The solvent used to dissolve the polymer was 1,1,1,3,3,3-hexafluoroisopropanol (HFIP) from Merck (Singapore).

5.2.3.2 Materials for cell culture

The materials used for cell culture are listed as follows: Papain from papaya latex, 0.5U/mg solid (Sigma, P3250), collagenase Type II from Clostridium histolyticum, 366U/mg solid (Sigma, C6885), soybean trypsin inhibitor, >7000 Nα-Benzoyl-L-Arginine Ethyl Ester (BAEE) Units/mg (Gibco, 17075-029), bovine serum albumin (BSA, Sigma A7906), HEPES (4-(2-hydroxyethyl)-1-piperazineethanesulfonic acid) buffer solution, 1M (Gibco, 15630-080), sodium bicarbonate ($NaHCO_3$, Life Technologies, 11810-033), Dulbecco's modified Eagle's medium (DMEM, HyClone, SH30022.01), fetal bovine serum, research grade (FBS, HyClone, CH30160.03), antibiotic-antimycotic solution, 100× (AAS, contains 10,000U/ml penicillin, 10mg/ml streptomycin and 25μg/ml, Sigma, A5955), kanamycin, 50mg/ml (Sigma, K0254), DMEM without Ca^{2+} and Mg^{2+} (HyClone, SH30262.01), Dispase from bacillis polymyxa (1.10U/mg, Gibco 17105-041), 0.25% trypsin/0.02% ethylene diamine tetraacetic acid (EDTA) (Sigma, T4049), fibronectin from bovine plasma (Sigma F4750), 0.1% Collagen Type I solution from calf skin (Sigma C8919), Defined keratinocyte serum free medium (Defined keratinocyte serum-free medium K-SFM, Gibco 10785), Defined K-SFM growth supplement (Gibco 10784), ethylenedinitrilotetraacetic acid, disodium salt dihydrate (Titriplex-EDTA, Merck 108418), Epidermal growth factor (EGF, Sigma E9644), hydrocortisone (Sigma

H6909), insulin human recombinant (10mg/ml, Sigma I9278), Ham F12 nutrient mixture (Gibco 21700-075) and 3-(4,5-dimethylthiazol-2-yl)-5-(3-carboxymethoxyphenyl)-2-(4-sulfophenyl)-2H-tetrazolium MTS proliferation assay (CellTiter96 Aqueous One, Promega G3580).

The materials used for histology are as follows: Accustain Harris hematoxylin solution (Sigma, HT107), Eosin Y solution (Sigma, 318906), Accustain Masson's trichrome stain kit (Sigma, HT15), Accustain Weigert's iron hematoxylin solution set (Sigma, HT1079) and Direct red 80 (Sigma, 365548).

5.3 Frost formation experiments

Since the cryogenic electrospinning technique uses ice crystals to expand the pores of the electrospun scaffolds, it is important to understand the effect of electric field, relative humidity and mandrel temperature on the ice crystals formed on the rotating mandrel.

5.3.1 Effect of electric field on frost formation

It has been reviewed that frost formation is affected in the presence of electric field. In this experiment, the effect of electric field on frost formation was studied.

The electrospinning machine was operated similarly as all other cryogenic electrospinning trials, but without polymer solution in the syringe. Frost formation data was collected at 50% RH and a mandrel temperature of -35°C. These conditions were selected because the thick CES fabricated under these conditions had the largest

pores, and were used for mechanical properties characterization, *in vitro* and *in vivo* studies.

Images of the ice crystal template that forms on the mandrel were taken with a high magnification camera (Keyence VH 6300 with VH-Z25 zoom lens and Olympus LG-PS2 illuminator) at time intervals of 2, 5, 10, 15, 20, 25, 30 minutes. The mass of ice crystals deposited on a release paper (9 × 5 cm) wrapped around the mandrel was weighed at 10 minutes.[196] Two trials were conducted, one with and the other without the electric field. All other parameters were kept constant and shown in Table 5.1.

Table 5.1 Parameters that were kept constant for this experiment.

Parameters	**Values**
Voltage	25kV
Vertical displacement	100mm
Horizontal displacement	50mm
Mandrel rotation	350rpm

5.3.2 Effects of humidity and mandrel temperature on frost formation

It has been reviewed that the environment's humidity and the substrate temperature affect frost formation. In this experiment, the effects of humidity and mandrel temperature on frost formation were studied.

Frost formation data was collected at different humidities (25%, 40%, 50% and 70%) and temperatures (-30°C and -35°C). All other parameters were kept constant as shown in Table 5.1 unless otherwise stated. The mass of ice crystals deposited on a release paper (9 × 5 cm) wrapped around the mandrel was weighed at time intervals of 10, 20 and 30 minutes at known relative humidities and temperatures (n=3). The thickness of the frost layer was measured with a thickness gauge (Peacock, Model G) as described in this report.[196] Images of the ice crystal template that formed on the

mandrel were taken with a high magnification camera at time intervals of 2, 5, 10, 15, 20, 25, 30 minutes during dry runs (without the polymer solution) at various relative humidities and temperatures. The porosity of the frost depositing on the mandrel was determined using an image analysis software on the area of interest, typically 6.2 × 3.0mm (n=3).

The deposited mass and thickness of the frost layer at -35°C and at various predetermined humidities after 15 minutes of frosting time were used to determine the values C_1 and C_2 graphically. C_1 and C_2 are used in the empirical correlation between frost porosity and absolute humidity as represented by Equation 4.6.

5.4 Process development

5.4.1 Cryogenic electrospinning[175,176]

In order to increase the pore size of electrospun scaffold, the cryogenic electrospinning technique is developed. This technique involves the processes of electrospinning and frost deposition on the mandrel. The procedures are described in the following section.

5.4.1.1 General procedure for cryogenic electrospinning

A solution of PLA in HFIP at a concentration of 0.15g/ml was prepared and placed in a 30ml syringe fitted with a 26 gauge metal needle. The syringe was placed into a holder, ensuring that the metal needle was in contact with the earthed plate. Electrospinning was carried out in an environmentally controlled chamber with the temperature maintained at 20 – 23°C, and the relative humidity controlled between 25 – 70%. The mandrel was cooled to a temperature of -30°C or -35°C by packing

different amounts of dry ice into the mandrel. The pneumatic pressure was used to regulate the PLA solution flow rate (1 – 3psi). A voltage between 20 to 25kV was applied to the mandrel until a stable Taylor cone formed at the needle tip, resulting in a stable polymer jet. The distance between the tip of the needle and mandrel surface (vertical displacement) was fixed at 100mm and the transverse displacement was fixed at 50mm. After a uniform frost layer was formed on mandrel (typically 5 minutes), electrospun fibers were deposited while ice crystals simultaneously deposited on the chilled rotating mandrel. After electrospinning was completed, the fibrous mesh was freeze-dried (Alpha 1-2, Germany) overnight to remove the embedded ice crystals by sublimation. The scaffold was then oven-dried at 58°C for 48 hours (Thermoline VORD-460-D, Australia) to remove residual solvent. The acronym, CHIEF, is coined with the letters representing the significant steps in the cryogenic electrospinning process (Figure 5.5).

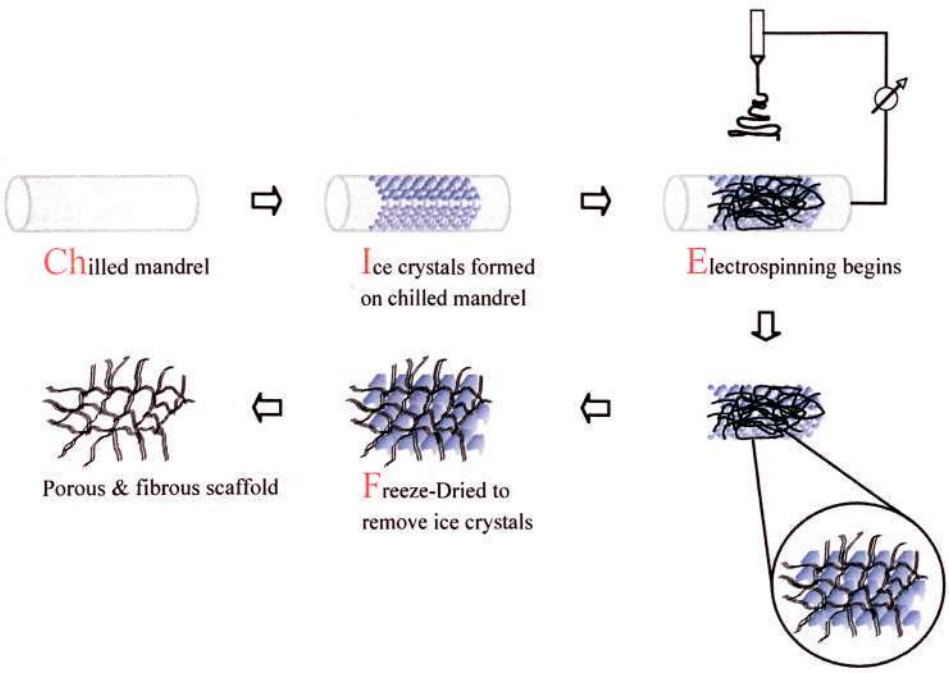

Figure 5.5 The "CHIEF" process.

The general parameters used in cryogenic electrospinning are summarized in Table 5.2. All subsequent studies involving electrospinning used these parameters unless otherwise stated in the experiment.

Table 5.2 Generic parameters for cryogenic electrospinning processes.

Parameters	Values
Concentration of PLA solution	0.15 g/ml
Ambient temperature	20 – 23°C
Mandrel temperature for cryogenic electrospinning	-35°C
Environment's humidity	50% RH
Voltage range	20 – 25kV
Syringe pneumatic pressure	2psi
Vertical displacement	100mm
Horizontal displacement	50mm
Mandrel rotation	350rpm
Needle size	26G

5.4.1.2 Study of mechanism of cryogenic electrospinning

Cryogenic electrospinning is a new technique that is being used to expand the pore size of electrospun scaffolds. The interaction between the ice crystals and the electrospun fibers is not well understood. The objective of this experiment is to study the mechanism of the cryogenic electrospinning technique. Two experiments were conducted. The first experiment was conducted to visualize the interaction between the ice crystals and the CES fibers under electron microscopy. The second experiment was conducted to measure the spacing between the ice crystals and compare it with the distance between the nodes of the CES.

In the first experiment, freshly formed CES (at -35°C and 50%RH) with ice crystals (without freeze-drying) was placed on a pre-chilled cold stage that was maintained at -20°C (Deben Research Coolstage, LT2) immediately to minimize melting of the ice in the scaffold structure. The specimen was in its pre-freeze-dried stage so that the ice crystals and fibers could be observed together. In addition, the low vacuum

(approximately 10 – 230Pa) and cold temperature (-20°C) delayed the melting of the ice crystals within the specimens in the chamber, and allowed the freeze drying process to be observed under high magnification.[198] The CES was observed under low vacuum SEM (LV-SEM) as described in Section 5.8.1.2.

In the second experiment, frost pictures formed at -35°C and 40%RH were taken with a high magnification camera at 15 minutes. The conditions were chosen because previous studies have shown that the spacing between the frost columns at these conditions were distinct enough for measurements to be taken. An image analysis software (ImageJ 1.38x, National Institutes of Health, USA) was used to measure the distance between two ice crystal columns (n=3). CES was fabricated at the same conditions after 15 minutes of frosting time and continued for 5 minutes. The inter-nodal distance of the CES, which was the distance between two neighboring fiber clusters, was measured using the same image analysis software on SEM micrographs taken at 50x (n=3).

5.4.2 General procedures for conventional electrospinning

Conventional electrospun scaffolds (ES) were used as controls for all experiments. The preparation of the conventional electrospun scaffold was similar to the CES, except that the mandrel was kept at room temperature (without the use dry ice) and the construct was oven-dried at 58°C for 48 hours after electrospinning.[69] All other parameters were kept constant unless otherwise stated in the experiment (Table 5.2).

5.4.3 Process study for cryogenic electrospinning

Cryogenic electrospinning technique uses ice crystals to enlarge the pores of electrospun scaffolds. Hence, the parameters that affect ice crystal formation will affect the pore size of the CES. In addition, the amount of fibers deposited on the frost layer that was forming on the mandrel could also affect the CES pore size. In this section, the effect of these parameters, such as mandrel temperature, environment's humidity and rate of fiber deposition, on the pore size of CES were studied.

5.4.3.1 Effect of environment's humidity on pore size of CES

From the frost formation experiments, it has been shown that the humidity of the environment affected the spacing between ice crystals. Since the ice crystals are used to separate the fibers in CES, the humidity effect on inter-crystal spacing will in turn affect the pore size of the CES. The objective of this experiment is to study the effect of environment's humidity on the pore size of the CES.

In this experiment, the relative humidity of the chamber was set at 25%, 40%, 50% and 70%. The humidity effects on CES pore size were studied at both temperatures of -30°C and -35°C. All the other parameters were kept constant and shown in Table 5.2. Collection of the CES started 15 minutes after loading the mandrel with dry ice and continued for 5 minutes. The collection started after 15 minutes to allow formation of a uniform layer of ice crystals before fiber deposition, while the process duration was kept to 5 minutes such that only the initial layer of fibers was collected. This is to prevent excessive fiber accumulation from obscuring the effect of humidity on the pore size of the CES. Hence, the effect of the ice crystal template on the organization of the deposited fibers can be studied.

The humidity effect on pore size was also studied for thicker CES (~400μm), as opposed to the initial layer (< 50μm). A thicker CES was obtained by starting at the 5th minute and the process duration was extended to 30 minutes. Scaffolds were fabricated at different relative humidities of the chamber at 25%, 40%, 50% and 70%. All other parameters were kept constant as shown in Table 5.2. Samples of ES were fabricated as control using the same set of conditions described in this section. The pore sizes between CES and ES were compared (n=5).

5.4.3.2 Effect of mandrel temperature on pore size of CES

It has been discussed that the temperature of the cold surface on which frost is deposited affects frost porosity. This temperature effect on frost porosity can in turn affect the pore size of CES in cryogenic electrospinning. The objective of this experiment is to study the effect of mandrel temperature on the pore size of the CES.

To investigate this effect, 60g and 180g of dry ice was used to maintain the mandrel at different temperatures of -30°C and -35°C respectively in separate experiments. All other parameters were kept constant as shown in Table 5.2. Collection of the CES started 15 minutes after loading the mandrel with dry ice and continued for 5 minutes for the same reasons stated in the previous section. The pore sizes between CES and ES were compared (n=5).

5.4.3.3 Effect of rate of fiber deposition on pore size of CES

As the cryogenic electrospinning technique involves electrospinning and ice crystal formation, the relative rates of fiber deposition and ice crystal formation becomes important. If the deposition of fibers dominates the formation of ice crystals, the

density of the fibrous mesh will increase and vice versa. The objective of this experiment is to study the effect of fiber deposition rate on the pore size of CES while keeping the conditions for ice crystal formation constant.

To study this effect, the rate of fiber deposition was changed by setting the syringe pneumatic pressure at different values of 1, 2, and 3psi. All other parameters were kept constant and shown in Table 5.2. CES was obtained by electrospinning at the 5^{th} minute and the process continued for 30 minutes. ES fabricated at the stated pneumatic pressures were used as controls. The pore size of ES and CES were compared (n=5).

5.5 Scaffold fabrication

After studying the process parameters that affect the pore size of CES, we can fabricate different types of scaffolds for physical characterizations, *in vitro* and *in vivo* evaluations. This section documents the parameters used to fabricate the three different types of scaffold (CES, ES and BLES).

5.5.1 Cryogenic electrospun scaffold (CES)

The CES was fabricated according to the procedures described in Section 5.4.1. The process started 5 minutes after the dry ice was packed in the mandrel and continued for 30 minutes. All other parameters are listed in Table 5.2. The parameters were chosen as the thick CES fabricated under these conditions had the largest average pore size based on previous studies.

The CES fabricated were used for mechanical testing, cytotoxicity testing, *in vitro* cell culture experiments and *in vivo* subcutaneous implantation.

5.5.2 Conventional electrospun scaffold (ES)

The ES was fabricated according to the procedures described in Section 5.4.2. The duration of electrospinning was 30 minutes and all other parameters were kept constant as shown in Table 5.2. The parameters were chosen such that the conditions, other than the mandrel temperature, were the same for both CES and ES.

The ES samples fabricated were used for mechanical testing, cytotoxicity testing, *in vitro* cell culture experiments and *in vivo* subcutaneous implantation.

5.5.3 Bilayered electrospun scaffold (BLES)

From the literature review (Section 2.1.2) and the study on the histoarchitecture of the porcine oesophagus (Section 5.1), the scaffold design should consist of two layers, one with small pores to mimic the basement membrane of the oesophageal ECM to support the epithelium while the other with large pores to mimic the loose fibrous connective tissue of the mucosal-submucosal tissue. This provides the basis for the design of a bilayered scaffold using the electrospinning technique.

The BLES consists of a layer of ES and a layer of CES in a single construct. To fabricate the BLES, the CES was first fabricated according to procedures described in Section 5.5.2. The process started 5 minutes after the dry ice was packed into the mandrel and continued for 15 minutes. Thereafter, the relative humidity of the chamber was lowered to 25% according to the procedures and the rate of fiber

deposition increased from 0.16ml/hr to 0.24ml/hr. Based on previous study, the chamber's low humidity limited ice crystal deposition. With the increase in fiber deposition, the combined process changes resulted in the fabrication of a dense ES layer on top of the already formed CES. The entire BLES was freeze-dried to remove the ice crystals and oven dried under vacuum at 58°C for 48 hours to remove residual solvent.

Similarly, the BLES samples fabricated were used for mechanical testing, cytotoxicity testing, *in vitro* cell culture experiments and *in vivo* subcutaneous implantation.

5.6 *In vitro* cell-scaffold interactions

5.6.1 Cytotoxicity testing

Cytotoxicity refers to the toxic effects at cellular level. A material is considered cytotoxic if it releases sufficient quantities of chemical to cause cell death directly or indirectly by affecting important metabolic processes[64]. Cytotoxicity tests should be conducted to assess the toxicity of materials prior to using the materials in *in vitro* and *in vivo* studies.

The cytotoxicity test was conducted in accordance with ISO 10993-5 Tests for *In Vitro* Cytotoxicity test standard. The extraction test was used. Samples were sterilized in 70% ethanol and placed on an orbiter shaker for 24 hours. The samples were then rinsed 5 times, each time with 40ml of PBS for 15 minutes. Subsequently, the samples were extracted by immersing in culture medium (DMEM, 10% FBS and 1% AAS) at a concentration of 0.1g/ml and incubated at 37°C for 24 hours. The positive control

used was powder free latex gloves while tissue culture polystyrene plates (TCPS) were used as negative control.

3T3/NIH fibroblasts were passaged twice prior to the test. The cells were then cultured to sub-confluence in a 24-wells tissue culture polystyrene plates (TCPS) at a density of 2.5 x 10^4 cells/cm^2. During the test, the supernatants in the wells were discarded and the sub-confluent layers of cells were rinsed with PBS. 1ml of extract from each specimen was added to each well and the cells were further incubated for 24 and 48 hours. The tests were conducted with 4 replicates per specimen per time point. Qualitative assessment of cytotoxicity was carried out by observing the cell morphology, presence of cell vacuoles and cell lysis within the wells. A cytotoxicity rating was assigned according to the ISO 10993-5 test standard. The recommended cytotoxicity rating scale is: 0 for non-cytotoxic, 1 for mildly cytotoxic, 2 for moderately cytotoxic and 3 for severely cytotoxic. Quantitative assessment of cytotoxicity was carried out after 48 hours in culture using MTS proliferation assays as described in Section 5.8.4.

5.6.2 To study the effect of pore size on *in vitro* cell infiltration

One of the limitations of conventional electrospun scaffold is the prevention of cell infiltration *in vitro* due to its small pore size. The development of the cryogenic electrospinning technique is to expand the pores of electrospun scaffold so that cell infiltration can be supported. The objective of this experiment is to study the effect of pore size on *in vitro* cell infiltration under static culture conditions.

3T3/NIH fibroblasts were cultured in DMEM supplemented with 10% FBS and 1% AAS. The scaffolds, CES and ES, were sterilized in 70% ethanol, rinsed thoroughly with PBS and immersed in culture medium for 24 hours prior to use. Each scaffold was seeded with $1x10^5$ cells/cm^2, and the constructs were maintained for up to 14 days with a change of media every other day. Care was taken that the cells were seeded on the top surface of the scaffolds without spillage to ensure that any cell infiltration occurred only from above. The constructs were fixed with 10% formalin at the endpoints and sectioned for histochemical staining.

5.6.3 Co-culture of porcine oesophageal epithelial cells (PEECs) and smooth muscle cells (PESMCs) on electrospun scaffolds (ES and BLES)

The objective of this experiment is to evaluate the feasibility of using a bilayered electrospun scaffold with different pore sizes for oesophageal tissue regeneration. The BLES was used to support the co-culture of PEECs and PESMCs. In the co-culture experiment, the PEECs were seeded on the dense ES side while the PESMCs were seeded on the CES side of the BLES. This combination mimics the mucosa-submucosa of the oesophagus, where the PEECs are supported on a basement membrane while the PESMCs are scattered within the loose connective tissues.

5.6.3.1 Isolation of PEECs

The muscularis externa was first removed and the remaining submucosa-mucosa portion was cut into less than 5 × 5mm^2 pieces. Neutral enzyme, dispase was reconstituted in DMEM without Ca^{2+} and Mg^{2+} at 0.6%(w/v) and filtered. The tissue pieces were digested in the dispase solution at 37°C for 3h. After digestion, intact epithelium was removed from the underlying tissue. Epithelium was further subjected

to trypsinization with 5ml of 0.25% trypsin/0.02% EDTA for 1 to 5 minutes. About 1g of tissues resulted in 8 million epithelial cells after trypsinization for 3 minutes. The trypsin was subsequently deactivated with 5ml of 10% FBS containing culture medium. Isolated cells were plated on Fibronectin/BSA/Collagen Type I-coated tissue culture plate at a density of 25,000 cells/cm^2 and cultured in Defined K-SFM with growth supplements. The culture medium was changed the next day and it took about 3-4 days to reach 80% confluence. Before subculture, cells were washed in 1mM EDTA in PBS twice at room temperature for 2 minutes each followed by final incubation at 37°C for 10 minutes. 3-5 minutes of trypsinization was carried out to detach the cells. Detached cells were neutralized with serum-containing medium, centrifuged and re-plated at 10,000 to 25,000 cells/cm^2. Cells at passage 4 were used in the experiment.

5.6.3.2 Isolation of PESMCs

Porcine oesophageal smooth muscle cells were isolated from 2cm oesophageal segment about 1 inch above the stomach where there is abundance of smooth muscle cells within the muscularis externa. The muscularis externa was dissected from the submucosa and washed in PBS containing 1% antibiotic-antimycotics solution three times. The muscle layer was cut into small cubes (about 5 × 5mm^2) and digested in enzyme solution containing 10U/ml papain, 1mg/ml collagenase II, 2mg/ml BSA, 2mg/ml soybean trypsin inhibitor, 10mM HEPES and 4mM $NaHCO_3$ in Hank's balanced salt solution (HBSS) at 37°C. After 30 minutes of digestion, the solution was aspirated with 1ml pipette for 10 minutes to release the cells from the extracellular matrix. The solution was allowed to settle for 3 minutes and the supernatant was collected and passed through a 100-μm cell strainer. The filtrate was

centrifuged at 3000rpm for 5 minutes and the supernatant was removed and the cell pellet was re-suspended in 1ml complete medium which is composed of Dulbecco's Modified Eagle Medium (DMEM) supplemented with 10% fetal bovine serum, 1% antibiotic-antimycotic solution (100U/ml penicillin, 100µg/ml streptomycin and 0.25µg/ml) and 0.2% kanamycin (0.1mg/ml). Suspension of PESMCs was transferred to 25cm^2 tissue culture flasks and 4ml complete medium was added to each flask. The culture medium was changed the next day and subsequently every other day. Cells were cultured in 37°C, 5% CO_2 incubator for 10 days to reach confluence. Cells at passage 4 to 8 were used in the experiment.

5.6.3.3 Co-culture of PEECs and PESMCs on electrospun scaffolds (ES and BLES)

The specimens (ES and BLES) were solvent bonded to empty inserts of Transwell® plates for this experiment. Briefly, the membrane on the insert of the Transwell® plate was removed. The electrospun scaffold was cut to size and solution bonded to the Transwell® plate using dichloromethane. The inserts were subsequently oven dried under vacuum at 40°C for 48 hours to remove residual solvent. For the BLES, the specimen was placed such that the dense ES layer faces upward when the insert was upright.

The constructs consisting of the inserts and the scaffolds were hydrated in PBS for 30 minutes and then sterilized in 70% ethanol for 1 minute. They were subsequently rinsed with sterile PBS three times and dried in a laminar flow hood. PESMCs were seeded at 50,000 cells/cm^2 on the bottom side (CES), which was faced up. On the next day, the whole construct was inverted and cultured for 7 days in PESMC medium described in Section 5.6.3.2. On day 7, PEECs were seeded at the density of

80,000 cells/cm^2 on the ES side of the BLES. PEEC culture medium was added to the well within the Transwell® insert the next day. For the next 7 days, epithelial cells were fed with PEEC medium described in Section 5.6.3.1 and kept submerged while the PESMCs on the bottom side were maintained in PESMC medium. On day 14, the medium was switched to DMEM/ Ham F12 (3:1) supplemented with 5% FBS, 10ng/ml EGF, 1nM hydrocortisone, 10mg/ml insulin, 1% AAS and 0.2% kanamycin and from this time point onwards, the medium was only added to the bottom of the Transwell® plate such that the epithelial cells were exposed to air. This air-liquid interface configuration was maintained for the next 6 weeks, with medium changes every other day, and nutrient support for epithelial cells was purely dependent of diffusion from the bottom side.

The constructs were fixed in 10% formalin after 2 months and sectioned for histochemical staining to observe the organization of the 2 cell types on the BLES. The conventional ES was used as control for this experiment.

5.7 *In vivo* subcutaneous implantation study

The animal experiment described in this section was approved by the Nanyang Technological University Institutional Animal Care and Use Committee (NTU-IACUC) (Approval Reference: ARF-SBS/NIE-A0023). The ES, CES and BLES were cut into 1 × 1cm square specimens, sterilized in 70% ethanol and washed thoroughly with PBS. Wistar rats weighing 300 to 350g were used for the subcutaneous implantation study. The rats were anaesthetized with inhalational isoflurane and oxygen. The dorsum was shaved and cleansed with chlorhexidine and iodine and a single 3cm midline incision was made. Four subcutaneous pockets were created on

either side away from the incision by blunt dissection. The ES, CES and two BLES were inserted into each pocket, ensuring that placement was flat. The two BLES consist of one BLES with the dense ES layer facing the subcutaneous tissue (BLDU) while another BLES with the dense ES layer facing the underlying muscle (BLDD). The incision was closed with interrupted 3/0 polypropylene sutures. The sample size was 3 animals for each time point (14, 28 and 56 days). The time points were selected such that *in vivo* cell infiltration, vascularization and foreign body capsule formation could be studied.

Postoperatively, an intramuscular injection of tolfedine (0.1ml) was administered in the thigh for pain relief. Sutures were removed on the tenth post-operative day. At the specified endpoint (14, 28 and 56 days post implantation), the rat was euthanized by carbon dioxide inhalation. The dorsum was shaved and the previous incision reopened as shown in Figure 5.6. All scaffolds were retrieved with the surrounding tissue and placed in 10% formalin for processing and histological sectioning as described in Section 5.8.5. The number and the depth of infiltrating cell within the scaffolds were determined according to procedures described in Sections 5.8.6 and 5.8.7 respectively.

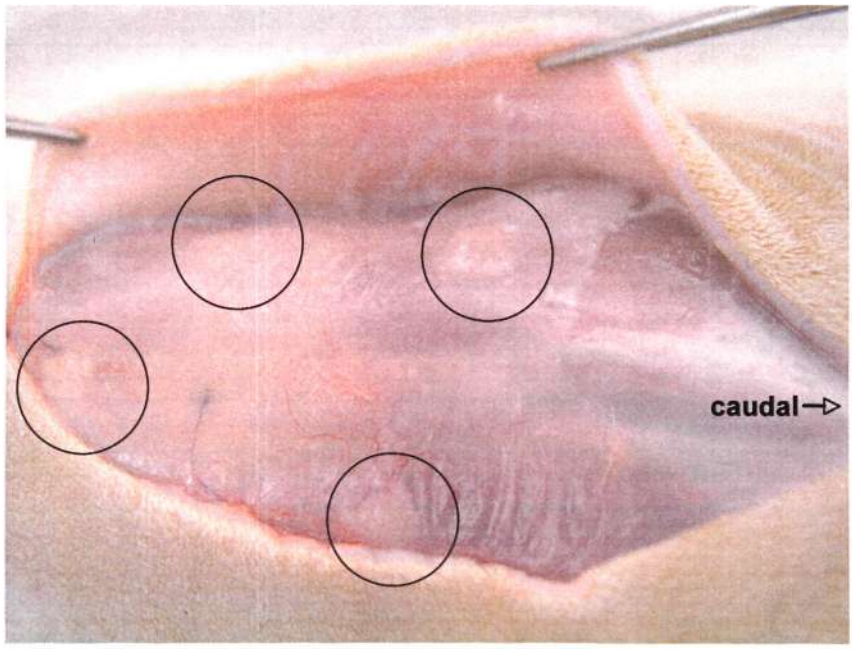

Figure 5.6 Picture showing the positions of the 4 specimens on the dorsum of the Wistar rat during explantation.

5.8 Methods of characterization

5.8.1 Electron microscopy

5.8.1.1 Scanning electron microscopy (SEM)

Vacuum dried electrospun specimens were gold sputtered (JEOL JFC 1600 Auto Fine Coater) and observed by scanning electron microscope (SEM) (JEOL 5600 LV) at an accelerating voltage of 10 kV.

5.8.1.2 Dynamic low vacuum LV-SEM (backscattering) on a cold stage

In order to observe the interactions between the ice crystals and electrospun fibers, the dynamic LV-SEM was used.[198] The specimen used was freshly formed CES with ice crystals before the freeze-drying step. No gold sputtering or any other specimen treatment was used. The specimen was placed on a pre-chilled cold stage that was maintained at -20°C and transferred into the SEM chamber immediately to minimize

melting of the ice crystals in the scaffold structure. Once the low vacuum was established (up to 230Pa), backscattering mode was used to image the specimen immediately.

5.8.2 Mechanical properties

Mechanical testing was conducted in accordance with the American Society for Testing and Materials ASTM D638-03 Standard Test Method for Tensile Properties of Plastics. Dumbbell shaped specimens (Type V) were die cut from an electrospun mesh using a precision cutter (Super Dumbbell Co. Cutter D638 Type V) and the thicknesses of the specimens were measured using a dial gauge. The specimens were mounted on a picture-frame cardboard so that it could be easily handled and aligned. The specimens were tested on an Instron Universal Tensile Tester (Model 5566) set at a cross-head speed of 1mm/s and the load force was recorded with a 1kN load cell. The load and extension of the specimens were measured. The failure mode of the mechanical testing was specimen fracture. The ultimate tensile stress and strain at break were determined accordingly. The values were expressed as mean ± standard deviation (SD). Two-tailed paired Student's t-test was used to determine if the difference between the means was significant.

5.8.3 Pore size measurement

Pore size of the scaffolds was determined using an image analysis software (ImageJ software 1.38x, National Institutes of Health, USA) on the SEM micrographs taken at 50x and 500x magnification for CES and ES respectively. Different magnifications were used as the pore size of the CES and ES were very different. The large pores of the CES (typically 10 – 500μm) could only be analyzed under low magnification

while high magnification was needed to analyze the small pores of the ES (typically < 5μm). The micrographs were optimized to threshold the appropriate fiber layers. As the pores of electrospun scaffolds are polygonal in shape, pore sizes were determined by measuring the pore areas (if necessary, pore area can be converted to pore diameter of a circle of the same area by assuming the pore to be spherical). The measurements were normalized to the same area of interest ($2560 \times 1660 \mu m^2$) for comparison. Porosity of the scaffolds was calculated from the total pore area divided by the area of interest. One measurement per scaffold was taken on 5 scaffolds fabricated for each of the investigated set of parameters. All data was expressed as mean ± SD. Mann-Whitney-Wilcoxon rank-sum test was used to determine if the difference between the means was significant. A sample measurement of the image analysis is included in Appendix D.

5.8.4 MTS proliferation assay

The viability of the cells was determined with Colorimetric MTS assays (CellTiter 96® Aqueous One Assay). MTS proliferation assays determine the number of viable cells in a culture. The quantity of formazan, a bioreduction product by the cells, is directly proportional to the number of living cells. A colorimetric method is used to detect the quantity of the luminous yellow formazan product. High absorbance represents higher number of living cells in the specimens.

The supernatant that was used to culture the cells in the wells were removed and the cells were rinsed with sterile PBS and incubated in MTS assays for 4 hours. After incubation, the absorbance of the supernatants was measured using a micro-plate reader. The background absorbance, measured from the MTS assays that were placed

in wells not seeded with cells, was subtracted from the readings. The experiment was conducted in quadruplicates. The values were expressed as mean ± SD. Two-tailed paired Student's t test was used to determine if the difference between the means was significant.

5.8.5 Histochemical staining

Histochemical staining allows the study of structure and function of cells and tissues. In our experiments, it was used to study *in vitro* cell infiltration and *in vivo* cell infiltration and vascularization in CES, ES and BLES.

5.8.5.1 Paraffin embedding

The specimens were fixed with 10% formalin for 8 hours. Subsequently, the specimens were dehydrated through a series of graded ethanol (from 70 to 100vol.%) and finally in xylene before being embedded in paraffin. Specimen embedded paraffin blocks were then cut using a microtome to obtain 7μm slices and collected on polylysine treated glass slides. These sections are stained with hematoxylin and eosin, Masson's Trichrome, Sirus red and Hoechst stains as described in the following sections.

5.8.5.2 Hematoxylin and eosin staining (H&E)

Hematoxylin dye stains nuclei proteins dark purple, while eosin dye stains cytoplasm in tissues red.

Paraffin embedded tissue slides were deparaffinized in 3 xylene baths for 5 minutes each and hydrated through a series of graded ethanol (from 100 to 70vol.%).

Subsequently, the slides were immersed in deionized water for 5 minutes prior to staining. The staining process includes (1) immersing slides in filter Harris Hematoxylin solution for 20 minutes and rinsing in water, (2) removing excessive stains in acid alcohol and rinsing in water, (3) placing slides in Scott's blue solution for 5 minutes and rinsing in water and (4) dipping slides into working Eosin solution 3 times and rinsing in water. The stained slides were dehydrated through a series of graded ethanol (from 70 to 100vol.%) and xylene baths. Eventually, stained specimens were sealed under cover slips with mounting medium. The slides were then dried in the fume hood overnight before viewing under light microscope (Carl Zeiss Axioskop 40, Germany).

5.8.5.3 Masson's trichrome staining

This procedure stains nuclei proteins dark purple, cytoplasm and muscle fibers red, and collagen blue.

Paraffin embedded tissue slides were deparaffinized in 3 xylene baths for 5 minutes each and hydrated through a series of graded ethanol (from 100 to 70vol.%). Subsequently, the slides were immersed in deionized water for 5 minutes prior to staining. The staining process includes (1) mordant tissue sections in Bouin's fixative at 60°C for 45 minutes and rinse in water, (2) immersing slides in Weigert's iron hematoxylin stain for 10 minutes and rinsing in water, (3) immersing slides in Biebruch's scarlet acid fushsin stain for 5 minutes and rinsing in water, (4) immersing slides in phosphomolybdic-phosphotungstic acid solution for 12 minutes, (5) immersing slides in aniline blue solution for 5 minutes and rinsing in water, and (6) immersing slide in 1% acetic acid solution for 1 minute. The stained slides were

dehydrated through a series of graded ethanol (from 70 to 100vol.%) and xylene baths. Eventually, stained specimens were sealed under cover slips with mounting medium. The slides were then dried in the fume hood overnight before viewing under light microscope (Carl Zeiss Axioskop 40, Germany).

5.8.5.4 Sirius red staining

This procedure stains collagen red on a pale yellow background. It was used as a complement to the Masson Trichrome stained pictures to provide a better analysis for the distribution of the collagen fibers within the tissue.

Paraffin embedded tissue slides were deparaffinized in 3 xylene baths for 5 minutes each and hydrated through a series of graded ethanol (from 100 to 70vol.%). Subsequently, the slides were immersed in deionized water for 5 minutes prior to staining. The staining process includes placing the slides in Direct Red 80 mixed with saturated picric acid solution for 1 hour. Excessive dyes were rinsed in water. The stained slides were dehydrated through a series of graded ethanol (from 70 to 100vol.%) and xylene baths. Eventually, stained specimens were sealed under cover slips with mounting medium. The slides were then dried overnight before viewing under light microscope (Carl Zeiss Axioskop 40, Germany).

5.8.6 Counting of cell nuclei within scaffold

Cell counting was carried out using digital images of fluorescence histology.[199] Paraffin embedded sections were stained with Hoechst stain for 20 minutes and viewed under the microscope. The images were threshold based on a binary color model. An area of interest $450 \times 150 \mu m^2$ was used as a rectangular grid overlay on

the images, with the midlines of the rectangular grid overlapping those of the scaffolds in the images. This was to ensure that only nuclei in the middle section of the scaffold were counted to assess cellular infiltration within the scaffold. An image analysis software (ImageJ 1.38x, National Institutes of Health, USA) was used to measure the total area of nuclei within the grid and this area was used to estimate the number of cells. Measurements were made on scaffolds from 3 different animals (n=3), with 3 microscope images analyzed per specimen (9 data points for each scaffold). The data was expressed as mean ± SD. Two-tailed paired Student's t test was used to determine if the difference between the means was significant. A sample measurement using image analysis is included in Appendix D.

5.8.7 Measuring depth of cell infiltration[176]

The depth of cell infiltration was measured using digital images of tissue sections stained with hematoxylin and eosin. The images were captured at 200x magnification and printed $9 \times 6.8 cm^2$ in size. Depth of cell infiltration, expressed as a percentage of the scaffold thickness, was determined by measuring the total distance of the inner most cells from the periphery of the scaffold along an axis perpendicular to the midline of the scaffold. Measurements were made on scaffolds from 3 different animals (n=3), with 3 microscope images analyzed per specimen (9 data points for each scaffold). The data was expressed as mean ± SD. Two-tailed paired Student's t test was used to determine if the difference between the means was significant.

5.9 Statistical analysis

All quantitative data were presented as mean ± SD. Statistical comparisons were carried out by Mann-Whitney-Wilcoxon rank-sum test for data with non-normal

distribution and two-tail paired Student's t test for data with normal distribution. A value of $p<0.05$ was considered to be statistically significant.

Chapter 6 Results and Discussion

In this chapter, the results of the various experiments are presented. The sections are listed as follows:

- Section 6.1 – Analysis of histoarchitecture of porcine oesophagus. In this section, the results from the histochemical characterization of the oesophagus are presented. These characteristics are used as the basis for the design of a scaffold suited for oesophageal tissue engineering.

- Section 6.2 – Study on frost formation. In this section, the results from the frost formation experiments are presented. This includes pictures showing ice crystals deposition on the mandrel at different conditions, measurement of the mass of frost layer over time and an empirical correlation on frost porosity with humidity. The knowledge gained from this section is applied to the development of the cryogenic electrospinning process.

- Section 6.3 – Cryogenic electrospinning. In this section, the mechanism of the CES is established with evidence from LV-SEM showing the interactions between ice crystals and electrospun fibers. The effects of relative humidity, mandrel temperature and rate of fiber deposition on pore size of CES are presented and compared to ES.

- Section 6.4 – Bilayered electrospun scaffold (BLES) for oesophagus regeneration. In this section, a bilayered electrospun scaffold was fabricated to mimic the structure of the oesophageal ECM. The morphology of the BLES is presented. The mechanical properties of all three types of scaffolds (ES, CES and BLES) are compared.

- Section 6.5 – *In vitro* cell-scaffold interactions. In this section, the results for the scaffold cytotoxicity tests are presented. In addition, the effect on *in vitro* cell infiltration of the CES and the co-culture of PEECs and PESMCs using BLES are presented.

- Section 6.6 – *In vivo* subcutaneous implantation study. In this section, the *in vivo* assessment on cell infiltration and vascularization of the three scaffolds are presented.

6.1 Analysis of histoarchitecture of porcine oesophagus

The objective of this study is to identify the biomimetic features present in the porcine oesophageal ECM. These observations served as the basis for the design of electrospun scaffolds for tissue engineering of the oesophagus.

Figure 6.1(a) shows exposed basement membrane of a porcine oesophagus after the epithelium has been removed using dispase. The porcine oesophageal basement membrane is dense with small pores (less than 1μm) sparsely dispersed on the surface of the membrane. This corresponds with the description of typical surface morphologies of basement membranes in the literature.[26] From Figure 6.1(b), the abluminal side of the mucosal-submucosal layer, which is the loose connective tissue, is highly fibrous and porous. The diameters of the fiber bundles are less than 5μm. The range of pore sizes can be from few microns to few hundreds of micron. Both mucosal surfaces are very different in terms of pore sizes and topography.

Histochemical staining of the cross-section of the porcine oesophagus reveals the cellular and extracellular features of the oesophagus. From Figure 6.1(c), the epithelium is made up of several layers of epithelial cells (15 – 20 layers). The submucosa is made up of loose connective tissues, and the muscularis externa is striated. From Figure 6.1(d) there is a dense collagen fibrous layer beneath the epithelium, which is the basement membrane shown in Figure 6.1(a). Beyond this dense basal layer away from the lumen, the collagen fibers, which appear as blue

streaks, are loosely dispersed in the mucosa, submucosa and the muscularis externa (Figure 6.1(d)).

Based on these observations, a tissue engineered scaffold for the oesophagus should incorporate a dense fibrous layer to serve as the basement membrane, with an adjacent highly fibrous, porous layer for cell in-growth, structural support and muscle regeneration. The fiber and pore features range from nanometer to micrometer in size. In order to mimic these features of the ECM, the technique used to fabricate the tissue engineering scaffold should have the capability of producing nano to micro-scale fibrous and porous features. This project aims to develop the electrospinning technique to fabricate scaffolds that contain these features. However, conventional electrospinning techniques can only fabricate fibrous meshes with pore sizes less than 5μm. A cryogenic electrospinning is developed to create the highly fibrous and porous scaffold that mimics the loose connective tissue, which will be discussed in Section 6.3. In addition, the observations presented in the histochemical analysis of the porcine oesophagus provide the basis for the design of the BLES, which consists of a dense ES layer and a porous CES layer to mimic the basement membrane and the porous loose connective tissue respectively. This development of the BLES will be discussed in Section 6.4.

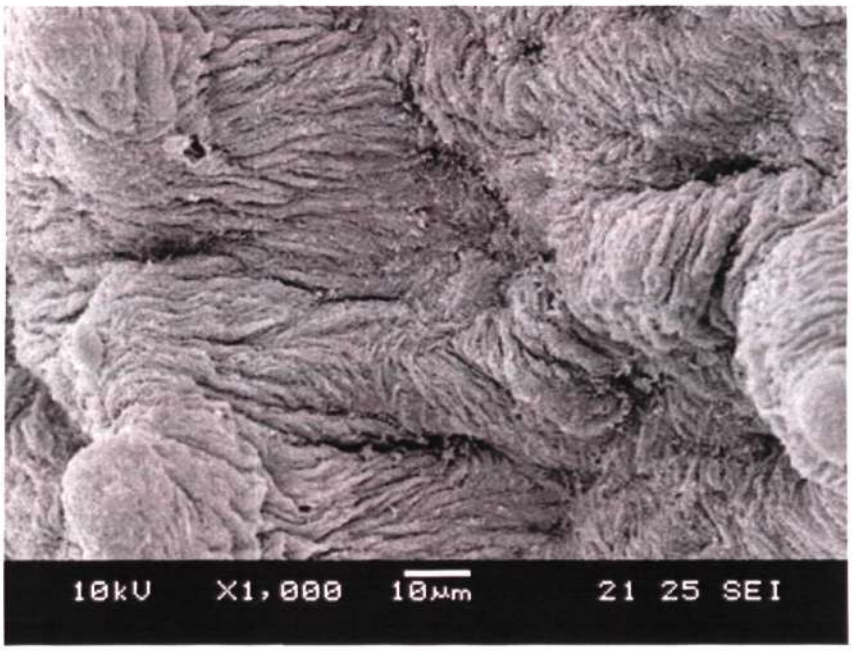

(a)

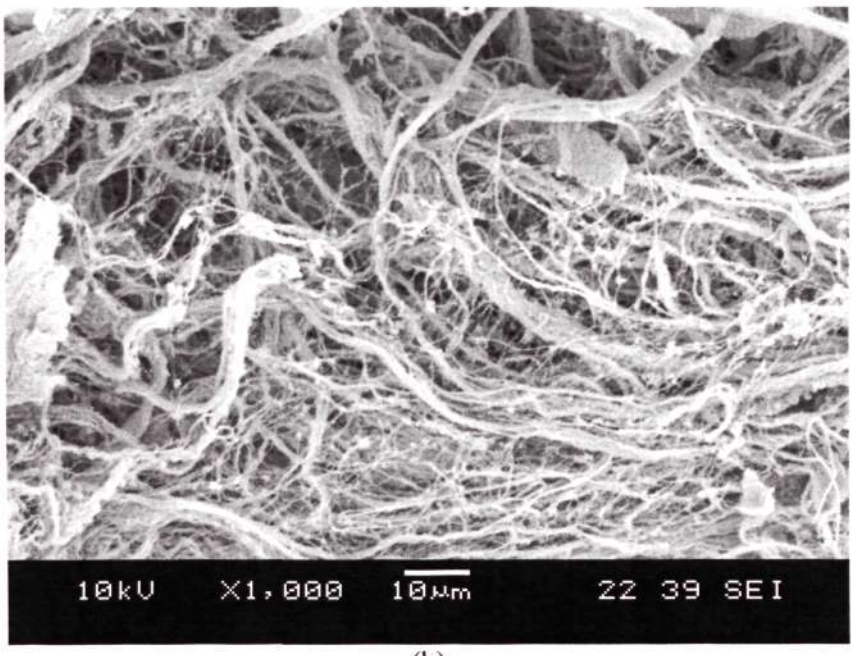

(b)

Figure 6.1 SEM micrographs showing the surfaces of the porcine oesophageal tissue. (a) Basement membrane and (b) abluminal side of mucosal-submucosal tissue.

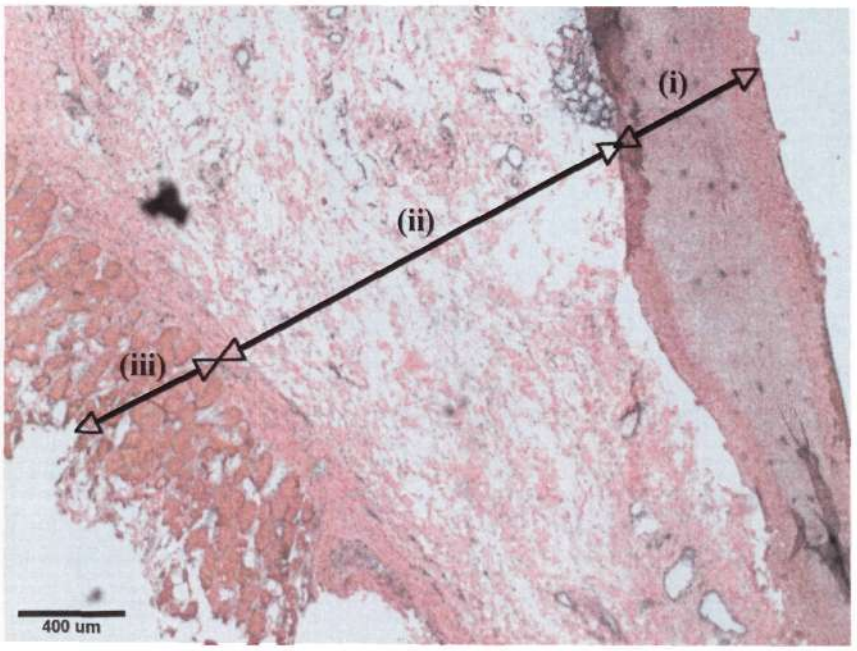

(c)

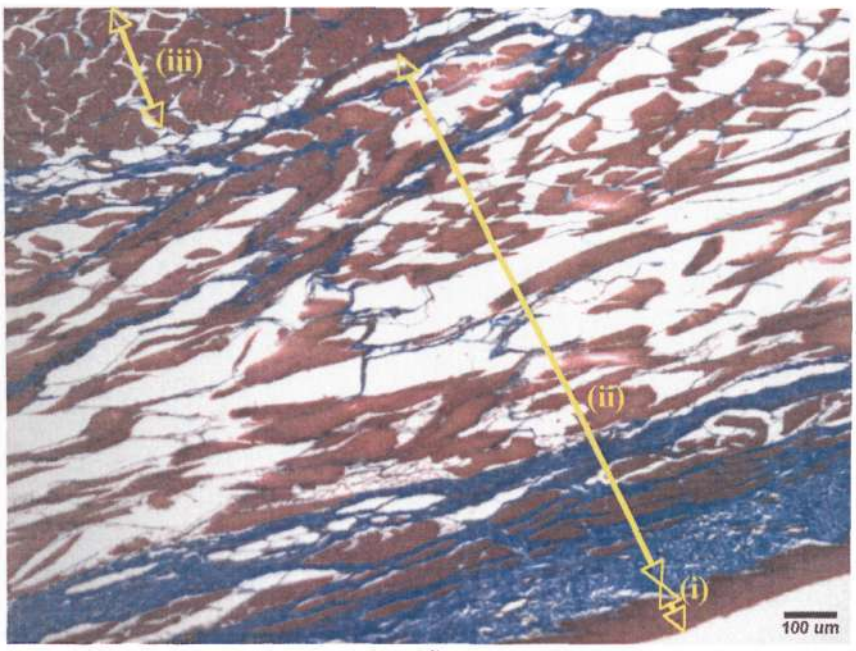

(d)

Figure 6.1 (c) H&E staining of the cross-section of the oesophagus and (d) Masson's Trichrome staining of the cross-section of oesophagus. Symbols: (i) Epithelium, (ii) mucosal-submucosal tissue and (iii) muscularis externa.

6.2 Study on frost formation

Preliminary results have shown the effect of frost formed on the mandrel on the pore size of the CES. The results shown in this study provide fundamental insight into the mechanism for creating and controlling the pore size of the scaffold using frost. The effects of environment's humidity and mandrel temperature on the mass, deposition rate and density of frost are studied in this section.

6.2.1 Effects of electric field on frost formation

This experiment was conducted to study the effects of electric field on frost formation. These effects are the alignment of ice crystals and the amount of frost deposited on the chilled mandrel.

Figures 6.2(a) and (b) shows the frost layer deposited on the mandrel without an electric field. At 5 minutes, a mixture of needle-shaped and dendritic ice crystals can be seen on the mandrel surface (Figure 6.2(a)). The major axes of both needle-shaped and dendritic ice crystals were parallel to the surface of the mandrel. At 10 minutes, the ice crystals present are predominantly dendritic in shape (Figure 6.2(b)). The crystals look collapsed, closely packed and without any orientation. Few spacings between the ice crystals were visible from the top of the frost layer, as most of these spacings were blocked by the collapsed dendritic ice crystals (Figure 6.2(b)).

On the contrary, in the presence of an electric field, the major axes of both needle-shaped and dendritic ice crystals were perpendicular to the surface of the mandrel at the early stage of frost formation (Figure 6.2(c)). The crystals aligned in the direction of the electric field, as evident from the shadows cast by the crystals (Figure 6.2(c)).

At 10 minutes, it can be observed that more dendritic ice crystals were deposited and aligned in the direction of the electric field (Figure 6.2(d)). Columns of ice crystal were observed in an upright position, with visible spacing between them.

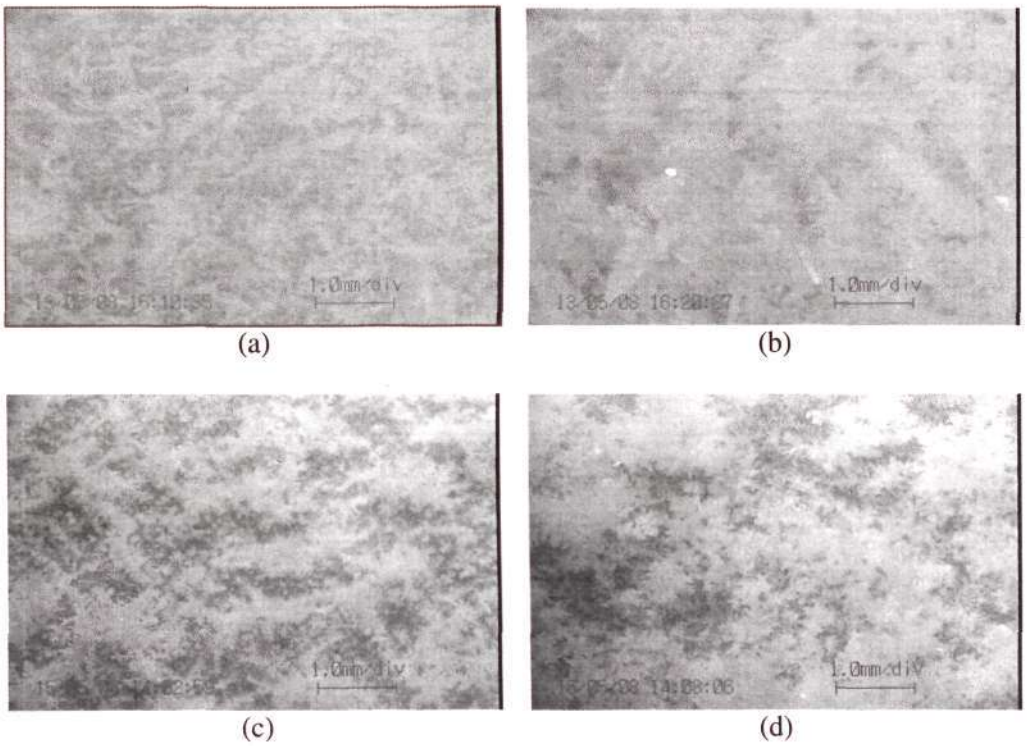

Figure 6.2 Pictures showing top view of frost layer at 50% and mandrel temperature at -35°C. (a) and (b) are frost formation without the electric field at 5 and 10 minutes respectively. (c) and (d) are frost formation in the presence of an electric field (2.5kV/cm) at 5 and 10 minutes respectively.

The electric field aligned the ice crystals that were deposited on the mandrel surface. The aligned ice crystals provided distinct nucleation surfaces for subsequent deposition of ice crystals. In this way, columns of ice crystals were accumulated and maintained in an upright position, as shown in Figure 6.2(d) where the spacings between the columns of ice crystal were still visible. However, in the absence of the electric field, the initial layers of ice crystals deposited on the mandrel surface were not aligned upright on the mandrel. This random orientation of the ice crystals provided multiple nucleation surfaces for subsequent deposition of ice crystals. This,

coupled with the collapse of subsequent ice crystals, resulted in a frost layer that was close-packed and randomly oriented (Figure 6.2(b).

Next, the effect of electric field on the amount of ice crystals collected on the mandrel is reported. In the absence of an electric field, the mass of ice crystals collected on the mandrel was 0.40 ± 0.03g at 50% RH, -35°C after 30 minutes. This was significantly higher than the mass of ice crystals collected (0.30 ± 0.02g) in the presence of an electric field under the same conditions ($p<0.01$, $n=3$).

The decrease in mass was due to the break-off effect caused by the electric field described by *Wang et al.*[190] Ice crystals deposited on top of each other were supported by fragile contact points. As the strength of the applied electric field increased above a certain value, $E_{break\text{-}off}$, the charged ice crystals on the mandrel broke away from the underlying frost layer and accelerated towards the oppositely charged electrode. This decrease in mass indicated a reduction in frost density and thickness, and caused non-homogeneity in the frost layer. In the frost experiments conducted, a significant amount of break-off was observed at 2.5kV/cm. The typical electric field strength used for electrospinning was 2.0 – 3.0kV/cm. Hence, to reduce the break-off effect and to maintain a stable Taylor cone for electrospinning, the electric field strength was maintained between 2.0 – 2.5kV/cm for cryogenic electrospinning experiments.

In summary, the effects of electric field on frost formation have been presented in this section. The presence of an electric field aligned the ice crystals and packed subsequent ice crystals deposited on the mandrel into columns. The spacings between these ice columns are important features of the frost layer that will be utilized to

control the pore structures of the CES, which will be discussed in later sections. In addition, the electric field removed ice crystals from the frost layer when the field strength was above a certain critical value (2.5kV/cm). As the presence of ice crystal in cryogenic electrospinning is essential, this observation suggests that the value of the electric field strength should not exceed this critical value during cryogenic electrospinning to prevent excessive removal of the ice crystals.

6.2.2 Effect of humidity and mandrel temperature on frost formation

The environment's humidity and mandrel temperature are two parameters that can affect frost formation. This experiment was conducted to study the effects of these parameters on the amount of frost formation (mass and rate of deposition) and the structure and spatial distribution of the frost on the chilled mandrel.

6.2.2.1 Effect of humidity and mandrel temperature on amount of frost formation

Figure 6.3 shows results of the mass of ice crystals collected on the mandrel in an electric field (E = 2.5kV/cm) at different humidities and temperatures over a frosting period of 30mins. In Figures 6.3(a) and (b), it can be observed that the mass of ice crystals was linearly proportional to the frosting time at -30°C and -35°C respectively. When a linear relationship was fitted to each set of data at different humidities, the equation contained a y-intercept. This indicates that at t = 0 minute, there were ice crystals accumulated on the mandrel surface. The gradients of the fitted lines are compared in Figure 6.3(c) to show the effects of humidities and temperatures on deposition rates of ice crystals. The deposition rate of ice crystals increased with humidity at both mandrel temperatures tested (-30°C and -35°C).

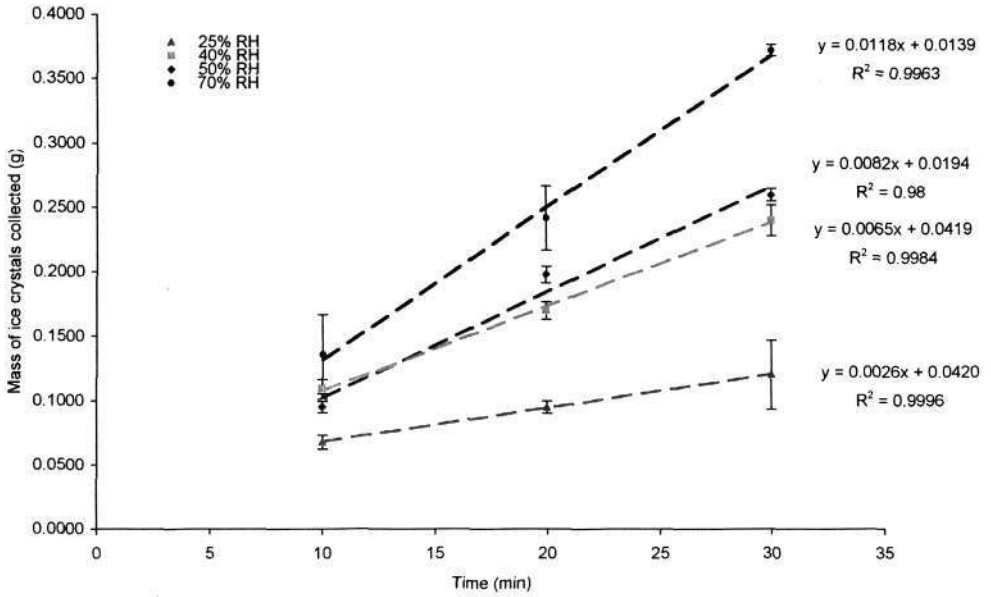

(a)

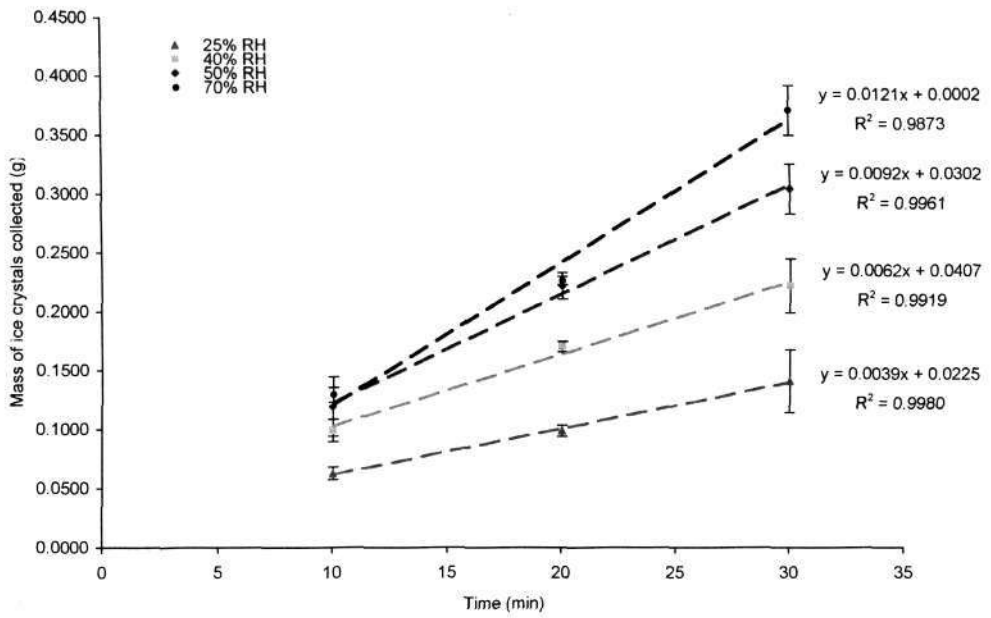

(b)

Figure 6.3 (a) and (b) Graphs of mass of ice crystals collected on the mandrel vs. frosting time in the presence of an electric field. Mandrel temperature maintained at (a) -30°C and (b) -35°C. Data presented as Mean ± SD. n = 3.

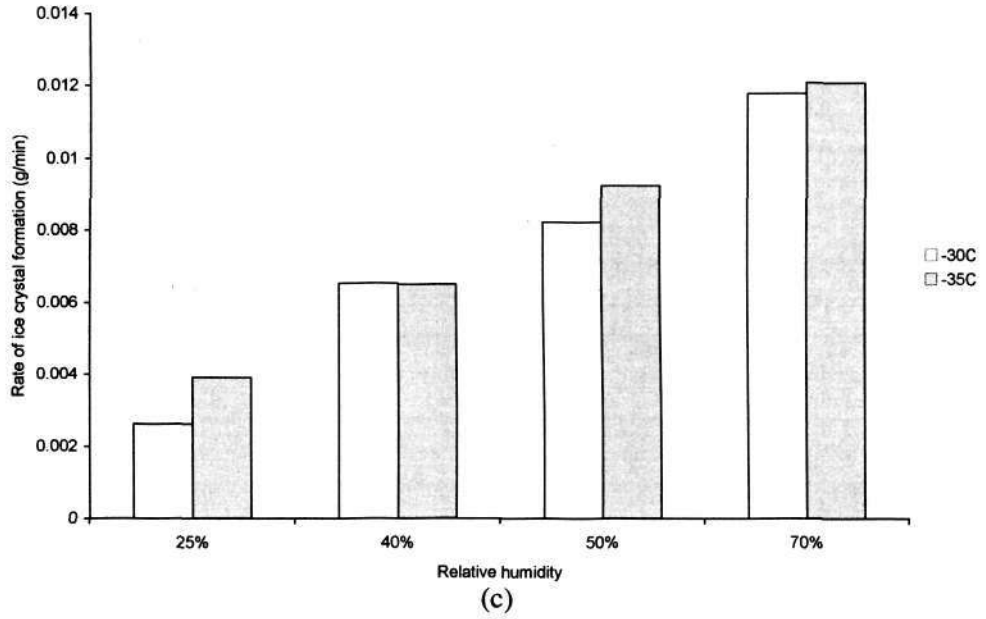

(c)

Figure 6.3 (c) Graph showing the rate of ice crystal formation at different relative humidities and temperatures. Rates of ice crystal formation are obtained from the corresponding gradients of the fitted trend line in (a) and (b). No statistical analysis was carried out as only one gradient was obtained for one set of data.

Firstly, the effect of humidity on the amount of frost formation (mass and rate of deposition) is discussed. From Figure 6.3(c), it can be observed that the rate of deposition of ice crystals increased with increasing humidity. This is because, with higher humidity, the moisture concentration gradient between the surrounding air and the mandrel surface increased, thereby driving more water vapour towards the cold mandrel surface where deposition occurred. The water vapour was deposited either on the surface of the frost layer to increase frost thickness or diffused into the frost layer and deposited between the already formed ice crystals. As humidity increased, the concentration driving force was able to cause significant increase in the diffusion of water vapour into the frost layer, thereby increasing the frost density. Typically, deposition of new ice crystals between already formed ice crystals reduced the spacing between the ice crystals.

The y-intercepts of the fitted linear relationships represent the mass accumulation during the dry ice packing phase. While dry ice was being packed in the mandrel, ice crystals began to accumulate on the surface of the mandrel. This represents the transient state of the temperature profile shown in Figure 5.3, which typically lasts for 3 minutes. In cryogenic electrospinning, fiber deposition usually starts 5 minutes after the loading of dry ice so that a steady mandrel temperature is established. Hence, this transient state is disregarded in our analysis.

Secondly, the effect of mandrel temperature on the amount of frost formation is discussed. The deposition rates of ice crystals obtained at temperatures of -30°C and -35°C are compared in Figure 6.3(c). The effect of mandrel temperature on the deposition rate of ice crystal was only obvious at 25%RH. At 25%RH, the deposition rate at -35°C was 1.5 times more than at -30°C. At higher humidities, the effect of temperature on deposition rate of ice crystals was less obvious.

Decreasing the mandrel temperature increased the temperature difference between the surrounding and the frost surface on the mandrel. This provided an increase in temperature gradient for faster heat transfer from the surrounding to the frost surface, thus providing the driving force for ice crystal formation. At 25%RH, the frost thickness was thin and heat transfer between the mandrel temperature and the surrounding was not hindered significantly by the presence of the frost layer. Hence, deposition rate of ice crystals and frost density increased with decreasing mandrel temperature (Figures 6.3(c)). This effect was not observed for higher relative humidities (40%, 50% and 70%). At high humidities, there were two conflicting processes that affected the amount of frost formed. At lower mandrel temperature, the

formation of ice crystals was faster due to the increase in temperature gradient for frost deposition on the mandrel. However, frost being a poorer conductor of heat than the surrounding air, reduced the temperature gradient between the surrounding and the frost surface. This negated the increase in temperature difference between the mandrel surface and the surrounding at lower mandrel temperature. Hence the difference between the amounts of frost formation for the two temperatures tested (-30°C and -35°C) was less obvious at higher relative humidities (40%, 50% and 70%).

6.2.2.2 Effect of humidity and mandrel temperature on spatial distribution of frost

The effect of humidity on the spatial distribution of ice crystals is shown in Figure 6.4. The spacing between the ice crystals decreased with increasing humidity. At 25%RH and 40%RH, the spacings between the ice crystals were distinct (Figures 6.4(a) and (b)). The ice crystals were organized in columns perpendicular to the mandrel, with the dark areas in the pictures representing the spacings between the ice columns. As the humidity increased to 50%, more ice crystals could be observed (Figure 6.4(c)). The branches of the dendritic ice crystals began to cover the spacings between the ice crystal columns. At 70%RH, the spacings were not visible from the top of the frost as they were blocked by the dendritic ice crystals (Figure 6.4(d)).

The spacings between the ice crystals decreased with increasing humidity due to densification. Densification is a process in which diffusion of water vapour into the frost layer causes more ice crystals to be deposited between existing ice crystals on the mandrel surface. As the environment's humidity increased, the increase in concentration gradient of water vapour between the surrounding and the mandrel

surface promoted densification of the frost layer, which resulted in a decrease in the spacings of the ice crystals.

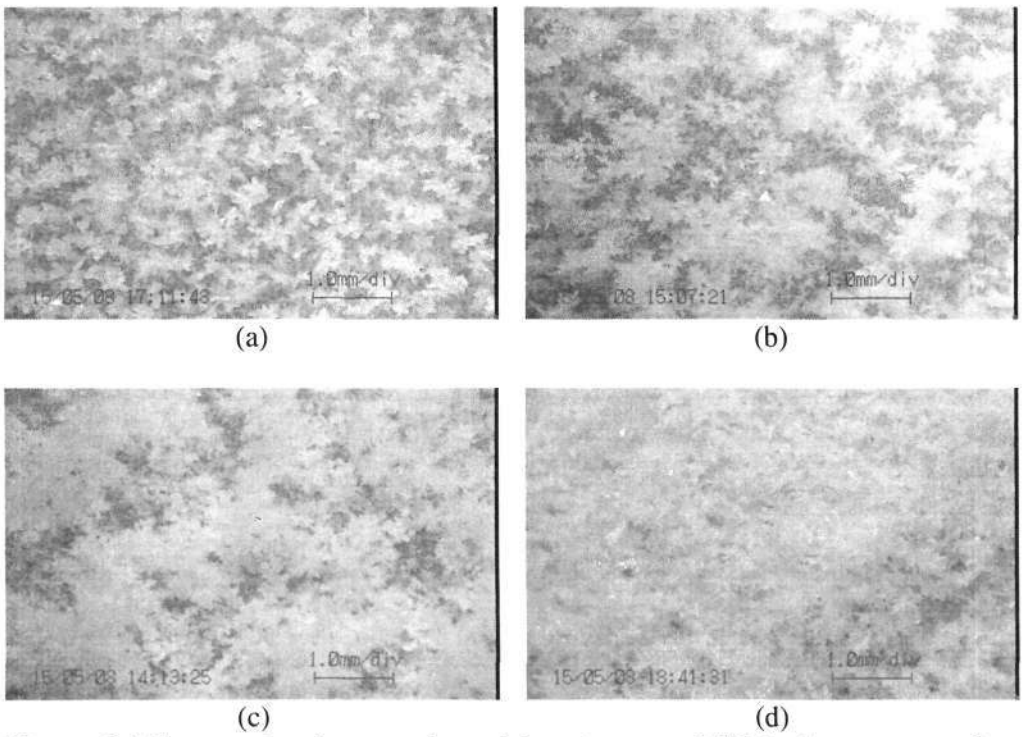

(a) (b)

(c) (d)

Figure 6.4 Pictures showing top view of frost layer at -35°C in the presence of an electric field (2.5kV/cm) after 15 minutes of frosting time. (a) 25%RH, (b) 40%, (c) 50%RH and (d) 70%.

Next, the effect of mandrel temperature on the spatial distribution of ice crystals is presented. Figure 6.5 shows the comparison of frost formation for 2 different mandrel temperatures (-30°C and -35°C) at different humidities (25% and 50%). At 25%RH, the spacings between the ice crystals were smaller at -35°C than at -30°C (Figures 6.5(a) and (b)). There were more ice crystals and smaller and lesser dark areas, which were the spacings between the ice crystals, on the mandrel surface at -35°C (Figure 6.5(b)). At other humidities (40%, 50% and 70%), the difference between the ice crystal spacing at -30°C and -35°C was not obvious. This is represented by comparing the frost pictures taken at 50%RH (Figures 6.5(c) and (d)).

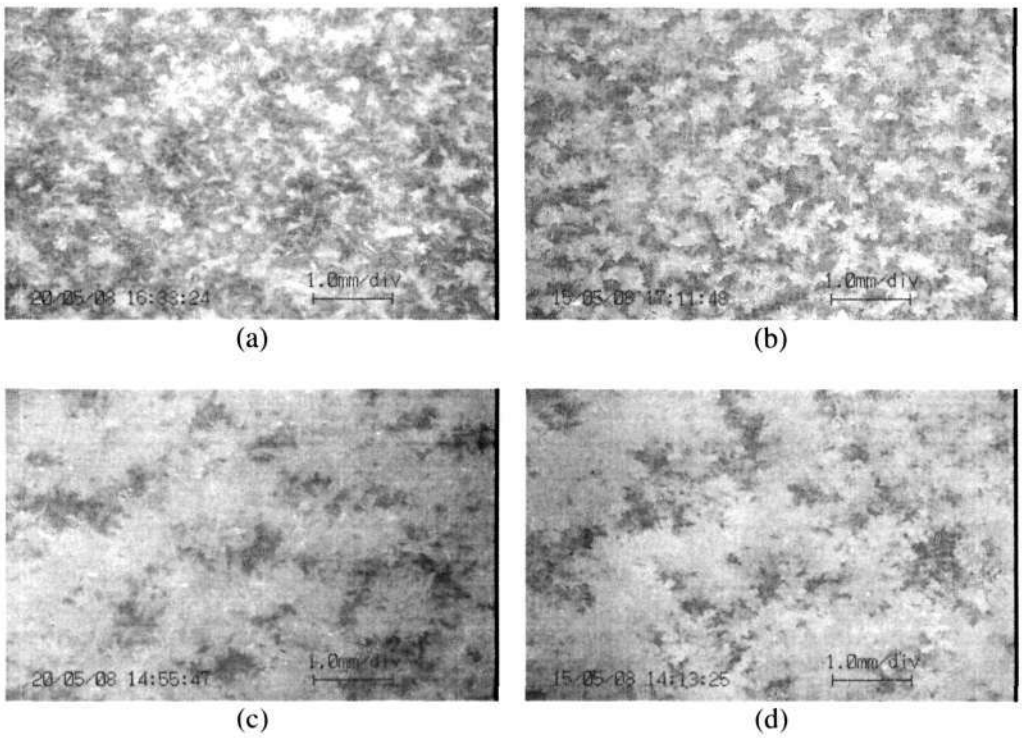

Figure 6.5 Pictures showing top view of frost layer in the presence of an electric field (2.5kV/cm) after 15 minutes of frosting time. (a) and (b) are frost pictures at low humidity of 25%RH at -30°C and -35°C respectively. (c) and (d) are frost pictures at high humidity of 50%RH at -30°C and -35°C respectively.

The temperature effect on the inter-crystal spacing was obvious at 25%RH but not obvious at higher humidities for reasons discussed earlier. The study on temperature effect was also limited by our process ability to control mandrel temperature. Based on the setup described in Section 5.2.2.2, the temperature values were confined to 2 distinct values of -30°C and -35°C, which had a small difference of 5°C. The temperature effect might be better studied if large temperature differences can be established. Subsequent studies on the cryogenic electrospinning process and fabrication of scaffold were carried out at a mandrel temperature of -35°C as the temperature profile was more stable and sustainable for the duration of the process as shown in Figure 5.3.

In summary, the effects of humidity and mandrel temperatures on the amount of frost formation and spatial distribution of the ice crystals were presented in this section. The increase in deposition rates of ice crystals and densification with humidity are important observations and provide the fundamental knowledge to understand pore size variations in CES. These relationships allow the control of ice crystal spacing by varying humidity, which in turn provides control of the pore size of the CES to be discussed later. The effects of mandrel temperature on the amount and spatial distribution of frost were not obvious. Hence, the mandrel temperature was fixed at -35°C for all subsequent experiments.

6.2.3 The frost template

The purpose of this section is to present the frost pictures that were taken at different humidities (25%, 40%, 50% and 70%) and temperatures (-30°C and -35°C) over a duration of 30 minutes. This collection of frost pictures will serve as design templates in the fabrication of the CES, which will become apparent in Section 6.3.

Figures 6.6(a) and (b) show the top view of the frost layers formed in the presence of an electric field (2.5kV/cm) at different humidities at -30°C and -35°C respectively. The frost pictures are organized into two collages to show the progression of ice crystal deposition over time. Other than the picture taken at 2 minutes at 25%RH and -30°C, all other pictures are made up of predominantly branched ice crystals. This indicates that the crystal growth period had ended and the frost layers shown in these pictures were in the frost crystal growth period. There was no evidence of melting in the frost period of 30 minutes at all conditions tested. It is important that there was no melting of the ice crystals as the melting process might collapse the pores of the CES.

With this information, the cryogenic electrospinning process was restricted to 30 minutes of frosting time.

The frost template shown in Figure 6.6 shows the variations in ice crystal spacing at different frosting conditions and thus, can be used to select the operating conditions for cryogenic electrospinning. In cryogenic electrospinning, the ice crystals are used to provide anchorage for the electrospun fibers such that the fibers are organized around the spacing between the ice crystals. Thus, the spacing of the ice crystals affects the eventual pore size of the CES. Based on Figure 6.6, it can be hypothesized that for smaller CES pore sizes, the frost formation could be carried out in higher humidities and lower temperatures since the ice crystal spacings were smaller at these conditions. In addition, for subsequent studies on the effect of process parameters on CES pore size, the studies were conducted after 15 minutes of frosting time. This was because based on Figure 6.6, the frost formation was observed to have stabilized and the difference in ice crystal spacing was obvious enough to allow the studies on pore size variations to be conducted. These studies are presented in Section 6.3.

Time (mins)	Relative humidity			
	25%	40%	50%	70%
2	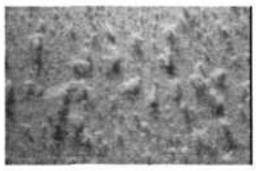	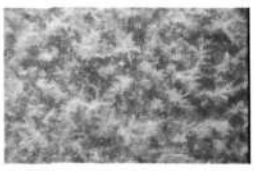		
5	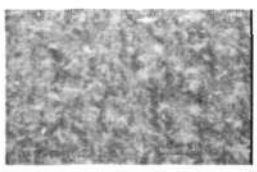	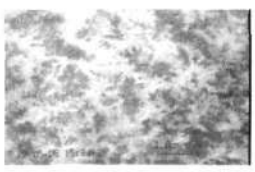		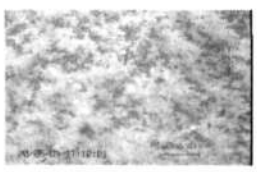
10	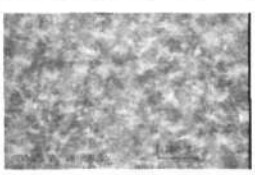			
15		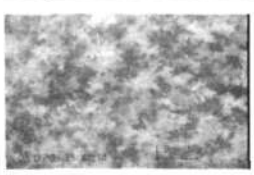		
20		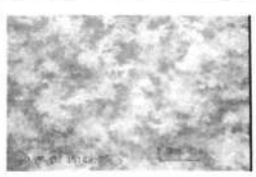		
25		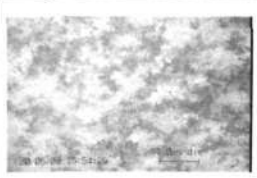	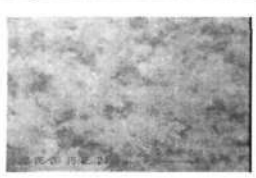	
30		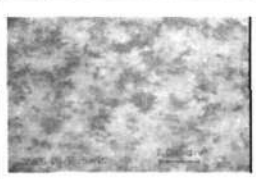	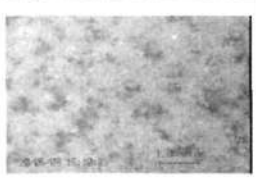	

Figure 6.6(a) Top view of frost template deposited on the mandrel at different humidities over time. The temperature of the mandrel was maintained at -30°C. Scale bar ▬ represents 1mm.

Time (mins)	Relative humidity			
	25%	40%	50%	70%
2			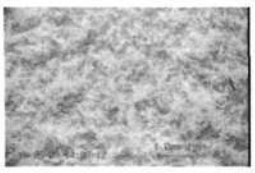	
5	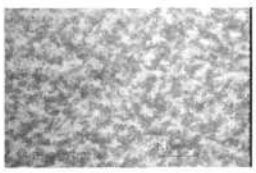			
10	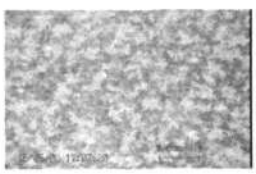		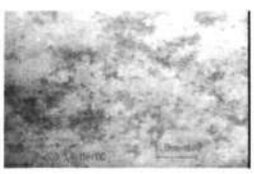	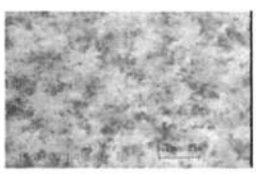
15		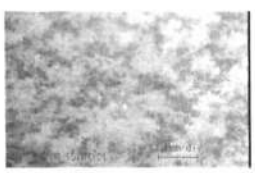		
20	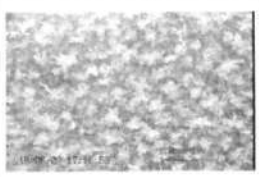	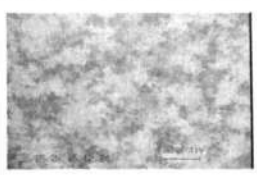		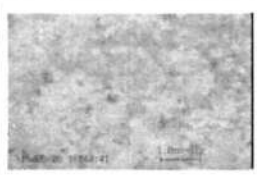
25	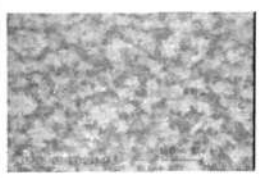	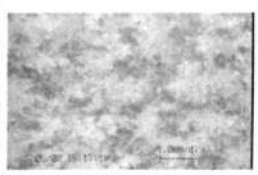		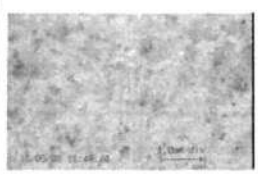
30	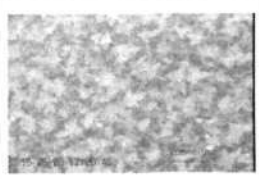	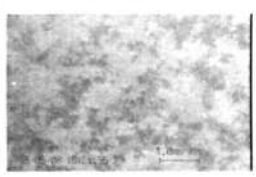	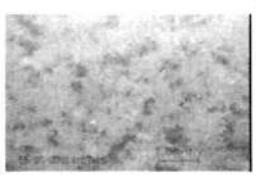	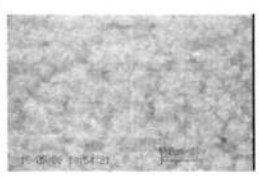

Figure 6.6(b) Top view of frost template deposited on the mandrel at different humidities over time. The temperature of the mandrel was maintained at -35°C. Scale bar ▬ represents 1mm.

6.2.4 Empirical correlation for frost formation

A preliminary empirical correlation for frost formation is developed in this section. This empirical correlation is used to provide a first approximation to predict the pore size of CES in later sections. The mass (m_f) and thickness (y_f) of the frost layer was measured after 15 minutes of frosting time and at a mandrel temperature of -35°C. A graph of log (m_f/y_f) against log ω was plotted. The graph is shown in Figure 6.7. From the graph, the values of C_1 and C_2 were calculated to be 1.81 and 0.473 respectively. Hence, Equation 4.6 is empirically determined as follows:

$$\text{Porosity} = (1 - 1.81 \times \omega^{0.473}) \times 100\% \qquad \textbf{Eq 6.1}$$

Equation 6.1 is valid at a fixed temperature of -35°C, electric field strength of 2.5kV/cm and at frosting time equals to 15 minutes. As the conditions change, other dimensionless groups such as the Reynolds and Fourier number, the dimensionless terms such as dimensionless electric field strength and temperatures in Equation 4.5 are affected, hence changing the values of C_1 and C_2.

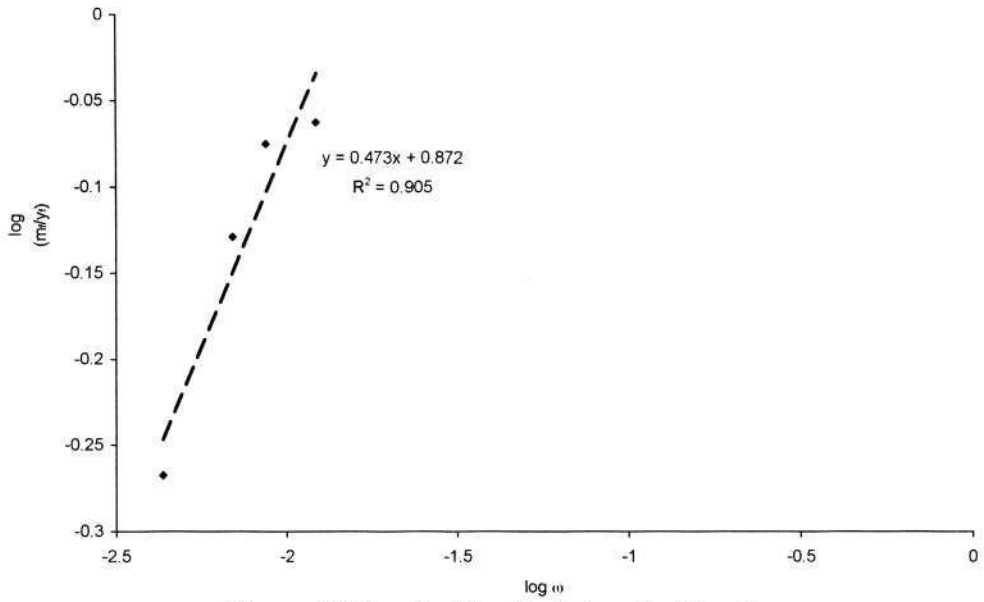

Figure 6.7 Graph of log (m_f/y_f) against log ω.

To verify the accuracy of Equation 6.1 in predicting the frost porosity, the pictures showing the top view of the frost layer are analyzed using an image analyzing software. These pictures are taken at the conditions where Equation 6.1 is valid. Figure 6.8 shows the porosity determined by the analyzing software and the correlation represented by Equation 6.1.

The correlation in Equation 6.1 predicts the trend that porosity decreases as humidity increases due to the densification of the frost layer. However, it did not predict the experimental values of the frost porosity. This is because the image analyzing software was not able to measure the porosity beyond the top layer as the dendritic ice crystals at the frost surface blocked the underlying inter-crystal spacing. Hence, the experimental value determined using the software is smaller than the actual porosity of the frost layer. Another reason for the discrepancy may be due to the measurement of frost thickness with the thickness gauge. The gauge might compress or melt the frost layer during measurement, giving significant inaccuracy to the thickness measured.

The establishment of the empirical correlation is important in understanding the effect of humidity on the porosity of the CES. As the ice crystals provide anchorage surfaces for the fibers, the spacings between the ice crystals represent the maximum possible pore size of the CES. Therefore, Equation 6.1 provides an estimate for the porosity of the CES at various humidities at a fixed temperature of -35°C, electric field strength of 2.5kV/cm and a frosting time of 15 minutes. This relationship will become apparent in the next section.

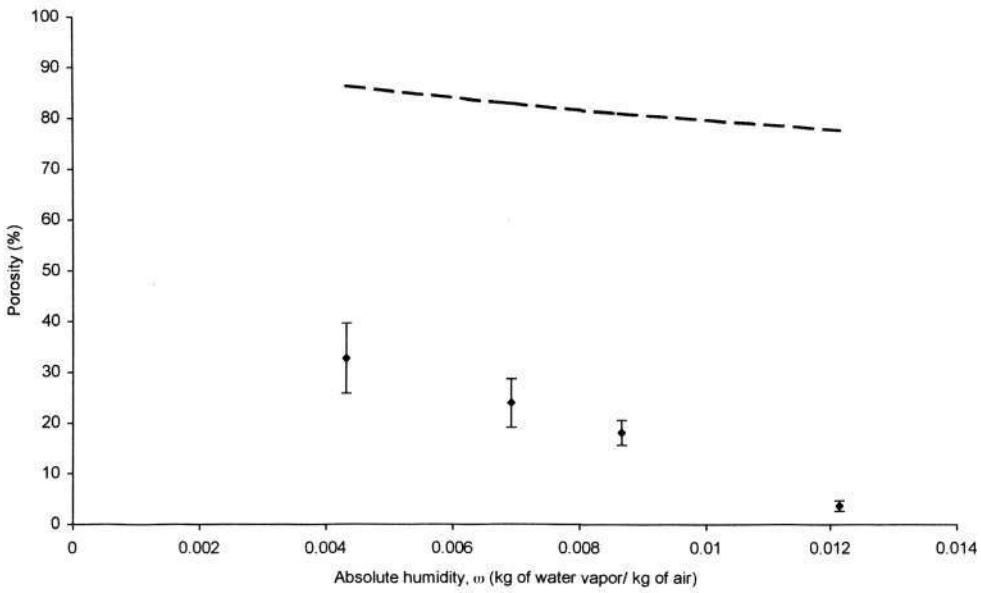

Figure 6.8 The comparison of the experimental values of porosity (♦) against the correlation (dotted line) in Equation 6.1. Values presented as Mean ± SD. n = 3.

6.3 Cryogenic electrospinning

In this section, the mechanism of the CES is established with evidence from the LV-SEM micrographs showing the interactions between ice crystals and electrospun fibers. In addition, the effects of mandrel temperature, environment's humidity and rate of fiber deposition on the pore size of the CES are also shown.

6.3.1 Study of mechanism of cryogenic electrospinning

This experiment was conducted to understand the mechanism of the cryogenic electrospinning technique. The interaction between ice crystals and electrospun fibers was studied by observing the specimen under LV-SEM.

6.3.1.1 Formation of nodes and struts of CES

Figure 6.9(a) shows the SEM micrographs taken immediately after the freshly prepared CES specimen was loaded onto a pre-chilled stage in the vacuum chamber

of the SEM. Ice crystals could be observed with the electrospun fibers. As time progressed, the ice crystals sublimed in the SEM chamber that was maintained at conditions similar to the freeze-drying process.[198] The removal of the ice crystals revealed the structure of the CES (Figure 6.9(b)). The structure was preserved without any visible collapse. The pictures shown in Figure 6.9 shows the interactions between ice crystals and electrospun fibers in cryogenic electrospinning and allows one to relate the mechanism of frost formation to electrospinning, which will be discussed in the next few paragraphs.

Next, the features of the CES, namely nodes and struts, are described. From Figure 6.9(a), it can be observed that the nodes are formed at the location of the ice crystals. These nodes of the CES structure are where the electrospun fibers congregate. These nodes served as structural supports for the CES.

The struts of the CES structure represent the bundles of fibers that extend between two neighboring nodes. These struts are the fibrous and porous walls which surround regions with low fiber density, which is referred to as the pore of the CES in this study.

Consequently, the fibers are organized in a network of nodes and struts supported by the ice crystals. The removal of the ice crystals leaves behind a three-dimensional structure of the CES as shown in Figure 6.9(b).

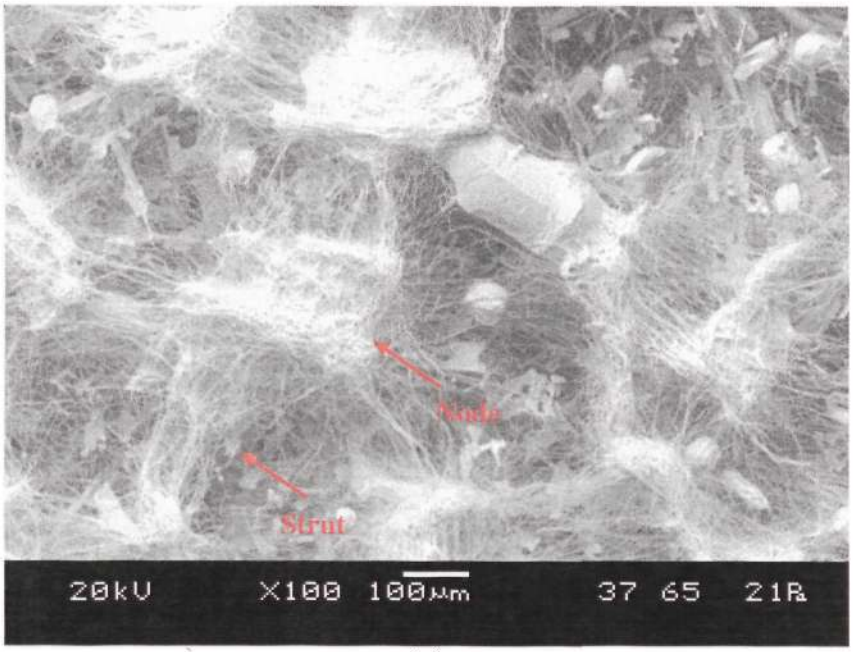

(a)

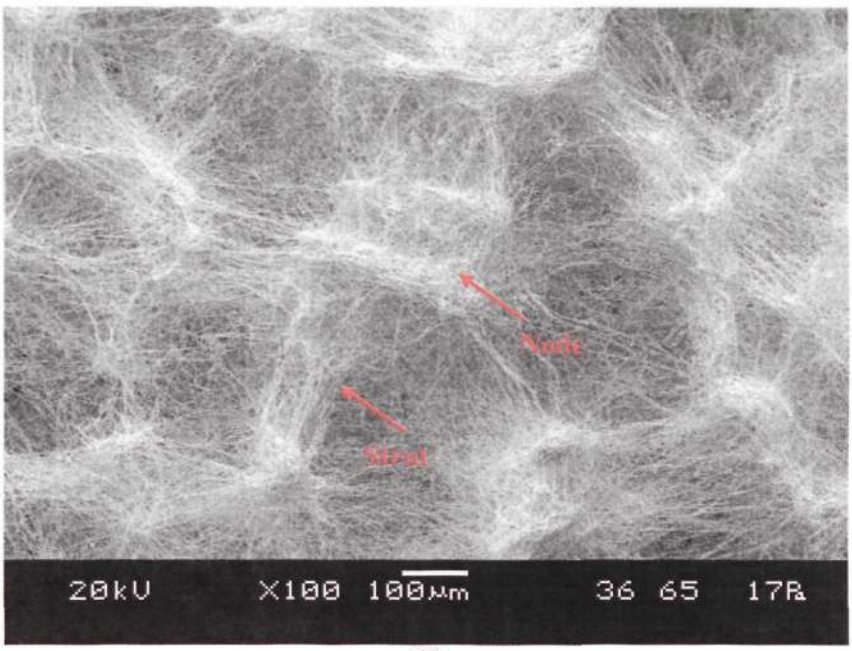

(b)

Figure 6.9 SEM micrographs showing the interactions between the ice crystals and electrospun fibers under LV-SEM (a) immediately after specimen was loaded into the chamber and (b) 10 minutes after specimen was loaded into the chamber.

Next, the mechanism of the cryogenic electrospinning technique is described based on the evidence shown in Figures 6.9(a) and (b). Prior to electrospinning, water vapour in the environmental chamber deposited on the chilled mandrel to form ice crystals that accumulated to form a template on which fibers were deposited. These ice crystals, which were deposited on the mandrel and aligned in the direction of the oppositely charge electrode, provided surfaces on which the fibers were deposited. In addition, the ice crystals, having pointed branches, focused the electric charges at the tip of the ice columns and provided preferred anchorage surfaces for the fibers to congregate to form the nodes during electrospinning. The struts of the CES were formed due to the rotation of the mandrel and the transverse motion of the robotic axis, both of which stretched the fibers between neighboring nodes. Regions without ice crystals resulted in low fiber density as the ice crystals elevated the nodes and struts, and stretched the fibers above and across these regions, with little fibers landing on the mandrel surface. This process continued as more ice crystals and electrospun fibers were deposited until a network of nodes and struts was obtained.

6.3.1.2 Relationship between ice crystals spacing and pore size of CES

Figure 6.10(a) and (b) shows the frost picture and SEM micrograph of the corresponding CES collected at -35°C and 40%RH. The measured value for the spacing between ice crystals at these conditions is 760 ± 120μm (Figure 6.10(a)). The measured inter-nodal distance for the corresponding CES is 670 ± 150μm (Figure 6.10(b)). The two values are comparable to one another.

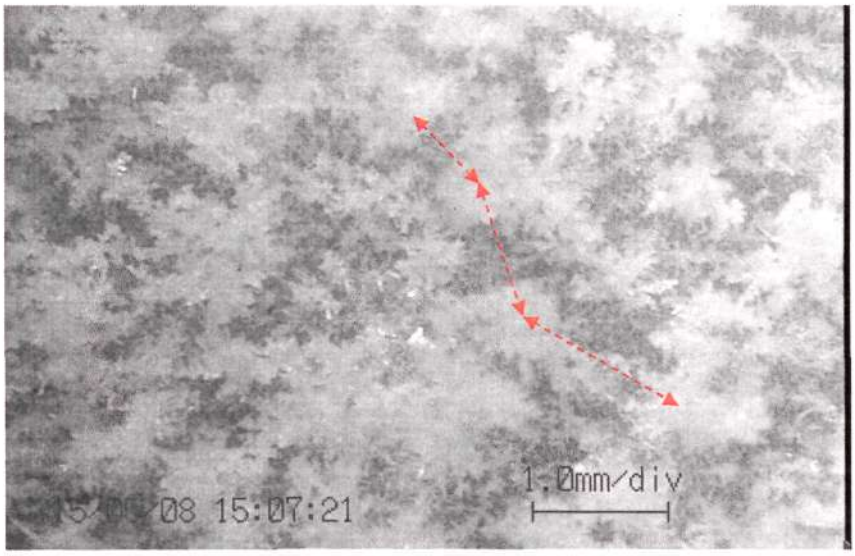

(a)

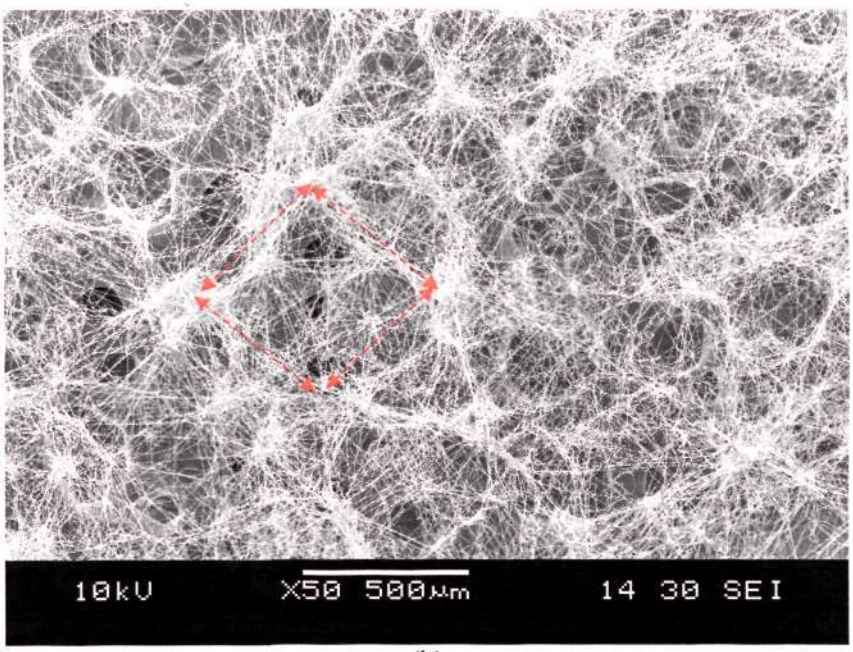

(b)

Figure 6.10 The process conditions for these pictures were -35°C and 40%RH. (a) Top view of frost and (b) SEM micrograph of the CES. The arrows show examples of the measurements taken.

Within the limitations of the experimental conditions, the measured values serve as rough estimates to support the mechanism proposed. The errors were due to the poor resolution of the frost picture and the difficulty in defining the centre of the ice column and the nodes from Figure 6.10(a) and (b), Nevertheless, these estimates show that the spacing between the ice crystals and the distance between the nodes are comparable. This close resemblance substantiates the mechanism of the cryogenic electrospinning technique proposed previously.

From the above results, the spacing between the ice crystal columns becomes an important parameter in controlling the pore size of the CES. It has been presented that the polygonal pores of the CES are surrounded by struts, which are anchored at the nodes that form the corners of the polygons. The length of the struts determines the size of the pores of the CES. The length of the struts, which is the distance between two neighboring nodes (inter-nodal distance), depends on the spacing of the ice crystals during frost formation. Hence, larger ice crystal spacing will result in longer struts, which can surround a larger pore consequently.

In summary, the mechanism of the cryogenic electrospinning was presented in this section. The formation of the network of nodes and struts in relation to the ice crystals was described. From this mechanism, it was shown that the spacing of the ice crystals is an important parameter that affects the pore size of the CES. Hence, process parameters that affect the spacing of the ice crystals, such as environment's humidity and mandrel temperature, can be used to control the pore size of CES. The effects of these parameters on pore size of the CES will be presented in the next section.

6.3.2 Process study

The mechanism of the cryogenic electrospinning has been established in the previous section. In this section, the effects of environment's humidity, mandrel temperature and rate of fiber deposition on the pore size of the CES are studied.

6.3.2.1 Effect of environment humidity on pore size of CES

In cryogenic electrospinning, frost is used to expand the pore size of the electrospun scaffold. Previous studies have shown that humidity affects the deposition rate, spatial distribution and thickness of the frost layer. Hence, the pore characteristics of the CES can be controlled by manipulating the humidity of the environment. This experiment was conducted to study the effects of humidity on the pore size of CES.

Figure 6.11 shows SEM micrographs of the initial layers of CES fibers as humidity was varied at a fixed mandrel temperature of -35°C. The conditions described here correspond to the conditions that produced the frost template shown in Figure 6.4. At 25%RH, the fibrous mesh was dense and the average pore size was small (2200 ± 200μm^2) (Figure 6.11(a)). The nodes and struts were not distinct. As relative humidity increased to 40%, the node and strut network of the CES became obvious and the pore size was significantly larger (4300 ± 600μm^2) (Figure 6.11(b)). A further increase of relative humidity to 50% caused a significant drop in pore size (3300 ± 500μm^2) from 40% (Figure 6.11(c)). However, the strut and node network remained distinct. Finally, as relative humidity increased to 70%, the pore size decreased significantly and the fibrous mesh looked like the specimen obtained at 25%RH (Figure 6.11(d)).

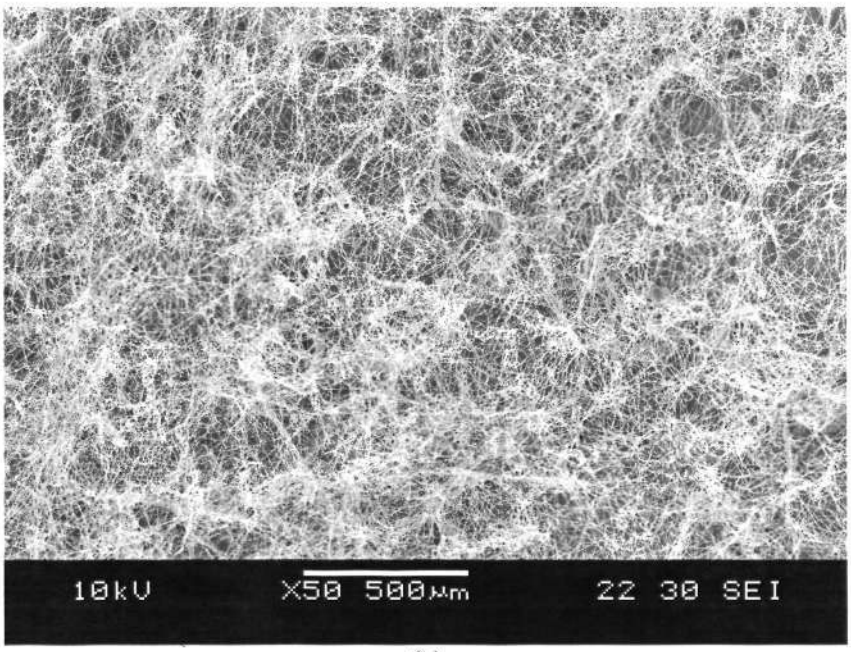

(a)

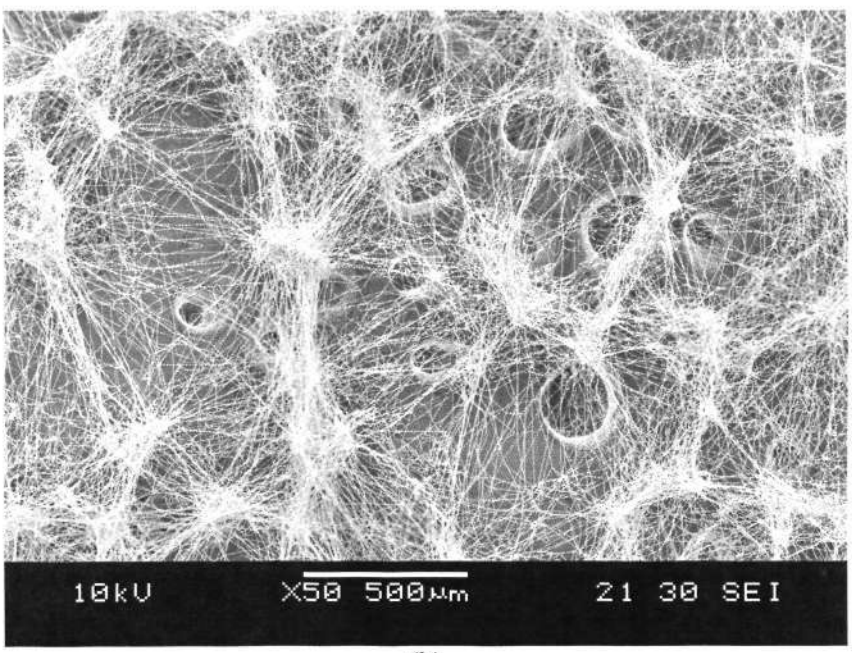

(b)

Figure 6.11 SEM micrographs of initial layers of CES fibers at mandrel temperature of -35°C and (a) 25% RH and (b) 40% RH.

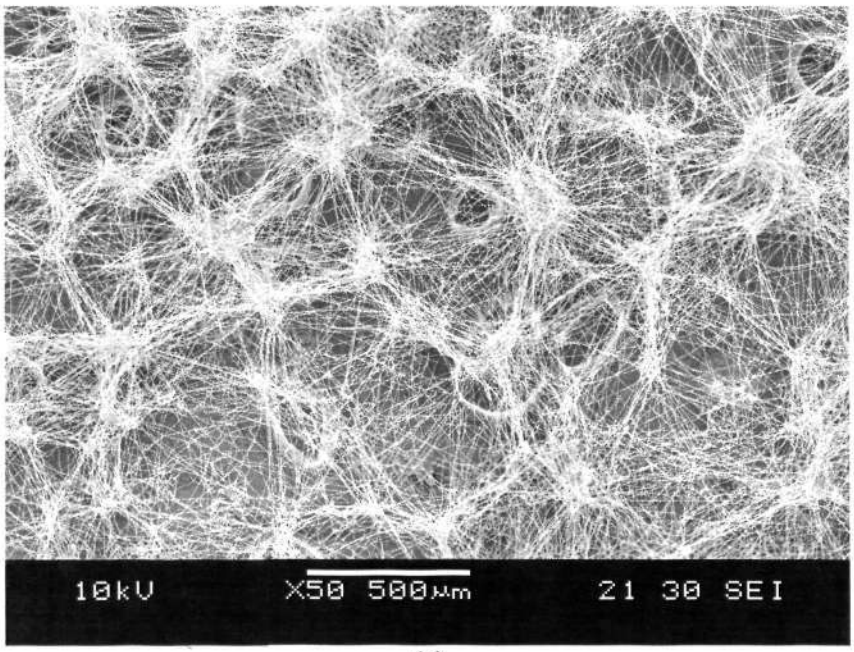

(c)

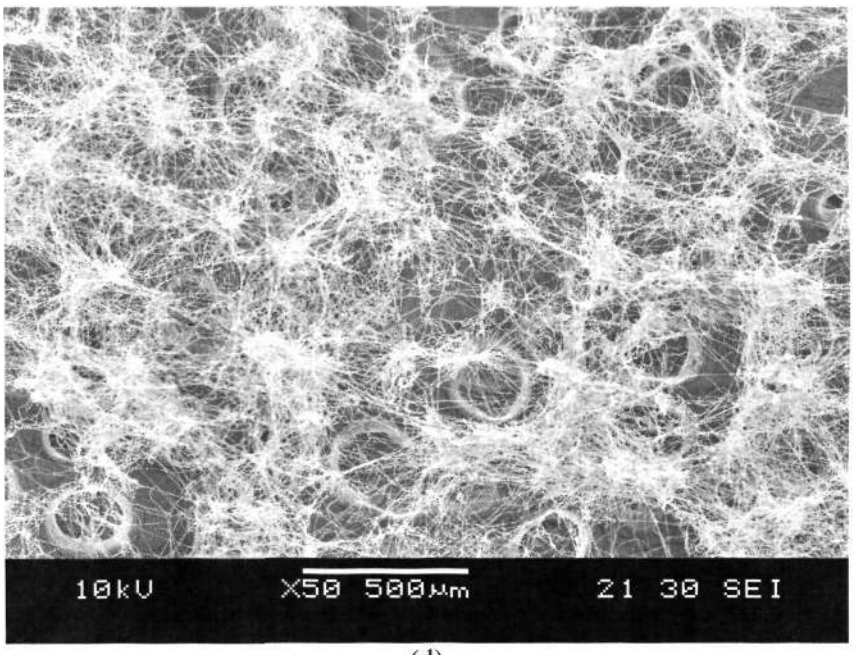

(d)

Figure 6.11 SEM micrographs of initial layers of CES fibers at mandrel temperature of -35°C and (c) 50% RH and (d) 70% RH.

The same trend for pore size was observed for different humidities at a fixed temperature of -30°C. Figure 6.12 shows the graph of average CES pore size obtained at different mandrel temperatures against relative humidity. The pore size of conventional electrospun scaffold was included for comparison. The pore size of conventional electrospun scaffold was not affected by changes in humidity of the environment and remains significantly smaller than the CES fabricated at mandrel temperatures of -30°C and -35°C.

The effect of environment's humidity on pore size of ES and CES can be explained as follows. Variations in humidity had no effect of conventional ES. This was because the mandrel surface is a flat continuous surface. During conventional electrospinning, the fibers were deposited randomly on the mandrel surface. As there was no external artifact (such as ice crystals) on the mandrel to anchor or disrupt the deposition of fibers, the small pore size resulted from the random deposition of fibers landing on top of each other. Hence, changing the environment humidity did not affect the pore size of the ES.

On the contrary, variations in humidity resulted in changes in the pore size of the CES. It has been shown that as humidity increased, the deposition rate of ice crystal increased while the spacing between ice crystals decreased. The proportional increase or decrease relationship with humidity was not observed for CES pore size. This is because the pore size of the CES is dependent on two separate processes, which are the deposition of ice crystals and the deposition of electrospun fibers. The details are provided as follows.

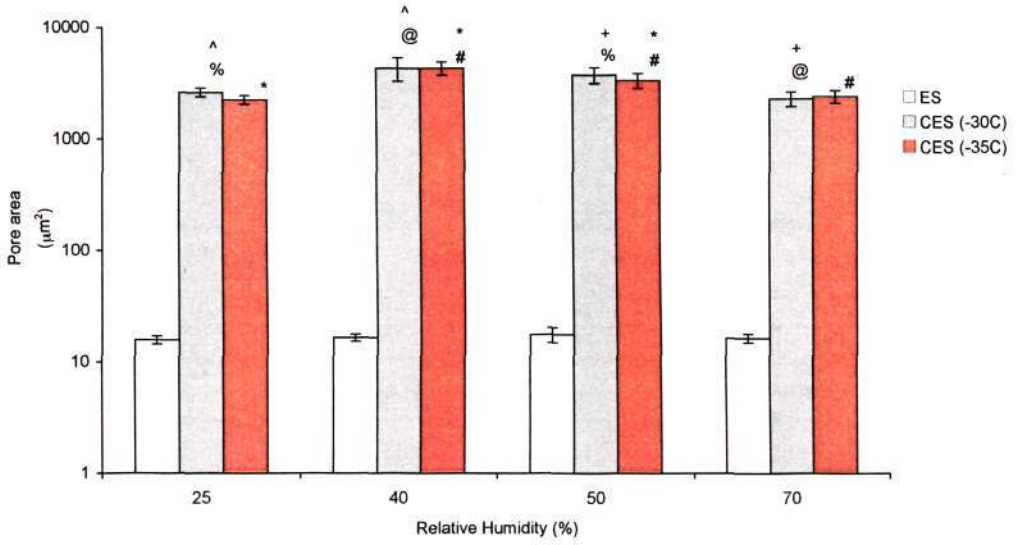

Figure 6.12 Average pore area as a function of relative humidity. %, ^, *, @, #, + are symbols showing significant differences when the relevant data is compared ($p<0.05$). Pore sizes for all CES are significantly different from pore size of ES ($p<0.01$). Mean ± SD. n = 5.

Previous studies have shown that the spacing between the ice crystals was the largest at 25%RH as compared to the spacing at other humidities studied at -35°C (Figure 6.4). However, the pore size of the CES was the smallest at 25%RH in this experiment. This could be due to 2 reasons. Firstly, the deposition rate of the ice crystals at 25%RH was the slowest (0.0039g/min) as compared to the rate at other humidities (Figure 6.3(c)). The rate of deposition of ice crystals was slower than the rate necessary to provide enough ice crystals to anchor the electrospun fibers in a strut-like framework. As a result, the spacing between the ice crystals was filled up by the fibers. Secondly, the spacing between the ice crystals might be too large such that the struts slacked between the two nodes. As such, the fibers landed on the flat mandrel surface and resulted in smaller pores. Hence, these 2 factors might have contributed to the small pore size of the CES obtained at 25%RH.

As the relative humidity was increased to 40%, the deposition rate of ice crystals increased (0.0062g/min) and there were enough ice crystals on the mandrel to space out the deposited fibers. Hence, the characteristic network of struts and nodes of the CES was obtained (Figure 6.11(b)). The pore size of the CES at 40% was the largest because the spacing between ice crystals was the largest as compared to the inter-crystal spacing at 50%RH and 70%RH (Figure 6.4). As relative humidity increased further to 50% and 70%, the deposition rate of ice crystals increased (0.0092 and 0.0121g/min respectively) and the pore size of the CES decreased due to densification, which caused the decrease in inter-crystal spacing. Hence, with the two processes of frost formation and electrospinning happening *in situ*, the pore size of the CES increased from 25%RH to a maximum at 40%RH and decreased again as higher humidity was reached (Figure 6.12).

Having studied the effect of humidity on pore size of the initial layers of CES, the knowledge is applied to build a thicker CES. This is important as tissue engineered scaffolds has to be sufficiently thick (~200 – 400μm) to fabricate large tissue constructs. Figure 6.13 shows the SEM micrographs on the effect of humidity on the pore size of a thick CES. It was observed that the pore size of the CES became more defined with greater depth as the bundles of fibers adopted a more distinct strut-like framework as the environment humidity was increased from 25%RH to 50%RH (Figures 6.13(a) – (c)). At 70%RH, the pore size of the CES decreased (Figure 6.13(d)).

The effect of humidity on CES pore size has been established earlier. As a thicker CES was built, the humidity effect remained approximately similar for the same reasons. The only difference was that the pore size at 40%RH was smaller than at 50%RH, unlike the trend shown previously in Figure 6.12. This could be attributed to the inability of the deposition of ice crystals to keep pace with the deposition of electrospun fibers as the thickness of the CES was built. As such, the spacing between the ice crystals became filled with more fibers as fiber deposition predominated. Figure 6.14 shows the trend in the pore size of the thick CES with humidity. The maximum pore size was obtained at 50%RH and -35°C. Hence, this set of conditions was used to fabricate CES for mechanical characterization, *in vitro* and *in vivo* studies.

In summary, the effect of humidity on the pore size of CES was studied. The largest pore sizes were obtained at 40%RH and 50%RH for the thin and thick CES respectively. Therefore, the thick CES fabricated at 50%RH and a mandrel temperature of -35°C was used for mechanical properties characterization, *in vitro* and *in vivo* studies.

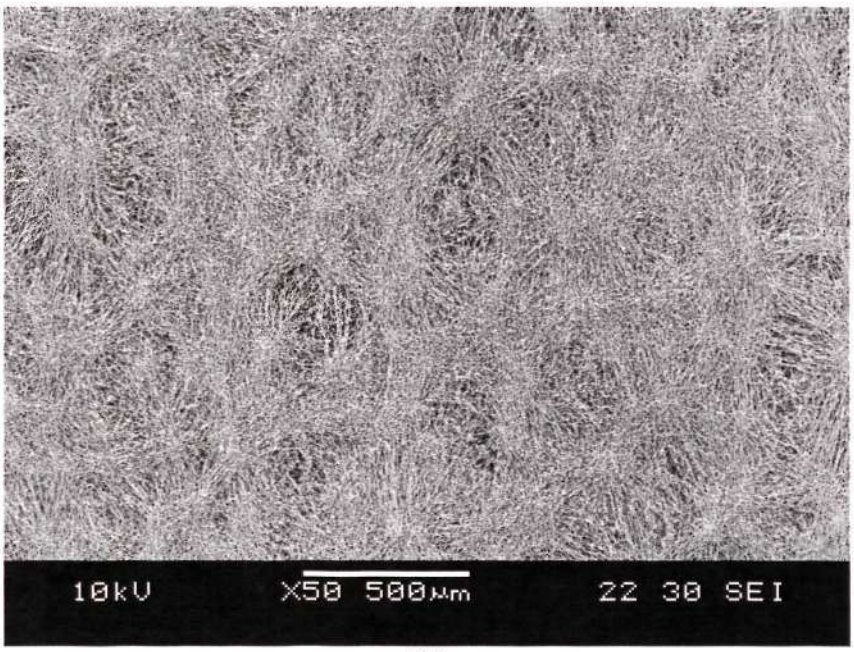

(a)

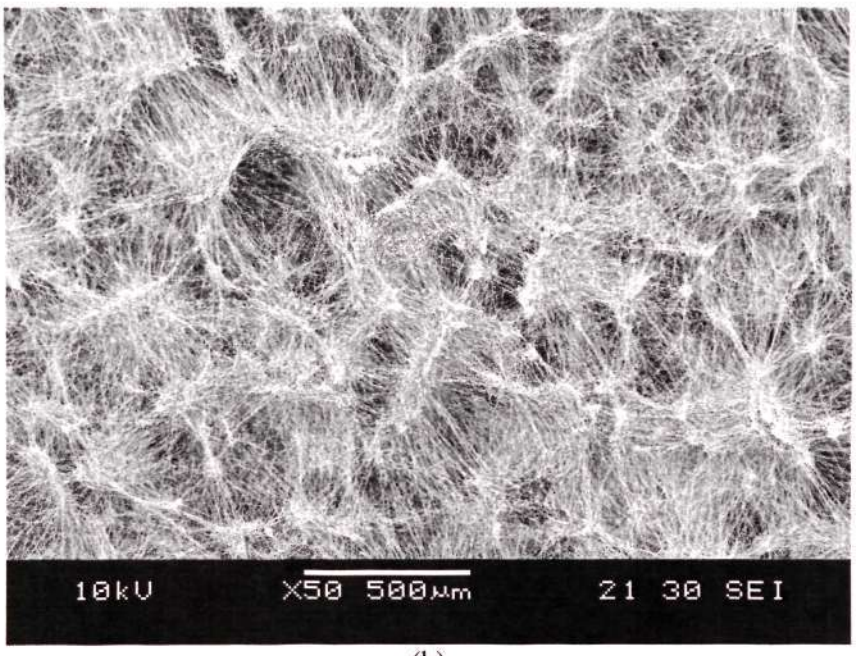

(b)

Figure 6.13 SEM micrographs of thick CES at -35°C and (a) 25% RH and (b) 40% RH.

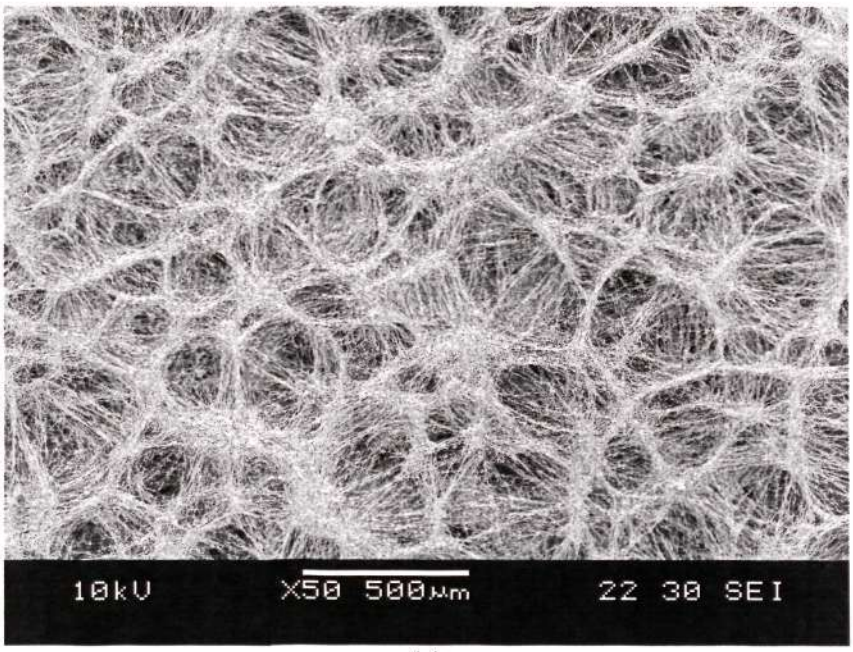

(c)

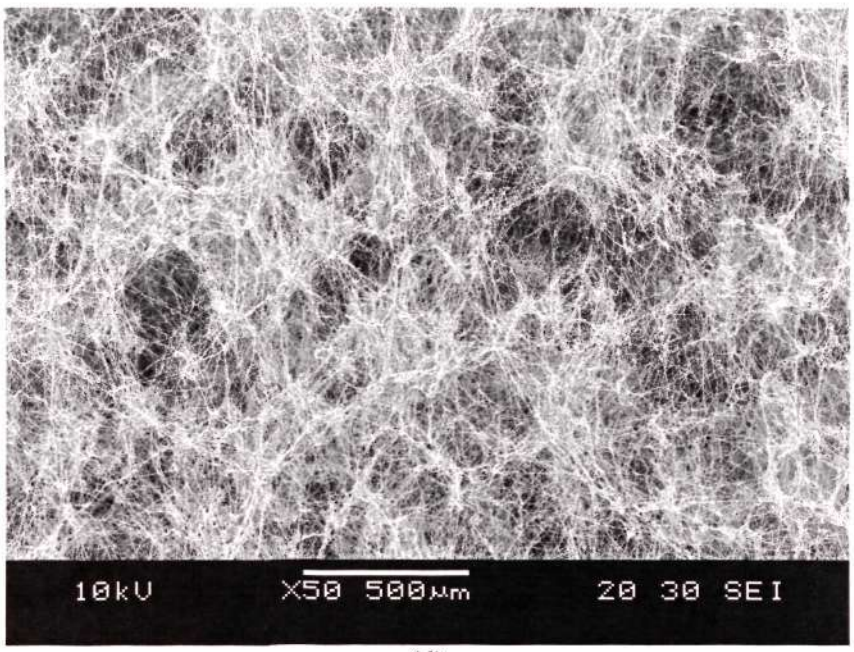

(d)

Figure 6.13 SEM micrographs of thick CES at -35°C and (c) 50% RH and (d) 70% RH.

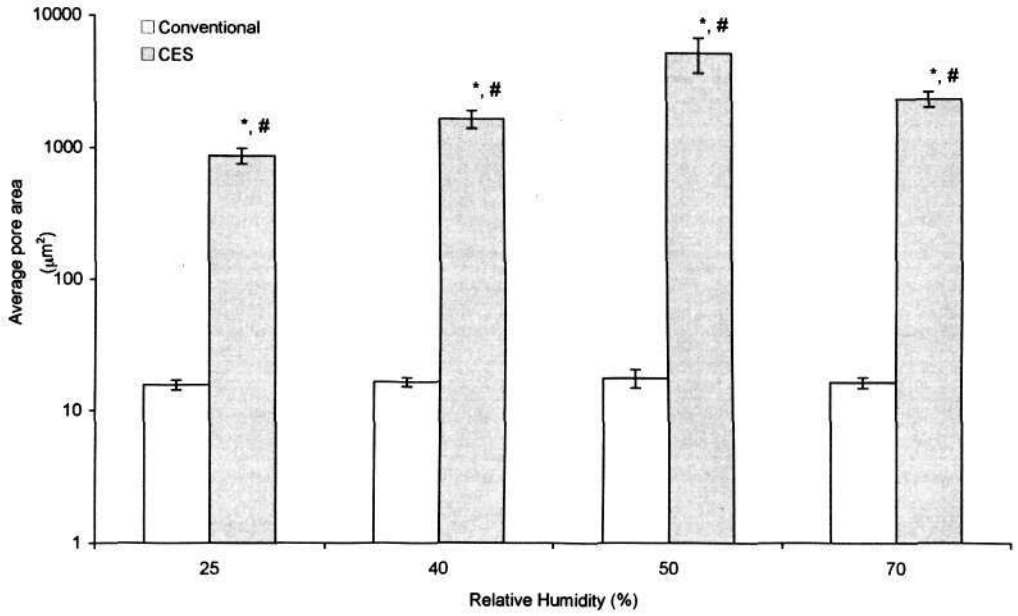

Figure 6.14 Effect of humidity on pore structure of thick CES. The average pore area is plotted as a function of relative humidity. * denotes inter-group significant difference at the same relative humidity ($p<0.01$) and # denotes significant difference between same group at different relative humidities ($p<0.05$). Temperature of mandrel was maintained at -35°C. Mean ± SD. n = 5.

6.3.2.2 Empirical correlation for CES pore size with humidity

Next, the empirical correlation developed to predict the porosity of the frost layer is used to predict the porosity of the CES. With the assumption that the frost layer is homogeneous such that the spacing between the ice crystals are equal, the uniform inter-crystal spacing represents the maximum distance between the nodes of the CES. Hence, Equation 6.1 can be used to predict the maximum porosity of the CES at different humidities.

From Figure 6.15, it can be observed that Equation 6.1 over estimates the porosity of the CES. The reasons for the discrepancy may be due to the dendritic shape of the ice crystals, which is illustrated in Figure 6.16. The model did not take into account the dendritic shape of the ice crystal, which could affect the distance between the nodes

of the CES. As the charged dendritic ice crystals were erected perpendicularly on the mandrel surface in the direction of the electric field, the probability of fibers entangling on the charged tip of the dendritic ice crystal was higher than on the surface of the mandrel. As a result, the distance between the nodes of the CES, λ_{CES}, was smaller than the distance between the ice crystal spacing predicted by the model, λ_{model} as illustrated in Figure 6.16. Equation 6.1 fails to account for this contribution by the dendritic shape of the ice crystal. Nevertheless, Equation 6.1 predicts the trend of the porosity for humidity between 40-70%RH. As humidity increases, the densification of the frost layer resulted in the decrease in pore size of the CES.

It is further proposed to introduce a shape correction factor into Equation 4.5 to account for this discrepancy. Thus, a modification to Equation 4.5 is proposed to include this shape correction factor as follows:

$$\text{Porosity of CES} = [1 - f(\text{Re}, \text{Fo}, \psi, T^*, \omega, \lambda^*)] \times 100\% \qquad \textbf{Eq 6.2}$$

where $\lambda^* = f(\frac{\lambda_{CES}}{\lambda_{model}})$

It is also important to highlight that Equation 6.1 is derived with the assumption that the remaining dimensionless groups in Equation 4.5 is a weak function of humidity. This assumption affects the accuracy of the correlation as the environment's humidity and temperature are inter-related. However, during the experiments, it was observed that the environment's temperature was relatively stable between 20 – 23°C for all the humidities (25 – 70%) studied. Thus, given the stability of the conditions and the limitations of the experimental setup, the correlation is a reasonable prediction of the trend between humidity and porosity of the CES at the given conditions.

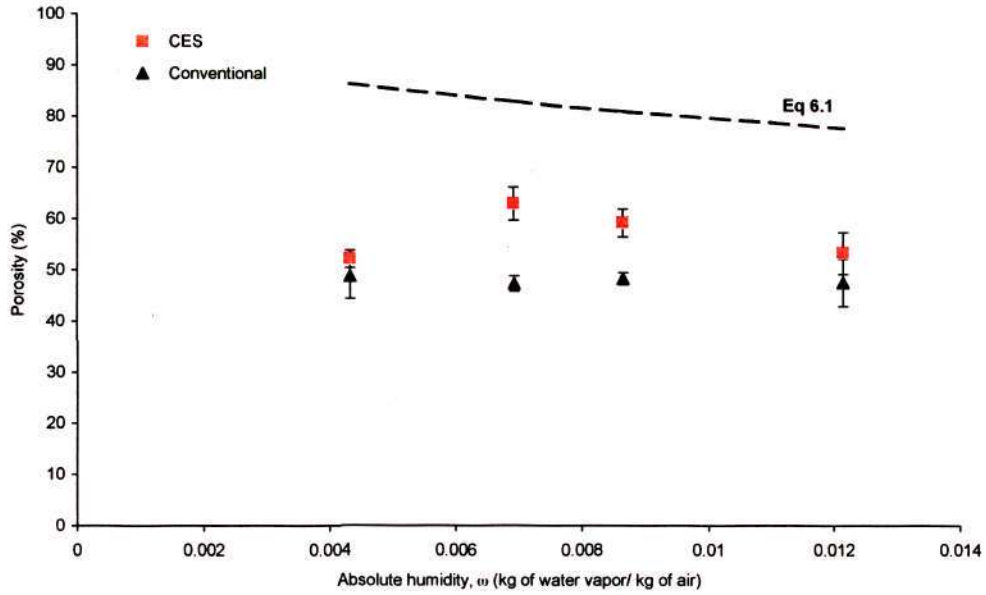

Figure 6.15 Porosity of the frost layer, CES and ES vs. absolute humidity. The frost formation and CES fabrication were carried out at -35°C. Data presented as Mean ± SD.

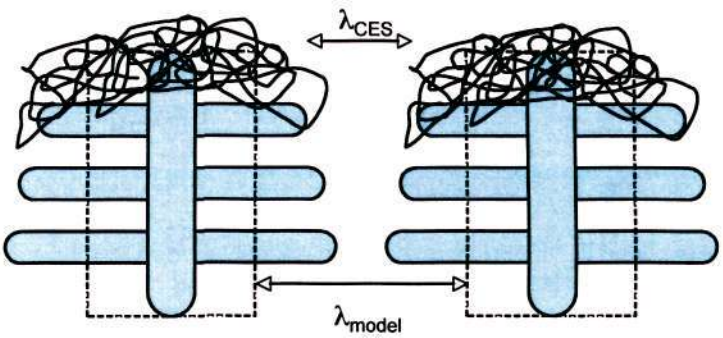

Figure 6.16 Illustration on the effect of the dendritic shape on the pore size of CES.

6.3.2.3 Effect of mandrel temperature on pore size of CES

This experiment was conducted to study the effect of mandrel temperature on pore size of the CES. Figure 6.17 shows the SEM micrographs of the CES obtained at a mandrel temperature of -30°C at different humidities. This set of micrographs can be compared to the micrographs in Figure 6.11 (-35°C) at the corresponding humidities. The measured pore sizes of the CES at different temperatures are shown in Figure

6.12. There is no significant difference between the pore size of the CES fabricated at -30°C and -35°C.

It has been mentioned that the spacing between the ice crystals was approximately 1.5 times smaller at -35°C compared to -30°C at 25%RH. However, this temperature effect on inter-crystal spacing had no effect on the pore size of CES at 25% RH. This is because the deposition of fibers was too fast for the deposition of ice crystals at 25%RH, a phenomenon that has been discussed. The inconclusive data trend for the study on the effect of temperature is largely due to the limitation of the process ability to control mandrel temperature. The difference between the two stable temperatures that could be maintained was only 5°C. Hence the temperature effect is not well characterized due to this limitation.

In summary, the effect of mandrel temperature on pore size of the CES was inconclusive. The lower temperature was used to fabricate CES for further studies as the temperature profile has been shown to be more stable for the process duration in previous studies.

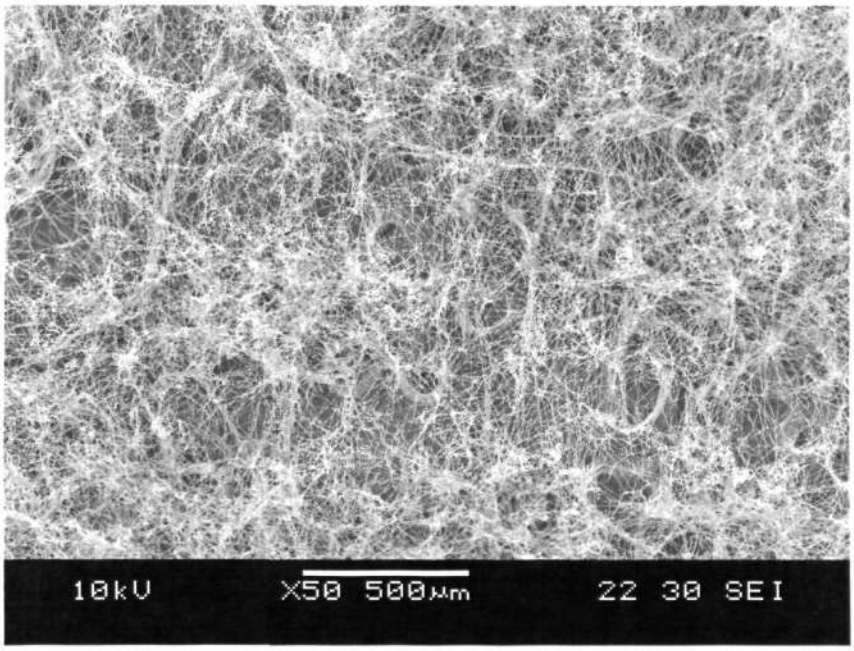

(a)

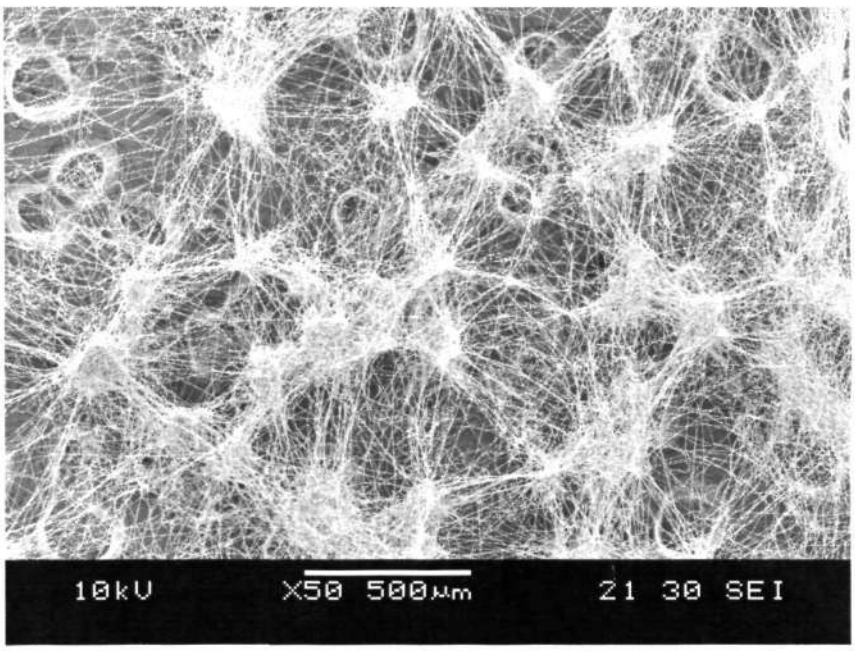

(b)

Figure 6.17 SEM micrographs of initial layers of CES fibers at mandrel temperature of -30°C and (a) 25% RH and (b) 40% RH.

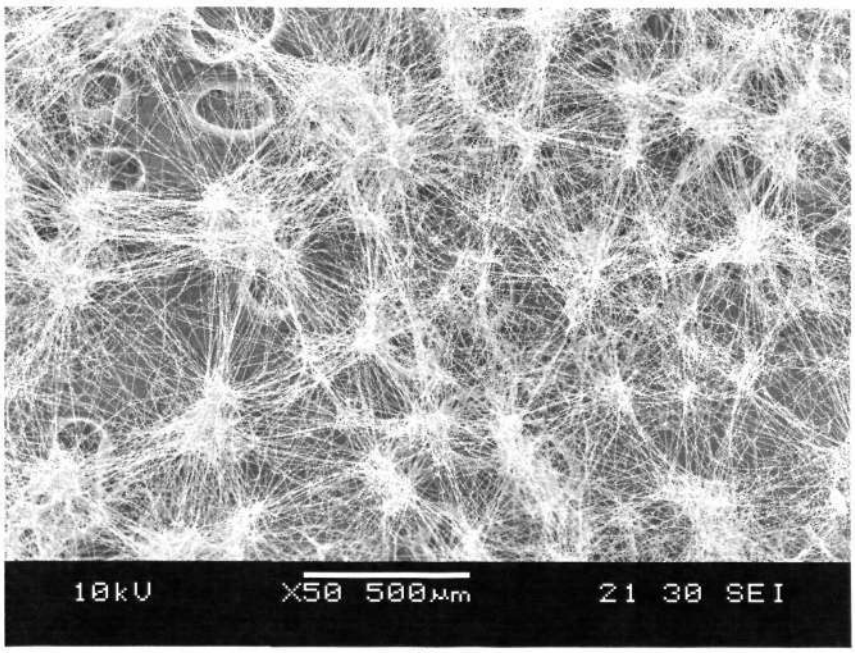

(c)

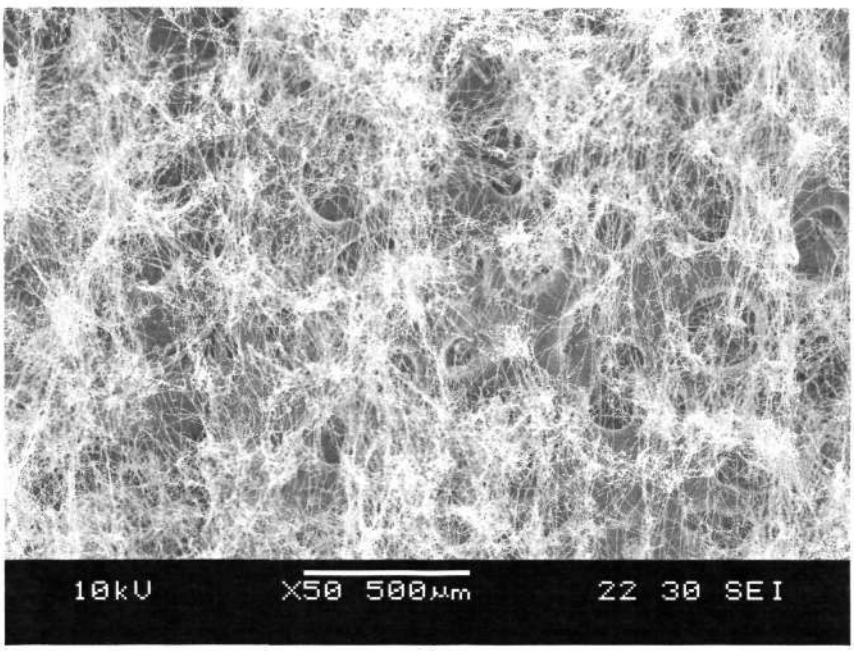

(d)

Figure 6.17 SEM micrographs of initial layers of CES fibers at mandrel temperature of -30°C and (c) 50% RH and (d) 70% RH.

6.3.2.4 Effect of deposition rate of fiber on pore size of CES

Cryogenic electrospinning involves the processes of ice crystal deposition and electrospinning. It has been shown that the rate of deposition of ice crystal, which is varied by humidity control, can affect the pore size of the CES. In this section, the effect of deposition rate of electrospun fiber on the pore size of CES is studied by keeping the environment's humidity (50%RH) and mandrel temperature (-35°C), and hence deposition rate of ice crystal constant.

Figure 6.18 shows the SEM micrographs of the CES and ES as the syringe pneumatic pressure was varied from 1psi, 2psi to 3psi. This corresponds to solution flow rates of 0.095ml/hr, 0.16ml/hr and 0.24ml/hr respectively. For the ES, it can be observed that the pore size of ES was not affected by the change in solution flow rate (Figures 6.18(a), (c) and (e)). This epitomizes the limitation of conventional electrospinning technique, which is the inability to obtain large pores, even at low solution flow rate. This is because in conventional electrospinning, the fibers were deposited randomly on each other on a flat mandrel surface within the same deposition zone. The flat surface had equal electric field strength and it was equally likely for the fibers to land on any location on the mandrel. This random deposition of fibers resulted in small pores of the ES and the pore size is independent of the deposition rate of the fibers as shown in Figure 6.19.

In contrast, the pore sizes of the CES were significantly larger than the pore size of ES at all flow rates (Figure 6.19). The difference in CES pore size between low (0.095ml/hr) to intermediate (0.16ml/hr) solution flow rates was not significant (Figures 6.18(b) and (d)). However, as the solution flow rate was increased to a high

level at 0.24ml/hr, the pore size of the CES decreased and the nodes and struts framework became less distinct (Figure 6.18(f)). This was due to the increase in deposition of fiber on the ice crystals. It can be observed in Figures 6.18(a), (c) and (e) that as the flow rate of solution increased, the fiber diameter remained approximately the same. By conservation of mass, this implied that increasing solution flow rate increased the number of fibers deposited per unit area. As the ice crystals formation was not able to keep pace with this increase in fiber deposition, more fibers were deposited to fill up the spacing between the ice crystals, resulting in a decrease in pore size as shown in Figure 6.18(f).

The understanding of the effect of solution flow rate on the pore size of CES reveals two important aspects of CES. Firstly, the relative rates of deposition of ice crystal and electrospun fiber are important in creating the strut-like framework of the CES. When flow rate increases and dominates, the pores of the CES will decrease and eventually, dense layers of fibers with large inter-layer distance are obtained. Secondly, on the manufacturing platform, high solution flow rate is preferred to maximize the throughput of the polymer and process it into a fibrous form. However, there is a maximum limit to which the solution flow rate can be increased before the pore size of the CES decreases. In this study, it has been shown that this maximum value is 0.16ml/hr.

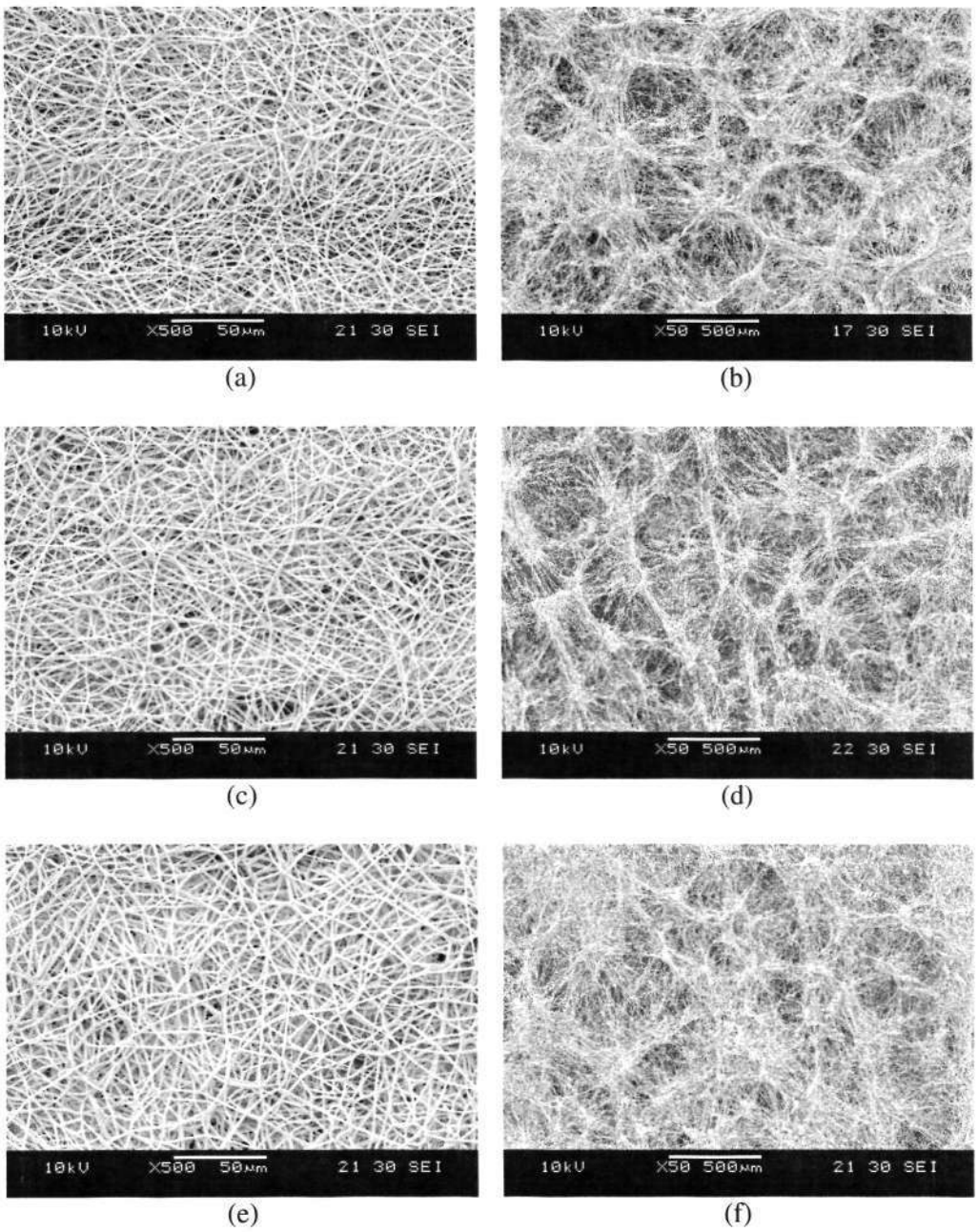

Figure 6.18 SEM micrographs of electrospun scaffolds fabricated at -35°C and 50% RH at different solution flow rates. (a) and (b) are ES and CES at 0.095ml/hr respectively, (c) and (d) are ES and CES at 0.16ml/hr respectively and (e) and (f) are ES and CES at 0.24ml/hr respectively.

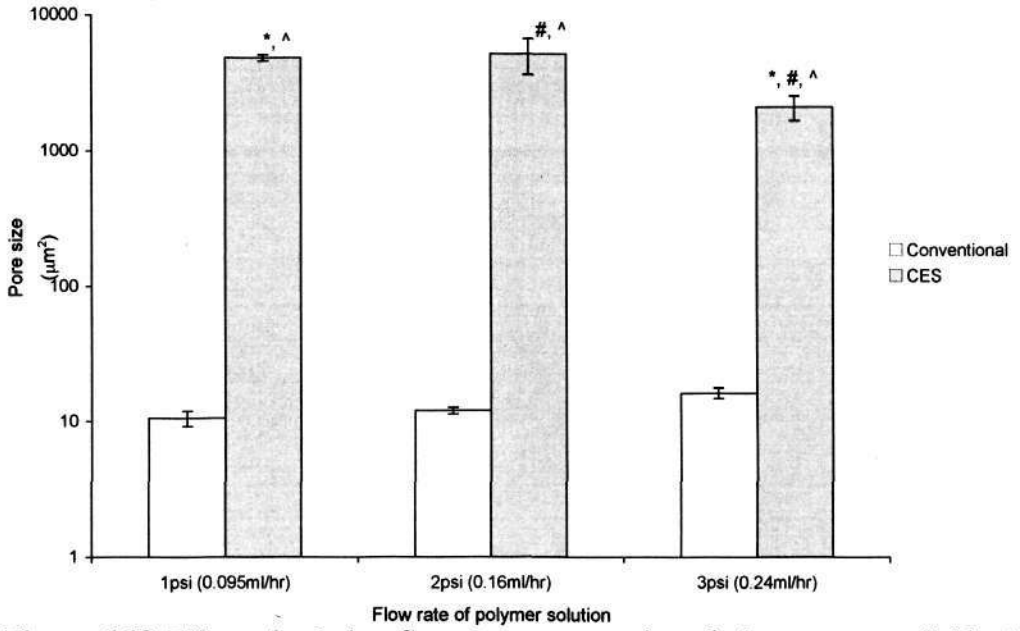

Figure 6.19 Effect of solution flow rate on pore size of electrospun scaffolds. ^ denotes inter-group significant difference at the same flow rate. *, # denotes significant difference between the same group at different flow rates. $p<0.05$. Mean ± SD. n=5

6.3.3 Comparing cryogenic electrospun scaffold (CES) and conventional electrospun scaffold (ES)

It has been shown that CES has very different pore structures from conventional ES. In this section, the pore structure and the distribution of the pore sizes for the ES and CES are presented and compared.

Figure 6.20 shows the differences in morphology of the ES and CES. The conventional ES is a highly porous and dense meshwork of non-woven submicron fibers, randomly arranged in a planar orientation as shown in Figure 6.20(a). The interconnected pores are small, measuring approximately 5μm across and are bounded by individual fibers (Figure 6.20(b)).

In contrast, the CES has a much more open structure due to the inclusion of large pores, which measure approximately between 10 to 500μm in size. These are bounded by bundles of fibers arranged in a network of struts and nodes (Figure 6.20(c)). As illustrated in the oblique view of the CES sample, the large pores have a well-defined three-dimensional spatial structure (Figure 6.20(d)). They are interconnected via their thin fibrous walls, which themselves have small pores like those of conventional electrospun fibers. These fibrous and porous pore walls maintain interconnectivity throughout the CES.

The pore sizes and pore size distribution of the CES and ES are shown in Figure 6.21. Approximately 90% of the pores in the ES have pore area less than $50\mu m^2$ with a median at approximately $10\mu m^2$ as shown in Figure 6.21(a). The CES, on the other hand, shows a tri-modal pore area distribution, that is, with one distribution for small pores between 10 μm^2 to $250\mu m^2$ (Figure 6.21(b)) and another bimodal distribution for large pores having area larger than $1000\mu m^2$ (Figure 6.21(c)). Due to the presence of these large three-dimensional pores, the porosity of the CES (63 ± 5%) is significantly higher than that of the conventional electrospun scaffold (52 ± 4%).

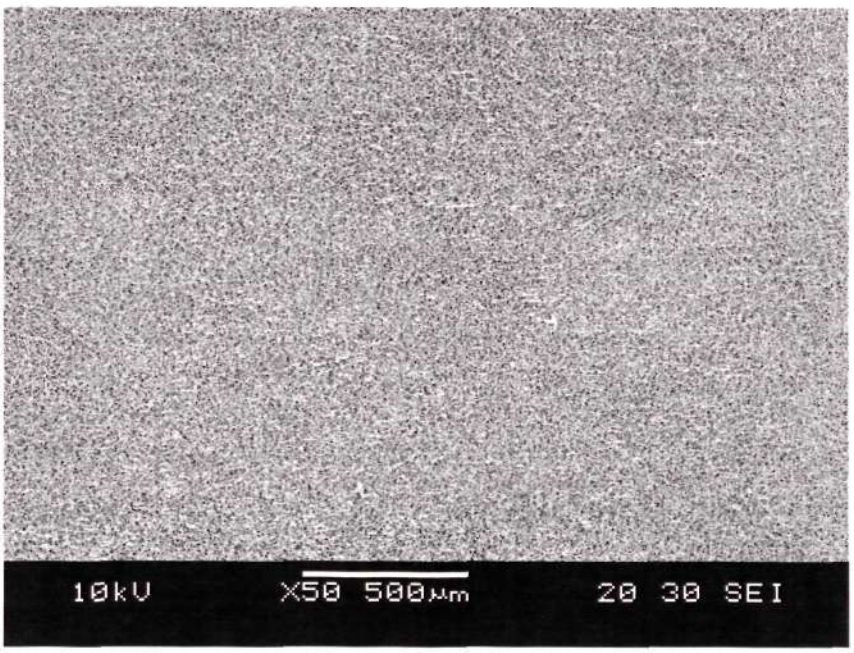

(a)

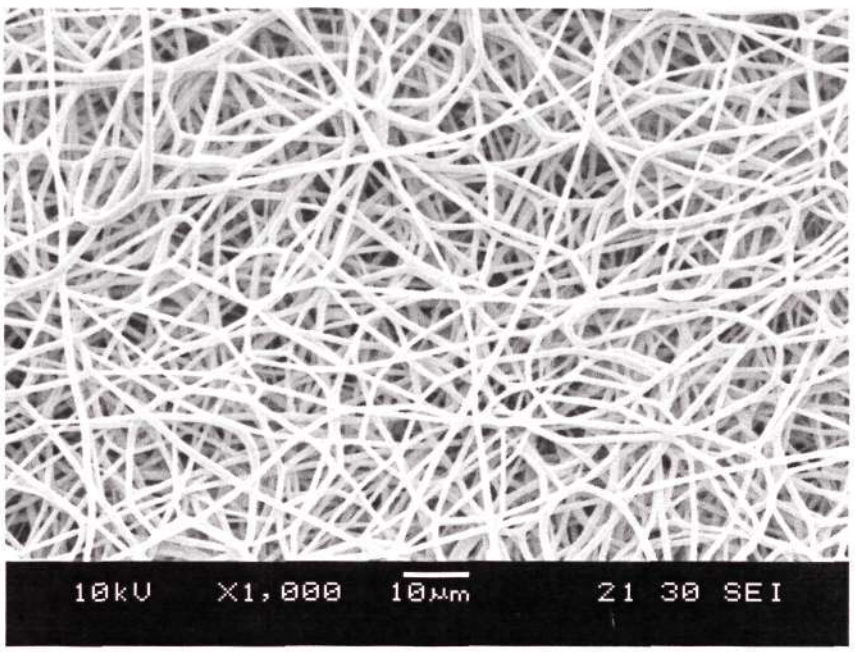

(b)

Figure 6.20 Comparison of morphologies under SEM. (a) ES under low magnification and (b) ES under high magnification.

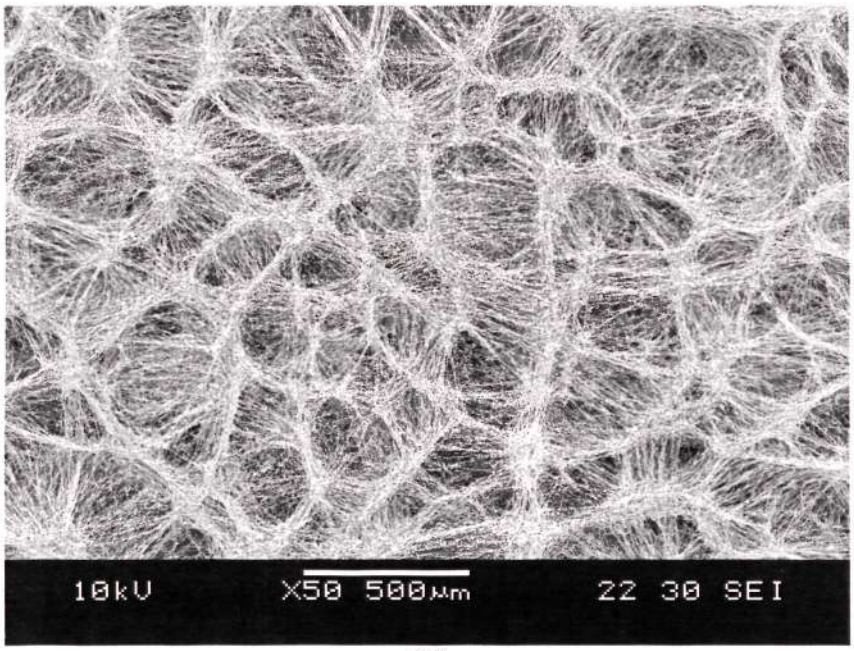

(c)

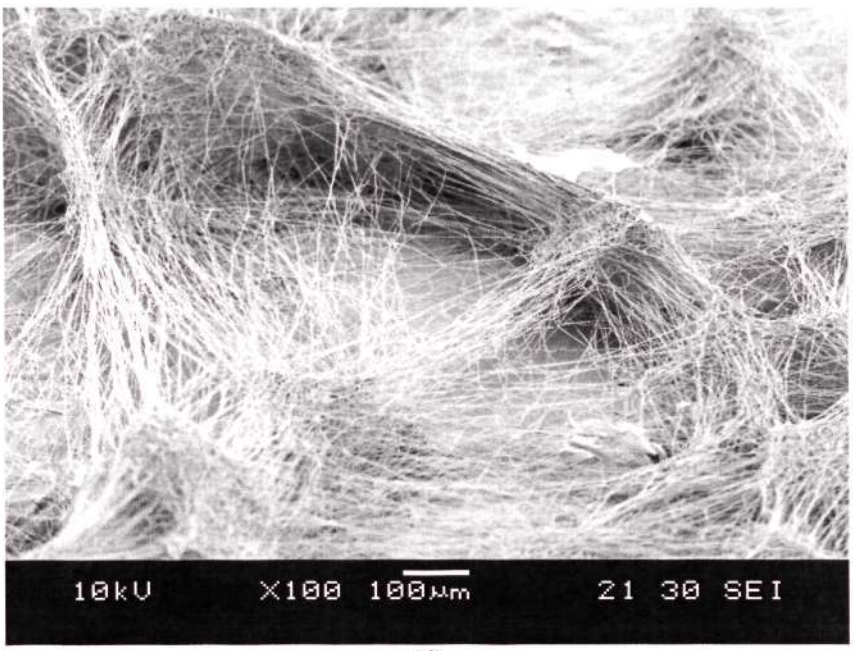

(d)

Figure 6.20 Comparison of morphologies under SEM. (c) CES under the same magnification as (a), showing a network of nodes and struts and (d) CES under high magnification, oblique view showing the three-dimensional structure of a pore in CES.

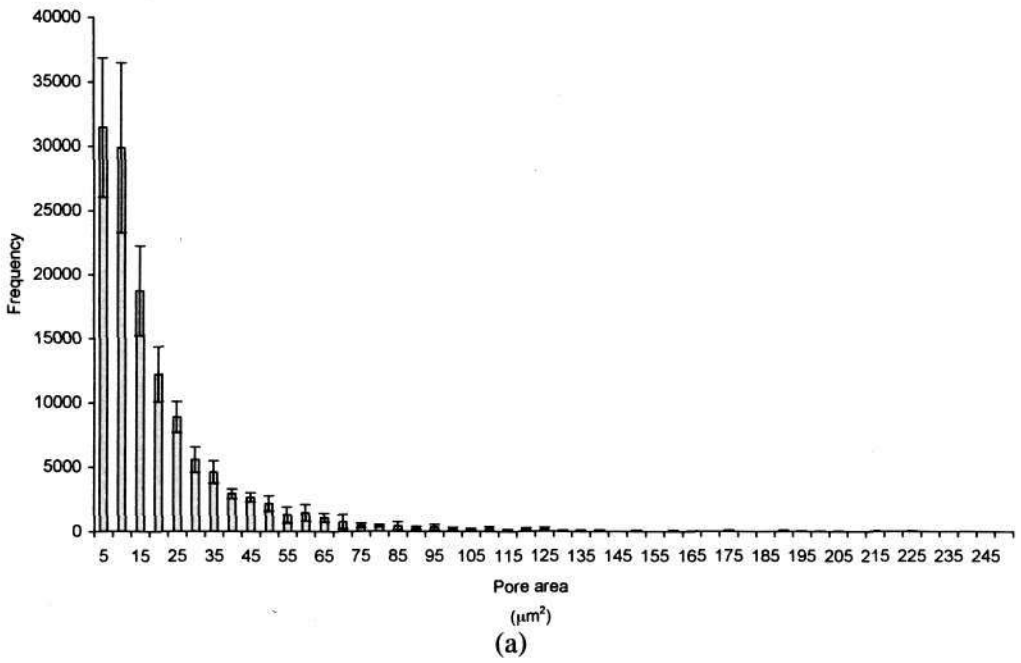

(a)

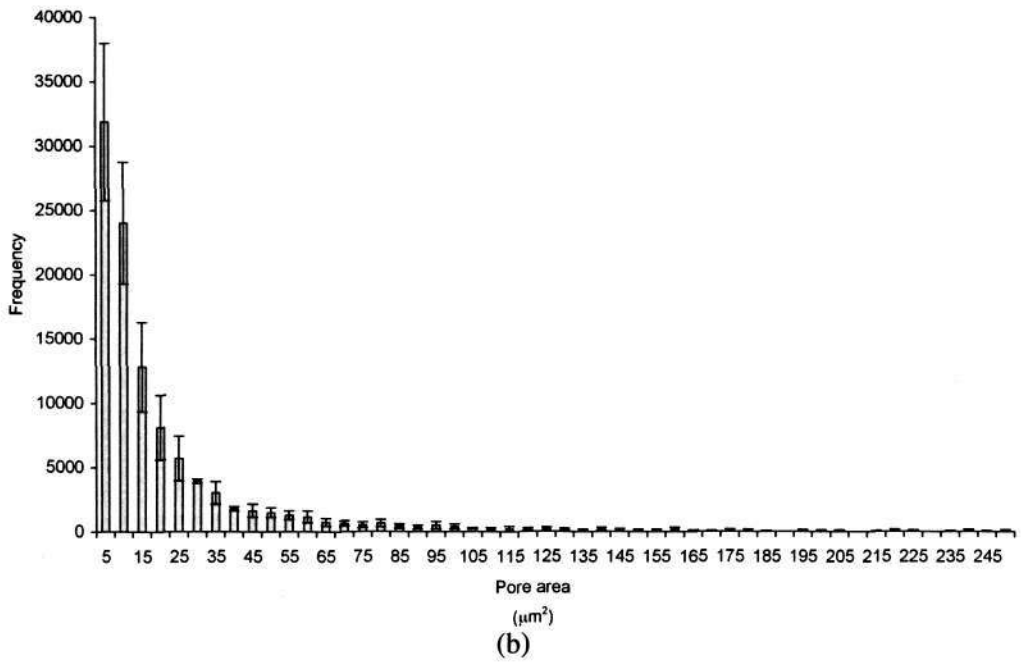

(b)

Figure 6.21 Comparison of pore size between CES and ES. (a) Pore size distribution of ES and (b) CES small pores. Mean ± SD. n = 5.

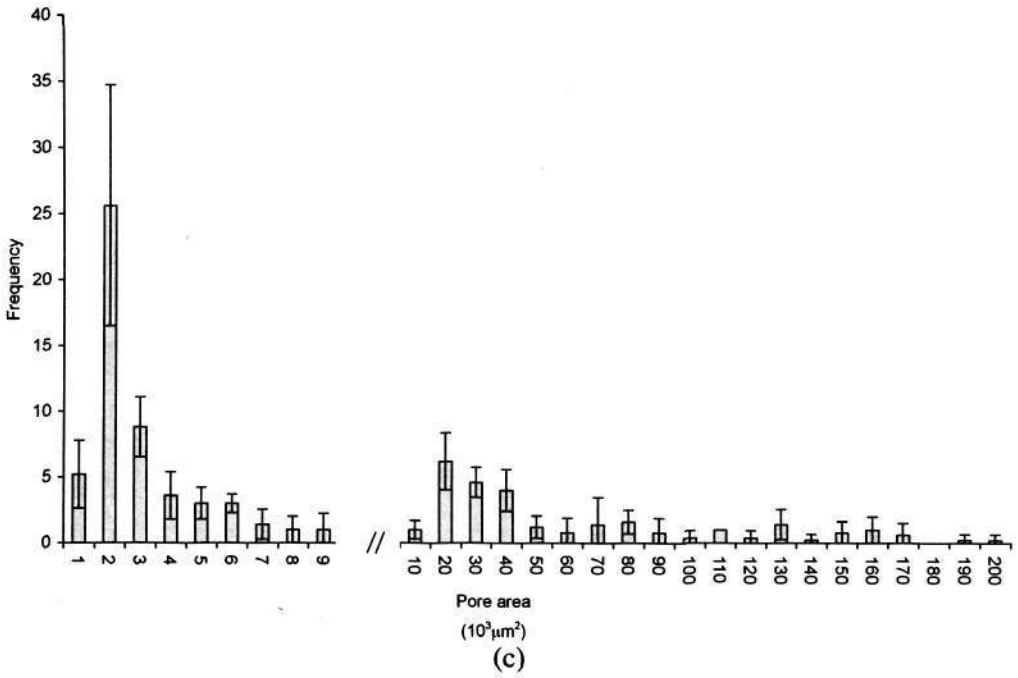

Figure 6.21 Comparison of pore size between CES and ES. Pore size distribution of (c) CES large pores. Mean ± SD. n = 5.

The technology edge of the cryogenic electrospinning technique over conventional electrospinning lies in its ability to expand the pores of electrospun scaffold beyond 5µm and at the same time, control the pore size. This increases its versatility in tissue engineering applications. The CES scaffold has a unique architecture of large three-dimensional bowl-shaped pores that are interconnected (Figures 6.20(c) and (d)). Interconnectivity is maintained throughout the entire CES as the walls are porous, which is important for nutrient and waste transfer. In addition, this interconnected network of large pores is vital for the improved *in vitro* cell infiltration and *in vivo* cell infiltration and vascularization of CES over the conventional electrospun scaffold as will be shown in Section 6.5 and 6.6.[176] The ability of a scaffold in supporting cell infiltration and vascularization is important in creating large tissue constructs. In addition, different pore sizes are required for engineering different tissue constructs. Hence, by having large interconnected pores within the electrospun scaffold, yet

retaining the nano-fibrous structure that mimics the physical environment of the ECM[139,164], one can use it to make more varied tissue constructs and thicker tissue replacements.

In summary, the pore structure and pore size distribution for the ES and CES were compared in this section. The effect of the large pores of the CES on *in vitro* cell infiltration and *in vivo* cell infiltration and vascularization will be discussed in Section 6.5 and 6.6.

6.4 Bilayered electrospun scaffold (BLES) for oesophagus regeneration

The oesophagus ECM consists of a dense basement membrane (thickness less than 1μm) with small pores (< 100nm) to support the epithelium and physically separate it from the underlying connective tissue[27]. The adjacent mucosal-submucosal connective tissue consists of collagen fiber bundles and large pores with infiltrated fibroblasts and smooth muscle cells. It is important to replicate this structure when fabricating scaffolds for tissue engineering of the oesophagus. It has been shown that electrospun scaffolds with small pores (ES) and large pores (CES) can be fabricated separately. In this section, a bilayered electrospun scaffold (BLES) design that consists of a dense ES (pore size < 5μm) and an open porous CES with large pores was fabricated in a single uninterrupted process to mimic the physical structure of the oesophagus ECM.

6.4.1 Structure of the BLES

The cross-section of the BLES is shown in Figure 6.22. The BLES consists of an ES layer that is approximately 5μm thick (few fibers thick) and a CES layer that is

250μm thick (Figure 6.22(a)). While the transition between the ES and CES layers is distinct, there is no observable delamination between the two layers. The characteristic planar surface of the dense ES layer can be observed at the top surface of the BLES (Figure 6.22(b)). The nodes and struts framework of the underlying CES layer is faintly visible. However, the density of fiber is high and the pore size remains small. The large pore structure is visible throughout the thickness of the CES layer (Figure 6.22(a) and 6.22(c)). The fibers are organized in the characteristic nodes and struts framework of the CES.

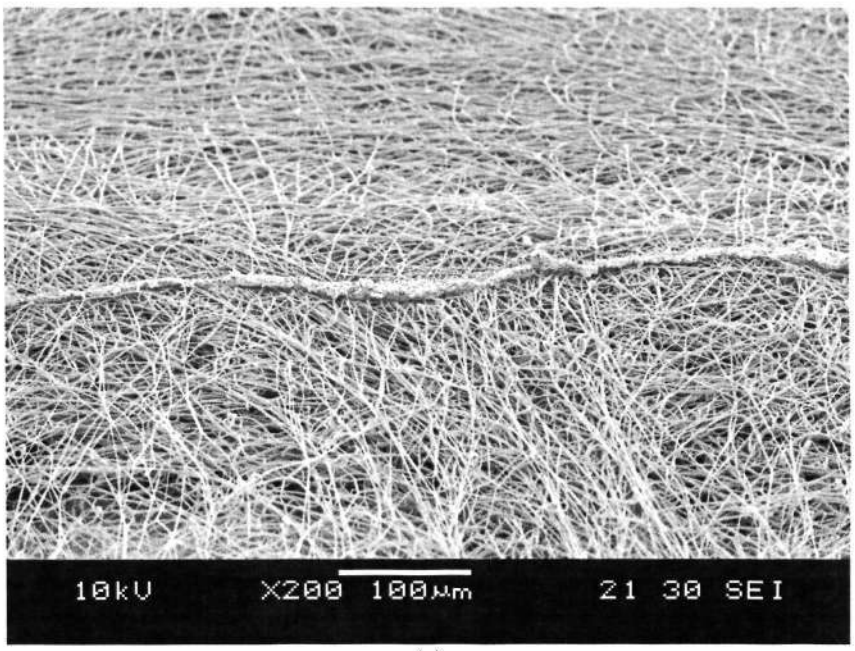

(a)

Figure 6.22 (a) SEM micrographs of the BLES cross-section.

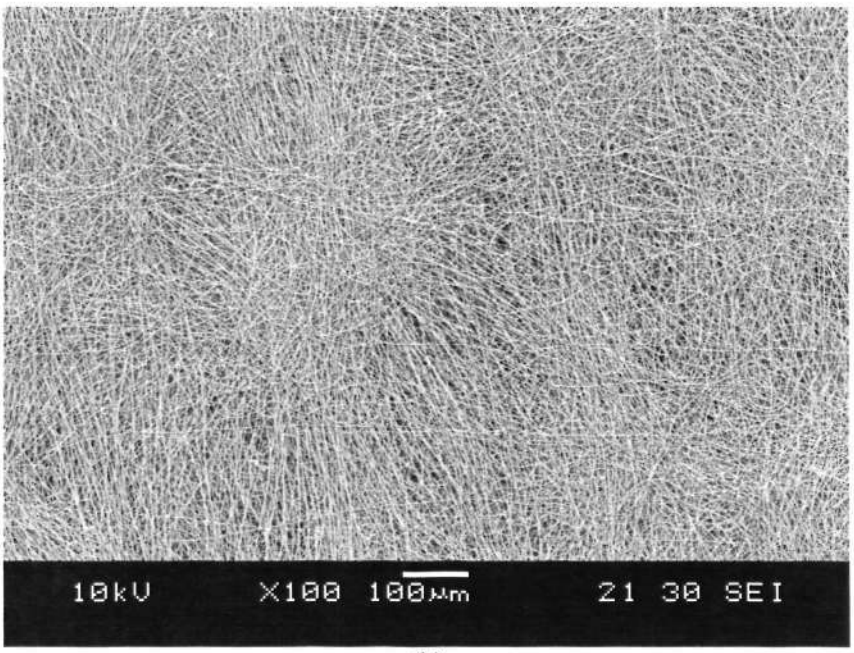

(b)

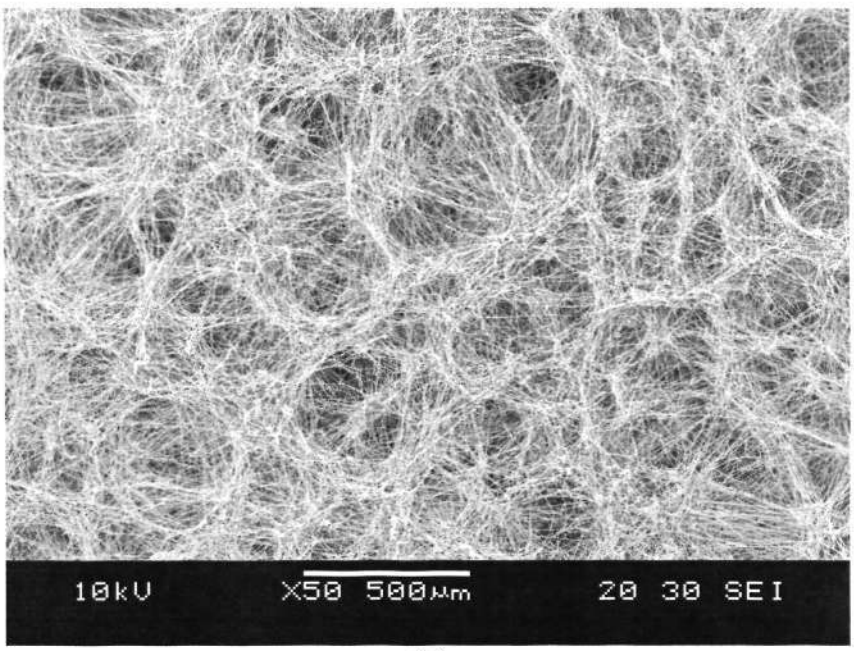

(c)

Figure 6.22 SEM micrograph of the BLES. (b) ES layer and (c) CES layer.

The results shown in Figure 6.22 demonstrate that a BLES can be fabricated in a single uninterrupted process. The CES layer was first formed by depositing fibers on the ice template that formed on the chilled mandrel at 50%RH and -35°C. The processing conditions were maintained for 15 minutes. After 15 minutes, the relative humidity was lowered to 25%, resulting in the reduction in the rate of ice crystal deposition. In addition, the rate of fiber deposition was increased from 0.16ml/hr to 0.24ml/hr. As fewer ice crystals formed on the chilled mandrel and the existing CES layer, the pores of the uppermost section of the CES layer were covered with an increased amount of fibers, resulting in the dense ES layer. Electrospinning continues for 2 minutes such that the ES layer formed was only a few fibers thick to mimic the thin basement membrane. In this way, the fabrication of the BLES with 2 layers of distinct pore size and thickness was achieved in a single uninterrupted process.

In the process described above, the CES layer was fabricated before the ES layer on a cylindrical mandrel. This resulted in a cylindrical BLES with the CES as the inner layer of the construct. Ideally, the ES layer should be fabricated first such that it formed the inner layer of a cylindrical construct to mimic the basement membrane at the luminal surface of the oesophagus. In this experiment, the BLES was fabricated in this way due to limitations with the equipment setup. Ice crystals started to accumulate on the mandrel surface during the loading of dry ice into the mandrel. As such, it was not possible to fabricate the dense ES layer first due to the presence of the ice template at the beginning of the electrospinning process. As such, the CES layer was fabricated first, followed by the dense ES layer. The resulting BLES could then be inverted inside out to obtain the correct configuration with the inner ES layer. An alternative would be to integrate a chiller to cool the mandrel within the

environmental chamber in which the relative humidity was maintained at 25%. In this way, the initial deposition of the ice crystals could be prevented while the mandrel was chilled to -35°C.

When the BLES shown in Figure 6.22 was used in *in vitro* and *in vivo* studies, it was difficult to distinguish between the two layers when the specimens were sectioned for histochemical analysis. During mechanical testing, it was also difficult to observe for failure of the scaffold caused by delamination of the two layers. This was because the ES layer was too thin to be visualized. Hence, for subsequent experiments, the ES layer was intentionally made 50μm thick such that the two layers could be distinguished in histochemical analysis and mechanical testing. Figures 6.23(a) and (b) show the cross-section of the BLES, which consists of a 50μm thick ES layer and a 250μm thick CES layer. The morphologies of the ES and CES layer were similar to that of the BLES shown in Figure 6.22.

In summary, the fabrication of the BLES in a single uninterrupted process demonstrates the flexibility of the cryogenic electrospinning technique. Process parameters such as humidity and deposition rate of fibers could be changed during the process to obtain electrospun scaffold with distinct pore sizes. The BLES fabricated in this experiment is used for mechanical testing, *in vitro* and *in vivo* studies which will be discussed later.

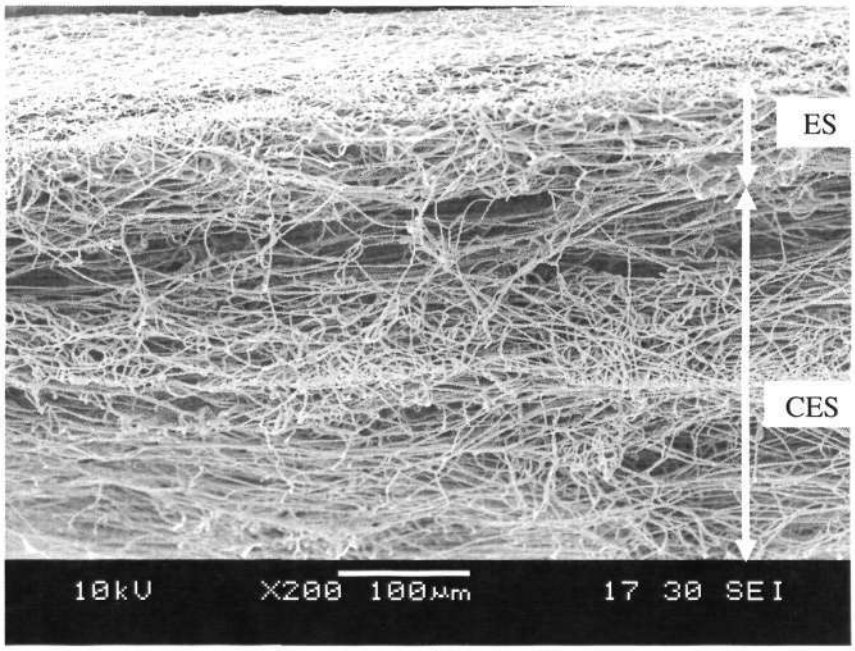

(a)

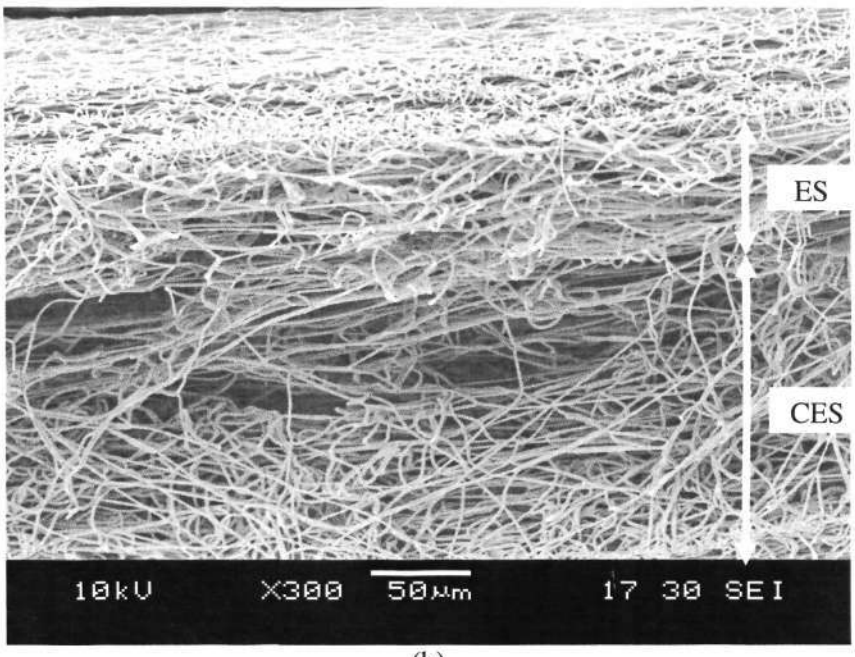

(b)

Figure 6.23 SEM micrographs showing the cross-section of the BLES. (a) Low magnification showing the difference in thickness of the ES and CES layers in the BLES and (b) high magnification showing the transition from dense ES to open porous CES.

6.4.2 Mechanical properties of ES, CES and BLES

The human cadaveric oesophagus is reported to have an ultimate tensile stress of 1.3 ± 0.5MPa and strain at break of 1.4 ± 0.3.[200] This experiment was conducted to determine the mechanical properties of ES, CES and BLES and compared the tensile strength and strain at break to that of the human oesophagus.

The mechanical test results of ES, CES and BLES are shown in Figure 6.24. The tensile strength of the CES (0.04 ± 0.01MPa) is significantly lower than that of the ES (1.5 ± 0.1MPa), while its strain at break (1.4 ± 0.3) is significantly higher than the latter (0.16 ± 0.02). The CES is a weaker and more ductile scaffold while the ES is stronger and more brittle. The BLES has a tensile strength of 0.33 ± 0.03MPa and a strain at break of 0.14 ± 0.02. The strength of the BLES is significantly higher than the CES but remains significantly lower than the ES. The difference between the strain of the BLES and ES is not significant.

The results show that CES is very weak and hence has severe limitation. The tensile strength of the CES is approximately 40 times weaker than the ES. This is largely due to the increase in porosity of the scaffold and the reduction in fiber fusions as the presence of the ice crystals prevents effective bonding of the deposited fibers. The increase in strain observed in the CES is due to the flexibility of the fibrous network. As the CES was being stretched, the struts of the fibers reorganized in the direction of deformation before the individual fibers were subjected to the tensile stress. This fiber reorganization was more limited in the ES as the fibers were fused together, forming a more rigid network. When the CES (approximately 250μm thick) was combined with the ES (approximately 50μm), the mechanical strength of the BLES remained low.

This was because although the ES layer was withstanding the load, the measured tensile load was normalized over the entire thickness of the BLES, which reduced the value of the tensile strength. The strain of the BLES was limited by the strain of the ES layer. No delamination of the BLES was observed, indicating a good bonding at the interface between the ES and CES layers.

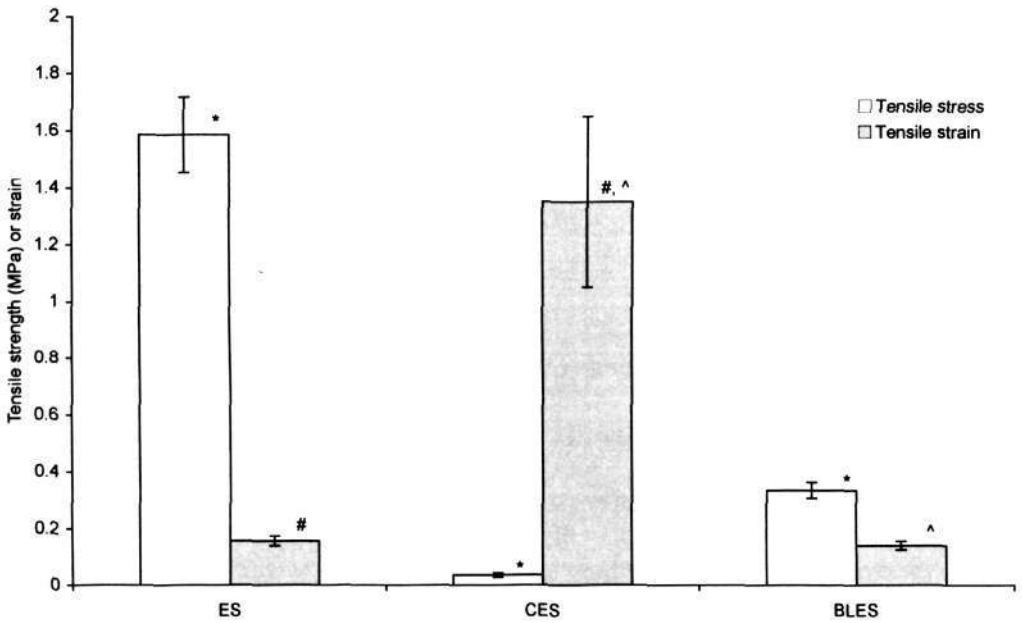

Figure 6.24 Mechanical properties of the ES, CES and BLES. *, # and ^ denote significant difference between the relevant data groups. A solvent-cast PLA film has an ultimate tensile stress of 23.6±1.9MPa and strain at break of 0.15±0.01MPa.[69] The strength of the electrospun scaffolds (ES, CES and BLES) are significantly weaker than the bulk polymer ($p<0.01$). Mean ± SD. n=5.

The tensile strength and strain at break of the ES, CES and BLES are compared to the human oesophagus. The tensile strength of the ES is comparable while its strain is significantly lower when compared to the human oesophagus. For the CES, the tensile strength is significantly lower than that of the cadaveric oesophagus while the strain is comparable. The strength of the BLES remains low as compared to the oesophagus. Hence, the mechanical strength of the CES needs to be improved significantly before it can be used for load bearing applications. Improvements can be made by supporting

the CES on a mechanically stronger substrate to form a composite porous scaffold with both strength and strain comparable to that of the oesophagus. One such example is an acellular porcine oesophageal ECM-CES hybrid scaffold filed in this patent by Chian *et al.*[201] This work was part of a collaboration in the oesophageal tissue engineering project. It is postulated that the mechanical properties of this hybrid scaffold will be comparable to the acellular tissue, since the acellular tissue forms part of the hybrid scaffold. As the work is not within the scope of this thesis, the analysis of the hybrid scaffold is left for the future work.

6.5 *In vitro* cell-scaffold interactions

This section presents the results of *in vitro* studies using ES, CES and BLES scaffolds. The purpose of *in vitro* study is to assess the cytotoxicity of the scaffolds, study cell infiltration into the scaffolds and evaluate the feasibility of using the scaffolds for co-culture of porcine oesophageal epithelial (PEECs) and smooth muscle cells (PESMCs).

6.5.1 *In vitro* cytotoxicity test

In vitro cytotoxicity test was conducted in accordance with ISO 10993-5 Tests for *In Vitro* Cytotoxicity test standard. Cytotoxicity was assessed qualitatively by observing the morphology of cells cultured in the medium extracts of the scaffolds and quantitatively using MTS proliferation assay.

6.5.1.1 Qualitative assessment of cytotoxicity

Figure 6.25 shows the light microscope pictures of the 3T3/NIH fibroblasts cultured using the extracts from the scaffolds. For the negative control, there was no visible

cytotoxic effect on the fibroblasts for up to 48 hours (Figures 6.25(a) and (b)). The morphologies of the fibroblasts were well defined and cell-to-cell contacts were observed. The cells remained attached and exhibited the characteristic spindle-like morphology. In addition, no cell lysis or cell debris was observed. Figures 6.25(c) and (d) show the fibroblasts cultured in the extract of the positive control. There were no discernable spindle-shaped cells after 48 hours in culture. There was cell debris in the culture medium, indicating that cell lysis had occurred due to the cytotoxicity of the specimens (Figure 6.25(d)). Figures 6.25(e) to (j) show the fibroblasts cultured in separate extracts of all three electrospun scaffolds (ES, CES and BLES). The morphologies of the fibroblasts were comparable to the negative control (Figures 6.25(a) and (b)). There was no visible cell lysis or debris. The fibroblasts remained attached and exhibited the characteristic spindle-like morphology.

6.5.1.2 Quantitative assessment of cytotoxicity

Figure 6.26 shows the absorbance of the supernatant with the MTS assay measured using a micro-plate reader at 490nm. The absorbance for the negative control was 1.33 ± 0.10 after 48 hours in culture. The absorbance for the positive control was significantly lower when compared to the negative control and all the electrospun specimens. There was no significant difference between the absorbances for the MTS assays between all three electrospun specimens with the negative control. This indicates that the cytotoxicity levels of the electrospun scaffolds were comparable with the negative control.

Sample extract	24 hours	48 hours
Negative	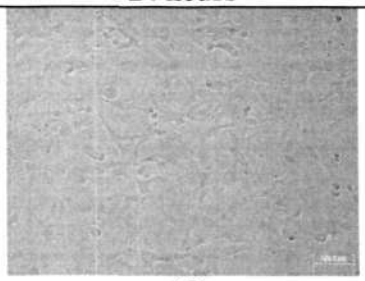 (a)	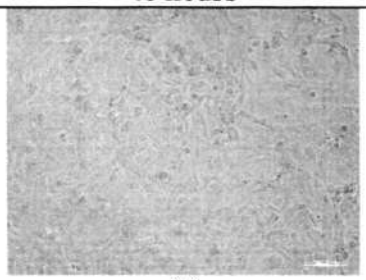 (b)
Positive	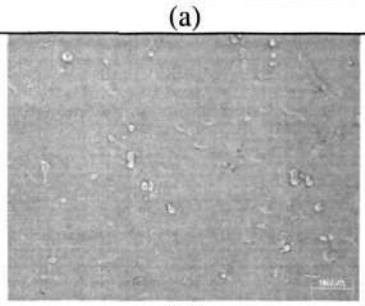 (c)	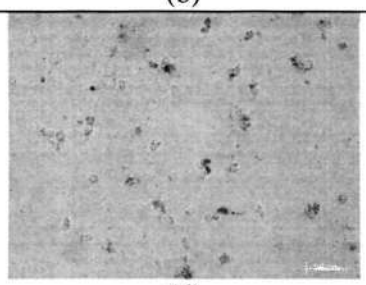 (d)
ES	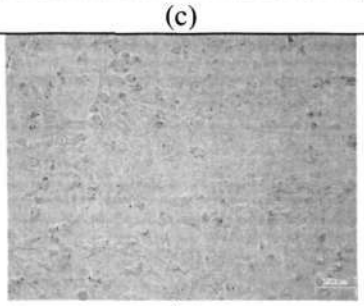 (e)	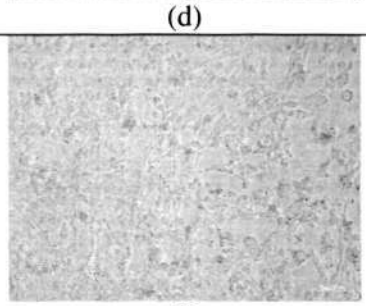 (f)
CES	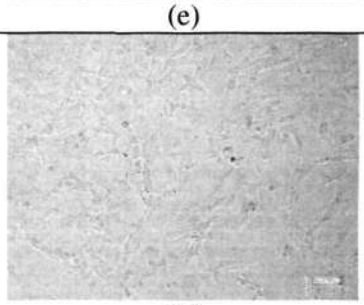 (g)	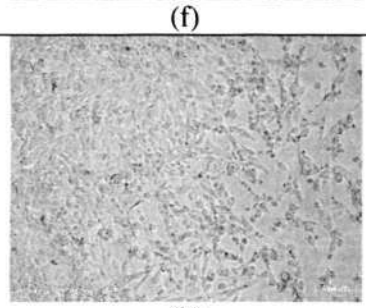 (h)
BLES	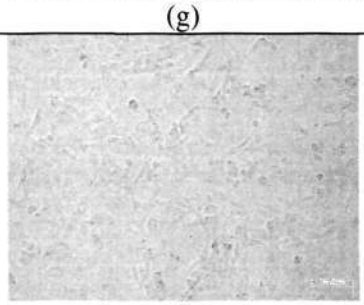 (i)	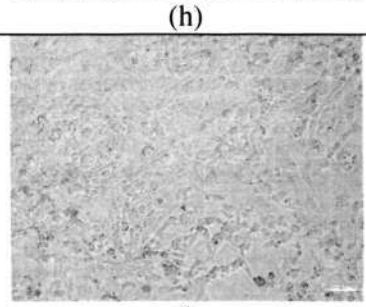 (j)

Figure 6.25 Light microscope pictures showing 3T3/NIH fibroblasts cultured in the extracts of the specimens for 24 and 48 hours. (a) and (b) are negative control, (c) and (d) are positive control, (e) and (f) are ES specimens, (g) and (h) are CES specimens and (i) and (j) are BLES specimens.

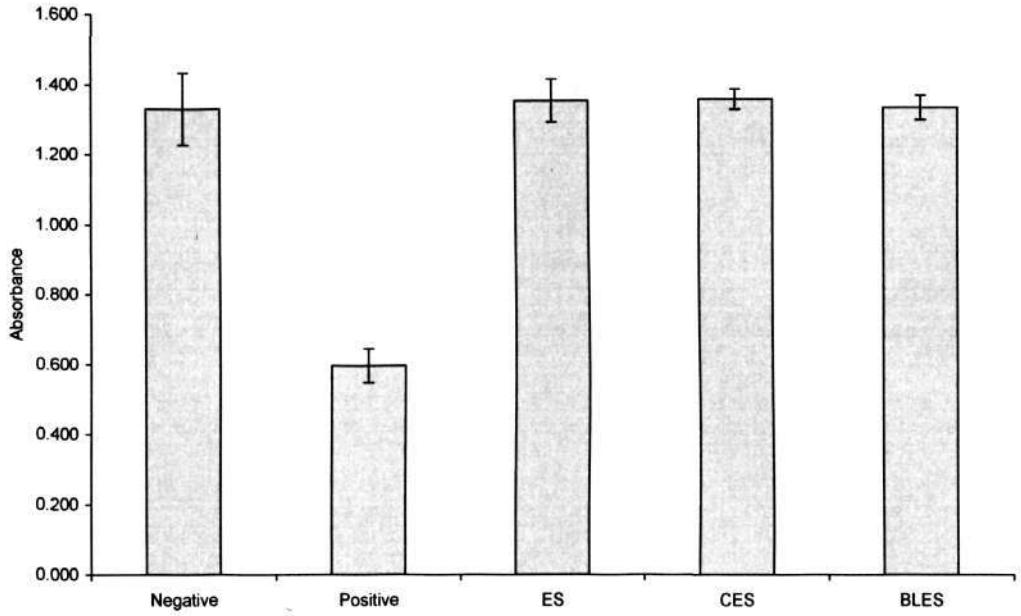

Figure 6.26 MTS data for cytotoxicity test at 48 hours. The differences between the negative control, ES, CES and BLES from the positive control were significant ($p<0.05$). Mean ± SD. n=4.

Based on the qualitative and quantitative assessments, the cytotoxicity rating according to the ISO 10993-5 test standard for the ES, CES and BLES specimens is 0. The ratings for the negative and positive controls are 0 and 3 respectively. This means that the toxic agents, if any, that leached out of the electrospun specimens into the extract are within tolerable limits. In addition, the results from the cytotoxicity test validate that the processes used to fabricate the ES, CES and BLES specimens were able to make scaffolds that had cytotoxicity rating of 0. Hence, this qualifies the electrospun scaffolds for further *in vitro* and *in vivo* studies.

6.5.2 To study the effect of pore size on cell infiltration

This experiment was conducted to evaluate the effect of the pore size on *in vitro* cell infiltration. 3T3/NIH fibroblasts on the surface of both CES and ES, and maintained the cell-scaffold constructs under static culture conditions for 2 weeks.

Figures 6.27(a) and (c) show the H&E stained pictures of the cross-sections of the ES-fibroblast constructs at day 7 and 14 respectively. Fibroblasts cultured on 50μm thick ES did not infiltrate the scaffold but proliferated on its surface. At day 14, several layers of fibroblasts can be seen stacking on top of the surface of ES (Figure 6.27(c)).

In contrast, fibroblasts cultured on CES of the same thickness infiltrated the entire cross-section by day 7 and were observed to be within the CES on day 14 (Figures 6.27(b) and (d)). The nodes of the CES were not infiltrated with cells up till day 14, as indicated by regions of dense fibers in Figure 6.27(d). However, when thicker CES were used, we observed that cells did not infiltrate beyond 50μm by day 14 (data not shown).

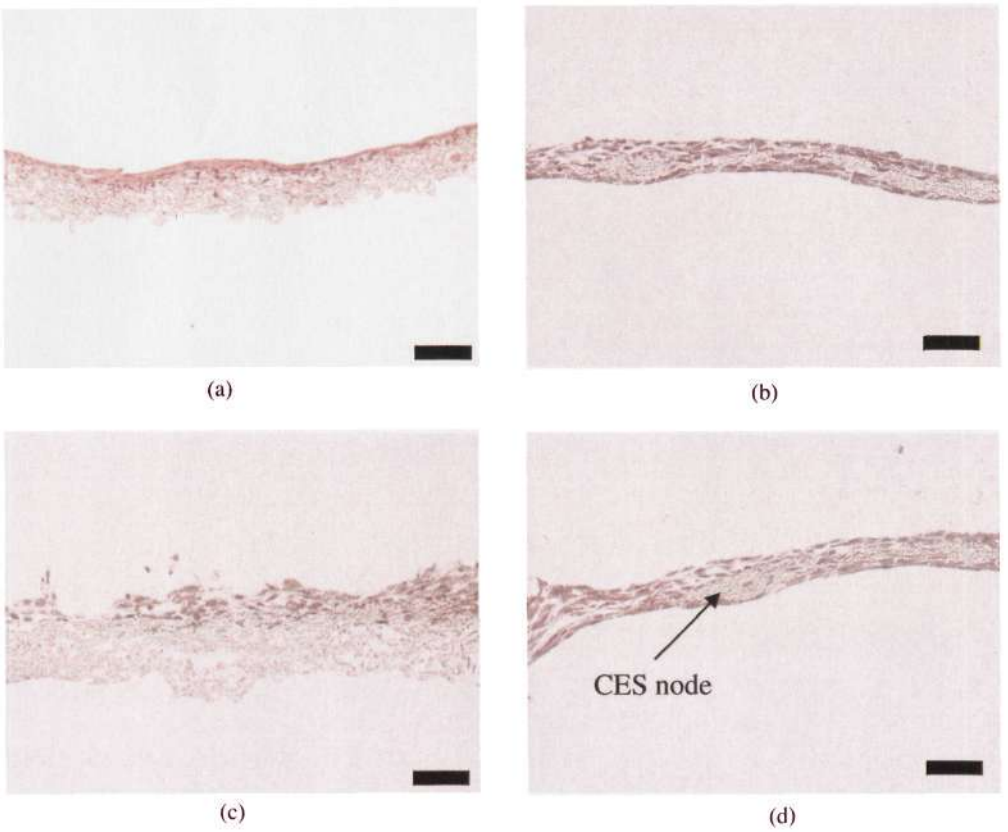

Figure 6.27 Histological analysis of *in vitro* studies. Scaffold cultured with 3T3/NIH fibroblasts and stained with H&E. (a) ES at day 7, (b) CES at day 7, (c) ES at day 14 and (d) CES at day 14. Scale bar represents 50μm.

The *in vitro* cell infiltration studies show that cells were unable to infiltrate the conventional ES, which had an average pore area of 17 ± 3μm^2 (corresponding to a pore diameter of approximately 5μm). This is evident from Figures 6.27(a) and (c), which show that cells remained on the surface of the ES. This agrees with a published report, which suggested that the pore size of a scaffold should be at least 10μm to support cell infiltration.[202] In contrast, the fibroblasts infiltrated the CES up to a depth of 50μm under static culture conditions at day 14. This demonstrates that the large three-dimensional pores of the CES presented less of an impediment to cell infiltration even under static culture conditions. However, there are still limitations with the use of CES for *in vitro* cell infiltration under static conditions. Cell

infiltration was not observed for CES with thickness greater than 50μm. In addition, the nodes of the CES, which pore size resembles that of the ES, remained dense and prevented *in vitro* cell infiltration under static conditions at day 14. It has been suggested that nutrient diffusion could be limited within the thick construct under static culture conditions.[202] Diffusion of nutrients may be further affected by the infiltrated cells in the scaffolds. Hence, for single cell-type under static culture conditions, the limitations of the CES are the maximum thickness of infiltration was approximately 50μm and the nodes remained unpopulated with cells after 14 days.

In summary, it has been demonstrated in this section that the small pores in the ES prevented cell infiltration while the large pores in the CES supported cell infiltration when fibroblasts were cultured under static conditions. The results provide the basis of combining the ES and the CES in a single BLES construct such that the ES can be used to separate the PEECs from the PESMCs while the CES can be used to support PESMCs infiltration. This is discussed in the next section.

6.5.3 Co-culture of PEECs and PESMCs on electrospun scaffolds (ES and BLES)

The fabrication of BLES was to mimic the structure of the oesophageal ECM. It consists of a dense ES layer, which mimics the basement membrane, and an open porous CES layer, which mimics the porous and fibrous structure in the loose connective tissue. In this experiment, PEECs and PESMCs were co-cultured on BLES to demonstrate the feasibility of using electrospun scaffold for oesophageal tissue engineering.

Figure 6.28 shows the porcine oesophageal cells. The PEECs exhibit characteristic cobblestone morphology in culture[203,204] (Figure 6.28(a)) while the PESMCs have the characteristic spindle-like morphology[205] (Figure 6.28(b)). These cells were co-cultured on the BLES and the ES (control) as described in Section 5.6.3.3.

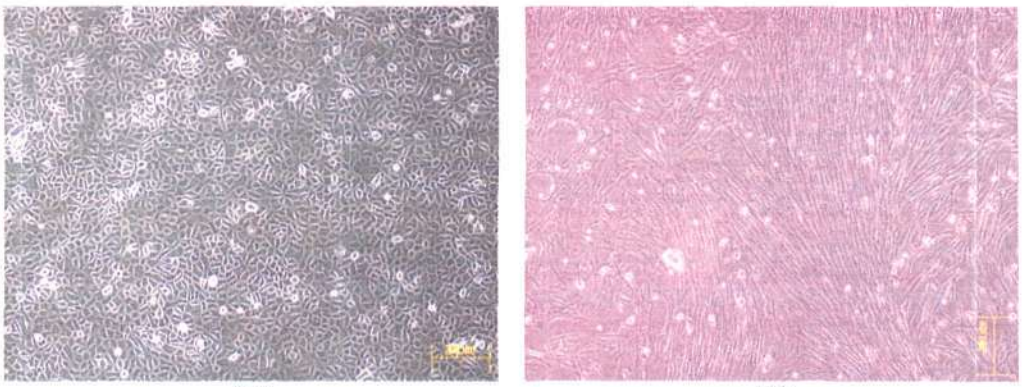

(a) (b)

Figure 6.28 Pictures of (a) PEECs and (b) PESMCs.

6.5.3.1 Co-culture of PEECs and PESMCs using ES

Figure 6.29(a) shows the cross-section of the cell-scaffold construct when the PEECs and PESMCs were co-cultured on the ES. There were 1 to 2 layers of PEECs on one side and 1 layer of PESMCs on the other side of the ES (Figure 6.29(a)). Both cell types attached and remained on the surface of the ES up to 2 months in culture. There was no cell infiltration by either cell type.

The results of the co-culture experiment using the ES show that the dense ES physically separated the two oesophageal cell types. This physical barrier could serve as a basement membrane for the PEECs. However, the ES also prevented the PESMCs from infiltrating the scaffold, which formed a monolayer of cells on the surface of the ES. This is not desirable as the muscularis mucosa in the mucosal-submucosal layers and the muscularis externa were shown to be three-dimensional

thick muscle bundles in our previous studies. When the construct was lifted to air-liquid interface, nutrient support for the PEECs depended solely on diffusion through the ES. The PEECs remained attached and viable, which is an indication that nutrient diffusion was not obstructed even at thickness of approximately 50μm. However, there was no evidence of stratification of the PEECs on the ES scaffold despite the air-liquid interface for 6 weeks, as the PEECs appear to have spread morphology.

6.5.3.2 Coculture of PEECs and PESMCs using BLES

The co-culture of PEECs and PESMCs on BLES is shown in Figure 6.29(b). There were approximately 2 layers of PEECs on the ES side and multiple layers of PESMCs on the CES side of the BLES (Figure 6.29(b)). Both cell types remained attached to the construct for the duration of the study. There was no cell infiltration by both cell types within the ES layer of the BLES. The PESMCs were observed to infiltrate the CES layer of the BLES to a depth of approximately 100μm. Further evidence is shown in Appendix E, which indicates that the PESMCs infiltrated from the outside of the CES layer, as can be observed from the shiny appearance of the fibers that are distributed among the PESMCs. The presence of the PEECs indicates that the ES layer and the infiltrated PESMCs did not obstruct nutrient diffusion after the construct was lifted into air-liquid interface. Several cuboidal epithelial cells could be seen at the surface of the ES. However, there was no observable stratification of the PEECs on the BLES after the construct was maintained in air-liquid interface culture for 6 weeks.

The results show good potential for using the BLES as a scaffold for oesophageal tissue engineering. The BLES design was effective in separating the two different

oesophageal cell types *in vitro*. The dense ES layer served as the basement membrane that supported the growth of the PEECs. It was effective in preventing the infiltrating PESMCs in the CES layer from advancing into the ES layer and physically separated the PEECs from the underlying PESMCs. It has been reported that an intact and continuous basement membrane is important in the development of a normal oesophageal epithelium.[27] A structurally compromised basement membrane would otherwise lead to hyperplastic and dyplastic epithelium and eventually, the development of squamous cell carcinoma. Hence, the role of the ES layer in the BLES is important.

The role of the CES layer in the BLES is discussed next. The CES layer, with larger pores, allowed full infiltration of the PESMCs. This is important in constructing the muscularis mucosa in the underlying connective tissues and also the muscularis externa. It has been shown in previous studies that the muscle bundles in the mucosal-submucosal tissue and the muscularis externa are thick and three-dimensional. Hence, in comparison, the CES layer is able to support PESMCs infiltration to build a three-dimensional muscular construct, whereas the ES, when used alone, had only one layer of muscle cells attached on its surface.

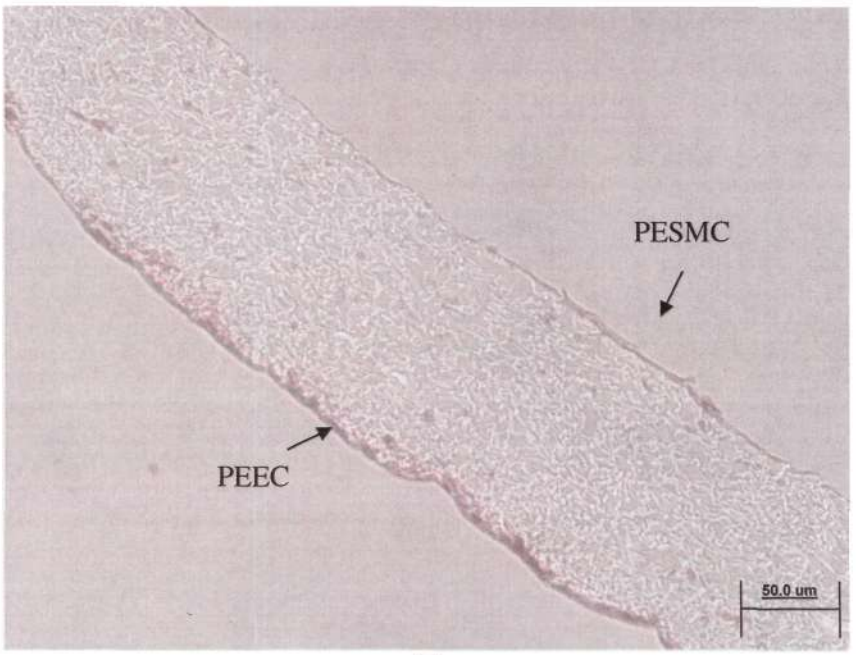

(a)

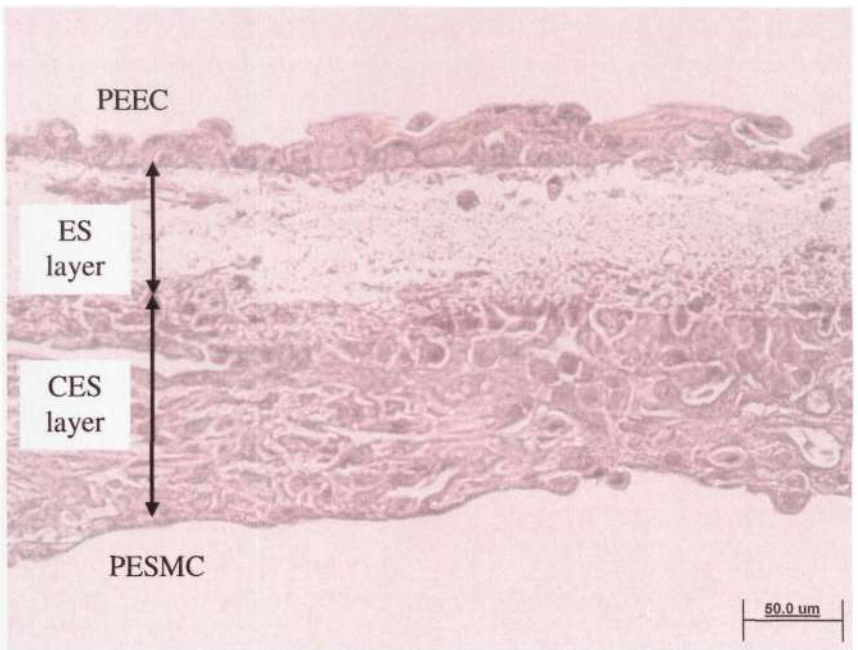

(b)

Figure 6.29 Pictures showing the co-culture of PEECs and PESMCs on electrospun scaffolds after 2 months. (a) Conventional ES used as control and (b) BLES.

It has been mentioned that the ES layer was fabricated to be 50μm thick for the purpose of visualization in histology. The actual thickness of the basement membrane is 10 times thinner than the ES layer in the BLES. However, based on the evidence provided in Figure 6.29(b), it can be observed that this thick ES layer did not obstruct nutrient diffusion as the PEECs continued to remain attached on the scaffold after 2 months. This indicates that diffusion of the nutrients was not obstructed by the thickness of the ES layer.

Ideally, the epithelium should differentiate and stratified on the bilayered construct. These were not observed in Figure 6.29. This might be due to the co-culture protocol, which did not promote the differentiation and stratification of the cells. More studies on refining the protocol need to be conducted to rectify this.

In summary, the design of the BLES is successful in mimicking the physical structure of the oesophageal ECM. The BLES consists of an ES layer that served as a physical barrier in separating PEECs from PESMCs and a CES layer that supported infiltration of the PESMCs. This same design can also be used for tissues, which consist of two or more cell types that require a basement membrane for separation. Examples of these tissues are the skin, which consists of keratinocytes supported on a basement membrane separated from the dermal fibroblasts and blood vessel, which consists of endothelial cells separated from the vascular smooth muscle cells.

6.6 *In vivo* subcutaneous implantation study

This section presents the results from the subcutaneous implantation study conducted for ES, CES and BLES. The objectives of this study are to evaluate *in vivo* cell infiltration, vascularization and foreign body response of the scaffolds.

6.6.1 Examples of observations that were made in the histochemical analysis

In this section, examples are provided to illustrate the features and cellular components that were present in the histochemical analysis of the explants. The tissues were sectioned and stained with hematoxylin and eosin, Masson's Trichrome and Sirius red stains. The important observations are cell infiltration, vascularization and foreign body response that includes capsule formation, presence of macrophages and foreign body giant cells.

Figure 6.30(a) shows the H&E stained picture of a CES explanted 28 days post-operative. Hematoxylin dye stains nuclei proteins dark purple while eosin dye stains cytoplasm in tissues pink. The approximate boundary for the CES implant and the foreign body capsule is indicated. The foreign body giant cells are identified as multi-nucleated cells as they are formed by the fusing of many macrophages. The fibroblasts are identified as spindle-shaped cells with a spread out morphology for the nucleus as shown in the Figure 6.30(a). The formation of capillary is identified by the presence of non-nucleated red blood cells as shown in Figure 6.30(a). Figures 6.30(b) and (c) show the Masson's Trichrome and Sirius red stained pictures of the same tissue explant respectively. The collagen fibers are stained blue by the Trichrome stain and red by the Sirius red stain. Collagen fibers are present within the foreign

body capsule and are also formed by the infiltrating cells (such as fibroblasts) within the scaffold as shown in Figures 6.30(b) and (c).

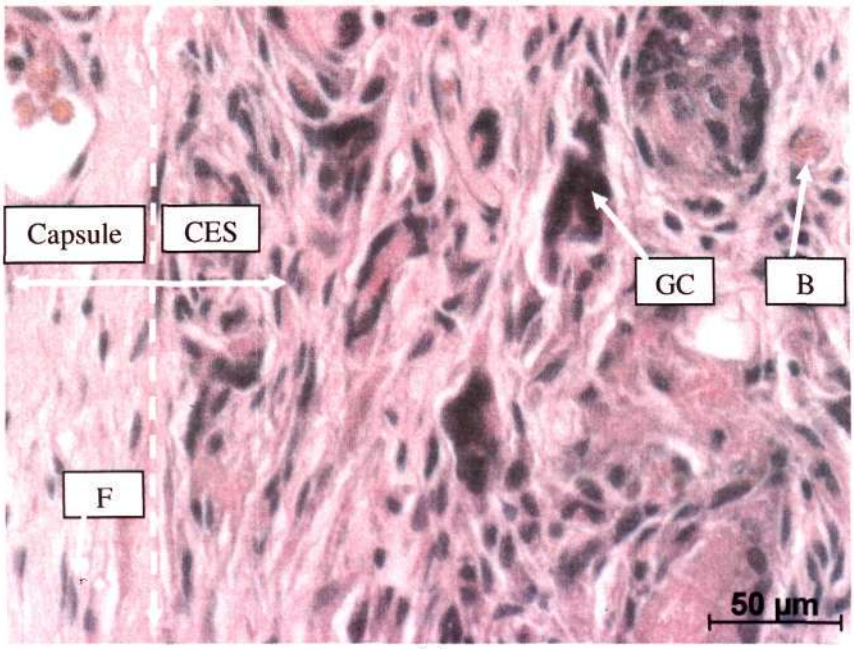

(a)

Figure 6.30 (a) H&E stained picture of a CES explant at 28 days. F : Fibroblasts, GC : Foreign body giant cells and B : Capillary formation.

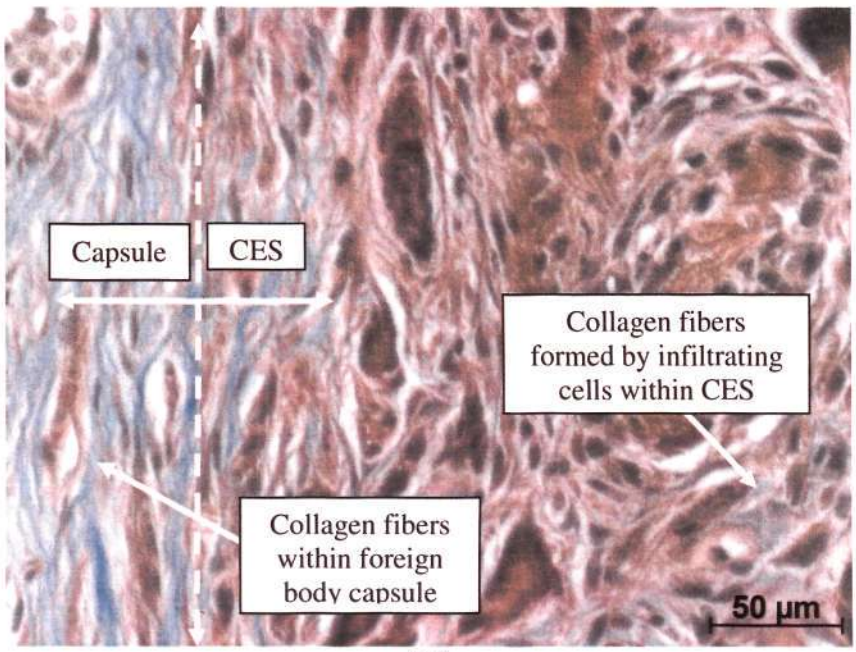

(b)

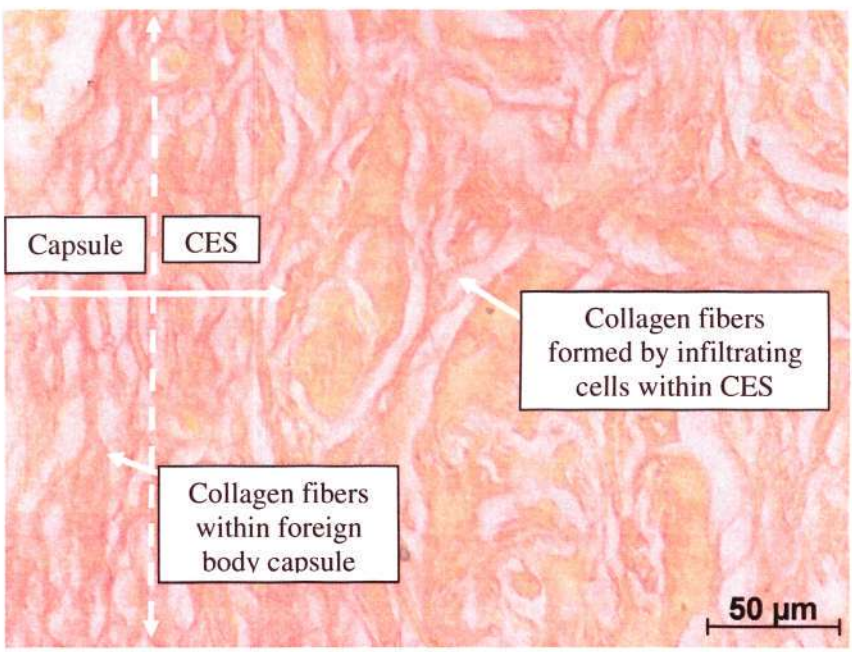

(c)

Figure 6.30 (b) Masson's trichrome stained picture and (c) Sirius red stained picture of the same explant a few microtome sections away.

6.6.2 Histochemical analysis of the ES and CES explants

Results of the histochemical analysis of the explants are presented and discussed in this section. The histochemical stained pictures are first shown at high magnification to illustrate *in vivo* cell infiltration and vascularization. Quantitative assessments of cell infiltration are carried out by measuring the depth of cell infiltration and counting the cell nuclei within the implanted scaffolds. The foreign body response of both ES and CES are then described and compared. A collage of the histochemical stained pictures at low magnification is included at the end of this section to show the histological response of the ES and CES in the 56-day implantation study.

6.6.2.1 Cell infiltration in ES and CES

At day 14, cell infiltration is limited as individual isolated cells are seen within the ES (Figure 6.31(a)). At day 28, localized cell infiltration is observed from the periphery of the ES at a few locations (Figure 6.31(b)). Sirius red stained pictures shows more collagen fibers are deposited at these localized areas where cell infiltration is observed (Figure 6.31(c)). At day 56, the majority of the ES remains unpopulated, with individual isolated cells scattered within the ES (Figure 6.31(d)).

The histochemical results presented here show that ES, with its small pores, limited cell infiltration *in vivo*. The localized cell infiltration observed at day 28 might be due to weaknesses in the structure of the ES. These weaknesses might have been caused by the motion of the animals when the scaffolds are implanted. Overall, the ES specimens have limited cell infiltration as shown in Figure 6.31.

In contrast, the CES are completely infiltrated with cells for 2 out of the 3 specimens implanted by day 14 (Figure 6.32(a)). The remaining CES is partially infiltrated with cells as shown in Figure 6.32(b). By day 28 and 56, all CES specimens are completely infiltrated with cells (Figure 6.32(c) and (d)).

The histochemical results of the CES explants show that the large pores of the CES supported cell infiltration *in vivo*. The infiltrated cells consist of fibroblasts, macrophages and foreign body giant cells. These cells are part of the foreign body response, which will be addressed later.

Results from the histochemical analysis have shown qualitatively that pore size of the scaffold is important in supporting in vivo cell infiltration. The large pores of CES allowed better cell infiltration as compared to the ES. Further comparisons are made quantitatively by measuring the depth of cell infiltration and counting the number of cell nuclei within the scaffolds. The depth of cell infiltration measures how far the cells have infiltrated the thickness of the scaffold, while the nuclei counting measures the number of infiltrated cells within the scaffolds.

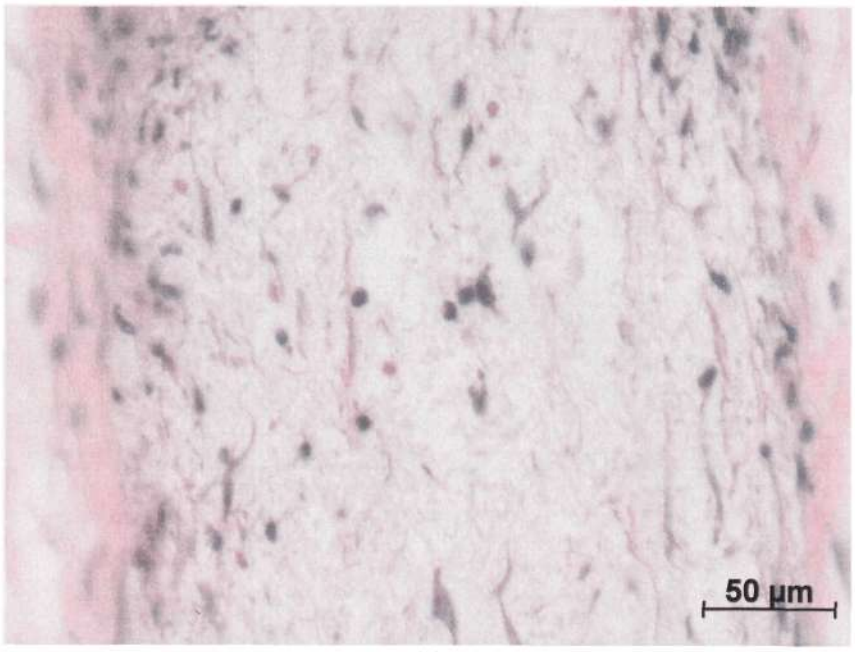

(a)

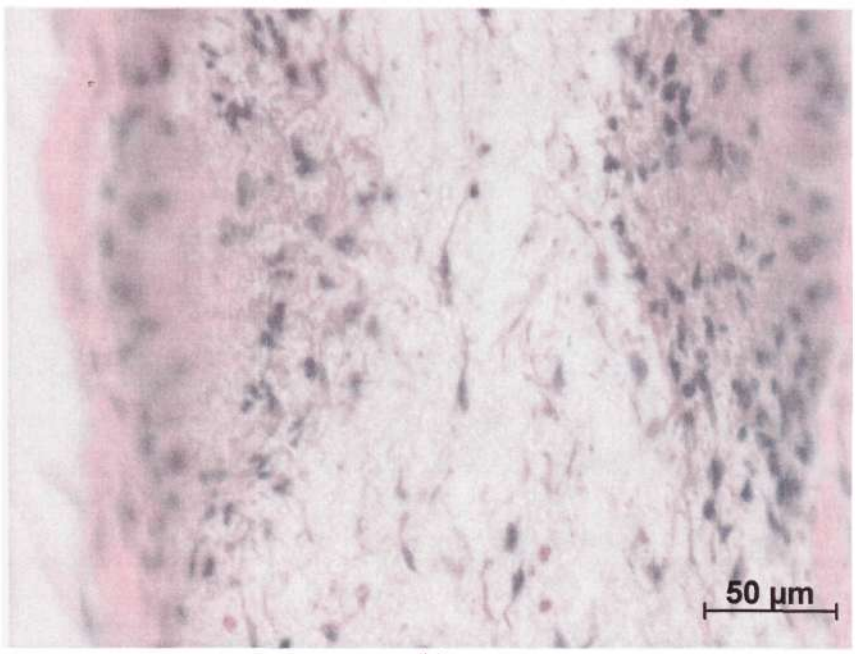

(b)

Figure 6.31 High magnification H&E stained pictures of (a) implanted ES at day 14 and (b) implanted ES at day 28.

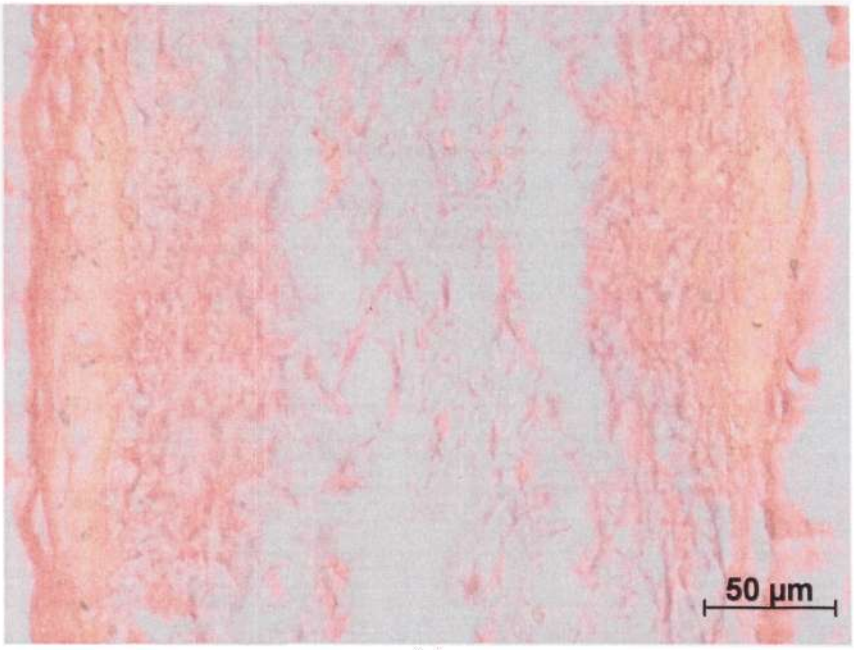

(c)

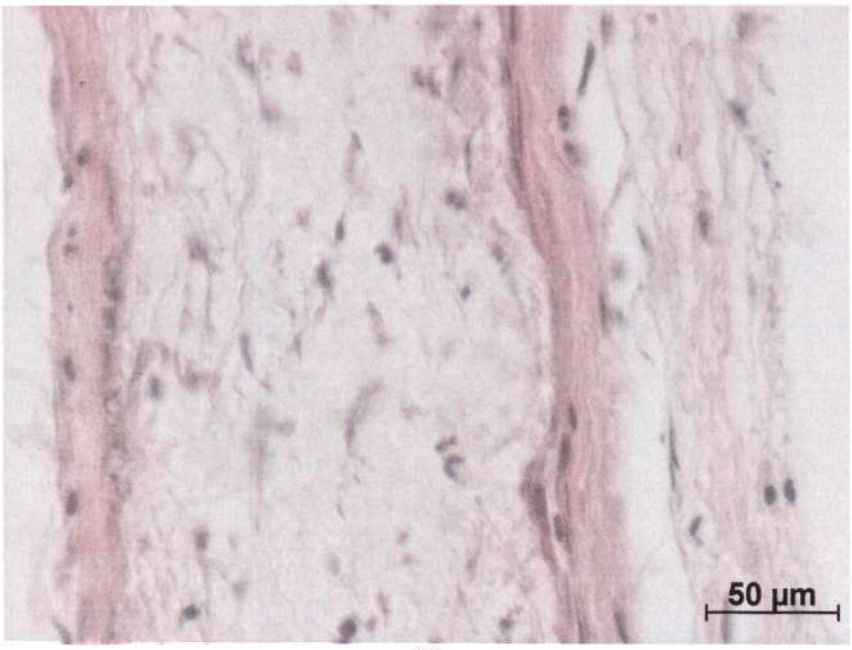

(d)

Figure 6.31 High magnification of (c) Sirius red stained picture of implanted ES at day 28 and (d) H&E stained picture of implanted ES at day 56.

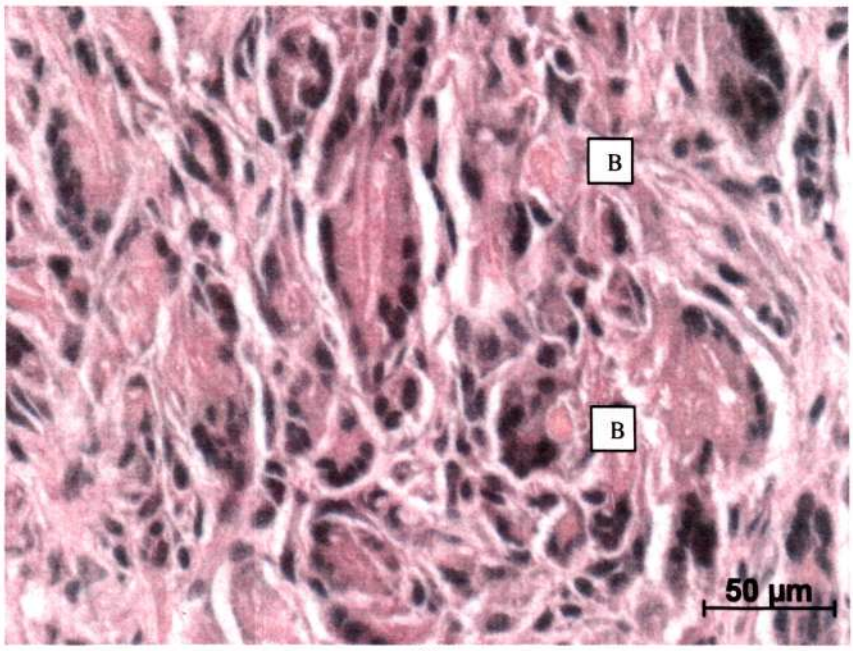

(a)

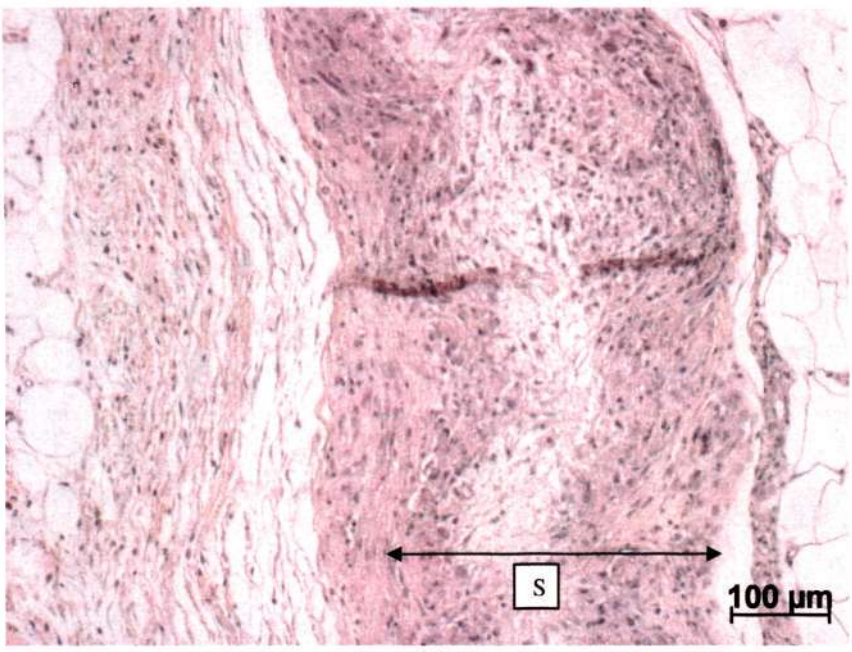

(b)

Figure 6.32 High magnification of (a) H&E stained picture within implanted CES at day 14. (b) H&E stained picture of partially infiltrated implanted CES specimen at day 14.

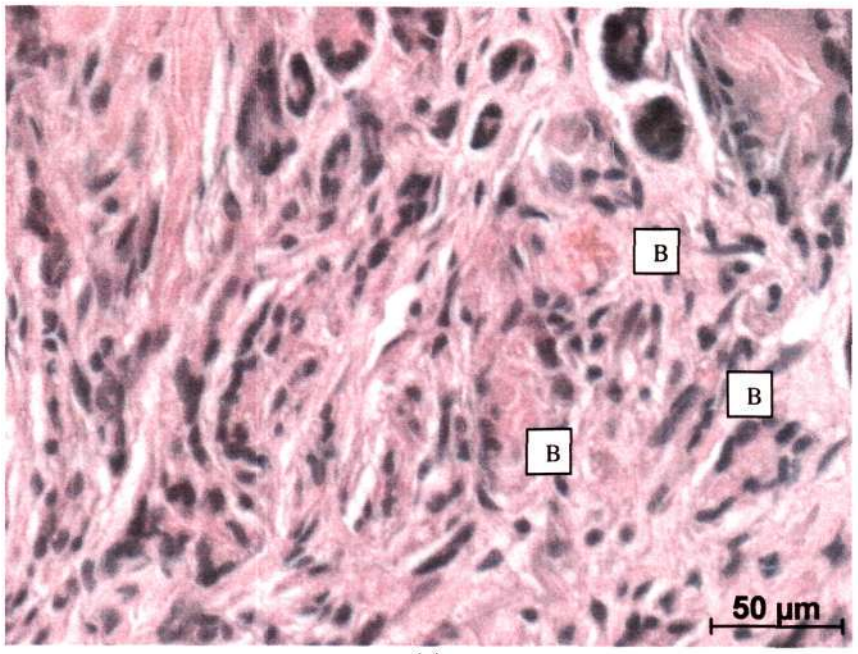

(c)

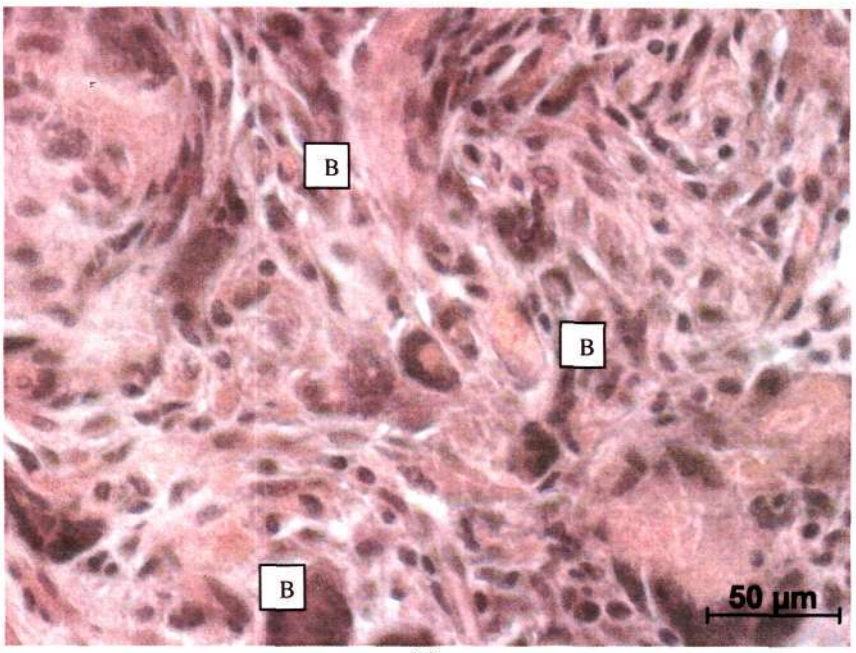

(d)

Figure 6.32 High magnification of (c) H&E stained picture within implanted CES at day 28. (d) H&E stained picture within implanted CES at day 56.

Figure 6.33 shows the depth of cell infiltration for the implanted ES and CES specimens up to 56 days. There was poor cell infiltration into the ES with cells predominantly limited to the periphery observed at all three time points. The maximum depth of cell infiltration for the ES was 36 ± 9% of scaffold thickness at day 56. This measured depth of cell infiltration arises from the presence of individual isolated cells within the ES as observed in the histochemical analysis. In contrast, the depth of cell infiltration was 78 ± 15% at day 14 and 100% of scaffold thickness for the CES at day 28 and 56, which were significantly higher than the ES at all three time points ($p<0.01$). The measured values for depth of cell infiltration were normalized to the thickness of the scaffolds as the CES (~400μm) used in the experiments were thicker than the ES (~200μm). Despite being thicker, there was still significantly better cell infiltration in the CES as compared to the ES.

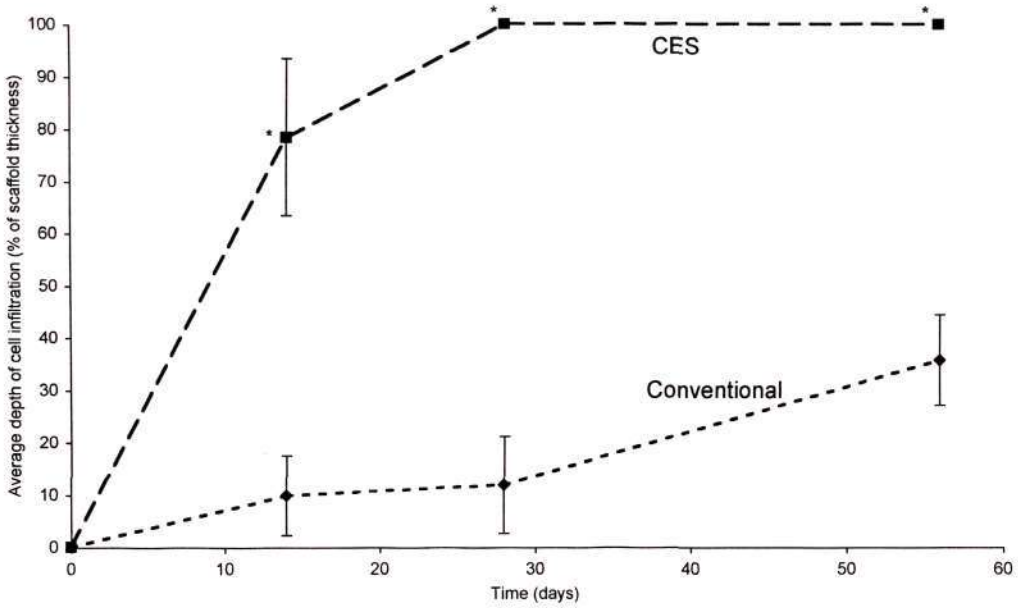

Figure 6.33 Comparison of the depth of cell infiltration in the conventional ES and CES at various time points. Depth of cell infiltration for all CES specimens is 100% of its thickness at 28 and 56 days, hence the standard deviations for these data are zero. * denotes inter-group significant difference at the same time point ($p<0.01$). Mean ± SD. n=3.

Figure 6.34 shows the results from the quantification of nuclei of the infiltrated cells within the implanted scaffolds. The analysis does not take into account the type of cell infiltrating the scaffolds. It should be noted that the area of nuclei occupied by a foreign body giant cell is larger than a fibroblast. However, since foreign body giant cells resulted from the fusing of many macrophages, the large area measured represents the number of individual macrophages that infiltrated the scaffolds before fusing to form giant cells. Based on the total area of nuclei of the infiltrated cells, the CES has approximately 4 times the number of infiltrated cells compared to the ES at all three time points ($p<0.01$). The small area of nuclei measured for the ES specimen also indicates that although the ES has cells infiltrating the thickness of the scaffold, as reflected in the depth of infiltration, these cells are isolated individual cells.

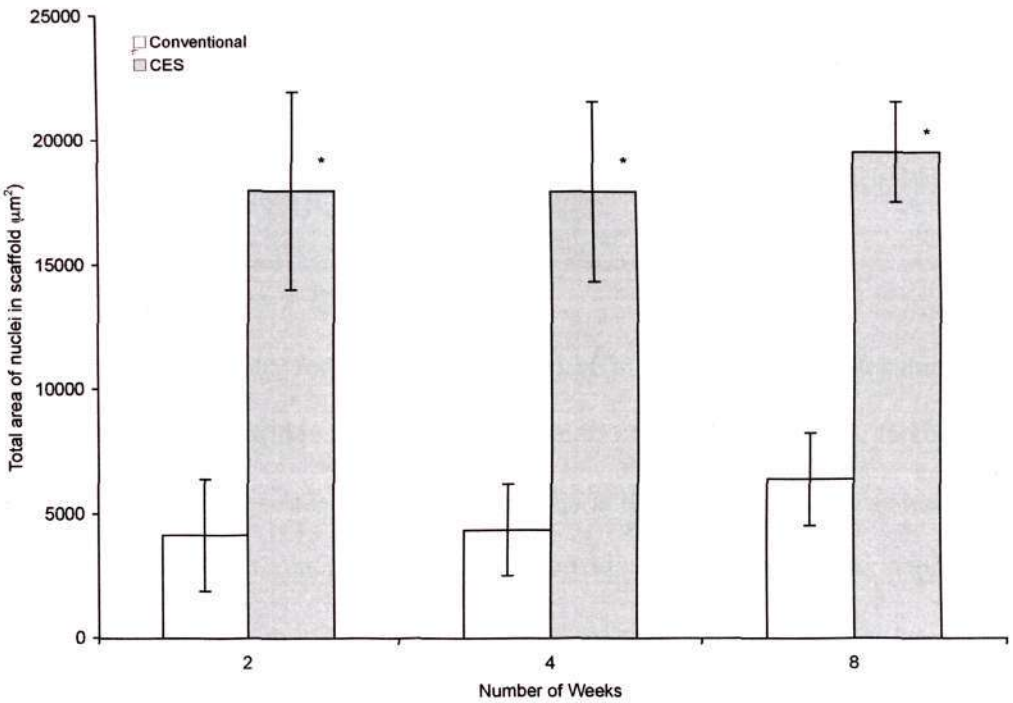

Figure 6.34 Comparison of the number of infiltrated cells within the conventional ES and CES at various time points. The total area of nuclei that are within the scaffolds represents the total number of infiltrated cells. * denotes inter-group significant difference at the same time point ($p<0.01$). Mean ± SD. n=3.

The results presented in this section indicate a significant improvement of the CES over the ES in terms of *in vivo* cell infiltration. The small pores of the ES prevented cell infiltration *in vivo*. Both the depth of cell infiltration and the number of infiltrated cells remained significantly lower as compared to the CES for up to 56 days. In contrast, cells infiltrated the entire CES by day 28, indicating the large interconnected pores allowed cell migration from the periphery to the bulk of the CES when they were implanted in the host. The porous walls of the pores, shown in Figure 6.20(d), allow cells to penetrate through them. The presence of the porous walls in an important feature in the CES as it maintains interconnectivity between neighboring pores, allows nutrients transportation and cell infiltration throughout the CES. These *in vivo* results clearly show that the cryogenic electrospinning technique successfully overcomes the inherent small pores of the ES, while maintaining the fibrous features and pore interconnectivity within the electrospun scaffold, to enable host cells to infiltrate and populate a thick construct.

6.6.2.2 Vascularization in ES and CES

The absence of capillary formation in Figures 6.31(a), (b) and (d) indicates that there is no vascularization within the ES for the explants at day 14, 28 and 56. In contrast, formation of capillary is observed within the CES at the three time points as indicated in Figure 6.32(a), (c) and (d). Intraluminal red blood cells are present within the capillaries, indicating that the blood vessels formed within the CES are integrated with the host vasculature system.

The presence of blood vessels within the CES *in vivo* allows a thick cell-scaffold construct to be supported using the CES. This could also account for the greater depth

of cell infiltration in CES observed *in vivo* (approximately 400μm) compared to under static culture conditions *in vitro* (approximately 50μm). The results also indicate that these blood vessels are integrated with the host vasculature system, which is a requirement for the successful biointegration of the construct. This finding can be attributed to the large pore size of the CES compared to conventional electrospun scaffolds, as other studies have observed that optimal pore sizes between 5 to 35μm are needed for inducing angiogenesis.[56,57] Moreover, it is postulated that the macrophages within the CES produced angiogenic factors that stimulated vacularization.[206] The presence of functional blood vessels within the CES is vital for nutrient and waste transfer *in vivo* and allows for thick cell-scaffold constructs, thus overcoming a major limitation of conventional electrospun scaffolds.

6.6.2.3 Foreign body response of ES and CES

Figure 6.35 shows a collage of the histochemical stained pictures obtained for the ES explants. At day 14, a focal foreign body reaction is observed at the tissue-scaffold interface (Figure 6.35(a)). The fibrous capsule is thin with fibroblasts scattered within loose collagenous matrices (Figure 6.35(d)). The Sirius red stained picture shows oriented collagen fibers that are packed loosely in the capsule and limited strands of collagen randomly dispersed within the ES structure (Figures 6.35(g)). The histological responses at day 28 and 56 are similar to day 14. Foreign body reaction is observed at the tissue-scaffold interface (Figures 6.35(b) and (c)). At day 56, a dense and thin capsule is observed at the scaffold-tissue interface (Figures 6.35(f) and (i)).

Figure 6.36 shows a picture collage of the histochemical analysis obtained for the CES explants. At day 14, normal foreign body reaction with fibroblasts, macrophages

and FBGCs is observed within the CES (Figure 6.32(a) and 6.36(a)). Trichrome staining shows that the fibrous capsule is thin, with fibroblasts scattered within the collagenous matrix (Figure 6.36(d)). The collagen fibers within the CES are transmural as shown by the Sirius stained picture (Figure 6.36(g)). The histological responses at day 28 and day 56 are similar to that of day 14. At day 28 and 56, the FBGCs within the CES contain many nuclei and appear to be mature (Figures 6.32(c) and (d)). The fibrous capsule remains loose and thin (Figures 6.36(e) and (f)). Sirius red staining shows transmural collagen within the CES for both day 28 and day 56 CES explants (Figures 6.36(h) and (i)).

The histochemical analysis shows that the foreign body reaction occurred at the tissue-scaffold interface for the ES and within the scaffold for the CES. This difference is due to the difference in pore size between the ES and the CES. The small pores of the ES limited cell infiltration. Hence, the host cells responsible for the foreign body reaction were largely limited at the periphery of the scaffold. In contrast, the large pores of the CES allowed these host cells to infiltrate the bulk of the scaffold. Hence, the foreign body reaction could be observed within the CES.

In summary, the results from the histochemical analysis of the ES and CES explants show that the small pores of ES limited *in vivo* cell infiltration and prevented vascularization whereas the large interconnected pores of the CES allowed *in vivo* cell infiltration and vascularization. These results provide the basis behind the use of the BLES as a scaffold for tissue engineering of the oesophagus. The results for the *in vivo* studies of the BLES are presented in the next section.

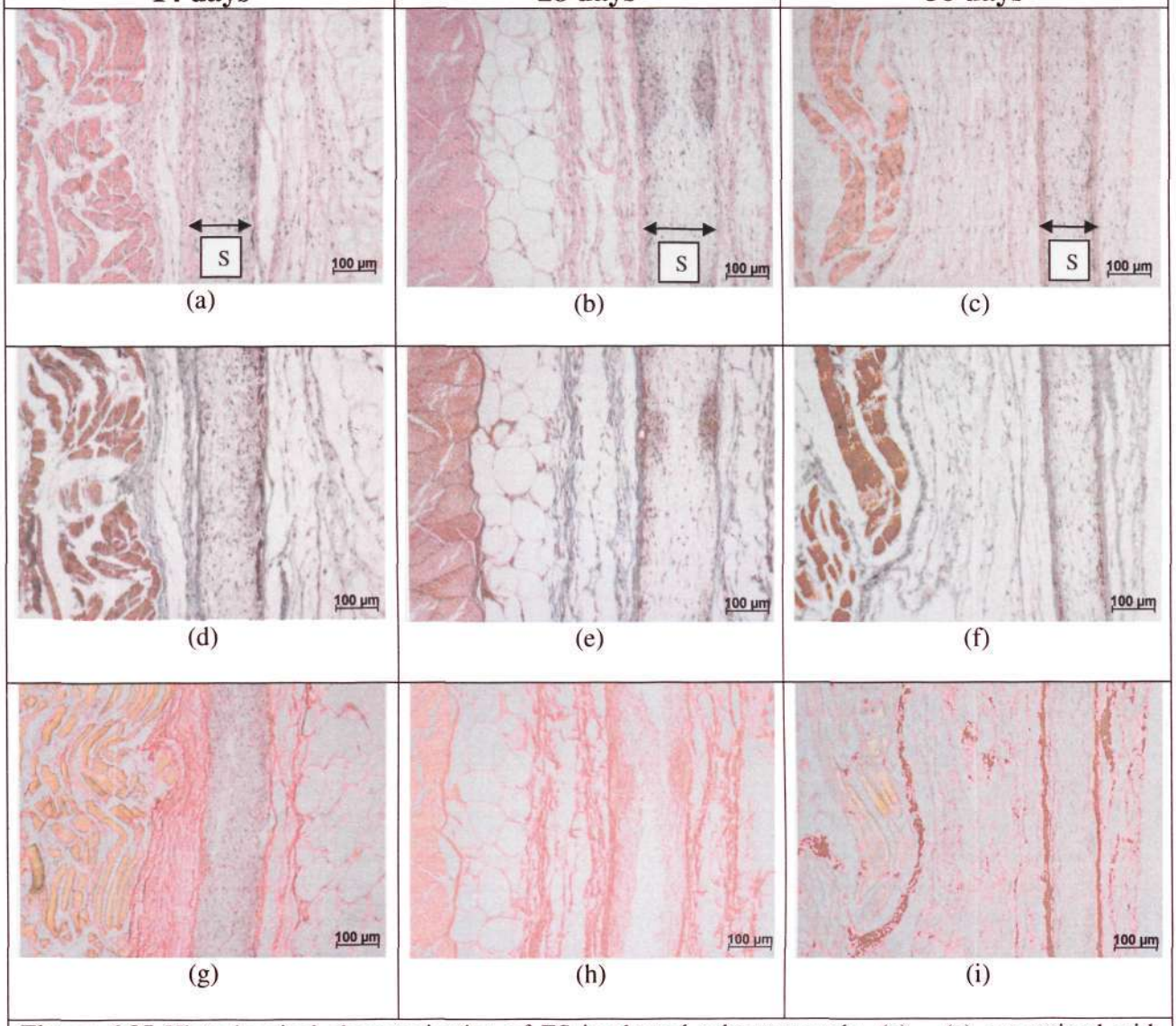

Figure 6.35 Histochemical characterization of ES implanted subcutaneously. (a) – (c) are stained with H&E, (d) – (f) are stained with Masson's Trichrome and (g) – (i) are stained with Sirius red. (S: Scaffold)

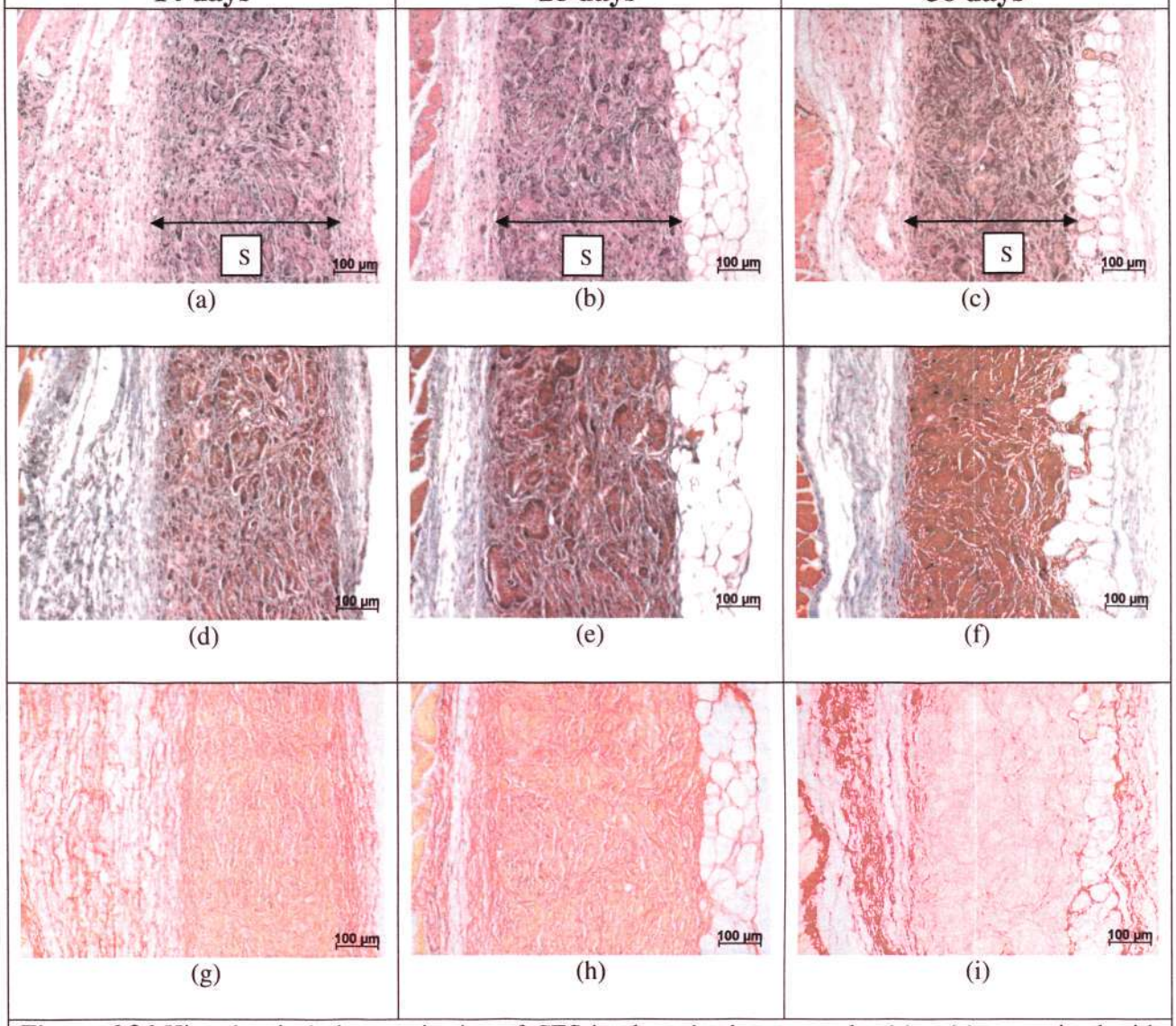

Figure 6.36 Histochemical characterization of CES implanted subcutaneously. (a) – (c) are stained with H&E, (d) – (f) are stained with Masson's Trichrome and (g) – (i) are stained with Sirius red. (S: Scaffold)

6.6.3 *In vivo* study of BLES

This experiment was conducted to evaluate the feasibility of using the BLES for *in vivo* scaffold applications. The BLES consists of an ES layer, which is intended to limit cell infiltration and a CES layer, which is intended to support cell infiltration and vascularization to construct thick tissue replacements. The BLES was implanted in two orientations, BLDU (BLES with ES layer facing up) and BLDD (BLES with ES layer facing the underlying muscle) to study the effect of orientation on the histological response of the implanted BLES.

6.6.3.1 Cell infiltration in ES and CES layers of BLES (BLDU and BLDD)

At day 14, cell infiltration is limited in the ES layer of the BLDU with isolated cells scattered within the layer (Figure 6.37(a)). There is partial cell infiltration within the CES layer. By day 28 and 56, cells have completely infiltrated the CES layer of the BLDU whereas infiltration is limited for the ES layer (Figure 6.37(b) and (c)). The BLDD shows similar outcome. Cell infiltration is limited to the periphery in the ES layer up to 28 days (Figure 6.37(d) and (e)). At 56 days, more isolated cells can be seen within the ES (Figure 6.37(f)). The CES is partially infiltrated at 14 days (Figure 6.37(d)) and become completely infiltrated with cells at day 28 and 56 (Figure 6.37 (e) and (f)).

The results from the histochemical analysis are consistent in terms of cell infiltration in ES and CES layers with the individually implanted ES and CES respectively discussed in the previous section. Despite being in the same subcutaneous pocket, there was significantly better cell infiltration in the CES layer than the ES layer from

day 14 to 56. The histochemical analysis does not show any difference in cell infiltration in the two orientations, BLDU and BLDD.

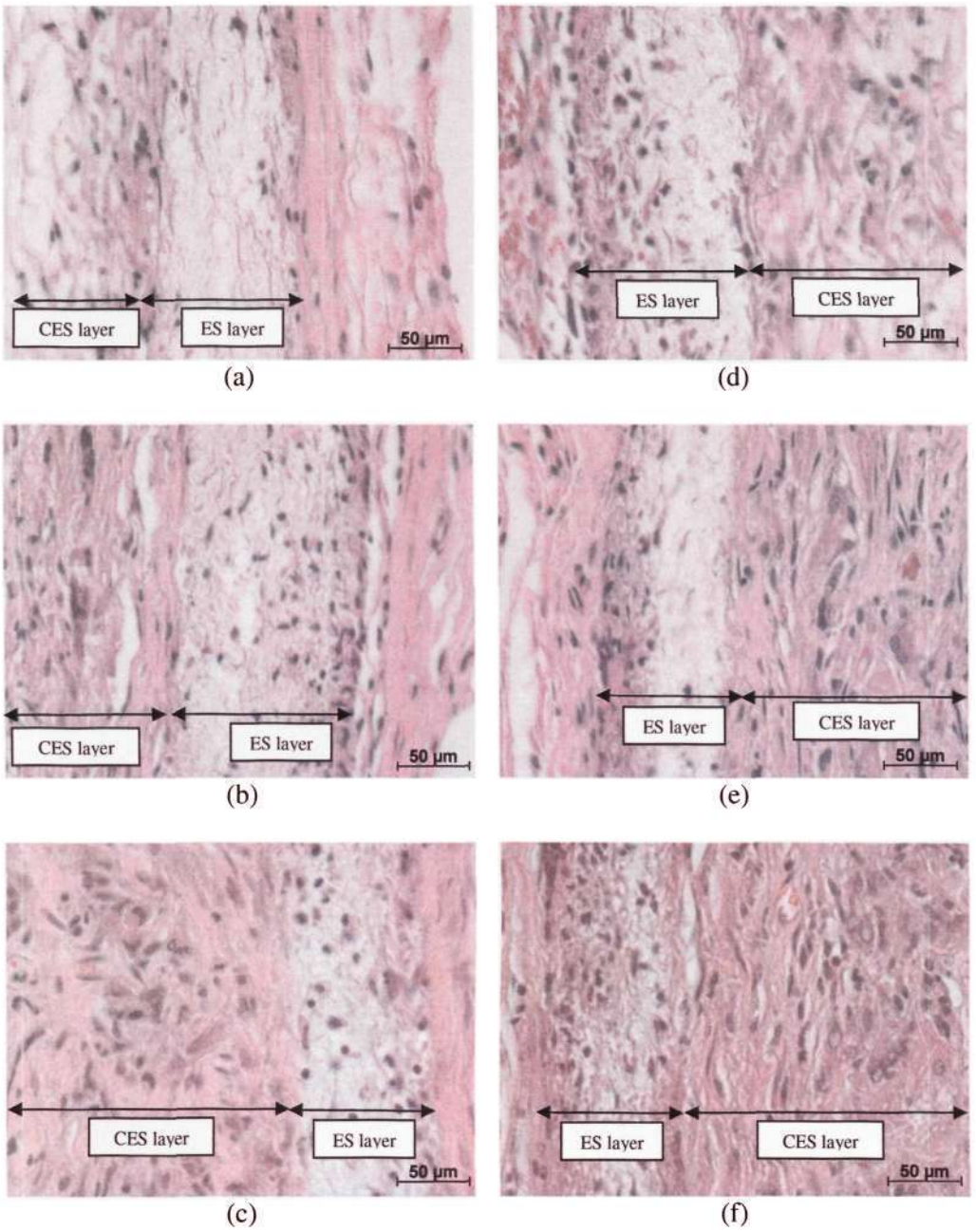

Figure 6.37 H&E stained pictures of (a) BLDU at 14 days, (b) BLDU at 28 days, (c) BLDU at 56 days, (d) BLDD at 14 days, (e) BLDD at 28 days and (f) BLDD at 56 days.

BLDU: BLES with ES layer facing up.
BLDD: BLES with ES layer facing underlying muscle.

The results for the depth of cell infiltration are shown in Figure 6.38. The depth of cell infiltration of the CES layer was significantly larger than the ES layer at all three time points (both BLDU and BLDD) ($p<0.01$). At day 14, the depth of cell infiltration for the CES layer in the BLDU and BLDD was $46 \pm 7\%$ and $50 \pm 20\%$ respectively. The depth of cell infiltration for the CES layer in BLDU and BLDD increased to 100% at day 28 and 56. The maximum depth of cell infiltration for the ES layer was $40 \pm 20\%$ for BLDU (at day 28) and $50 \pm 20\%$ for BLDD at (day 56).

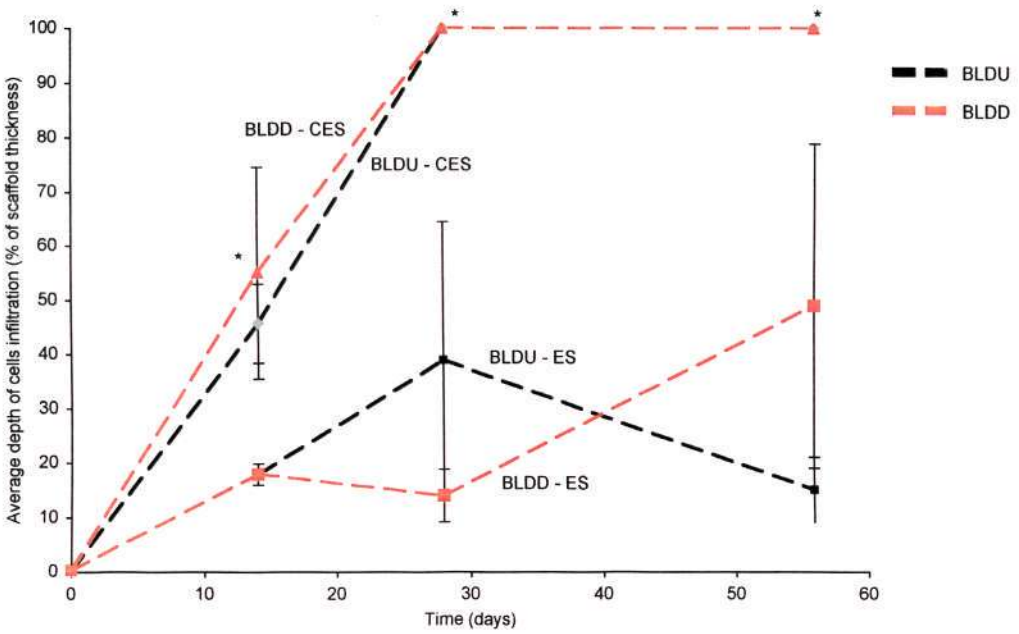

Figure 6.38 Comparison of the depth of cell infiltration in the ES layer and CES layer of BLES at various time points. Depth of cell infiltration for all CES layers is 100% of its thickness at 28 and 56 days, hence the standard deviations for these data are zero. * denotes significant difference between the CES layers and ES layers for all specimens at the same time point ($p<0.01$). Mean ± SD. n=3.

The large values measured for the depth of infiltration of the ES layer in BLDU and BLDD was largely due to the presence of localized areas that are infiltrated with cells or the presence of isolated individual cells observed within the ES layer. Localized areas that are infiltrated with cells might be due to the weaknesses in the ES structure discussed earlier. Overall, cell infiltration remains limited in the ES layer as compared

to the CES layer. The depth of cell infiltration at day 14 for the CES layers in BLDU and BLDD is lower than the CES that was individually implanted (presented in previous section). Although the difference is not significant, this comparison suggests that the lower depth of cell infiltration in the CES layer might be due to the infiltration of cells from only one exposed scaffold-tissue interface of the BLES, since the other exposed surface is obstructed by the ES layer. Hence, depth of cell infiltration is lower compared to the individually implanted CES, which has two exposed scaffold-tissue interfaces to the host.

The results for the quantification of nuclei of the infiltrated cells within the implanted scaffolds are shown in Figure 6.39. Based on the total area of nuclei of the infiltrated cells, the CES has approximately twice the number of infiltrated cells compared to the ES after 56 days (1.8 times for BLDU and 2.4 times for BLDD) ($p<0.05$). At 2 weeks, the CES in the BLDU has significantly more cell nuclei than the CES in the BLDD (approximately 2.3 times more). There is no significant difference in cell infiltration in the layers within the BLDU and BLDD with regards to the orientation of the BLES in the subcutaneous pocket.

Both sets of result from measuring depth of cell infiltration and quantification of cell nuclei indicate that although the cells penetrated the ES layer, the number of cells present within the ES layer is less than the CES layer. In contrast, large number of cells completely infiltrated the CES. The stark difference in cell infiltration between the ES and CES layers is due to their differences in pore size. The results derived from the implantation of the BLES are especially significant as both ES and CES

layers are implanted in the same subcutaneous pocket and thus, the *in vivo* conditions are very similar.

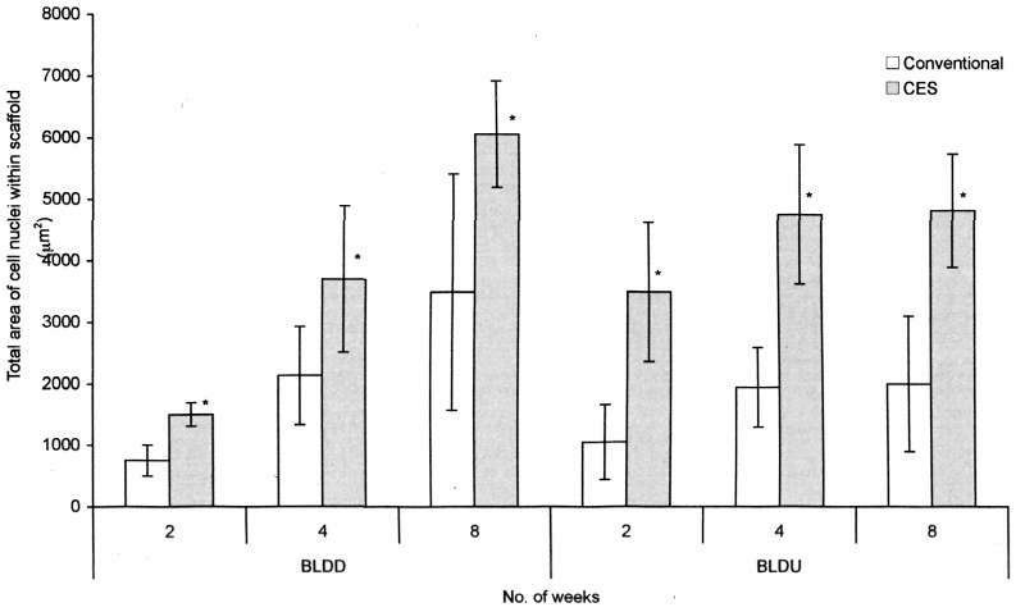

Figure 6.39 Comparison of the number of infiltrated cells within the conventional ES and CES of the BLES at various time points. The total area of nuclei that are within the scaffolds represents the total number of infiltrated cells. * denotes inter-group significant difference at the same time point ($p<0.05$). Mean ± SD. n=3.

The results on cell infiltration presented in this section shows that the BLES is effective for its intended application as a bilayered scaffold for oesophageal regeneration. When combined in a single construct, the ES and CES layers served their intended functions. The ES layer, with its small pores, prevented *in vivo* cell infiltration while the CES layer supported cell infiltration and vascularization. Such a construct can thus be used to separate different cell types and help organize the oesophageal cells *in vivo*.

6.6.3.2 Vascularization in ES and CES layers of BLES (BLDU and BLDD)

The ES layers in the BLDU and BLDD have no vascularization for all three time points (Figure 6.37). The CES layers have capillary formation at day 28 and 56 for the BLDU and at all three time points for the BLDD (Figure 6.37).

In Section 6.6.2, it was shown that there was a marked difference in the ability of the CES and ES to promote vascularization *in vivo* and this was demonstrated again in the BLES implantation (Figure 6.37). The inability of the ES layer to support vascularization has to be taken into account when designing the BLES. The ES layer has to be sufficiently thick and dense to act as a physical barrier for cell infiltration. However, it cannot be so thick that the entire ES layer is encapsulated as an avascular acellular construct. The CES layer, on the other hand, supports vascularization and is thus a potential candidate as a scaffold for regeneration of the vascularized muscle tissues of the oesophagus.

6.6.3.3 Foreign body response of the BLES (BLDU and BLDD)

Figures 6.40 shows a collage of the histochemical stained pictures obtained for the BLDU (BLES with ES layer facing up) explants. At day 14, a focal normal foreign body reaction consisting of fibroblasts, macrophages and FBGCs is observed at the scaffold-tissue interface on the ES side and partially within the CES layer (Figure 6.40(a)). There is partial cell infiltration with collagen deposition within the CES layer as shown by the Trichrome and Sirius Red stains (Figures 6.40(d) and (g)). Under high magnification at the two scaffold-tissue interfaces, it can be observed that the collagen capsule adjacent to the ES layer is denser than the capsule adjacent to the CES layer (Figures 6.41(a) and (b)). By day 56, the foreign body response consisting

of fibroblasts, macrophages and FBGCs is observed at the ES-tissue interface and within the CES layer. The density of the thin fibrous capsule at the CES-tissue interface remains low. Under high magnification, a dense collagen capsule can be observed at the ES-tissue interface and the ES-CES interface as shown by the Sirius Red stain (Figure 6.41(c)).

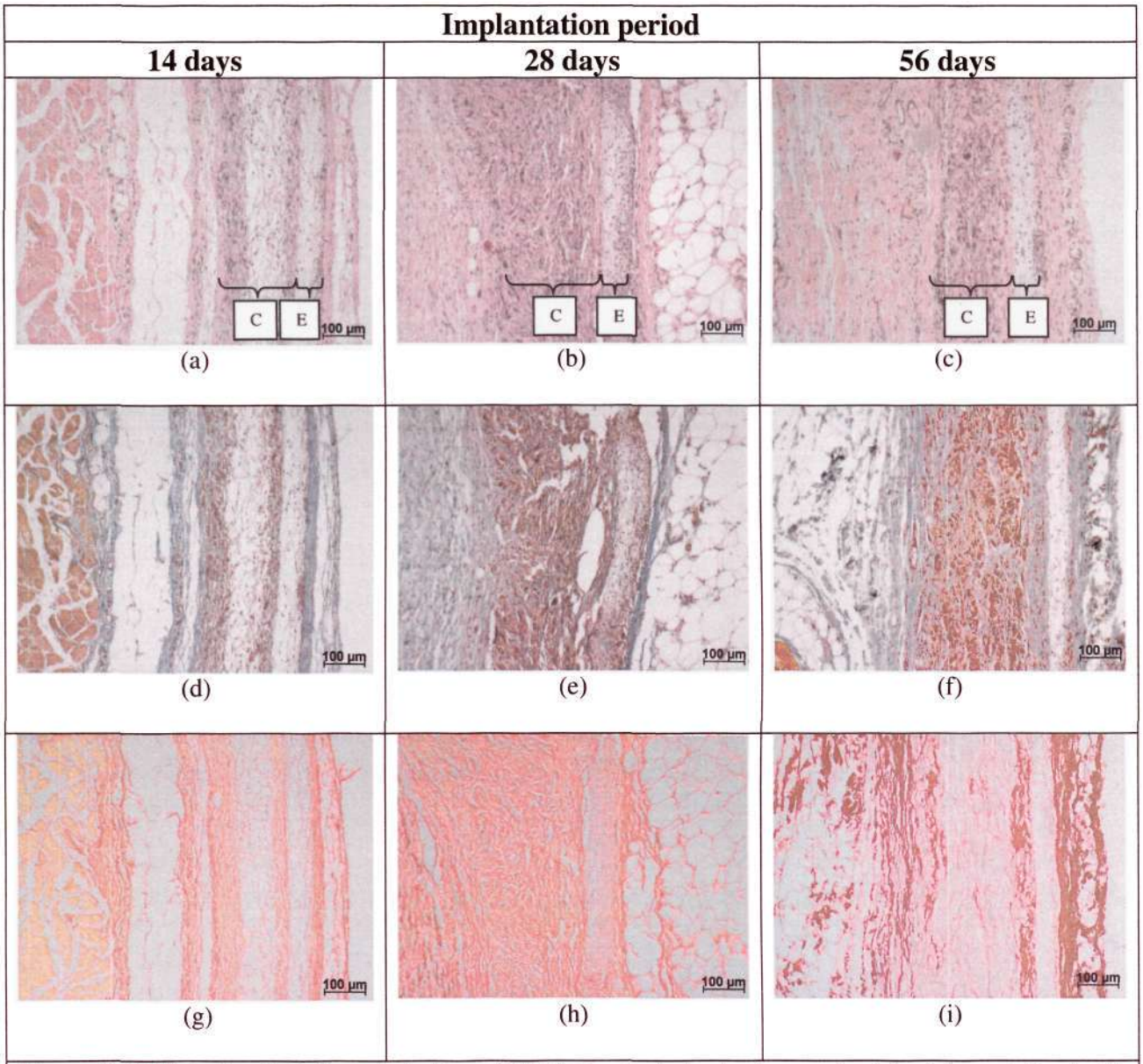

Figure 6.40 Histochemical characterization of BLDU implanted subcutaneously. (a) – (c) are stained with H&E, (d) – (f) are stained with Masson's Trichrome and (g) – (i) are stained with Sirius red.
(C: Cryogenic electrospun scaffold layer, E: conventional electrospun scaffold layer)
BLDU: BLES with ES layer facing up.

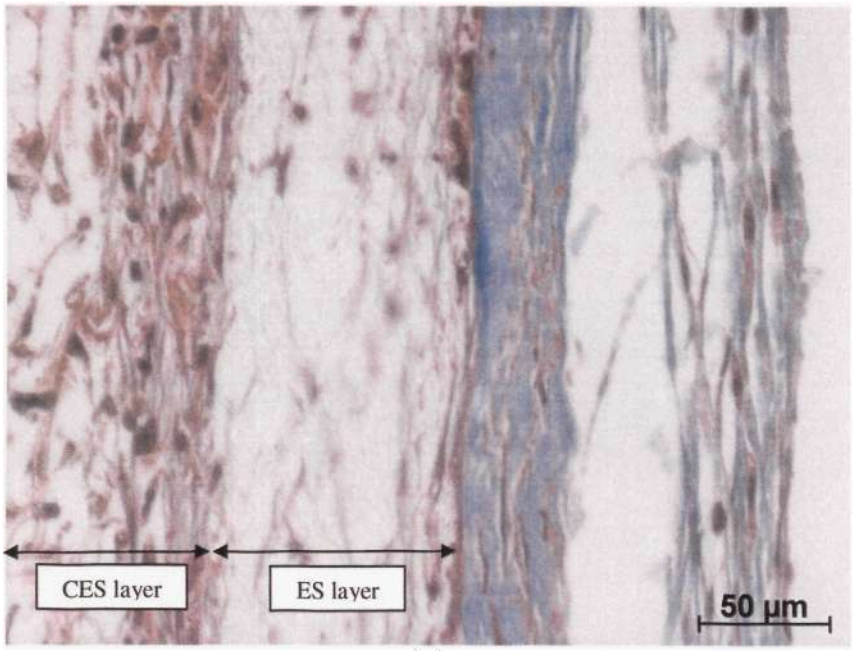

(a)

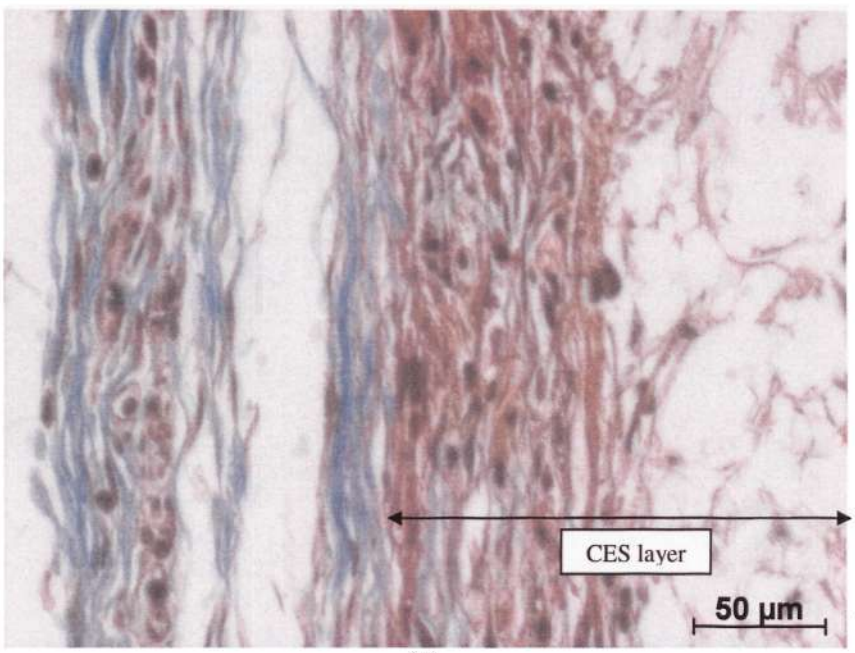

(b)

Figure 6.41 Masson's Trichrome stained pictures showing different capsule density on both sides of the BLDU at day 14. (a) ES-tissue interface and (b) CES-tissue interface.
BLDU: BLES with ES layer facing up.

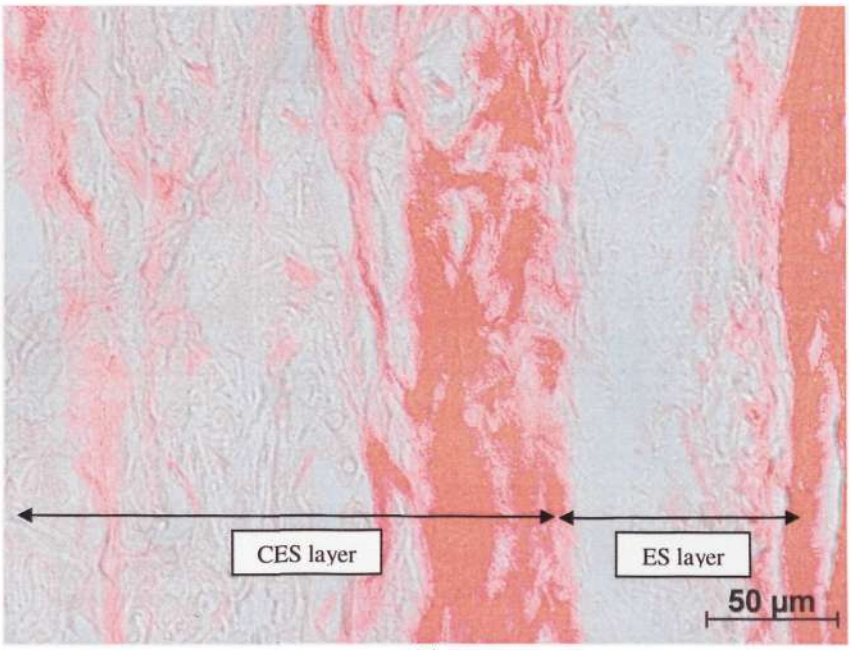

(c)

Figure 6.41 (c) Sirius red stained picture of the ES-CES interface of BLDU showing the dense fibrous capsule on both sides of the ES layer at day 56.

Figures 6.42 shows a collage of the histochemical stained pictures obtained for the BLDD explants. The histological response of the BLDD is similar to the BLDU. At day 14, a focal normal foreign body reaction consisting of fibroblasts, macrophages and FBGCs is observed at the scaffold-tissue interface on the ES side and partially within the CES layer (Figure 6.42(a)). There is partial cell infiltration with collagen deposition within the CES layer as shown by the Trichrome and Sirius Red stains (Figures 6.42(d) and (g)). The capsule adjacent to the ES layer is dense and vascularized while the capsule adjacent to the CES layer is dense. At day 28, transmural collagen can be observed within the CES layer as shown by the Trichrome and Sirius Red stains (Figures 6.42(e) and (h)). The foreign body response consisting of fibroblasts, macrophages and FBGCs is observed at the ES-tissue interface and within the CES layer. By day 56, the FBGCs contain many nuclei and appear to be mature. Transmural collagen fibers are observed within the CES as shown by the

Sirius red stain (Figure 6.42(i)). The fibrous capsules at both scaffold-tissue interfaces of the BLDD are thin.

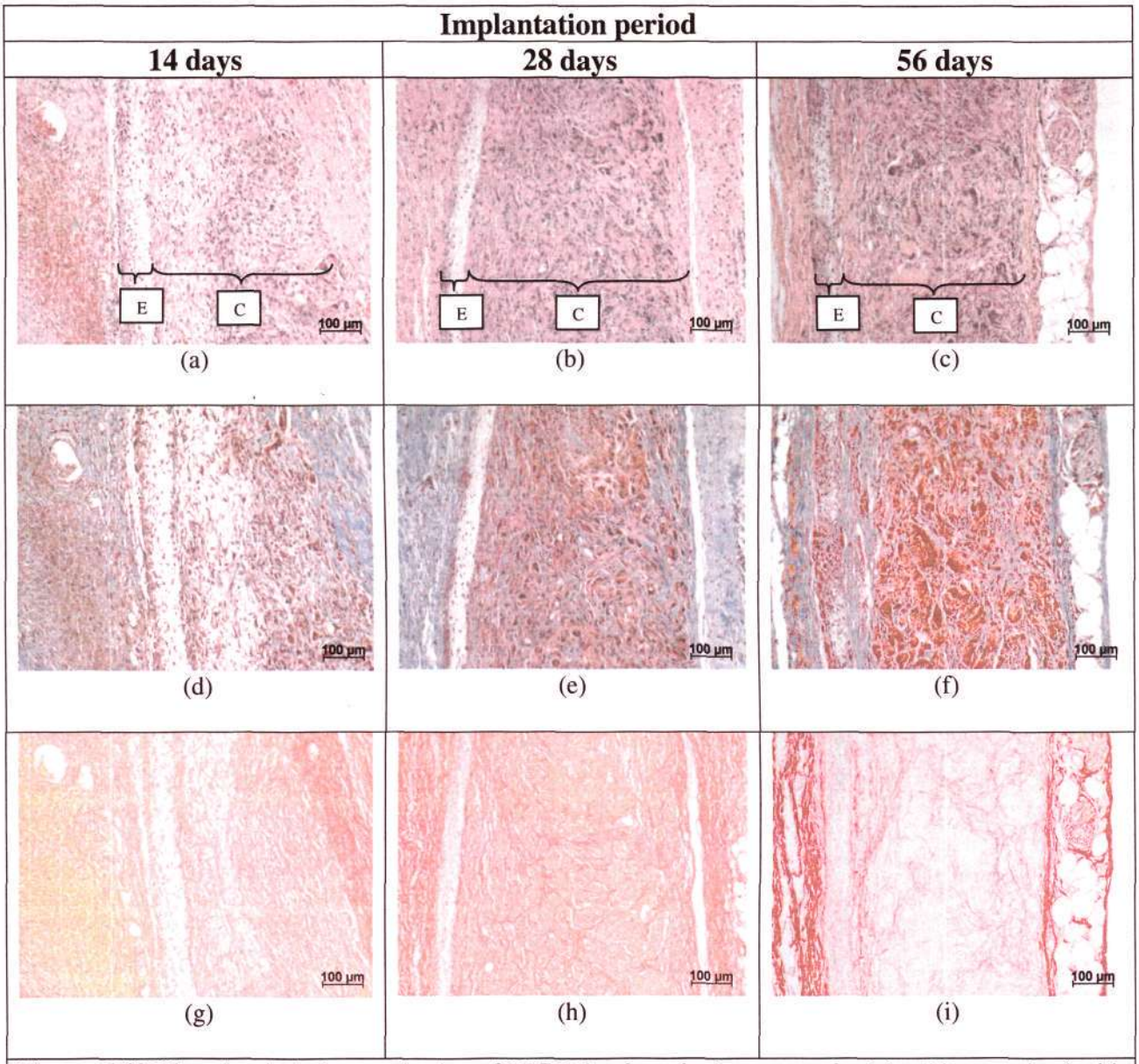

Figure 6.42 Histochemical characterization of BLDD implanted subcutaneously. (a) – (c) are stained with H&E, (d) – (f) are stained with Masson's Trichrome and (g) – (i) are stained with Sirius red.
(C: Cryogenic electrospun scaffold layer, E: conventional electrospun scaffold layer)
BLDD: BLES with ES layer facing underlying muscle.

The foreign body reactions for the BLDU and BLDD are observed at the scaffold-tissue interface at the ES layer and within the CES layer. This observation is similar to the previous section, when the ES and CES were implanted individually. The large pores of the CES layer allow cell infiltration and vascularization, thus, the foreign body reaction is observed within the CES.

It is also observed that a dense fibrous collagenous capsule surrounded the ES layer of the BLDU and BLDD at 56 days (Figures 6.40(f) and (i), Figures 6.42(f) and (i)). One capsule was at the scaffold-tissue interface whereas the other was within the CES layer at the ES-CES interface. In the same scaffold, the capsule on the CES-tissue interface was thin and loosely packed. This suggests that there was a less distinct scaffold-tissue boundary at the CES-tissue interface because the CES allowed cell infiltration. In contrast, at both interfaces of the ES layer, a dense capsule was formed since cells were unable to penetrate the scaffold.

In summary, the results shown in Section 6.6 demonstrate the ability of the CES to promote *in vivo* cell infiltration and vascularization when implanted individually and as part of the BLES. Conventional ES, which was used as a control in both cases, hindered cell infiltration and prevented vascularization *in vivo*. These results show that the cryogenic electrospinning technique has overcome a major limitation of conventional electrospinning and advance the adoption of cryogenic electrospinning in fabricating scaffolds for tissue engineering applications.

Chapter 7 Conclusions and Future Work

7.1 Conclusions

The cryogenic electrospinning technique developed in this project enables the fabrication of an electrospun scaffold with large inter-connected pores using the ice crystals as templates. This addresses the limitation of conventional electrospinning technique and thus, adds versatility to the use of electrospun scaffold in tissue engineering applications

The key contributions from this project are as follows:

(1) The successful development of the cryogenic electrospinning technique that expands the pores of electrospun scaffolds beyond 5μm in size. The porosity of the resulting CES is 63 ± 5% as compared to 52 ± 4% of the ES.

(2) The process study was successfully carried out and the effects of the environment's humidity, mandrel temperature and rate of fiber deposition on the pore size and porosity of the CES were determined. A correlation is proposed that relates the scaffold porosity as a function of the environment's humidity. This correlation can be used to predict the porosity of the CES for humidities between 40 – 70% RH at a mandrel temperature of -35°C.

(3) The successful fabrication of a BLES that consists of a conventional ES layer and a CES layer. The design of the BLES is derived from the understanding of the histo-architecture of the oesophageal mucosal-submucosal tissue, which consists of a dense basement membrane and an open porous loose connective tissue. The

fabrication was carried out in a single process by varying the environment's humidity from 50% RH, for fabricating the CES layer, to 25% RH for fabricating the ES layer. The BLES was used successfully in the co-culture of PEECs and PESMCs and the cells, guided by the different scaffold pore size, were organized in a way that resembles the oesophageal mucosa-submucosa tissue.

(4) The CES exhibits improved *in vitro* cell infiltration and *in vivo* cell infiltration and vascularization over the ES. For *in vitro* cell infiltration, a 50μm thick cell-CES construct can be maintained successfully under static culture conditions. No cell infiltration was observed for the ES under the same conditions. For *in vivo* studies, the CES were 100% infiltrated with cells by day 28 and remained permeated till day 56. In contrast, the depth of cell infiltration for the ES was 36 ± 9% at day 56. Histochemical analyses show that the CES was completely infiltrated with cells and there were vascularization within the CES as early as day 14. For ES, there was limited cell infiltration and no vascularization was observed till day 56. The CES and ES layers in the BLES exhibit similar *in vivo* histochemical responses as their counterparts, which were implanted separately.

In overcoming the pore size limitation of conventional electrospun scaffolds, it is believed that the contributions made in this project will advance the adoption of cryogenic electrospinning as a method of scaffold fabrication in tissue engineering.

7.2 Future work

7.2.1 Modeling of cryogenic electrospinning process

The novel cryogenic electrospinning technique developed in this project is a combination of two processes: conventional electrospinning and frost formation. The preliminary empirical correlation proposed used the frost porosity to predict the porosity of the CES in relation to the absolute humidity. However, this empirical correlation can be further enhanced and defined with more experimental investigations. Ultimately, an empirical model that correlates the CES porosity with the remaining dimensionless terms in Equation 6.3 should be established. It is predicted that the form of the empirical correlation should resemble that of Equation 4.3 closely.

7.2.2 Hybrid porcine oesophageal ECM-CES scaffold

An extension to this project is the development of a novel method of incorporating the CES onto the acellular porcine oesophageal ECM to form a hybrid scaffold[201]. The purpose of producing a hybrid scaffold is to combine the advantages of CES with that of the acellular ECM for tissue engineering applications. In addition, the hybrid scaffold allows the CES to be supported on an acellular ECM, which strengthens the CES mechanically and allows the mechanical properties of the hybrid scaffold to resemble that of the native oesophageal tissue more closely.

This method involves the use of an adhesive interface (e.g. fibrin glue) to bond the electrospun fibers to the ECM. Electrospun fibers were deposited on the fibrin interface, which was applied on the acellular ECM abluminal surface attached to the chilled mandrel. The aqueous based adhesive was further made porous as the ECM

was maintained below subzero temperatures such that ice crystals formed within the adhesive. Subsequent lyophilization removed the ice crystals by sublimation, forming a wholly porous hybrid scaffold.

Future work on the hybrid scaffold can involve characterizing its mechanical properties and degradation behaviour. The co-culture experiment shown in Section 6.5.3 can be applied to the hybrid scaffold. The basement membrane of the acellular ECM can be used to support the epithelium while the CES can be used to reconstruct the muscularis externa, which was removed in the decellularization process of the oesophageal tissue.

7.2.3 Functional replacement for oesophagus – *in vivo* patch model

The long-term goal of our research group is to engineer a functional tissue construct for replacement of the diseased oesophagus. While the results shown in this project focus mainly on scaffold engineering, scaffold-cell interactions and subcutaneous implantation, it is envisioned that these preliminary results will contribute to the understanding and development of more sophisticated tissue constructs in the long run. One possible milestone is to show the feasibility of an *in vivo* patch replacement of a defect created in the porcine oesophagus.[44] The patch can be made by pre-seeding porcine oesophageal cells on a hybrid acellular porcine oesophageal ECM-CES scaffold and conditioning the construct in a bioreactor. The construct can then be used as a patch replacement for a defect of the oesophagus to assess the biointegration of the graft into the recipient tissue.

References

1. Langer R, Vacanti JP, *Tissue engineering*. Science (1993); **260**: 920-26.

2. Fuchs JR, Nasseri BA, Vacanti JP, *Tissue engineering: A 21st century solution to surgical reconstruction*. Annals of Thoracic Surgery (2001); **72(2)**: 577-591.

3. Lechler RI, Sykes M, Thomson AW, Turka LA, *Organ transplantation - how much of the promise has been realized?* Nature Medicine (2005); **11(6)**: 605-613.

4. Kim BS, Mooney DJ, *Development of biocompatible synthetic extracellular matrices for tissue engineering*. Trends in Biotechnology (1998); **16(5)**: 224-230.

5. Persidis A, *Tissue engineering*. Nature Biotechnology (1999); **17(5)**: 508-510.

6. Petit-Zeman S, *Regenerative medicine*. Nature Biotechnology (2001); **19(3)**: 201-206.

7. Godbey WT, Atala A. *In vitro systems for tissue engineering*. In: Sipe JD, Kelley CA, McNicol LA, editors. Reparative Medicine: Growing Tissues and Organs: New York Academy of Sciences; (2002); 10-26.

8. *Transplant Data 1997-2006*. 2007 Annual Report of the U.S. Organ procurement and transplantation network and the Scientific Registry of Transplant Registry: United Network of Organ Sharing, Department of Health and Human Services, Health Resources and Services Administration, Healthcare Systems Bureau, Division of Transplantation, Rockville, MD; (2007).

9. Chapekar MS, *Tissue engineering: Challenges and opportunities*. Journal of Biomedical Materials Research (2000); **53(6)**: 617-620.

10. Zandonella C, *Tissue engineering: The beat goes on*. Nature (2003); **421(6926)**: 884-886.

11. Goldstein SA. *Tissue engineering - Functional assessment and clinical outcome*. Reparative Medicine: Growing Tissues and Organs; (2002); 183-192.

12. Lysaght MJ, Reyes J, *The growth of tissue engineering*. Tissue Engineering (2001); **7(5)**: 485-493.

13. Lysaght MJ, Hazlehurst AL, *Tissue engineering: The end of the beginning*. Tissue Engineering (2004); **10(1/2)**: 309-320.

14. Organogenesis. Apligraf product homepage (www.apligraf.com) accessed on 24th June 2008. 2008.

15. Ferlay J, Bray F, Pisani P, Parkin DM, *Globocan 2002: Cancer incidence, mortality and prevalence worldwide*. International Agency for Research on Cancer CancerBase (2004); **5(2)**.

16. Sato M, Ando N, Ozawa S, Nagashima A, Kitajima M, *A hybrid artificial esophagus using cultured human oesophageal epithelial cells*. American Society for Artificial Internal Organs Journal (1993); **39**: M554-M557.

17. Pham QP, Sharma U, Mikos AG, *Electrospinning of polymeric nanofibers for tissue engineering applications: A review*. Tissue Engineering (2006); **12(5)**: 1197-1211.

18. Ma ZW, Kotaki M, Inai R, Ramakrishna S, *Potential of nanofiber matrix as tissue-engineering scaffolds*. Tissue Engineering (2005); **11(1-2)**: 101-109.

19. Lannutti J, Reneker D, Ma T, Tomasko D, Farson D, *Electrospinning for tissue engineering scaffolds*. Materials Science & Engineering C-Biomimetic and Supramolecular Systems (2007); **27(3)**: 504-509.

20. Gavaghan M, *Anatomy and physiology of the esophagus*. Association of periOperative Registered Nurses Journal (1999); **69**: 372-386.

21. Lang IM, Shaker R, *Anatomy and physiology of the upper oesophageal sphincter*. American Journal of Medicine (1997); **103**: 50S-55S.

22. Denardi FG, Riddell RH, *The Normal Esophagus*. American Journal of Surgical Pathology (1991); **15(3)**: 296-309.

23. Squier CA, Kremer MJ, *Biology of oral mucosa and esophagus*. Journal of the National Cancer Institute Monographs (2001); **29**: 7-15.

24. Geboes K, Desmet V, *Histology of the esophagus*. Frontiers in Gastrointestinal Research (1978); **3**: 1-17.

25. Miki H, Ando N, Ozawa S, Sato M, Hayashi K, Kitajima M, *An artificial esophagus constructed of cultured human oesophageal epithelial cells, fibroblasts, polyglycolic acid mesh, and collagen*. American Society for Artificial Internal Organs Journal (1999); **45(5)**: 502-508.

26. Flemming RG, Murphy CJ, Abrams GA, Goodman SL, Nealey PF, *Effects of synthetic micro- and nano-structured surfaces on cell behavior*. Biomaterials (1999); **20(6)**: 573-588.

27. Zhang GH, Su M, Tian DP, Huang HH, Wu XY, Zheng RM, Li QS, *Analysis of basement membrane structure and inflammation during the development of oesophageal squamous cell carcinoma in the chinese chaoshan high risk region*. Cancer Investigation (2008); **26**: 296-305.

28. Leininger BJ, Peacock H, Neville WE, *Oesophageal mucosal regeneration following experimental prosthetic replacement of the esophagus*. Surgery (1970); **67(3)**: 468-473.

29. Lister J, Altman RP, Allison WA, *Prosthetic substitution of thoracic esophagus in puppies: use of Marlex mesh with collagen or anterior rectus sheath*. Annals of Surgery (1965); **162(5)**: 812-824.

30. Dumm JB, Macmanus JE, Anderson AA, McCormick RC, *Oesophageal reconstruction by prostheses*. Journal of Thoracic Surgery (1955); **30(3)**: 368-76.

31. Carachi R, Stokes KB, Brown TCK, Kent M, *Oesophageal anastomosis - an experimental model to study the anastomotic lumen and the influence of a transanastomotic tube*. Journal of Pediatric Surgery (1984); **19(1)**: 90-93.

32. Watanabe K, Mark JBD, *Segmental replacement of the thoracic esophagus with a silastic prosthesis*. The American Journal of Surgery (1971); **121**: 238-240.

33. Grikscheit T, Ochoa ER, Srinivasan A, Gaissert H, Vacanti JP, *Tissue-engineered esophagus: Experimental substitution by onlay patch or interposition*. Journal of Thoracic and Cardiovascular Surgery (2003); **126(2)**: 537-544.

34. Macdonald A, Carachi R, Gibson A, *A New Oesophageal Tube - Assessment of Collagen Vicryl Composite Membrane*. Journal of Pediatric Surgery (1992); **27(7)**: 856-858.

35. Natsume T, Ike O, Okada T, Shimizu Y, Ikada Y, Tamura N, *Experimental studies of a hybrid artificial esophagus combined with autologous mucosal cells*. American Society for Artificial Internal Organs Transactions (1990); **36**: M435-M437.

36. Ike O, Shimizu Y, Okada T, Natsume T, Watanabe S, Ikada Y, Hitomi S, *Experimental studies on an artificial esophagus for the purpose of neoesophageal epithelialization using a collagen-coated silicone tube.*

American Society for Artificial Internal Organs Transactions (1989); **35**: 226-228.

37. Takimoto Y, Nakamura T, Yamamoto Y, Kiyotani T, Teramachi M, Shimuzu Y, *The experimental replacement of a cervical oesophageal segment with an artificial prosthesis with the use of collagen matrix and a silicone stent.* Journal of Thoracic and Cardiovascular Surgery (1998); **116(1)**: 98-106.

38. Natsume T, Ike O, Okada T, Takimoto N, Shimizu Y, Ikada Y, *Porous Collagen Sponge for Oesophageal Replacement.* Journal of Biomedical Materials Research (1993); **27(7)**: 867-875.

39. Yamamoto Y, Nakamura T, Shimizu Y, Matsumoto K, Takimoto Y, Kiyotani T, Sekine T, Ueda H, Liu Y, Tamura N, *Intrathoracic oesophageal replacement in the dog with the use of an artificial esophagus composed of a collagen sponge with a double-layered silicone tube.* Journal of Thoracic and Cardiovascular Surgery (1999); **118(2)**: 276-286.

40. Yamamoto Y, Nakamura T, Shimizu Y, Takimoto Y, Matsumoto K, Kiyotani T, Yu L, Ueda H, Sekine T, Tamura N, *Experimental replacement of the thoracic esophagus with a bioabsorbable collagen sponge scaffold supported by a silicone stent in dogs.* American Society for Artificial Internal Organs Journal (1999); **45(4)**: 311-316.

41. Badylak S, Meurling S, Chen M, Spievack A, Simmons-Byrd A, *Resorbable bioscaffold for oesophageal repair in a dog model.* Journal of Pediatric Surgery (2000); **35(7)**: 1097-1103.

42. Isch JA, Engum SA, Ruble CA, Davis MM, Grosfeld JL, *Patch esophagoplasty using AlloDerm as a tissue scaffold.* Journal of Pediatric Surgery (2001); **36(2)**: 266-268.

43. Kaiitani M, Wadia Y, Hinds MT, Teach J, Swartz KR, Gregory KW, *Successful repair of oesophageal injury using an elastin based biomaterial*

patch. American Society for Artificial Internal Organs Journal (2001); **47(4)**: 342-345.

44. Marzaro M, Vigolo S, Oselladore B, Conconi MT, Ribatti D, Giuliani S, Nico B, Perrino G, Nussdorfer GG, Parnigotto PP, *In vitro and in vivo proposal of an artificial esophagus*. Journal of Biomedical Materials Research Part A (2006); **77A(4)**: 795-801.

45. Hollister SJ, *Porous scaffold design for tissue engineering*. Nature Materials (2005); **4(7)**: 518-524.

46. Woo KM, Chen VJ, Ma PX, *Nano-fibrous scaffolding architecture selectively enhances protein adsorption contributing to cell attachment*. Journal of Biomedical Materials Research Part A (2003); **67A(2)**: 531-537.

47. Yang SF, Leong KF, Du ZH, Chua CK, *The design of scaffolds for use in tissue engineering. Part 1. Traditional factors*. Tissue Engineering (2001); **7(6)**: 679-689.

48. Lu QJ, Ganesan K, Simionescu DT, Vyavahare NR, *Novel porous aortic elastin and collagen scaffolds for tissue engineering*. Biomaterials (2004); **25(22)**: 5227-5237.

49. Bezuidenhout D, Davies N, Zilla P, *Effect of well defined dodecahedral porosity on inflammation and angiogenesis*. American Society for Articial Internal Organs Journal (2002); **48(5)**: 465-471.

50. Chaikof EL, Matthew H, Kohn J, Mikos AG, Prestwich GD, Yip CM. *Biomaterials and scaffolds in reparative medicine*. In: Sipe JD, Kelley CA, McNicol LA, editors. Reparative Medicine: Growing Tissues and Organs: New York Academy of Sciences; (2002); 96-105.

51. Oh SH, Park IK, Kim JM, Lee JH, *In vitro and in vivo characteristics of PCL scaffolds with pore size gradient fabricated by a centrifugation method*. Biomaterials (2007); **28(9)**: 1664-1671.

52. Jain RK, Au P, Tam J, Duda DG, Fukumura D, *Engineering vascularized tissue*. Nature Biotechnology (2005); **23(7)**: 821-823.

53. Sipe JD. *Tissue engineering and reparative medicine*. In: Sipe JD, Kelley CA, McNicol LA, editors. Reparative Medicine: Growing Tissues and Organs: New York Academy of Sciences; (2002); 1-9.

54. Hodde J, *Naturally occurring scaffolds for soft tissue repair and regeneration*. Tissue Engineering (2002); **8(2)**: 295-308.

55. Ko IK, Iwata H, *An approach to constructing three-dimensional tissue*. Annals of the New York Academy of Sciences (2001); **944**: 443-455.

56. Brauker JH, Carrbrendel VE, Martinson LA, Crudele J, Johnston WD, Johnson RC, *Neovascularization of Synthetic Membranes Directed by Membrane Microarchitecture*. Journal of Biomedical Materials Research (1995); **29(12)**: 1517-1524.

57. Marshall AJ, Irvin CA, Barker T, Sage EH, Hauch KD, Ratner BD, *Biomaterials with tightly controlled pore size that promote vascular in-growth*. Abstracts of Papers of the American Chemical Society (2004); **228**: U386-U386.

58. Anderson JM. *Biocompatibility of tissue engineered implants*. In: Patrick Jr CW, Mikos AG, Mcintire LV, editors. Frontiers in Tissue Engineering: Pergamon; (1998); 152-165.

59. Anderson JM, *Biological responses to materials*. Annual Review of Materials Research (2001); **31**: 81-110.

60. Anderson JM, *Inflammatory response to implants*. American Society for Artificial Internal Organs Transactions (1988); **XXXIV**: 101-107.

61. Ratner BD, Bryant SJ, *Biomaterials: Where we have been and where we are going*. Annual Review of Biomedical Engineering (2004); **6**: 41-75.

62. Anderson JM, Rodriguez A, Chang DT, *Foreign body reaction to biomaterials*. Seminars in Immunology (2008); **20(2)**: 86-100.

63. Ratner BD, *Reducing capsular thickness and enhancing angiogenesis around implant drug release systems*. Journal of Controlled Release (2002); **78(1-3)**: 211-218.

64. Northup SJ. *Testing biomaterials: in vitro assessment of tissue compatibility*. In: Ratner BD, Hoffman AS, Schoen FJ, Lemons JE, editors. Biomaterials Science - An introduction to Materials in Medicine: Academic Press; (1996); 215-220.

65. Spector M, Lalor PA. *Testing biomaterials: in vivo assessment of tissue compatibility*. In: Ratner BD, Hoffman AS, Schoen FJ, Lemons JE, editors. Biomaterials Science - An introduction to Materials in Medicine: Academic Press; (1996); 220-228.

66. Choquet D, Felsenfeld DP, Sheetz MP, *Extracellular matrix rigidity causes strengthening of integrin-cytoskeleton linkages*. Cell (1997); **88(1)**: 39-48.

67. Griffith LG. *Emerging design principles in Biomaterials and scaffolds for tissue engineering*. In: Sipe JD, Kelley CA, McNicol LA, editors. Reparative Medicine: Growing Tissues and Organs: New York Academy of Sciences; (2002); 83-95.

68. Badylak SF, Vorp DA, Spievack AR, Simmons-Byrd A, Hanke J, Freytes DO, Thapa A, Gilbert TW, Nieponice A, *Oesophageal reconstruction with ECM and muscle tissue in a dog model*. Journal of Surgical Research (2005); **128(1)**: 87-97.

69. Zhu YB, Leong MF, Ong WF, Chan-Park MB, Chian KS, *Oesophageal epithelium regeneration on fibronectin grafted poly(L-lactic acid-co-caprolactone) (PLLC) nanofiber scaffold*. Biomaterials (2007); **28**: 861-868.

70. Leong MF, Chian KS, Mhaisalkar PS, Ong WF, Ratner BD, *Effect of electrospun poly(D,L-lactide) (PLA) fibrous scaffold with nanoporous surface on cell attachment and protein adsorption*. Journal of Biomedical Materials Research Part A (2007); **Submitted**.

71. Schenke-Layland K, Vasilevski O, Opitz F, Konig K, Riemann I, Halbhuber KJ, Wahlers T, Stock UA, *Impact of decellularization of xenogeneic tissue on extracellular matrix integrity for tissue engineering of heart valves*. Journal of Structural Biology (2003); **143(3)**: 201-208.

72. Gilbert TW, Sellaro TL, Badylak SF, *Decellularization of tissues and organs*. Biomaterials (2006); **27(19)**: 3675-3683.

73. Badylak SF, Geddes LA, Lantz G, Coffey AC; *Tissue graft composition*. United States Patent 4,956,178. (1990).

74. Badylak SF, Voytik SL, Brightman A, Waninger M; *Urinary bladder submucosa derived tissue graft*. United States Patent 5,554,389. (1996).

75. Wei HJ, Liang HC, Lee MH, Huan YC, Chang Y, Sung HW, *Construction of varying porous structures in acellular bovine pericardia as a tissue-engineering extracellular matrix*. Biomaterials (2005); **26(14)**: 1905-1913.

76. Lindberg K, Badylak SF, *Porcine small intestinal submucosa (SIS): a bioscaffold supporting in vitro primary human epidermal cell differentiation and synthesis of basement membrane proteins*. Burns (2001); **27(3)**: 254-266.

77. Badylak SF, Lantz GC, Coffey AC, Geddes LA, *Small intestinal submucosa as a large diameter vascular graft in the dog*. Journal of Surgical Research (1989); **47**: 74-80.

78. Chen F, Yoo JJ, Atala A, *Acellular collagen matrix as a possible "off the shelf" biomaterial for urethral repair*. Urology (1999); **54(3)**: 407-410.

79. Campodonico F, Benelli R, Michelazzi A, Ognio E, Toncini C, Maffezzini M, *Bladder cell culture on small intestinal submucosa as bioscaffold: Experimental study on engineered urothelial grafts*. European Urology (2004); **46(4)**: 531-537.

80. Yoo JJ, Meng J, Oberpenning F, Atala A, *Bladder augmentation using allogenic bladder submucosa seeded with cells*. Urology (1998); **51(2)**: 221-225.

81. Elkins RC, Dawson PE, Goldstein S, Walsh SP, Black KS, *Decellularized human valve allografts*. Annals of Thoracic Surgery (2001); **71(5)**: S428-S432.

82. Badylak SF, Park K, Peppas N, McCabe G, Yoder M, *Marrow-derived cells populate scaffolds composed of xenogeneic extracellular matrix*. Experimental Hematology (2001); **29(11)**: 1310-1318.

83. Sandusky GE, Lantz GC, Badylak SF, *Healing Comparison of Small-Intestine Submucosa and Eptfe Grafts in the Canine Carotid-Artery*. Journal of Surgical Research (1995); **58(4)**: 415-420.

84. Sottile J, *Regulation of angiogenesis by extracellular matrix*. Biochimica Et Biophysica Acta-Reviews on Cancer (2004); **1654(1)**: 13-22.

85. Freytes DO, Badylak SF, Webster TJ, Geddes LA, Rundell AE, *Biaxial strength of multilaminated extracellular matrix scaffolds*. Biomaterials (2004); **25(12)**: 2353-2361.

86. Yang SF, Leong KF, Du ZH, Chua CK, *The design of scaffolds for use in tissue engineering. Part II. Rapid prototyping techniques*. Tissue Engineering (2002); **8(1)**: 1-11.

87. Tan KH, Chua CK, Leong KF, Cheah CM, Cheang P, Abu Bakar MS, Cha SW, *Scaffold development using selective laser sintering of*

polyetheretherketone-hydroxyapatite biocomposite blends. Biomaterials (2003); **24(18)**: 3115-3123.

88. Das S, Hollister SJ, Flanagan C, Adewunmi A, Bark K, Chen C, Ramaswamy K, Rose D, Widjaja E, *Freeform fabrication of Nylon-6 tissue engineering scaffolds*. Rapid Prototyping Journal (2003); **9(1)**: 43-49.

89. Cao T, Ho KH, Teoh SH, *Scaffold design and in vitro study of osteochondral coculture in a three-dimensional porous polycaprolactone scaffold fabricated by fused deposition modeling*. Tissue Engineering (2003); **9**: S103-S112.

90. Woodfield TBF, Malda J, de Wijn J, Peters F, Riesle J, van Blitterswijk CA, *Design of porous scaffolds for cartilage tissue engineering using a three-dimensional fiber-deposition technique*. Biomaterials (2004); **25(18)**: 4149-4161.

91. Matsuzaka K, Walboomers F, de Ruijter A, Jansen JA, *Effect of microgrooved poly-l-lactic (PLA) surfaces on proliferation, cytoskeletal organization, and mineralized matrix formation of rat bone marrow cells*. Clinical Oral Implants Research (2000); **11(4)**: 325-333.

92. Deutsch J, Motiagh D, Russell B, Desai TA, *Fabrication of microtextured membranes for cardiac myocyte attachment and orientation*. Journal of Biomedical Materials Research (2000); **53(3)**: 267-275.

93. Murphy WL, Dennis RG, Kileny JL, Mooney DJ, *Salt fusion: An approach to improve pore interconnectivity within tissue engineering scaffolds*. Tissue Engineering (2002); **8(1)**: 43-52.

94. McGlohorn JB, Holder WD, Grimes LW, Thomas CB, Burg KJL, *Evaluation of smooth muscle cell response using two types of porous polylactide scaffolds with differing pore topography*. Tissue Engineering (2004); **10(3-4)**: 505-514.

95. Ma PX, Choi JW, *Biodegradable polymer scaffolds with well-defined interconnected spherical pore network*. Tissue Engineering (2001); **7(1)**: 23-33.

96. Levenberg S, Burdick JA, Kraehenbuehl T, Langer R, *Neurotrophin-induced differentiation of human embryonic stem cells on three-dimensional polymeric scaffolds*. Tissue Engineering (2005); **11(3-4)**: 506-512.

97. Beatty MW, Ojha AK, Cook JL, Alberts LR, Mahanna GK, Iwasaki LR, Nickel JC, *Small intestinal submucosa versus salt-extracted polyglycolic acid-poly-L-lactic acid: A comparison of neocartilage formed in two scaffold materials*. Tissue Engineering (2002); **8(6)**: 955-968.

98. Sarasam A, Madihally SV, *Characterization of chitosan-polycaprolactone blends for tissue engineering applications*. Biomaterials (2005); **26(27)**: 5500-5508.

99. Ma PX, Zhang RY, *Synthetic nano-scale fibrous extracellular matrix*. Journal of Biomedical Materials Research (1999); **46(1)**: 60-72.

100. Zhang RY, Ma PX, *Synthetic nano-fibrillar extracellular matrices with predesigned macroporous architectures*. Journal of Biomedical Materials Research (2000); **52(2)**: 430-438.

101. Mikos AG, Bao Y, Cima LG, Ingber DE, Vacanti JP, Langer R, *Preparation of Poly(Glycolic Acid) Bonded Fiber Structures for Cell Attachment and Transplantation*. Journal of Biomedical Materials Research (1993); **27(2)**: 183-189.

102. Marshall AJ, *Novel porous biomaterials that promote vascular in-growth - a "6S" story*. The Insider Newsletter University of Washington Engineered Biomaterials (2004); **6**: 3.

103. Whitesides GM, Grzybowski B, *Self-assembly at all scales*. Science (2002); **295**: 2418-2421.

104. Zhang SG, *Fabrication of novel biomaterials through molecular self-assembly*. Nature Biotechnology (2003); **21(10)**: 1171-1178.

105. Hartgerink JD, Beniash E, Stupp SI, *Peptide-amphiphile nanofibers: A versatile scaffold for the preparation of self-assembling materials*. Proceedings of the National Academy of Sciences of the United States of America (2002); **99(8)**: 5133-5138.

106. Malkar NB, Lauer-Fields JL, Juska D, Fields GB, *Characterization of peptide-amphiphiles possessing cellular activation sequences*. Biomacromolecules (2003); **4(3)**: 518-528.

107. Smith LA, Ma PX, *Nano-fibrous scaffolds for tissue engineering*. Colloids and Surfaces B-Biointerfaces (2004); **39(3)**: 125-131.

108. Formals A; *Process and apparatus for preparing artificial threads*. United States Patent 1,975,504. (1934).

109. Formals A; *Methods and apparatus for spinning*. United States Patent 2,160,962. (1939).

110. Formals A; *Artificial thread and method of producing same*. United States Patent 2,187,306. (1940).

111. Formals A; *Methods and apparatus for spinning*. United States Patent 2,349,950. (1944).

112. Scardino FL, Balonis JR; *Fibrous structures containing nanofibrils and other textile fibers*. United States Patent 6,106,913. (2000).

113. Bergshoef MM, Vansco GJ, *Transparent nanocomposites with ultrathin electrospun Nylon-4,6 fiber reinforcement*. Advanced Materials (1999); **11(16)**: 1362-1365.

114. Simm W; *Apparatus for the production of filters by electrostatic fiber spinning*. United States Patent 3,994,528. (1976).

115. Martin GE, Cockshott ID; *Fibrillar product of electrostatically spun organic material*. United States Patent 4,403,331. (1977).

116. Martin GE, Cockshott ID, Fildes FJT; *Fibrillar lining for prosthetic device*. United States Patent 4,044,404. (1977).

117. Bowlin GL, Wnek GE, Simpson DG, Terracio L; *Engineered muscle*. United States Patent 6,592,623. (2003).

118. Pinchuk L, Martin JBJ, Maurin AA; *Breast prostheses*. United States Patent 5,376,117. (1994).

119. Reneker DH, Chun I, *Nanometre diameter fibres of polymer, produced by electrospinning*. Nanotechnology (1996); **7(3)**: 216-223.

120. Taylor G, *Disintegration of water drops in an electric field*. Proceedings of the Royal Society of London, Series A, Mathematical and Physical Sciences (1964); **280(1382)**: 383-397.

121. Taylor G, *The force exerted by an electric field on a long cylindrical conductor*. Proceedings of the Royal Society of London, Series A, Mathematical and Physical Sciences (1966); **291(1425)**: 145-158.

122. Taylor G, *Electrically driven jets*. Proceedings of the Royal Society of London, Series A, Mathematical and Physical Sciences (1969); **313(1515)**: 453-475.

123. Matthews JA, Wnek GE, Simpson DG, Bowlin GL, *Electrospinning of collagen nanofibers*. Biomacromolecules (2002); **3(2)**: 232-238.

124. Deitzel JM, Kleinmeyer J, Harris D, Tan NCB, *The effect of processing variables on the morphology of electrospun nanofibers and textiles*. Polymer (2001); **42(1)**: 261-272.

125. Huang ZM, Zhang YZ, Kotaki M, Ramakrishna S, *A review on polymer nanofibers by electrospinning and their applications in nanocomposites*. Composites Science and Technology (2003); **63(15)**: 2223-2253.

126. Shin YM, Hohman MM, Brenner MP, Rutledge GC, *Experimental characterization of electrospinning: the electrically forced jet and instabilities*. Polymer (2001); **42(25)**: 9955-9967.

127. Fong H, Chun I, Reneker DH, *Beaded nanofibers formed during electrospinning*. Polymer (1999); **40(16)**: 4585-4592.

128. Bhattarai N, Edmondson D, Veiseh O, Matsen FA, Zhang M, *Electrospun chitosan-based nanofibers and their cellular compatibility*. Biomaterials (2005); **26**: 6176-6184.

129. Geng XY, Kwon OH, Jang JH, *Electrospinning of chitosan dissolved in concentrated acetic acid solution*. Biomaterials (2005); **26(27)**: 5427-5432.

130. Son WK, Youk JH, Lee TS, Park WH, *The effects of solution properties and polyelectrolyte on electrospinning of ultrafine poly(ethylene oxide) fibers*. Polymer (2004); **45(9)**: 2959-2966.

131. Bognitzki M, Frese T, Wendorff JH, Greiner A, *Submicrometer shaped polylactide fibers by electrospinning*. Abstracts of Papers of the American Chemical Society (2000); **219**: U491-U491.

132. Bird RD, Stewart WE, Lightfoot EN. *Chapter 1 - Viscosity and the mechanism of momentum transport*. Transport Phenomena: John Wiley & Sons; (1960).

133. Mo XM, Xu CY, Kotaki M, Ramakrishna S, *Electrospun P(LLA-CL) nanofiber: a biomimetic extracellular matrix for smooth muscle cell and endothelial cell proliferation*. Biomaterials (2004); **25(10)**: 1883-1890.

134. Reneker DH, Yarin AL, Fong H, Koombhongse S, *Bending instability of electrically charged liquid jets of polymer solutions in electrospinning*. Journal of Applied Physics (2000); **87(9)**: 4531-4547.

135. Theron A, Zussman E, Yarin AL, *Electrostatic field-assisted alignment of electrospun nanofibres*. Nanotechnology (2001); **12(3)**: 384-390.

136. Theron SA, Zussman E, Yarin AL, *Experimental investigation of the governing parameters in the electrospinning of polymer solutions*. Polymer (2004); **45(6)**: 2017-2030.

137. Reneker DH, Kataphinan W, Theron A, Zussman E, Yarin AL, *Nanofiber garlands of polycaprolactone by electrospinning*. Polymer (2002); **43(25)**: 6785-6794.

138. Shields KJ, Beckman MJ, Bowlin GL, Wayne JS, *Mechanical properties and cellular proliferation of electrospun collagen type II*. Tissue Engineering (2004); **10(9-10)**: 1510-1517.

139. Zeugolis DI, Khew ST, Yew ESY, Ekaputra AK, Tong YW, Yung LYL, Hutmacher DW, Sheppard C, Raghunath M, *Electro-spinning of pure collagen nano-tibres - Just an expensive way to make gelatin?* Biomaterials (2008); **29(15)**: 2293-2305.

140. Hirano S, Midorikawa T, *Novel method for the preparation of N-acylchitosan fiber and N-acylchitosan-cellulose fiber*. Biomaterials (1998); **19(1-3)**: 293-297.

141. Suh JKF, Matthew HWT, *Application of chitosan-based polysaccharide biomaterials in cartilage tissue engineering: a review*. Biomaterials (2000); **21(24)**: 2589-2598.

142. Min BM, Lee SW, Lim JN, You Y, Lee TS, Kang PH, Park WH, *Chitin and chitosan nanofibers: electrospinning of chitin and deacetylation of chitin nanofibers*. Polymer (2004); **45(21)**: 7137-7142.

143. Lee KH, Kim HY, Khil MS, Ra YM, Lee DR, *Characterization of nano-structured poly(epsilon-caprolactone) nonwoven mats via electrospinning*. Polymer (2003); **44(4)**: 1287-1294.

144. Yoshimoto H, Shin YM, Terai H, Vacanti JP, *A biodegradable nanofiber scaffold by electrospinning and its potential for bone tissue engineering*. Biomaterials (2003); **24(12)**: 2077-2082.

145. Khil MS, Bhattarai SR, Kim HY, Kim SZ, Lee KH, *Novel fabricated matrix via electrospinning for tissue engineering*. Journal of Biomedical Materials Research Part B-Applied Biomaterials (2005); **72B(1)**: 117-124.

146. You Y, Min BM, Lee SJ, Lee TS, Park WH, *In vitro degradation behavior of electrospun polyglycolide, polylactide, and poly(lactide-co-glycolide)*. Journal of Applied Polymer Science (2005); **95(2)**: 193-200.

147. Boland ED, Telemeco TA, Simpson DG, Wnek GE, Bowlin GL, *Utilizing acid pretreatment and electrospinning to improve biocompatibility of poly(glycolic acid) for tissue engineering*. Journal of Biomedical Materials Research Part B-Applied Biomaterials (2004); **71B(1)**: 144-152.

148. Agrawal CM, Ray RB, *Biodegradable polymeric scaffolds for musculoskeletal tissue engineering*. Journal of Biomedical Materials Research (2001); **55(2)**: 141-150.

149. Berkland C, Pack DW, Kim K, *Controlling surface nano-structure using flow-limited field-injection electrostatic spraying (FFESS) Of poly(D,L-lactide-co-glycolide)*. Biomaterials (2004); **25(25)**: 5649-5658.

150. Zong XH, Ran SF, Kim KS, Fang DF, Hsiao BS, Chu B, *Structure and morphology changes during in vitro degradation of electrospun*

poly(glycolide-co-lactide) nanofiber membrane. Biomacromolecules (2003); **4(2)**: 416-423.

151. Xu CY, Inai R, Kotaki M, Ramakrishna S, *Electrospun nanofiber fabrication as synthetic extracellular matrix and its potential for vascular tissue engineering*. Tissue Engineering (2004); **10(7-8)**: 1160-1168.

152. Li WJ, Laurencin CT, Caterson EJ, Tuan RS, Ko FK, *Electrospun nanofibrous structure: A novel scaffold for tissue engineering*. Journal of Biomedical Materials Research (2002); **60(4)**: 613-621.

153. Sawalha H, Schroen K, Boom R, *Mechanical properties and porosity of polylactide for biomedical applications*. Journal of Applied Polymer Science (2008); **107(1)**: 82-93.

154. Roether JA, Gough JE, Boccaccini AR, Hench LL, Maquet V, Jerome R, *Novel bioresorbable and bioactive composites based on bioactive glass and polylactide foams for bone tissue engineering*. Journal of Materials Science-Materials in Medicine (2002); **13(12)**: 1207-1214.

155. Anderson JM, Shive MS, *Biodegradation and biocompatibility of PLA and PLGA microspheres*. Advanced Drug Delivery Reviews (1997); **28(1)**: 5-24.

156. Sikavitsas VI, Bancroft GN, Mikos AG, *Formation of three-dimensional cell/polymer constructs for bone tissue engineering in a spinner flask and a rotating wall vessel bioreactor*. Journal of Biomedical Materials Research (2002); **62(1)**: 136-148.

157. Matsuda T, *Recent progress of vascular graft engineering in Japan*. Artificial Organs (2004); **28(1)**: 64-71.

158. Xu CY, Inai R, Kotaki M, Ramakrishna S, *Aligned biodegradable nanotibrous structure: a potential scaffold for blood vessel engineering*. Biomaterials (2004); **25(5)**: 877-886.

159. Shin M, Ishii O, Sueda T, Vacanti JP, *Contractile cardiac grafts using a novel nanofibrous mesh*. Biomaterials (2004); **25(17)**: 3717-3723.

160. Altman GH, Horan RL, Lu HH, Moreau J, Martin I, Richmond JC, Kaplan DL, *Silk matrix for tissue engineered anterior cruciate ligaments*. Biomaterials (2002); **23(20)**: 4131-4141.

161. Lee CH, Shin HJ, Cho IH, Kang YM, Kim IA, Park KD, Shin JW, *Nanofiber alignment and direction of mechanical strain affect the ECM production of human ACL fibroblast*. Biomaterials (2005); **26(11)**: 1261-1270.

162. Min BM, Lee G, Kim SH, Nam YS, Lee TS, Park WH, *Electrospinning of silk fibroin nanofibers and its effect on the adhesion and spreading of normal human keratinocytes and fibroblasts in vitro*. Biomaterials (2004); **25(7-8)**: 1289-1297.

163. Khil MS, Cha DI, Kim HY, Kim IS, Bhattarai N, *Electrospun nanofibrous polyurethane membrane as wound dressing*. Journal of Biomedical Materials Research Part B-Applied Biomaterials (2003); **67B(2)**: 675-679.

164. Li M, Mondrinos MJ, Gandhi MR, Ko FK, Weiss AS, Lelkes PI, *Electrospun protein fibers as matrices for tissue engineering*. Biomaterials (2005); **26**: 5999-6008.

165. Schindler M, Ahmed I, Kamal J, Nur-E-Kamal A, Grafe TH, Chung HY, Meiners S, *A synthetic nanofibrillar matrix promotes in vivo-like organization and morphogenesis for cells in culture*. Biomaterials (2005); **26(28)**: 5624-5631.

166. Stankus JJ, Guan JJ, Fujimoto K, Wagner WR, *Microintegrating smooth muscle cells into a biodegradable, elastomeric fiber matrix*. Biomaterials (2006); **27(5)**: 735-744.

167. Levenberg S, Rouwkema J, Macdonald M, Garfein ES, Kohane DS, Darland DC, Marini R, van Blitterswijk CA, Mulligan RC, D'Amore PA and others,

Engineering vascularized skeletal muscle tissue. Nature Biotechnology (2005); **23(7)**: 879-884.

168. Khong YM, Mang J, Zhou SB, Cheung C, Doberstein K, Samper V, Yu H, *Novel intra-tissue perfusion system for culturing thick liver tissue*. Tissue Engineering (2007); **13(9)**: 2345-2356.

169. Subbiah T, Bhat GS, Tock RW, Pararneswaran S, Ramkumar SS, *Electrospinning of nanofibers*. Journal of Applied Polymer Science (2005); **96(2)**: 557-569.

170. Ding B, Kimura E, Sato T, Fujita S, Shiratori S, *Fabrication of blend biodegradable nanofibrous nonwoven mats via multi-jet electrospinning*. Polymer (2004); **45(6)**: 1895-1902.

171. Gupta P, Wilkes GL, *Some investigations on the fiber formation by utilizing a side-by-side bicomponent electrospinning approach*. Polymer (2003); **44(20)**: 6353-6359.

172. Li Y, Ma T, Kniss DA, Lasky LC, Yang ST, *Effects of filtration seeding on cell density, spatial distribution, and proliferation in nonwoven fibrous matrices*. Biotechnology Progress (2001); **17(5)**: 935-944.

173. Lee YH, Lee JH, An IG, Kim C, Lee DS, Lee YK, Nam JD, *Electrospun dual-porosity structure and biodegradation morphology of Montmorillonite reinforced PLLA nanocomposite scaffolds*. Biomaterials (2005); **26(16)**: 3165-3172.

174. Simonet M, Schneider OD, Neuenschwander P, Stark WJ, *Ultraporous 3D polymer meshes by low-temperature electrospinning: Use of ice crystals as a removable void template*. Polymer Engineering and Science (2007); **47**: 2020-2026.

175. Leong MF, Lim TC, Chian KS; *Manufacturing three-dimensional scaffolds using electrospinning at low temperatures*. Patent Cooperation Treaty Patent Application PCT/SG2007/000413. (2006).

176. Leong MF, Rasheed MZ, Lim TC, Chian KS, *In vitro cell infiltration and in vivo cell infiltration and vascularization in a fibrous, highly porous poly(D,L-lactide) scaffold fabricated by cryogenic electrospinning technique*. Journal of Biomedical Materials Research Part A (2008); **accepted June 2008**.

177. Hayashi Y, Aoki A, Adachi S, Hori K, *Study of frost properties correlating with frost formation types*. Journal of Heat Transfer-Transactions of the Asme (1977); **99**: 239-245.

178. Cheng CH, Wu KH, *Observations of early-stage frost formation on a cold plate in atmospheric air flow*. Journal of Heat Transfer-Transactions of the Asme (2003); **125(1)**: 95-102.

179. Qu KY, Xu X, Duan ZW, *Experimental study on behavior of initial frost crystal formation under lower water vapor pressures*. International Communications in Heat and Mass Transfer (2006); **33(7)**: 819-826.

180. Cheng CH, Shiu CC, *Frost formation and frost crystal growth on a cold plate in atmospheric air flow*. International Journal of Heat and Mass Transfer (2002); **45(21)**: 4289-4303.

181. Monaghan PF, Grealish F, Oosthuizen PH, *Frost Growth and Heat-Transfer for a Row of Vertical Cylindrical-Tubes Located Outdoors-General Trends*. Experimental Thermal and Fluid Science (1991); **4(4)**: 406-417.

182. LeGall R, Grillot JM, Jallut C, *Modelling of frost growth and densification*. International Journal of Heat and Mass Transfer (1997); **40(13)**: 3177-3187.

183. Tao YX, Besant RW, Rezkallah KS, *A Mathematical-Model for Predicting the Densification and Growth of Frost on a Flat-Plate*. International Journal of Heat and Mass Transfer (1993); **36(2)**: 353-363.

184. Na BC, Webb RL, *Mass transfer on and within a frost layer*. International Journal of Heat and Mass Transfer (2004); **47(5)**: 899-911.

185. Lee KS, Jhee S, Yang DK, *Prediction of the frost formation on a cold flat surface*. International Journal of Heat and Mass Transfer (2003); **46(20)**: 3789-3796.

186. Tanda G, Fossa M, *Free convection frost growth in a narrow vertical channel*. International Journal of Heat and Mass Transfer (2006); **49(11-12)**: 1946-1957.

187. Fossa M, Tanda G, *Study of free convection frost formation on a vertical plate*. Experimental Thermal and Fluid Science (2002); **26(6-7)**: 661-668.

188. Yun R, Kim Y, Min MK, *Modeling of frost growth and frost properties with airflow over a flat plate*. International Journal of Refrigeration-Revue Internationale Du Froid (2002); **25(3)**: 362-371.

189. Saunders CPR, Rimmer JS, *The electric field alignment of ice crystals in thunderstorms*. Atmospheric Research (1999); **51(3-4)**: 337-343.

190. Wang CC, Huang RT, Sheu WJ, Chang YJ, *Some observations of the frost formation in free convection: with and without the presence of electric field*. International Journal of Heat and Mass Transfer (2004); **47(14-16)**: 3491-3505.

191. Libbrecht KG, Tanusheva VM, *Cloud chambers and crystal growth: Effects of electrically enhanced diffusion on dendrite formation from neutral molecules*. Physical Review E (1999); **59(3)**: 3253-3261.

192. Libbrecht KG, Crosby T, Swanson M, *Electrically enhanced free dendrite growth in polar and non-polar systems*. Journal of Crystal Growth (2002); **240(1-2)**: 241-254.

193. Libbrecht KG, Tanusheva VM, *Electrically induced morphological instabilities in free dendrite growth*. Physical Review Letters (1998); **81(1)**: 176-179.

194. McCabe WL, Smith JC, Harriott P. *Chapter 1 Definitions and Principles*. Unit Operations of Chemical Engineering: McGraw Hill International; (1993).

195. Hines AL, Maddox RN. *Chapter 6: Convective Mass Transfer*. Mass Transfer Fundamentals and Applications: Prentice Hall; (1985).

196. Yang DK, Lee KS, *Dimensionless correlations of frost properties on a cold plate*. International Journal of Refrigeration-Revue Internationale Du Froid (2004); **27(1)**: 89-96.

197. Helgeson ME, Wagner NJ, *A correlation for the diameter of electrospun polymer nanofibers*. American Institute of Chemical Engineers Journal (2007); **53(1)**: 51-55.

198. Jensen P, Jorgensen G, Schnell U. *Dynamic LV-SEM analyses of freezing processes for waterlogged wood*. Eighth ICOM Group on Wet Organic Archaeological Materials Conference; 2001; Stockholm.

199. West CA, He C, Su M, Rawn J, Swanson S, Hay JB, Mentzer SJ, *Stochastic regulation of cell migration from the efferent lymph to oxazolone-stimulated skin*. Journal of Immunology (2001); **166(3)**: 1517-1523.

200. Egorov VI, Schastlivtsev IV, Prut EV, Baranov AO, Turusov RA, *Mechanical properties of the human gastrointestinal tract*. Journal of Biomechanics (2002); **35(10)**: 1417-1425.

201. Chian KS, Leong MF, Gopal EW, Ratner BD; *Three-dimensional porous hybrid scaffold and manufacture thereof*. Patent Cooperation Treaty Patent Application PCT/SG2007/000414. (2006).

202. Pham QP, Sharma U, Mikos AG, *Electrospun poly(epsilon-caprolactone) microfiber and multilayer nanofiber/microfiber scaffolds: Characterization of scaffolds and measurement of cellular infiltration*. Biomacromolecules (2006); **7(10)**: 2796-2805.

203. Beckstead BL, Pan S, Bhrany AD, Bratt-Leal AM, Ratner BD, Giachelli CM, *Oesophageal epithelial cell interaction with synthetic and natural scaffolds for tissue engineering*. Biomaterials (2005); **26**: 6217-6228.

204. Mhaisalkar P, Chian KS, *Long-term culture of porcine oesophageal epithelial cells without use of feeder layers*. Cell Biology International (2007); **31(5)**: 433-437.

205. Wang J, Krysiak PS, Laurier LG, Sims SM, Preiksaitis HG, *Human oesophageal smooth muscle cells express muscarinic receptor subtypes M-1 through M-5*. American Journal of Physiology-Gastrointestinal and Liver Physiology (2000); **279(5)**: G1059-G1069.

206. Sunderkotter C, Goebeler M, Schulzeosthoff K, Bhardwaj R, Sorg C, *Macrophage-derived angiogenesis factors*. Pharmacology & Therapeutics (1991); **51(2)**: 195-216.

Appendices

Appendix A

Empirical correlation for frost formation

Derivation of correlation according to Buckingham Pi thereom

$$\pi_1 = \rho_a^{A} K_a^{B} L_c^{C} t^{D} E^{E} \mu_a$$

$$[=] [ML^{-3}]^{A} [MLT^{-3}K]^{B} [L]^{C} [T]^{D} [MLT^{-3}A^{-1}]^{E} [ML^{-1}T^{-1}]$$

By equating the sum of exponents for each primary dimension,

[M]: $A + B + E + 1 = 0$

[L]: $-3A + B + C + E - 1 = 0$

[T]: $-3B + D - 3E - 1 = 0$

[K]: $B = 0$

[A]: $E = 0$

Solving for A, C and D yields,

$A = -1$

$C = -2$

$D = 1$

This implies that

$$\pi_1 = \frac{t\mu_a}{L_c^{2}\rho_a}$$

$$= \frac{Nt_R\mu_a}{L_c^{2}\rho_a}$$

$$= \frac{N\mu_a}{L_c\rho_a V_a} \qquad , V_a = \frac{L_c}{t_R}$$

$$= \frac{N}{\mathrm{Re}} \qquad , \text{Reynolds number, } \mathrm{Re} = \frac{L_c\rho_a V_a}{\mu_a}$$

$$\pi_2 = \rho_a{}^A K_a{}^B L_c{}^C t^D E^E C_{p,a}$$

$$[=] [ML^{-3}]^A [MLT^{-3}K]^B [L]^C [T]^D [MLT^{-3}A^{-1}]^E [L^2T^{-2}K]$$

By equating the sum of exponents for each primary dimension,

[M]: $A + B + E = 0$

[L]: $-3A + B + C + E + 2 = 0$

[T]: $-3B + D - 3E - 2 = 0$

[K]: $B + 1 = 0$

[A]: $E = 0$

Solving for A, B, C and D yields,

$A = 1$

$B = -1$

$C = 2$

$D = -1$

This implies that

$$\pi_2 = \frac{\rho_a L_c{}^2 C_{p,a}}{K_a t}$$

$$= \frac{L_c{}^2}{\alpha_a t}$$

$$= \frac{1}{Fo} \qquad \text{, Fourier number, } Fo = \frac{\alpha_a t}{L_c{}^2}$$

$$\pi_3 = \rho_a{}^A K_a{}^B L_c{}^C t^D E^E \varepsilon$$

$$[=] [ML^{-3}]^A [MLT^{-3}K]^B [L]^C [T]^D [MLT^{-3}A^{-1}]^E [M^{-1}L^{-3}T^4A^2]$$

By equating the sum of exponents for each primary dimension,

[M]: $A + B + E - 1 = 0$

[L]: $-3A + B + C + E - 3 = 0$

[T]: $-3B + D - 3E + 4 = 0$

[K]: $B = 0$

[A]: $-E + 2 = 0$

Solving for A, C, D and E yields,

$A = -1$

$C = -2$

$D = 2$

$E = 2$

This implies that

$$\pi_3 = \frac{t^2 E^2 \varepsilon}{\rho_a L_c^{\,2}}$$

$$= \frac{N^2 E^2 \varepsilon}{\rho_a V_a^{\,2}}$$

$$= N^2 \psi \qquad \text{, Dimensionless E, } \psi = \frac{E^2 \varepsilon}{\rho_a v_a^{\,2}}$$

For the remaining dimensionless groups,

$$\pi_4 = T^* \qquad \text{, Dimensionless T, } T^* = \frac{(T_a - T_{tp})}{(T_a - T_p)}$$

$$\pi_5 = \omega$$

$$\pi_6 = \rho_f^* \qquad \text{, Dimensionless } \rho_f, \ \rho_f^{\,*} = \frac{\rho_f}{\rho_{ice}}$$

Appendix B

Pictures of electrospinning setup

The equipment setup is shown in Figure B.1 and the main components are labeled as follows:

(i) X-Y-Z axes plotting table
(ii) Plastic syringes with metal needle tips
(iii) Earthing plate
(iv) Air inlet (pneumatic control) to vary flow rates of polymeric solutions
(v) Rotating mandrel that is positively charged (max +35kV)
(vi) High voltage power cord
(vii) Environmental chamber

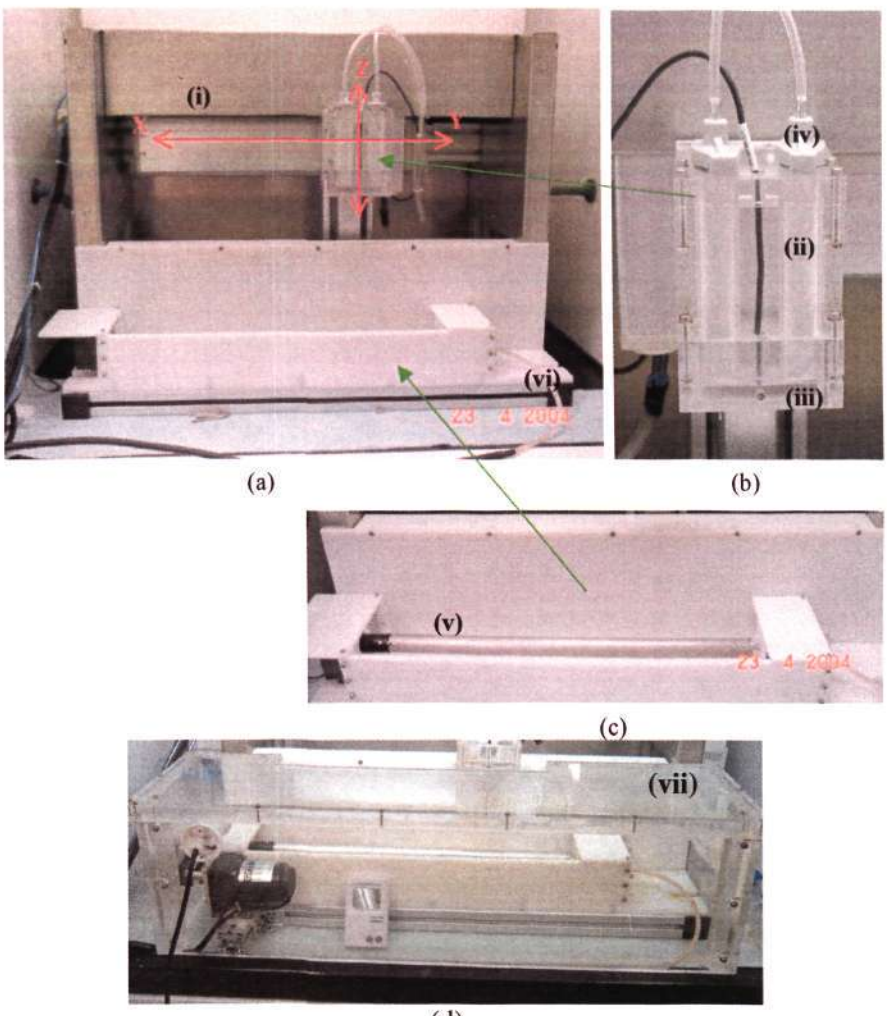

Figure B.1 (a) (a) Electrospinning setup with X-Y-Z axes, (b) housing for polymeric solution syringes with earthed electrode, (c) rotating mandrel that is positively charged and (d) the environmental chamber.

Appendix C

Determination of residual solvent content in electrospun scaffolds

The residual solvent content was determined using Thermogravimetric Analyzer (TGA). The temperature was increased from room temperature to 500°C at a ramp rate of 10°C/min. Figure C.1 shows complete solvent removal after the specimens have been placed in the vacuum oven at 58°C for 48 hours.

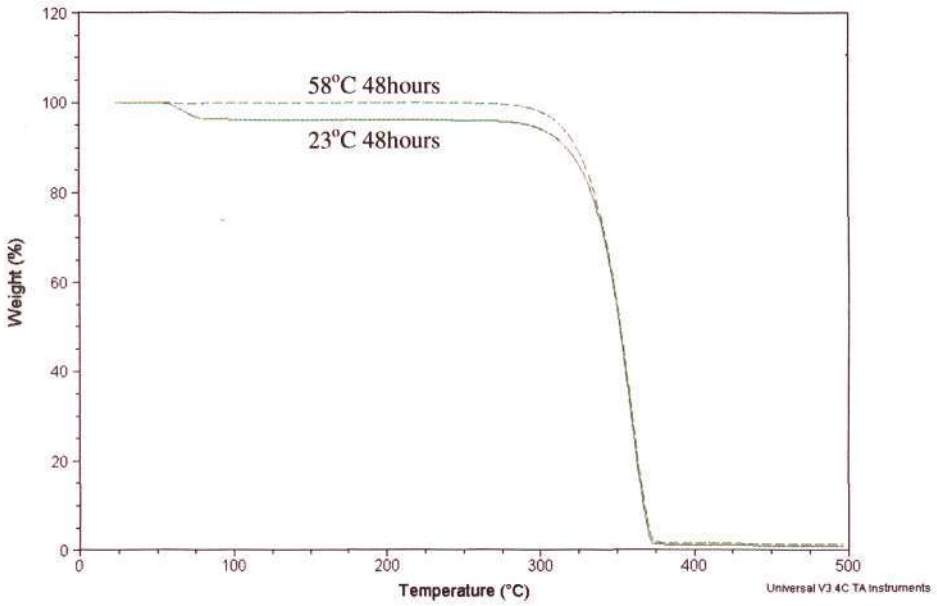

(a)

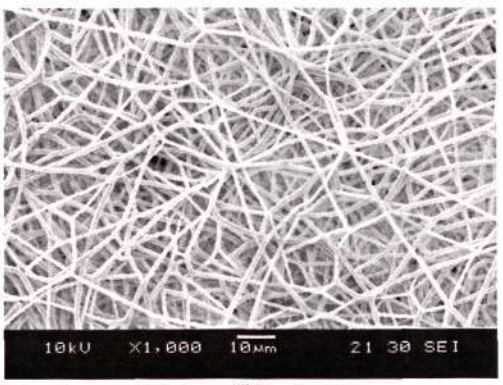

(b)

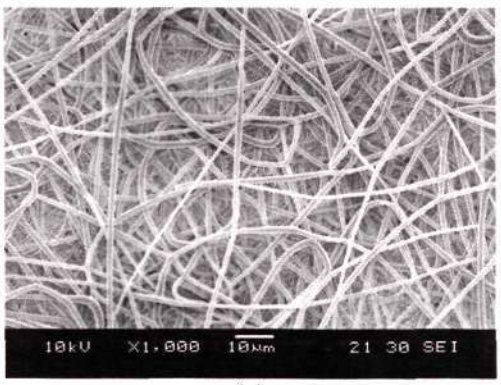

(c)

Figure C.1 (a) TGA graph showing effective removal of solvent after placing specimens in the vacuum oven at 58°C for 48 hours. (b) and (c) are SEM micrographs showing the preservation of the fiber morphology before and after the oven step respectively.

Appendix D

Examples of using image analysis software for measurements

Sample measurement of pore size of electrospun scaffolds

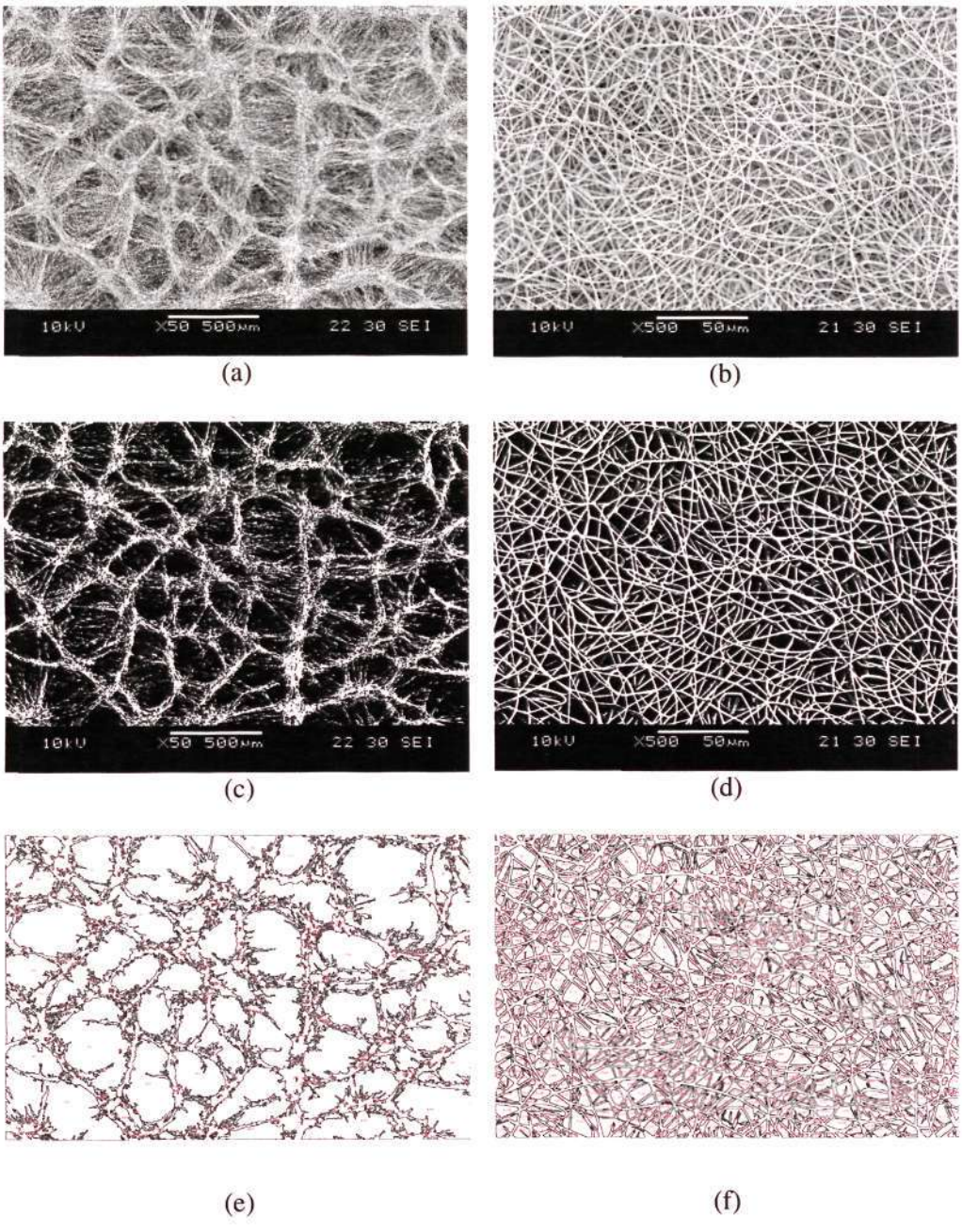

(a) (b)

(c) (d)

(e) (f)

Figure D.1 Pictures showing the process of pore size measurement using the image analysis software (ImageJ). (a) and (b) are SEM micrographs of CES and ES respectively, (c) and (d) are threshold pictures of CES and ES respectively, which eliminate the underlying fibers, (e) and (f) are the results of pore size measurements for CES and ES respectively.

Sample measurement of infiltrated cell nuclei within scaffold

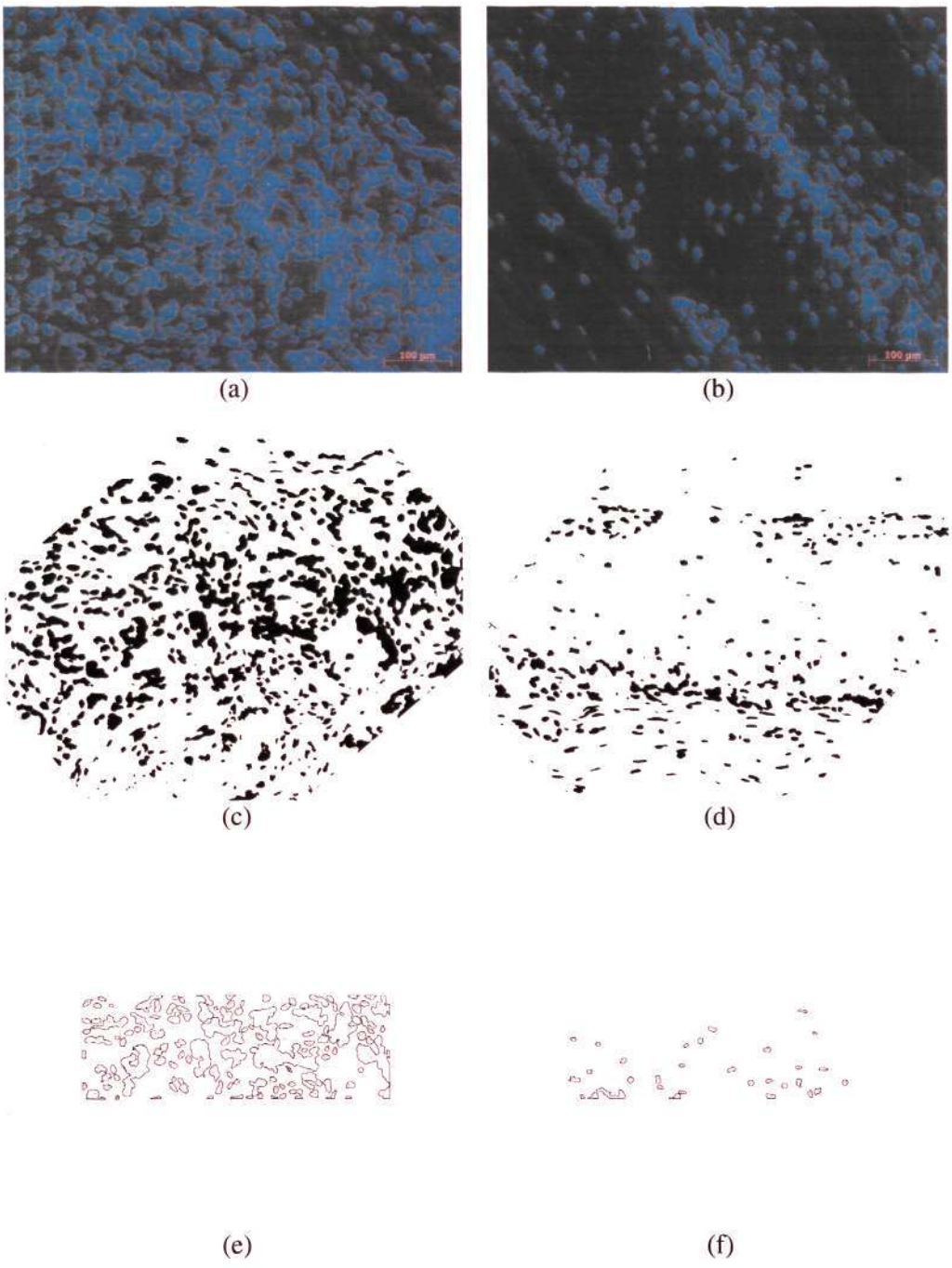

Figure D.2 Pictures showing the process of cell nuclei measurement using the image analysis software (ImageJ). (a) and (b) are Hoescht stained fluorescence pictures of CES and ES respectively, (c) and (d) are binary pictures of CES and ES respectively, which have been rotated such that the scaffold is horizontal, (e) and (f) are the results of cell nuclei area measurements within the specified grid for CES and ES respectively.

Appendix E

Picture shown here provides evidence that the PESMCs infiltrated from the outside of the CES layer of the BLES.

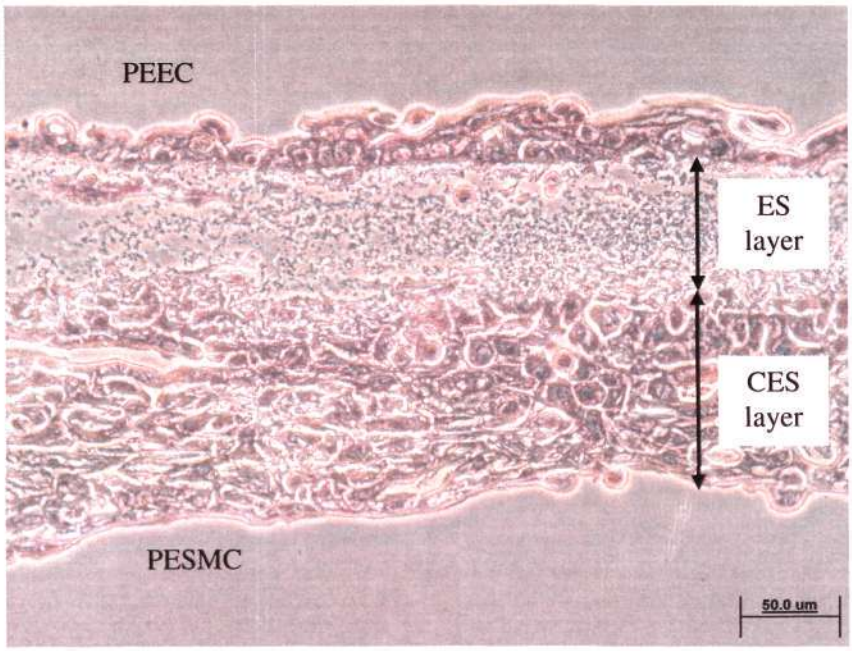

Figure E.1 Pictures showing the co-culture of PEECs and PESMCs on electrospun scaffold after 2 months. BLES taken with smaller aperture to show the location of the fibers (shiny appearance) among the cells.

Appendix F

Raw Data

Data for Figure 6.3(c)

Relative humidity (%)	Temperature (°C)	
	-30	-35
25	0.00261	0.00391
40	0.00654	0.00651
50	0.00823	0.00925
70	0.01179	0.01210

Data for Figure 6.12

Pore area (μm^2) (Std Dev)	Relative humidity (%)			
	25	40	50	70
ES	15.67 (1.36)	16.50 (1.26)	17.59 (2.75)	16.31 (1.46)
CES (-30 °C)	2609.09 (240.69)	4310.84 (1040.26)	3782.21 (623.03)	2318.04 (345.50)
CES (-35 °C)	2236.57 (211.33)	4319.51 (610.07)	3357.38 (517.08)	2410.73 (332.84)

Data for Figure 6.14

Pore area (μm^2) (Std Dev)	Relative humidity (%)			
	25	40	50	70
ES	15.67 (1.36)	16.50 (1.26)	17.59 (2.75)	16.31 (1.46)
CES	863.24 (114.11)	1627.99 (244.16)	5135.43 (1529.58)	2314.08 (307.97)

Data for Figure 6.19

Pore area (μm^2) (Std Dev)	Solution flow rate (ml/hr)		
	0.096	0.16	0.24
ES	10.55 (1.38)	12.05 (0.69)	16.31 (1.46)
CES	4811.39 (241.06)	5135.43 (1529.58)	2095.58 (431.57)

Data for Figure 6.24

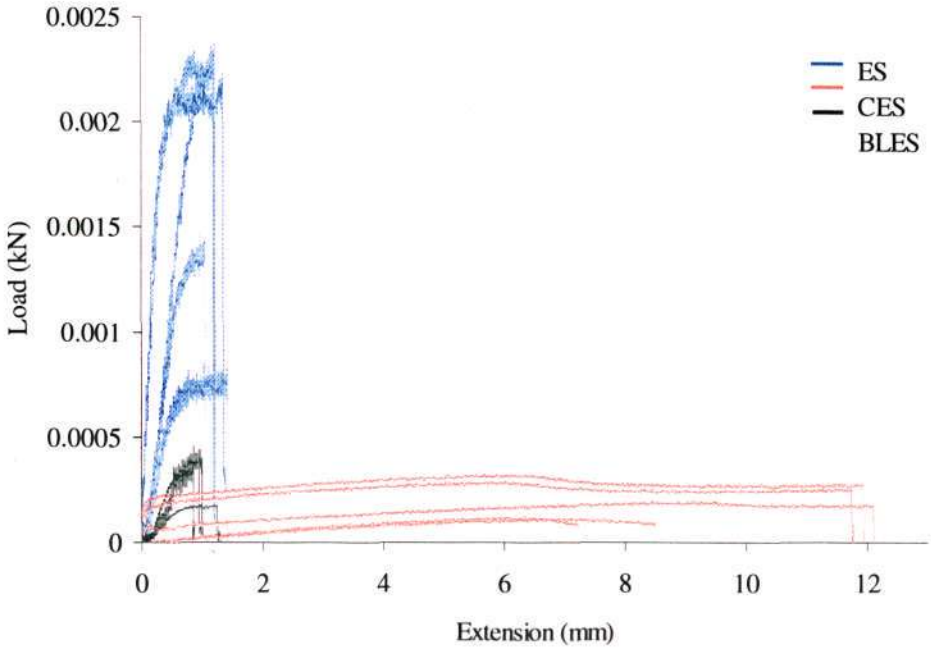

Values (Std Dev)	Tensile Strength (MPa)	Strain at break
ES	1.573 (0.141)	0.164 (0.019)
CES	0.035 (0.008)	1.352 (0.300)
BLES	0.303 (0.097)	0.128 (0.022)

Data for Figure 6.33

% infiltration (Std Dev)	No. of Days		
	14	**28**	**56**
ES	9.81 (7.61)	11.82 (9.25)	35.71 (8.66)
CES	78.30 (15.01)	100 (0.00)	100 (0.00)

Data for Figure 6.34

Area of nuclei (μm^2) (Std Dev)	No. of Days		
	14	**28**	**56**
ES	4145.53 (2245.87)	4357.03 (1844.69)	6403.36 (1856.71)
CES	17990.05 (3974.53)	17956.83 (3630.74)	19557.25 2022.31

Data for Figure 6.38

% infiltration (Std Dev)	No. of Days		
	14	**28**	**56**
BLDU-ES	17.78 (1.92)	38.89 (25.46)	15.00 (6.01)
BLDU-CES	45.57 (7.31)	100 (0.00)	100 (0.00)
BLDD-ES	17.78 (1.92)	13.89 (4.81)	48.89 (29.88)
BLDD-CES	54.92 (19.55)	100 (0.00)	100 (0.00)

Data for Figure 6.39

Area of nuclei (μm^2) (Std Dev)	No. of Days		
	14	**28**	**56**
BLDU-ES	1068.42 (595.92)	1951.05 (604.84)	1997.16 (1020.84)
BLDU-CES	3490.17 (997.27)	4694.88 (1074.73)	4860.83 (970.41)
BLDD-ES	756.67 (248.14)	2157.48 (779.75)	3493.62 (1919.24)
BLDD-CES	1470.61 (191.56)	3752.53 (1047.37)	6064.03 (860.02)